Low Emission Conversion of Fossil Fuels with Simultaneous or Consecutive Storage of Carbon Dioxide

ALI AKBAR EFTEKHARI

Low Emission Conversion of Fossil Fuels with Simultaneous or Consecutive Storage of Carbon Dioxide

Proefschrift

ter verkrijging van de graad van doctor
aan de Technische Universiteit Delft,
op gezag van de Rector Magnificus prof. ir. K.C.A.M. Luyben,
voorzitter van het College voor Promoties,
in het openbaar te verdedigen op donderdag 26 september 2013 om 15:00 uur

door

Ali Akbar EFTEKHARI

Master of Science in Chemical Engineering,
Sharif University of Technology
geboren te Estahban, Iran

Dit proefschrift is goedgekeurd door de promotoren:
Prof.dr. J. Bruinig

Copromoter   Dr. K.H.A.A. Wolf

Samenstelling promotiecommissie:

Rector Magnificus,	voorzitter
Prof. J. Bruining,	Technische Universiteit Delft, promotor
Dr. K.H.A.A. Wolf,	Technische Universiteit Delft, copromotor
Prof. D. Marchesin	Instituto de Matemtica Pura e Aplicada, Brazilië
Prof. S. Durucan	Imperial College London, UK
Prof. P.L.J. Zitha	Technische Universiteit Delft
Prof. C.P.J.W. van Kruijsdijk	Technische Universiteit Delft
Dr. H.J. van der Kooi	Technische Universiteit Delft
Prof.dr.ir. J.D. Jansen	Technische Universiteit Delft, reservelid

To Aida and Maryam,

نہایت امید و اعتماد

To my mother,

and to the memory of my father

Preface

> We have a habit in writing articles published in scientific journals to make the work as finished as possible, to cover up all the tracks, to not worry about the blind alleys or describe how you had the wrong idea at first, and so on. So there isn't any place to publish, in a dignified manner, what you actually did in order to get to do the work.
>
> Richard Feynman

This thesis was performed under the framework of a European Commission supported *HUGE* project: $\underline{H}$ydrogen-oriented $\underline{U}$nderground coal $\underline{G}$asification (UCG) for $\underline{E}$urope. The main goal was to make coal gasification products competitive with other fossil fuels in term of CO_2 emission, for countries with high coal reserves, such as Poland. As the thesis investigates the coal gasification process and methods to reduce its CO_2 footprint, it is divided into two parts: in the first part coal gasification process is studied, and in the second part important issues related to the aquifer storage of CO_2 are discussed.

In the first part, simple chemical equilibrium models are used to predict quality and carbon content of the UCG product. The CO_2 emission per unit energy of UCG product is at least three times higher than natural gas. Various options were considered to lower the CO_2 emission, including in-situ and ex-situ carbonation of synthetic/natural minerals, and aquifer storage of CO_2. The disadvantage of these options is that they require a large amount of energy, which results in a lower coal conversion efficiency. To quantify the energy penalties, based on the principles of thermodynamics and the *exergy* concept, a framework was designed to quantify – in a coherent and fundamental way – the effect of various process parameters on the effectiveness of an energy extraction process. The analysis shows that none of the mentioned processes are able to *effectively* reduce the carbon content of the UCG product. The next step was to analyze a UCG process with alternating injection of air/steam, based on a successful low pressure field experiment performed by a HUGE project partner in Poland. The results of the mathematical model and exergy

analysis showed that alternating injection process at high or low pressure cannot compete with lower CO_2 emission of using natural gas.

To reduce practically the high CO_2 emission value of UCG process to an acceptable level, the focus was shifted from coal conversion to aquifer storage of CO_2.

In the second part of the thesis, two issues related to the aquifer storage of CO_2 are investigated: (1) the permeability impairment due to salt precipitation near the CO_2 injection wells, and its effect on the injectivity and compression power (exergy) requirement; (2) increased storage capacity and long-term CO_2 sequestration due to enhanced transfer rate of CO_2 in water-saturated porous media. Exergetic applicability of carbon capture and sequestration for low emission carbon dioxide fuel consumption, can presently only be achieved if the energy-intensive step of nitrogen-CO_2 separation prior to injection can be avoided. New separation technology could help to make coal usage competitive with natural gas usage as to its carbon footprint.

Contents

Nomenclature

a Number of hydrogen atoms per carbon atom in char

a force parameter of Peng-Robinson EOS, [J/mol]

$\bar{a}$ Number of hydrogen atoms per carbon atom in coal

A_{coal} Coal surface area per unit cavity length [m^2/m]

A_{α} Area of surface α [m^2]

b Number of oxygen atoms per carbon atoms in coal

b volume parameter of Peng-Robinson EOS, [m^3/mol]

$\bar{b}$ Number of oxygen atoms per carbon atoms in coal

C^{α} total molar concentration of phase α, [mol/m^3]

C_{β} Specific heat capacity of β [J/(kg.K)]

$CExC_{M_i}$ cumulative exergy consumption in the production of M_i, [J/mol]

c_i^{α} molar concentration of component i in phase α, [mol/m^3]

$c_{p,i}(T)$ Ideal gas specific heat capacity of component i [J/(mol.K)]

$\mathcal{D}$ average diffusivity of the gas mixture [m^2/s]

$\mathcal{D}_i^{\alpha}$ Fickian diffusion coefficient of component i in phase α, [m^2/s]

$\mathcal{D}_{ij}$ Binary Diffusivity of component i in j [m^2/s]

e_{fuel} CO$_2$ emission per unit exergy of fossil fuel, [kg/J]

e_i error values for the five mass balance equations

e_l error values for the four energy balance equations [J/(m.s)]

$Em_{byproduct}$ by-product CO$_2$ emission per unit mole of M_i, [kg/mol]

Em_{M_i} total CO$_2$ emission in the production of M_i, [kg/mol]

e_{prod} CO_2 emission per unit exergy of final product, [kg/J]

Ex_{CCS} carbon capture and storage CO_2 requirement, [J/kg]

Ex_{CCS}^{prod} exergy requirement for the CCS of product's flue gas, [J/s]

Ex_{fuel} exergy of the extracted energy resource, [J/s]

Ex_i input exergy stream i (heat and power), [J/s]

$Ex_{i,heat}$ equivalent exergy value of heat stream i, [J/s]

$Ex_{i,power}$ equivalent exergy requirement of unit operation i, [J/s]

$Ex_{M_i}^{ch}$ chemical exergy of M_i, [J/mol]

$\widetilde{Ex}_{M_i}$ input exergy of material stream M_i, [J/s]

Ex_{net} net recovered/extracted exergy, [J/s]

Ex_{prod} exergy of the main product, [J/s]

$Ex_{prod,UCG}$ total exergy of the final UCG product, [J/s]

F_{1-2} View factor of surface 1 to surface 2

$\hat{f}_i^{\alpha}$ fugacity of component i in phase α, [Pa]

F_{M_i} input feed to the process/processes P_{M_i}, [mol/s]

g acceleration of gravity $= 9.8$ [m/s^2]

g^E excess Gibbs energy, [J/mol]

Gr Grashof number [dimensionless]

h Coal seam thickness [m]

H_{in} enthalpy of reactants, [J]

$h_i(T_\alpha)$ Enthalpy of component i at the temperature T_α [J/mol]

H_{out} enthalpy of products, [J]

k permeability, [m^2]

k_β Thermal conductivity of β [J/(m.K)]

$K_{carbonation}$ equilibrium constant of the CaO carbonation, [-]

2

K_i K-value of component i, [-]

K_j Equilibrium constant of reaction j [dimensionless]

$k_{r\alpha}$ relative permeability of phase α, [-]

L Length of heat transfer media (β) [m]

LHV_{CH_4} lower heating value of methane, [J/mol]

M matrix of coefficients for the Stefan-Maxwell equations

M_{coal} Coal molecular weight [kg/mol]

M_i input material stream i, [mol/s]

$\dot{m}_{rubble}$ mass flow of rubble in one time step per unit cavity length [kg/(m.s)]

$\mathcal{N}$ Number of gaseous components

N^α total number of moles of phase α, [mol]

n_i^α total number of moles of component i in phase α, [mol]

N_i^α Net flux of component i from the surface α per unit channel length [mol/(m.s)]

$\overline{N}_i^{rubble}$ Net flux of component i injected to the rubble zone per unit channel lenght [mol/(m.s)]

n_i^t total number of moles of component i, [mol]

P Pressure [bar]

p_c capillary pressure, [Pa]

Pe Peclet number [dimensionless]

P_{eq} equilibrium pressure of CaO carbonation reaction, [Pa]

P_i Partial pressure of component i in the cavity [bar]

P_{M_i} process/processes that converts F_{M_i} to M_i, [-]

P^o standard pressure, [Pa]

pr practical, superscript

Q_{1-2} Radiation heat flux from surface 1 to surface 2 [J/s]

q_1, q_2 MHV2 parameters, [-]

Q_{coal} Heat flux into coal seam during the timestep Δt [J/s]

$\dot{Q}_i$ heat stream i, [J/s]

Q_{roof} Heat flux into coal seam during the timestep Δt [J/s]

Q_{rubble} sensible heat of the newly formed rubble mass per unit cavity length [J/(m.s)]

R recovery factor, [-]

R Gas constant 8.314 J/(mol.K)

S^α volumetric phase fraction (saturation) of phase α, [-]

Sc Schmidt number [dimensionless]

Sh Sherwood number [dimensionless]

t time [s]

T_β Temperature of β [K]

$T_\beta^0(X)$ Initial temperature of β [K]

$T_{\beta,s}$ Temperature on the surface of β [K]

T_g bulk gas temperature in the cavity [K]

th theoretical, superscript

$T_{h,i}$ temperature at which $\dot{Q}_i$ is required, [K]

T_{in} Initial temperature, [K]

t_R Specific time in the heat conuction equation [s]

T_{rubble} Rubble zone temperature [K]

T_α Temperature of the interface α [K]

$\mathbf{u}^\alpha$ Darcy velocity of phase α, [m/s]

$U(x)$ Unit step function [dimensionless]

V^α total volume of phase α, [m^3]

V_{CaCO_3} volume of the generated CaCO$_3$, [m^3]

V_{CaO} volume of the unreacted CaO, [m^3]

4

V_{cavity} volume of the underground cavity, $[m^3]$

$v_{c,i}$ volume shift parameter of component i, $[\text{m}^3/\text{mol}]$

v_{coal} Rate of coal consumption [m/s]

W_{comp}^{rev} power requirement of a reversible compressor, [J/s]

W_{grind}^{rev} power requirement of a reversible grinding device, [J/s]

W_i^{rev} power required to drive reversible unit operation i, [J/s]

W_{pump}^{rev} power requirement of a reversible pump, [J/s]

X Dimensionless length [dimensionless]

x Distance from the coal surface inwards [m]

X_{CaO} conversion of CaO, [-]

x_i mole fraction of component i in the boundary layer [dimensionless]

x_i^α mole fraction of component i in phase α, [-]

x_i^b Mole fraction of component i in the cavity

x_i^c Mole fraction of component i on the coal surface

y_i equilibrium mole fraction of the UCG product, [-]

Z Compressibility factor [dimensionless]

Z compressibility of the gas phase, [-]

z Distance from the coal surface [m]

α interface index (roof, coal, rubble)

$\bar{\alpha}_\beta$ Thermal diffusivity $[\text{m}^2/\text{s}]$

$\alpha_i(T)$ vapor pressure parameter in Peng-Robinson EOS, [-]

β coal, roof

ΔH_{coal} Heat of reaction on the coal surface $[\text{J}/(\text{m}^2.\text{s})]$

δ boundary layer thickness [m]

$\Delta_{comb}h$ heat of combustion of coal at T_{in}, [J/mol]

ΔG_{ij} binary interaction parameters of NRTL model

$\Delta h^o_{0,i}$ Enthalpy of formation of component i at the standard temperature and pressure [J/mol]

ΔH_{rubble} Heat of reaction in the rubble zone per unit length of cavity [J/(m.s)]

Δh_{vap} heat of vaporization of water at T_{in}, [J/mol]

Δt Time step for the numerical scheme [s]

ze zero-emission, superscript

ϵ Emissivity of surface α [dimensionless]

ε_i Fraction of injected oxygen that reacts with component i

$\eta_{device,i}$ mechanical efficiency of device i, [-]

η_{driver} mechanical efficiency of an electric driver, [-]

η_{elec} electricity production efficiency, [-]

$\eta_{M_i}^{P_{M_i}}$ exergetic efficiency of process P_{M_i} in production of M_i, [-]

γ_i activity coefficient of component i, [-]

κ_i PRSV EOS parameters, [-]

λ_i eigenvalues of matrix M

$\hat{\mu}_i^{\alpha}$ chemical potential of component i in phase α, [J/mol]

μ^{α} viscosity of phase α, [Pa.s]

ω_1 convergence criteria for the mass balance equations [dimensionless]

ω_2 convergence criteria for the energy balance equations [J/(m.s)]

ω_3 convergence criteria for the boundary layer thickness [m]

φ porosity, []

Φ_{CaCO_3} porosity of the generated $CaCO_3$, [-]

$\hat{\Phi}_i^{\alpha}$ fugacity coefficient of component i in phase α, [-]

Ψ exergetic efficiency, [-]

Ψ^{α} molar phase fraction of phase α, [-]

ρ^{α} mass density of phase α, $[\text{kg/m}^3]$

ρ_{β} Density of β=coal or roof $[\text{kg/m}^3]$

ρ_{coal} Coal density $[\text{kg/m}^3]$

$\rho\left(x^c, T_{coal}\right)$ Density of gas on the coal surface

$\sum Ex_{i,UCG}$ total input exergy streams to the UCG process, $[\text{J/s}]$

$\sum Ex_{M_i,UCG}$ total input cumulative exergy consumption of material streams to the UCG process, $[\text{J/s}]$

τ Dimensionless time [dimensionless]

ζ Number of moles of H_2O releases from roof per unit mole of consumed coal

1. Introduction

> The law that entropy always increases holds, I think, the supreme position among the laws of Nature. If someone points out to you that your pet theory of the universe is in disagreement with Maxwell's equations – then so much the worse for Maxwell's equations. If it is found to be contradicted by observation – well, these experimentalists do bungle things sometimes. But if your theory is found to be against the second law of thermodynamics I can give you no hope; there is nothing for it but to collapse in deepest humiliation.
>
> Sir Arthur Stanley Eddington, The Nature of the Physical World (1915)

1.1. Energy requirement

Energy appears in many different forms, i.e., gravitational energy, kinetic energy, heat, chemical energy, radiant energy, electrical energy, nuclear energy, etc [65]. These forms can be converted to one another in a manner such that the total amount of energy always remains constant. We know the latter fact as the first law of thermodynamics. The former fact, that energy can be converted from one form to another, has given us the opportunity to convert energy from mostly immobile forms like chemical energy to heat and work, e.g. by using a burner and a steam engine. Our ability in the conversion of chemical energy to heat, i.e. the discovery and control of fire [25], and our ability to convert heat to mechanical work, i.e. the invention of steam engine [45] are two major turning points in human history. In addition, from a practical point of view, energy in the form of heat and work are

the forms of energy that are used in our daily life. Historically, heat is generated by combustion of hydrocarbons, i.e., biomass (wood), coal, oil, and gas. Easy combustibility and high energy density of hydrocarbons are the important properties of hydrocarbon that make them popular fuels. In general, conversion of different forms of hydrocarbons to heat is easy and in most cases transfer of the generated heat does not require complicated process equipment. The convenience in working with heat is one of the reasons that in the conversion of energy from one form to another, e.g., conversion of coal to electricity in a power plant, the energy source is first converted to heat and then heat is converted to the target energy form. Presently, almost the entire energy infrastructure relies on the combustion of fossil fuels [42]. One issue with the combustion of fossil fuels is that the optimal conversion of heat to work is a challenge. Sadi Carnot showed that it is not theoretically possible to convert heat to work with 100 % efficiency [32], and in fact part of the heat cannot be converted to work. In addition, in recent years, widespread consumption of fossil fuels has aroused two other issues: first, the societal concern about the role of carbon dioxide emission in climate change is increasing and secondly, the conventional resources of fossil fuels, i.e., the fossil fuel resources that can be extracted easily, are declining. One method that has been proposed to mitigate the effect of carbon dioxide emission is carbon capture and storage (CCS). In this process, carbon dioxide is separated from the combustion products and then transported and injected into an aquifer. To address the decline in conventional fossil fuel resources, unconventional methods of fossil fuels extraction and conversion must be implemented. A combination of unconventional extraction methods with carbon capture and storage has been considered as a solution to the concerns about the fossil fuels consumption [100]. This process can be called a low emission (unconventional) fossil fuels recovery. This thesis describes a methodology that can show the practicality of low emission fossil fuels recovery.

1.2. Recovery of the fossil fuels and carbon emission

Fossil fuels are organic compounds, mostly hydrocarbons (C_mH_n), where m denotes the number of carbon atoms C, and n denotes the number of hydrogen atoms H in one molecule of fossil fuel. Fossil fuels occur with approximate overal composition of CH_4 (natural gas), CH_2 (crude oil), and CH (coal), respectively. The most common method of using the chemical energy of a fossil fuel is to burn it and extract the energy in the form of heat. A fossil fuel reacts with oxygen in a combustion reaction, which reads

$$C_mH_n + \left(m + \frac{n}{4}\right) O_2 \rightarrow mCO_2 + \frac{n}{2}H_2O. \tag{1.1}$$
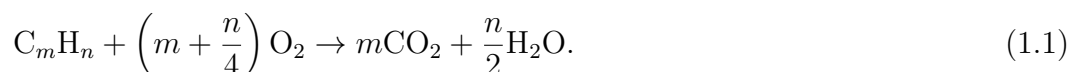
The molar heating value of a hydrocarbon can be estimated roughly by adding 400 kJ per mole of carbon and 100 kJ per mole of hydrogen atom for each mole of the

hydrocarbon fossil fuel. The CO_2 emission is also equal to the number of carbon atoms in a molecule of fossil fuel. In summary, one can estimate the heating value and CO_2 emission factor by

$$HV_{C_mH_n}[\text{kJ/mol}] = 400m + 100n, \tag{1.2}$$

$$C_{C_mH_n}[\text{kg/MJ}] = \frac{m \times MW_{CO_2}}{HV_{C_mH_n}} \times 1000, \tag{1.3}$$

where HV [kJ/mol] is the lower heating value of the fossil fuel, $C_{C_mH_n}$ [kg/MJ] is the CO_2 emission factor per unit energy of fossil fuel, and MW_{CO_2} [kg/mol] is the molecular mass of CO_2 and is equal to 0.044 kg/mol. The approximate heating value of fossil fuels and the CO_2 emission per unit heating value of fossil fuels are shown in Table 1.1. However, the CO_2 that is produced during the combustion of a fossil fuel, shown in Table 1.1, is not the only source of CO_2 emission of a fossil fuel. Fig. 1.1 shows a schematic representation of the life cycle of a fossil fuel from the

Table 1.1.: Approximate heating value and CO_2 emission of fossil fuels

Fossil fuel (C_mH_n)	Natural gas (CH_4)	Oil (CH_2)	Coal (CH)
Heating value [kJ/mol]	800	600	500
CO_2 emission [kg/MJ]	0.055	0.073	0.088

extraction stage to the combustion stage. Each stage requires a certain amount of energy, which is usualy provided from a fossil fuel source, and subsequently, emits CO_2.

1.3. Problem statement

Our fossil fuels requirement can be supplemented from various *sources*. The energy available in the resources first needs to be *recovered*, i.e., extracted, converted, processed, and transported to the final consumer, as shown in Fig. 1.1. Moreover, with current societal concern about the climate change, the CO_2 emission of the recovery and consumption steps should be minimized. All those steps are energy consumers. In other words, we need energy to extract energy and abate its hazardous footprint. These energy requirements, i.e., extraction energy and abatement energy highly depend on the *efficiency* of the implemented methods and devices (or the *extraction process*). Moreover, part of the energy resource will be wasted or converted to undesirable products. A schematic flow diagram of energy streams for an energy extraction process is shown in Fig. 1.2. The gray circle on the left shows the extractable part of an energy resource ($E_{resource}$). It will be extracted by an *extraction process* shown in Fig. 1.2 by a dashed rectangle. This extraction process requires
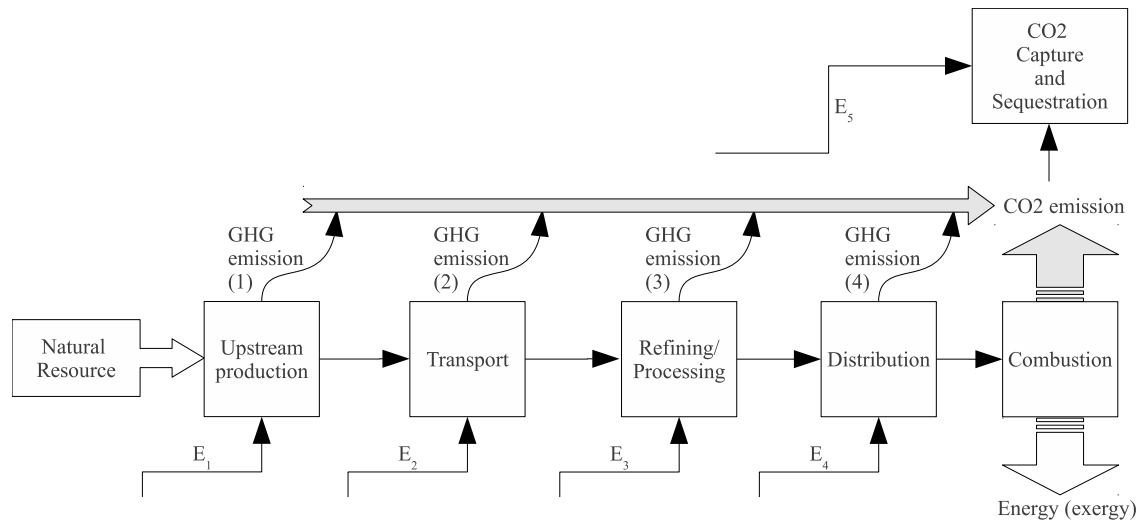
Figure 1.1.: Life cycle of a fossil fuel including carbon capture and sequestration; E_i shows the energy requirement of each step and GHG denotes the greenhouse gas emission from each step; E_1 to E_4 are the energy requirement in upstream production, transport, processing, and distribution of the energy source, respectively; E_5 shows the energy requirement of carbon capture and storage.

a certain amount of energy, which is indicated as the *extraction energy* ($E_{\text{extraction}}$) represented by square in Fig. 1.2. The energy requirement for the abatement of the total hazardous emissions of the process (including the emissions after the consumption of the extracted energy) is indicated as the *abatement energy* ($E_{\text{abatement}}$, shown by a black ellipse). Part of the energy resource will be converted to undesirable products, which is called *waste* (E_{waste}) in Fig. 1.2. The energy resource minus the wasted part is extracted as the desirable product ($E_{\text{product}}=E_{\text{resource}}-E_{\text{waste}}$), which is shown by a incomplete gray circle on the right side of Fig. 1.2.

Continued use of fossil fuels requires methodologies to decrease the carbon emission. Many extraction processes can be devised to reach this goal. The main questions to be answered are:

- Which extraction and abatement method is practical?

- How can we quantify the practicality?

1.4. Efficiency factors and practicality

In comparison of two methods or devices that are designed for the same purpose, the one that requires less and delivers more is called the more *efficient*. Traditionally,
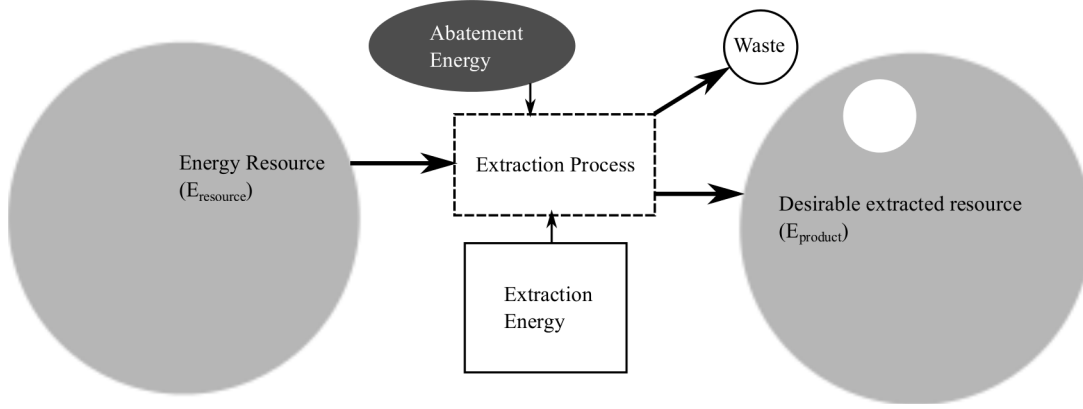
Figure 1.2.: A schematic representation of a fossil fuel extraction process; main input and output energy streams are shown.

efficiency is defined as the useful output divided by the total input. This definition along with the first law of thermodynamics can be applied to the energy extraction process shown in Fig. 1.2 to obtain its energetic efficiency value (η_e), i.e.,

$$\eta_e = \frac{E_{product}}{E_{resource} + E_{abatement} + E_{extraction}}. \tag{1.4}$$

The efficiency factor is informative in the sense that it shows the fraction of total input that is converted to a useful product. It can also be used to compare different methods and processes that serve the same purpose. However, using the efficiency factor in the evaluation of energy conversion processes can be potentially misleading. To clarify this statement, all the energy streams of Fig. 1.2 are redrawn in Fig. 1.3. This new figure shows all the input energy streams as a fraction of the energy resource. The remaining gray area of the large circle shows the *net* value of the extracted or recovered energy. The net recovered energy is defined as the total extracted energy from an energy resource minus the energy required for the extraction processes and abatement of hazardous footprints. It is obvious that the summation of the extraction energy, abatement energy, and wasted energy (white rectangle, black ellipse, and small white circle in Fig. 1.3) must be lower than the amount of extracted energy (the large circle) to make the extraction and abatement methods *practical*. The word practical refers to an energy recovery scheme, which leads to a positive *net recovered energy*, as depicted in Fig. 1.3. An energy recovery factor (R_e) can be defined as the net recovered energy divided by the total extracted energy source, i.e.,

$$R_e = \frac{E_{resource} - (E_{extraction} + E_{abatement} + E_{waste})}{E_{resource}}. \tag{1.5}$$

The important advantage of the recovery factor over the efficiency factor is that the recovery factor can be negative while the efficiency factor, by definition, is always

positive. A negative recovery factor means that the amount of energy required to extract an energy source and clean its environmental footprints is higher than the amount of extracted energy (a net negative recovery) and therefore the extraction method is not practical. This shows that although the efficiency factor can be used effectively to compare different processes, it is not a reliable measure to show whether a process is practical or not.
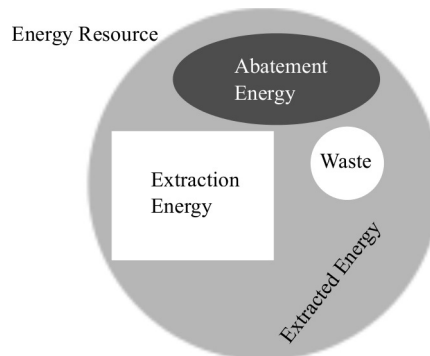
Figure 1.3.: Energy requirement in the extraction of energy and abatement of its hazardous environmental footprint; the recovery factor is defined as the net extracted energy divided by the total amount of energy in the energy resource, i.e., gray area divided by the total area of the big circle.

1.5. The quality of energy

The first law of thermodynamics states that heat can be converted to work and vice versa. However, Sadi Carnot (1796-1832) [32], a French engineer, showed that the conversion of heat to mechanical work in a heat engine has a maximum limit that cannot be surpassed. This limit is a function of the temperature of the heat source and the temperature of the surrounding (heat sink). Based on his calculations, a higher fraction of a heat source can be converted to work when it is at a higher temperature. In other words, at the same environmental condition, heat can have different *qualities* depending on the temperature of the heat source. This maximum fraction of heat that can be converted to work is called the exergy. Exergy can be defined as the maximum amount of work that can be extracted from a system by bringing it to a dead state via a reversible path[1] [43]. In the definition of the energy recovery factor, Eq. (1.5), the energy streams are directly added and subtracted in the numerator, despite the fact that each stream may have a different quality. The concept of exergy can be used to overcome this shortcoming and update the

---

[1]These notions will be explained in more details in the text.

definition of the energy recovery factor. The exergetic recovery factor is defined as

$$\mathrm{R} = \frac{Ex_{\mathrm{resource}} - (Ex_{\mathrm{extraction}} + Ex_{\mathrm{abatement}} + Ex_{\mathrm{waste}})}{Ex_{\mathrm{resource}}}, \qquad (1.6)$$

where Ex_{resource} is the exergy of the extracted fossil fuel resource, $Ex_{\mathrm{extraction}}$ is the exergy requirement for the extraction, processing, transport, and distribution of the fossil fuel, and $Ex_{\mathrm{abatement}}$ is the exergy requirement for the abatement of, mainly, the greenhouse gas emissions but also any other environmental hazardous effects during the whole life cycle of the fossil fuel.

1.6. Objectives

The core of this thesis is to set up a framework, through which practicality of low emission fossil fuels consumption can be evaluated. Here the concept of *exergy*, which describes the quality of energy, is used to define an *exergetic recovery factor*, which serves as a measure for the practicality of an energy conversion process.

The quantification of the extraction process is done by first identifying the most energy intensive steps. The exergy demands of those steps are mainly in three forms: heat streams, power streams, and material streams. Inspired by the classic work of Carnot on "the motive power of heat" [32] and the modern work of Szargut on the concept of exergy and the *cumulative degree of perfection* [154, 156, 157], the exergy streams are quantified in three steps.

The first step is called "*theoretical*"[1]. All devices are assumed to be reversible, i.e., work on a minimal exergy demand that is physically possible, and the exergy value of material streams are assumed to be equal to their chemical exergy. The phase and chemical equilibrium model are used for the quantification of the exergy requirements. The exergetic recovery factor that is calculated with these assumptions is called the *theoretical recovery factor*, which is a measure of the physical or natural obstacles for applying the proposed process.

The second step is called "*practical*". All the values calculated in the theoretical step are corrected by using the state of the art efficiency factors. The calculated exergetic recovery in this step is called the *practical recovery factor*, which is an indicator of the limitations due to state of the art technology.

The third and final step is performed by including $Ex_{\mathrm{abatement}}$, which in this work is the exergy requirement for the capture and storage of CO_2, in the calculation of the exergetic recovery factor. It converts the practical recovery factor to *zero-emission recovery factor*, which is a measure of the practicality of zero-emission recovery of fossil fuels using the state of the art carbon capture and storage technology. A schematic graph that depicts these three steps is shown in Fig. 1.4, where the three recovery factors are plotted versus process parameters.
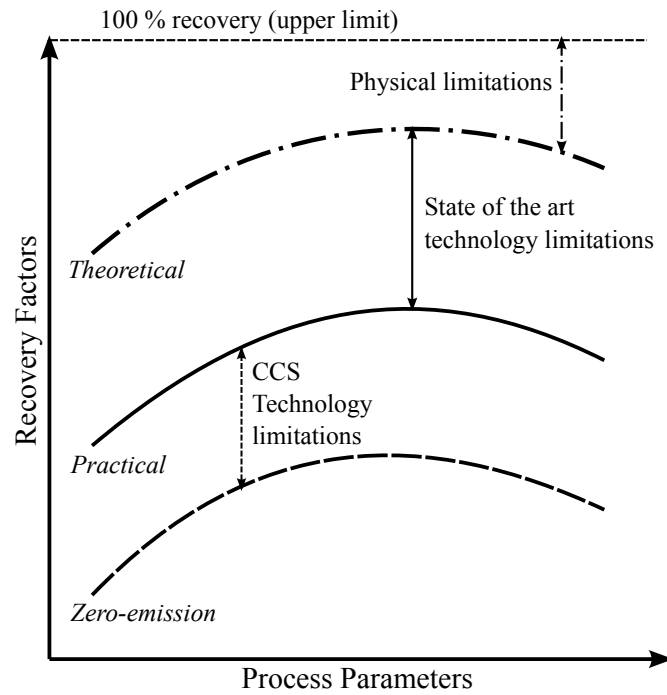
Figure 1.4.: A qualitative representation of the theoretical, practical, and zero-emission recovery factors as a function of parameters of an imaginary energy conversion process

These ideas will be explained by way of example based on an unconventional method of fossil fuels extraction, viz. underground coal gasification (UCG) and various methods to reduce the carbon emission. The same methodology can be applied to analyze any other energy conversion process. Some unconventional issues related to energy conversion methods and CO_2 capture and storage (CCS) will be addressed as well.

1.7. Outline

In order to meet the objectives of this thesis, its content is divided into the following chapters.

Chapter 2, which is the core of this thesis, uses the concept of exergy to establish the framework and specifically define the *recovery factor* as a measure of practicality of energy conversion processes and a methodology for the calculation of its value. Then, this methodology is used to analyze the underground coal gasification process, which is an unconventional method of extraction of deep coal energy. In this method air or oxygen is injected through an injection well in a coal layer. Oxygen reacts with coal and combustible gases and generates heat. This heat is used in the endothermic reactions between water and coal/gases to generate a gaseous product

containing combustible gases, mainly carbon monoxide, hydrogen, and methane. This product has a heating value that is around 20%-30% of the heating value of methane and hence can be considered a substitute for natural gas. However, compared to methane, the carbon content per unit combustion energy of the UCG product is higher. To improve the quality of this gas, i.e., lower its carbon content, two scenarios are considered. In the first scenario, calcium oxide is injected with the feed streams to react with carbon dioxide and bind it in the form of calcium carbonate. Moreover, adding calcium oxide to the reacting system increases the hydrogen content in the UCG product. The most important disadvantage of using CaO is that its production is very energy intensive. The second scenario considers the application of naturaly occuring minerals, e.g., wollastonite (calcium silicate) in ex-situ reactors to capture carbon dioxide from the UCG product in an aqueous carbonation process. A chemical equilibrium model is used to analyze the effect of process parameters on product composition. The equilibrium model is simple enough to minimize the technical details of the process and gives us the opportunity to focus more on the exergy analysis. The viability of the UCG process is analyzed in terms of theoretical (ideal unit operations), practical (state of the art technology), and zero-emission (applying current CO_2 capture and sequestration (CCS) to all sources of CO_2 emission) recovery factors.

One of the assumption made in modeling of the UCG reactions in chapter 2 is that all the reactants, i.e., oxygen, nitrogen, minerals, and coal reach chemical equilibrium also assuming adiabatic condition. This assumption results in an error in the prediction of carbon dioxide and carbon monoxide content of the UCG product. In addition, the process is dynamic and the product composition and the rate of conversion of coal changes with time. The conversion of coal enlarges the cavity which causes the roof of the cavity to collapse. In chapter 3, a model developed by Van Batenburg et al. [161] is extended to include the heat loss to the surrounding strata, mass transfer limitation in the reactions, and the rate of cavity growth for the alternating injection of air and steam in the underground gasification of deep coal. The results are compared to the pilot experiments of Stanczyk et al. [152] and again the exergy analysis is performed to analyze the practicality of the process combined with carbon capture and storage.

In the second part of this thesis, namely chapters 4 and 5, the unconventional issues in CO_2 storage are studied. Chapter 4 deals with salt precipitation in the aquifer due to the evaporation of connate water into supercritical CO_2. The precipitation of salt can decrease the permeability of the aquifer and causes a high pressure drop in particular near the injection well [131], which results in injectivity problems, i.e., high injection pressures [106]. First, a set of well known cubic equations of state and their mixing rules are analyzed with respect to their ability to predict the CO_2 solubility in brine and the density of the gas and liquid phase CO_2-brine mixture. Then the binary interaction parameters are optimized to improve the accuracy of a selected equation of state (and mixing rule) for the prediction of the physical properties of the CO_2-brine system. Then the negative saturation method

[1, 114], which is a combination of negative flash method [169] with the two phase flow relations in porous media by extending the relative permeability curves [74], is extended to a three-phase three-component system with a solid immobile phase. The effect of salt precipitation on the compression energy requirement is analyzed and the methods that can solve the precipitation problem, e.g., preflush with fresh water are discussed.

Injection of gaseous CO_2 in the aquifer does not guarantee a long term sequestration. A long term sequestration requires the gas to dissolve in water or react with the rock. In chapter 5, the enhanced dissolution of CO_2 in water is investigated experimentally and numerically. Due to gravity, the injected CO_2 migrates to the top of the water layer in an aquifer. The dissolution of CO_2 in water increases the mass density of the liquid. A high density layer of the liquid on top of a low density layer becomes unstable in the presence of gravity and convection effect occurs when the high density liquid flows downward and the low density liquid flows upward. The experimental work is done by using a closed vessel filled with sand. The lower half of the sand pack is saturated with water and the other half is saturated with high pressure CO_2 at constant temperature. The pressure of the vessel decreases with time due to the dissolution of CO_2 in water (the system is closed). Previous experimental work in the literature [59, 86, 108, 90] concern only either flow in bulk (no porous media) or flow in small vessels filled with large glass particles (very high permeability), which makes the system sensitive to even tiny fluctuations in temperature or small leakages. The experiment are performed in a relatively large vessel, i.e., 10 liters, and use small sand particles to overcome the above mentioned problems. In the theoretical analysis of this phenomenon, the effect of heat of solution of CO_2 in water and the effect of a capillary transition zone on the rate of mass transfer of CO_2 in water are investigated.

2. Exergy Analysis of Underground Coal Gasification with Simultaneous Storage of Carbon Dioxide

> In the Game of Energy and
> Thermodynamics You Can't Even
> Break Even.
>
> --- Isaac Asimov

Abstract

Various options are considered to reduce CO_2 emissions when utilizing deep coal by applying underground coal gasification (UCG), i.e., in combination with carbonation of synthetic minerals (CaO), conventional UCG followed by ex-situ separation of CO_2 and upgrading the product gas using naturally occurring minerals (wollastonite).

A chemical equilibrium model was used to analyze the effect of process parameters on product composition and use it for an exergy analysis. The result is presented in terms of theoretical (ideal unit operations), practical (state of the art technology), and zero-emission (applying current CO_2 capture and sequestration (CCS) to all sources of CO_2 emission) recovery factors. The results show that underground gasification of deep coal can optimally extract 52-68 % of the coal chemical exergy, but zero-emission extraction gives a negative recovery indicating that it is not practical with current state of the art CCS technology. Using insitu CaO, which will enhance the H_2 production, is theoretically feasible with a recovery factor around 80 %, but is not exergetically feasible with the current state of technology. Ex-situ upgrading of the conventional UCG product gas with wollastonite is exergetically feasible for both practical and zero-emission cases according to the equilibrium model.

2.1. Introduction

Concern with global warming has aroused interest in reducing CO_2 emissions from fossil fuels production. This is a challenge when using coal because, among the fossil fuels it has the largest CO_2 emission per unit combustion energy. For countries that have mainly coal as a fossil fuel resource it is difficult to achieve the targets set for reducing CO_2 emissions. The European Community has an interest to develop technology for reducing CO_2 emissions from coal so that countries with large coal reserves can meet greenhouse gas reduction targets. Poland consumes 1.8 % of the coal world-wide [27]. If CO_2 reduction technologies are economically feasible they may also be adopted by countries like China and India. China consumes 41.3 % of the world coal and accounts for two-third of the global coal consumption growth [27].

Conventional mining of coal has a number of disadvantages; it can leave a large environmental footprint in the form of hazardous gases and water pollutants. In some countries, like India, the coal is of very low quality, i.e., contains large volumes of environmentally undesirable components. Underground coal gasification can be considered as an alternative to mining. Fig. 2.1 shows schematically a UCG process. A feed stream that consists of oxygen (air) and water (steam) is injected to the underground coal layer through an injection well. The injection well should be connected to the production well, e.g., with a horizontal well. The reaction is triggered using a small burner near the production well. The coal consumption front moves towards the injection well and forms an underground cavity while the product gas is collected at the production well head. The reaction is continued by moving the reaction point upstream. This technology, depicted schematically in Fig. 2.1, is called CRIP (controlled retracting injection point). More details on the practical details of UCG can be found elsewhere [9, 69]. A typical composition of UCG product gas has been shown in Table 3.1. The challenge is to enhance the concentration of hydrogen by using the water shift reaction $CO + H_2O \rightleftharpoons CO_2 + H_2$ and simultaneously or subsequently to capture and sequester the CO_2.

Economical feasibility of UCG has been proven for gasification of steeply dipping beds [41]. Economical feasibility appears to be likely for insitu gasification of thick coal layers [76], using CRIP technology. Thin coal layers, which are abundantly occurring in Europe [9], still require more development before economical feasibility could be demonstrated [159]. On the medium term it is to be expected that UCG, even for thin coal layers becomes an important method to recover energy from coal world-wide. The combination of UCG with low CO_2 emissions could cover energy demands in the next few decades and simultaneously reduce concerns about the effect of coal usage on climate change.
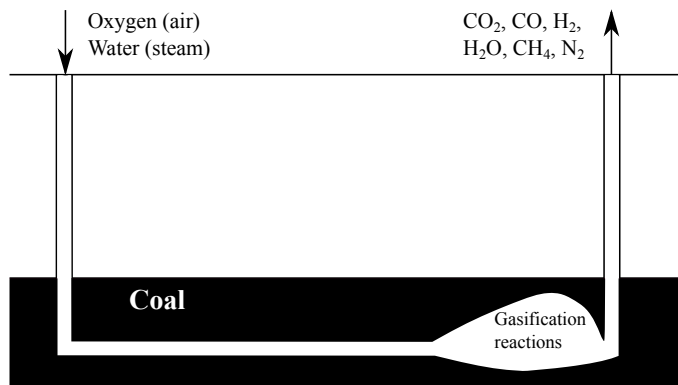
Figure 2.1.: Schematic representation of underground coal gasification process.

Table 2.1.: A typical composition of UCG product gas; average values from the compositions reported in [85]

Component	CO_2	CO	H_2	CH_4	N_2	Other
Mole percent	18.3	7.4	14.9	2.1	55.9	1.4

Based on the definition of exergy, a system that has a different temperature, pressure, or composition from the dead state can be used as an exergy source, which can be extracted in a process. The quality assessment of any energy extraction/conversion process needs an exergy analysis because it is the only available method that can evaluate the technical feasibility of an energy extraction/conversion process [46]. One of the purposes of this paper is to investigate the feasibility of zero-emission underground coal gasification using the result from this analysis.

In literature, exergy analysis has been performed to analyze the efficiency of the ex-situ coal gasification process. All of these studies ignore the capturing and sequestration process. Singh et al. [143] studied the ex-situ coal gasification process for the production of substitute natural gas in order to find the first law -energetic- and second law -exergetic- efficiencies for each significant step and for the overall process. The efficiency is the ratio between the useful output and all input values. They calculated for the ex-situ gasification process an exergetic efficiency of around 60 % for the overall process using relevant process data. They did not include the mining and transportation exergy of coal in the calculation. Rosen [140] calculated the energy and exergy efficiency of different hydrogen production processes including the ex-situ Koppers-Totzek process for the production of high purity and high pressure hydrogen (93 mole percent at 1000 psia). The process consists of air separation, acid gas removal, and two gas upgrading stages; Rosen used pure carbon instead of coal for simplicity and calculated 59 % energetic and 49 % exergetic efficiency. Prins and Ptasinski [128], divided the ex-situ combustion and gasification of coal into a few hypothetical steps and calculated the exergetic efficiency for each

step to clarify the reasons of exergy loss. Using this approach, they optimized the adjustable process parameters like reactor temperature, steam to coal ratio, and equivalence ratio (practical carbon/oxygen to stoichiometric carbon/oxygen ratio) to reduce the exergy loss in each step. They showed that 75 % of the carbon chemical exergy can be extracted in the form of combustible gases, mainly hydrogen and carbon monoxide. They also used carbon instead of coal for simplicity and assumed chemical equilibrium for combustion and gasification reactions. They also compared oxygen and air gasification and calculated their effect on the reaction equilibrium and product quality. They took into account the exergy consumption for separation of oxygen from air, but they did not consider the exergy consumption in mining, processing, and grinding of coal. Ignoring this consumption does not change the optimum temperature and pressure of the reactor; however, it overestimates the exergetic efficiency of the overall process. The paper gives an excellent explanation of exergy loss in a chemical process. Zhihua Wang et al. [168] implemented a chemical equilibrium calculation to study the reacting system of coal/oxygen/water/CaO for different types of coal. They proposed an optimum temperature range between 625-850°C for a gasifier based on the maximum amount of hydrogen that can be obtained and an optimum pressure range between 20-30 bar based on the maximum CO_2 capture efficiency. The research showed that a hydrogen composition of up to 85.9 mole percent can be achieved in the final product depending on the coal quality. They also showed that only 68% of carbon could be converted in the gasifier while the remaining part is used to regenerate CaO from $CaCO_3$.

This paper is divided into two main sections: first the chemical equilibrium calculation is used to model the UCG process with and without calcium oxide/silicate. This equilibrium model can also be implemented in the simulation of ex-situ coal and biomass gasification reactors. Secondly, the results of the first section are used to perform an exergy analysis and propose to use the comparison between theoretical, practical, and zero-emission exergetic recovery of the UCG process as a method to rank efficiencies of energy recovery processes including UCG.

Here three different scenarios are investigated (see Fig. 3.14 for the process flow diagrams): The first scenario, which is called the base case, is to separate CO_2 from the produced gas of a water/oxygen/coal underground gasification process by a currently used chemical process, e.g., the amine cycle and then store it in geological formations [101]. In the second one, CaO is injected in the UCG cavity for insitu capturing of the CO_2. The third scenario uses upgrading of the UCG product gas of the first scenario (before CO_2 separation) by ex-situ chemisorption of CO_2 on naturally occurring minerals (igneous rocks) like wollastonite ($CaSiO_3$), talc ($MgSi_4O_{10}(OH)_2$), serpentine ($Mg_3Si_2O_5(OH)_4$), olivine (Mg_2SiO_4) or other magnesium-calcium silicates. In this work, only wollastonite is considered because its reaction with CO_2 has the highest equilibrium constant at the relevant temperatures and pressures. [81]. For each process, the composition of the UCG product gas is calculated by assuming chemical equilibrium and use the result in the exergy analysis of the overall process.

The paper is organized as follows. Section 2.2 models the chemical reacting system of coal/oxygen/water/CaO. It also includes a thermodynamic analysis of the gas composition, based on volume and temperature constraints in section 2.3. Section 2.4 gives a short description of the UCG process with simultaneous capturing of CO_2. Section 2.5 defines the exergetic recovery and efficiency factors for the energy conversion processes and explains the calculation procedure for the theoretical, practical, and zero-emission recovery factors. The exergy consumption for various processes like pumping, grinding etc. is discussed in Section 2.6. The results are discussed in section 2.7 and finally the chapter ends with some conclusions.

2.2. Modeling of the chemical reacting system of coal/oxygen/water/CaO

2.2.1. Problem definition

The chemical equilibrium model of the underground coal gasification process consists of eight components: CH_aO_b, CaO, $CaCO_3$, CO_2, CO, H_2, H_2O, CH_4. The presence of sulfur and nitrogen compounds are disregarded except pure N_2 to avoid unnecessary complexity in analyzing the results. The system is considered at a constant user defined pressure. The initial temperature is $T_{in}=35^oC$. Heat transfer between the system and surrounding environment is disregarded, i.e., adiabatic conditions are considered. In practice, due to the presence of combustible gases in the cavity, the injected oxygen is instantaneously converted to CO_2 and H_2O [161]. Here, the presence of oxygen in the model system is avoided by assuming that the injected oxygen n_{0,O_2} [mol] is converted to CO_2 (n_{0,CO_2} [mol]) and H_2O, which is taken into account as part of the injected water n_{0,H_2O} [mol]. The combustion heat of coal is then added to the energy balance. The calculation procedure is shown in Fig. 2.2. The following equilibrium reactions can be considered:

$$CH_aO_b\,(s) + (2-b)\,H_2O\,(g) + CaO\ (s) \rightleftharpoons \left(2-b+\frac{a}{2}\right) H_2\,(g) + CaCO_3\,(s), \quad (2.1)$$

$$CH_aO_b\,(s) + (1-b)CO_2 \rightleftharpoons (2-b)\,CO + \frac{a}{2}H_2, \quad (2.2)$$

$$CH_aO_b\,(s) + (1-b)\,H_2O \rightleftharpoons CO + (1-b+\frac{a}{2})H_2, \quad (2.3)$$

$$CH_aO_b\,(s) + (2+b-\frac{a}{2})H_2 \rightleftharpoons CH_4 + (\frac{a}{2}-1)H_2O, \quad (2.4)$$
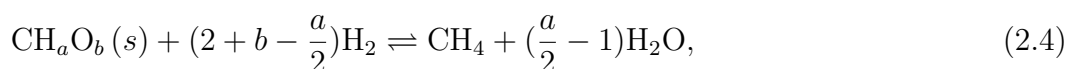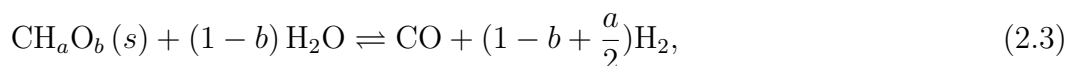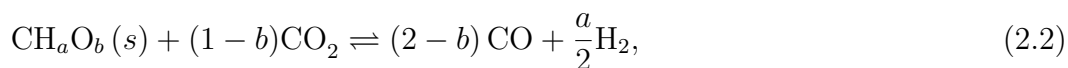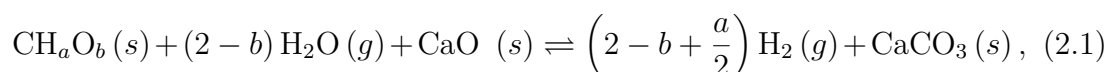
This same model can be used to describe ex-situ gasification of coal.

For the equilibrium calculations the theory in [146] is followed, which leads to the equilibrium relation

$$\prod_i \left(y_i \hat{\phi}_i \right)^{\nu_{i,j}} = \left(\frac{P}{P^o} \right)^{-\nu_j} K_j, \tag{2.5}$$

where P^o [bar] is the standard pressure and $\hat{\phi}_i$ is the fugacity coefficient of gas species i and is calculated as a function of pressure (P [bar]), temperature (T [K]), and equilibrium composition (y_i), using the Peng-Robinson's equation of state [118]. Details of the calculation of equilibrium constants can be found in 2.6.3.
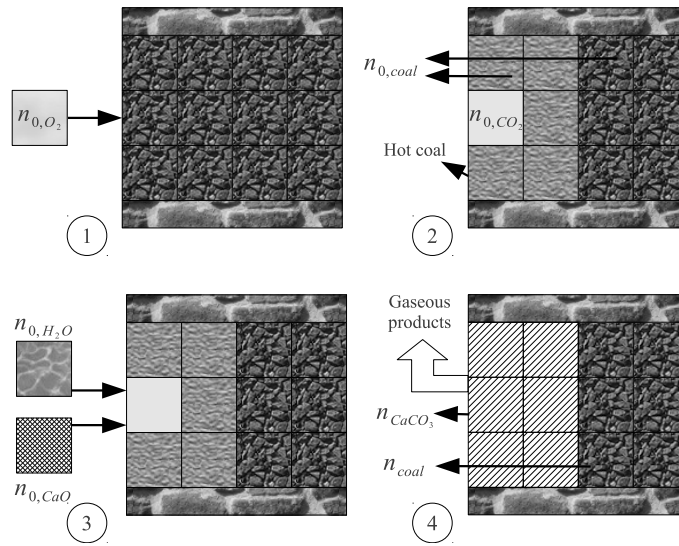
Figure 2.2.: Calculation procedure for the chemical equilibrium of underground coal gasification with CaO; step 1: injection of O_2 to burn one unit volume of coal; step 2: CO_2 and hot coal generated from the combustion reaction; step 3: injection of CaO and water to react with the hot coal and CO_2; step 4: generation of $CaCO_3$ and gaseous products. In the model these steps will occur simultaneously. Assumption: the UCG process is adiabatic.

2.2.2. Energy Balance

Here, the adiabatic assumption is used, i.e., the initial enthalpy of reactants is equal to the final enthalpy of the products (see Fig. 2.2). The process starts with the combustion of one unit volume of coal, and the heat of combustion of coal is added to the energy balance. It is also assumed that only ($n_{0,coal} - n_{coal}$) which is the number of moles of coal converted in the gasification reaction participates in the

energy balance. The energy balance can be written as

$$H_{in}\left(T_{in}, P, n_{0,i}\right) - H_{out}\left(T, P, n_i\right) + n_{0,\mathrm{CO_2}}\Delta_{comb}h - n_{0,\mathrm{H_2O}}\Delta h_{vap} = 0, \qquad (2.6)$$

where T_{in} [K] is the reactants (coal, O_2, and water) initial temperature, $H_{in}\left(T_{in}, P, n_{0,i}\right)$ [J] is the enthalpy of reactants, i.e., O_2, N_2, formed CO_2, and water vapor, all at T_{in} and P. Moreover, $H_{out}\left(T, P, n_i\right)$ [J] is the enthalpy of products, $\Delta_{comb}h$ [J/mol] is the heat of combustion of coal to form carbon dioxide and water at T_{in} and Δh_{vap} [J/mol] is the heat of vaporization of water at T_{in}, which is only considered when water is injected in liquid phase. $\Delta_{comb}h$ accounts for conversion of injected oxygen to CO_2. To simplify the calculation procedure, the enthalpy of solid, for which the effect of pressure on enthalpy is assumed negligible, and gas species, for which the residual enthalpy is calculated to consider the effect of pressure on enthalpy, are calculated separately. The enthalpy of the gas and solid species are calculated using the enthalpy of formation of each component at standard pressure and reference temperature T_0 as the reference state, for both the input and output enthalpy. The details of the calculation of enthalpy can be found elsewhere [146, 122].

2.2.3. Solution methodology

When the total pressure is given, there are 10 unknowns in the equations, viz., the number of moles of six gaseous species and three solid species, and the temperature. Consequently 10 equations are needed. There are four chemical equilibrium relations for Eq. (2.1-2.4), five atom balance equations for carbon, hydrogen, oxygen, calcium, and nitrogen, respectively, and one energy balance relation Eq. (2.6).

The output number of moles of each component (CO_2, CO, H_2, H_2O, CH_4, N_2, Coal, CaO, $CaCO_3$) and the equilibrium temperature (T) are found by solving the ten nonlinear equations using the Matlab nonlinear solver 'lsqnonlin' which is extensively explained in Matlab documents [97]. The Jacobian matrix is calculated analytically using the open-source computer algebra system 'Maxima' (webpage).

2.3. Volume and temperature constraints

Due to the consumption of coal during the underground gasification process, a cavity is formed with volume V_{cavity} [m³], which is filled with the unreacted CaO (V_{CaO} [m³]) and generated $CaCO_3$ ($V_{\mathrm{CaCO_3}}$). The void volume formed by the removal of coal must exceed the volume of unreacted CaO and formed $CaCO_3$. This can be written as

$$V_{cavity} \geqslant V_{\mathrm{CaO}} + V_{\mathrm{CaCO_3}}, \qquad (2.7)$$

or

$$[(n_{0,coal} - n_{coal}) + n_{0,CO_2}] v_{coal} \geqslant n_{CaO}v_{CaO} + n_{CaCO_3}v_{CaCO_3}/(1 - \Phi_{CaCO_3}), \quad (2.8)$$

where v_{coal}, v_{CaO}, and v_{CaCO_3} [m^3/mol] are the molar volumes of coal, calcium oxide, and calcium carbonate respectively, Φ_{CaCO_3} is the porosity of the generated calcium carbonate. As explained in Fig. 2.2, n_{0,CO_2} is the number of moles of coal combusted by the injected oxygen and $(n_{0,coal} - n_{coal})$ is the number of moles of gasified coal consumed by the injected water. The other constraint is that the temperature should be low enough so that CaCO$_3$ can be formed in the exothermic reaction between CO$_2$ and CaO,

$$CaO_{(s)} + CO_{2,(g)} \rightleftharpoons CaCO_{3,(s)}. \quad (2.9)$$

The equilibrium relation for this reaction is

$$K_{carbonation} = \frac{P^o}{y_{CO_2}\hat{\phi}_{CO_2}P}, \quad (2.10)$$

where $K_{carbonation}$ is the equilibrium constant of the CaO carbonation reaction Eq. (2.9), $\hat{\phi}_{CO_2}$ is the fugacity coefficient of CO$_2$, y_{CO_2} is the mole fraction of CO$_2$ in the gas phase, and P is the equilibrium pressure. In a system where CaCO$_3$ and CaO are exposed to an atmosphere of CO$_2$ at high temperatures and low pressures, this reaction shifts to the left, i.e., CaCO$_3$ dissociates into CaO and CO$_2$. In underground coal gasification, by changing the water to oxygen ratio, the reaction temperature can be adjusted such that the carbonation reaction of CaO shifts to the right. A 99% CaO conversion is arbitrarily chosen to define the temperature constraint, i.e.,

$$X_{CaO} = 0.99, \quad (2.11)$$

where X_{CaO} is the conversion of CaO. If an equimolar mixture of CaO and CO$_2$ at the initial pressure of P and constant temperature of T reacts at constant volume to reach the equilibrium pressure P_{eq}, the CaO conversion is calculated by $(n_{0,CaO} - n_{CaO})/n_{0,CaO}$, which can be written as

$$X_{CaO} = \frac{\frac{P}{Z(P,T,y_{initial})} - \frac{P_{eq}}{Z_{eq}(P_{eq},T,y_{eq})}}{\frac{P}{(1-y_{inert,initial})Z(P,T,y_{initial})}}, \quad (2.12)$$

where Z and Z_{eq} are compressibility factor of the gas phase at initial and equilibrium conditions, respectively and are calculated using Peng-Robinson equation of state, assuming that the inert gas is nitrogen. By substituting P_{eq} from Eq. 2.10 in Eq. 2.12, one obtains

$$X_{CaO} = \frac{1}{1 - y_{inert,initial}}\left(1 - \frac{Z(P,T,y_{initial})}{Z_{eq}(P_{eq},T,y_{eq})}\right)\frac{P^o}{y_{CO_2}\hat{\phi}_{CO_2}K_{carbonation}P}. \quad (2.13)$$

This defines a pressure dependent temperature constraint (see Fig. 2.3).
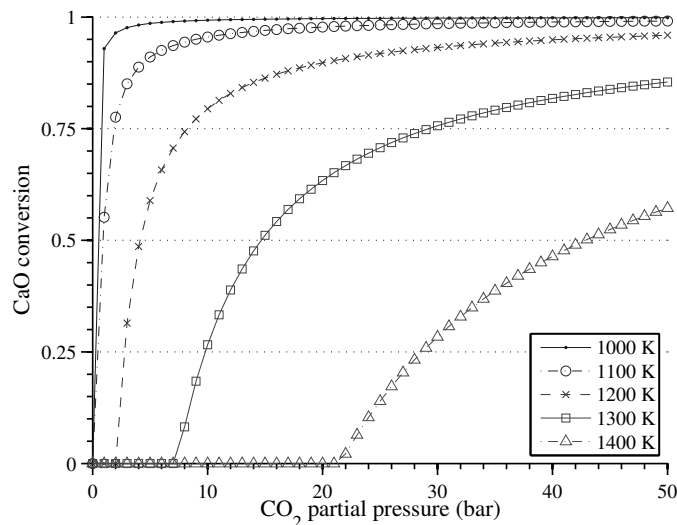
Figure 2.3.: The fraction of converted CaO as a function of CO_2 partial pressure and temperature for the system of $CaO/CaCO_3/CO_2$/inert gases

2.4. Process description

Two scenarios for the UCG process in terms of CO_2 removal and gas upgrading are considered. For the first scenario, depicted in Fig. 3.14-a, synthetic CaO is ground to an average particle size of 50 μm and injected into the UCG cavity to react insitu with CO_2. The reduced CO_2 concentration shifts the reaction $CO+H_2O \rightleftharpoons CO_2+H_2$ to the right, i.e., produces more hydrogen. The temperature and quality of the product were investigated as a function of the water/oxygen ratio. The input of CaO was calculated using the volume constraint, i.e., the volume of $CaCO_3$ produced must be equal to the volume of coal reacted, including the volume of 1.0 % of CaO left unreacted. A compressor is used to pressurize air/oxygen and inject it to the gasification cavity. A pump can be used for the injection of water. If the coal layer is connected to the underground water, depending on the the hydrostatic pressure and permeability, the flow of water into the cavity may be realized by controlling the pressure of the cavity and subsequently a water injection pump is not required. The product gas is combusted and generates heat and flue gas. The flue gas is transferred to a carbon capture and storage unit. The CCS exergy demand depends on the capture process and storage method, which will be discussed in 2.6.7 and 2.6.8.
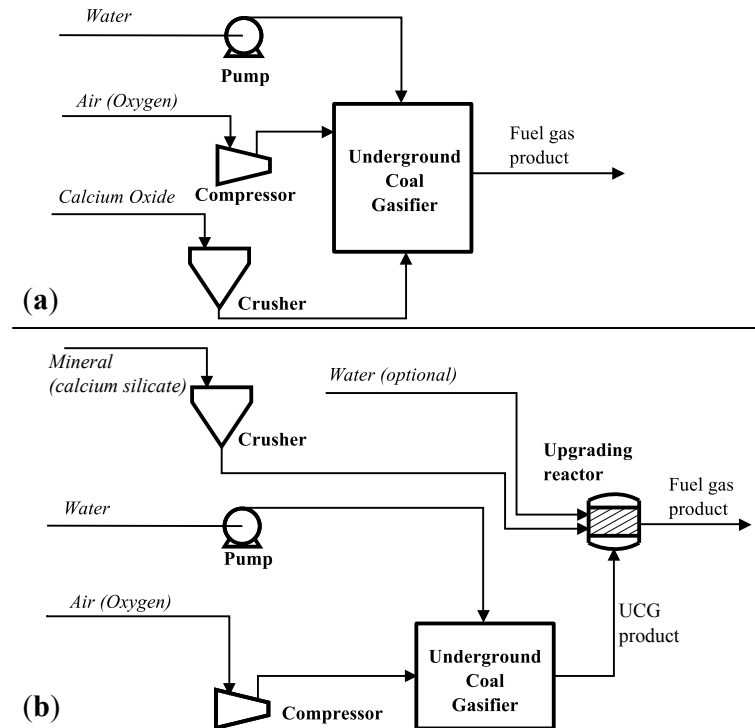
Figure 2.4.: Process flow diagram of the UCG process with: (a) insitu CO_2 adsorption on CaO; (b) ex-situ adsorption of CO_2 on wollastonite. Italic letters show the material and exergy streams; bold letters show the exergy consuming equipment; normal letters show the products.

Fig. 3.14-b shows the process flow diagram of oxygen/water gasification without the injection of minerals into the gasification cavity. The composition and temperature of the product gas is calculated using the same chemical equilibrium model and the effect of the water/oxygen ratio is investigated. The gasification product is transferred to an ex-situ reactor filled with fine and wet particles of wollastonite. Wollastonite reacts with CO_2 at high pressure (80 bar) and fixed temperature of 500 K to decrease the carbon content of the gas and to produce a gas richer in H_2 and CO. Again the product gas is combusted and the flue gas is transferred to a CCS unit.

More specifications of the solids and the process equipment are given in Table 2.2 and Table 2.3.

Table 2.2.: Unit operations specification

Unit	property	value	unit
Compressor	η_{comp}	0.80	-
	η_{driver}	0.9	-
	η_{elec}	0.45	-
	Pressure ratio	3.0	-
	Input temperature	308.15	K
Crusher	Feed size	0.1	m
	Product size	50×10^{-6}	m

Table 2.3.: physical properties of the solid reactants

Property	Value	Unit
CaO density (ρ_{CaO})	58.82	kmol/m^3
CaCO$_3$ density (ρ_{CaCO_3})	26.67	kmol/m^3
CaCO$_3$ porosity (Φ_{CaCO_3})	0.3	-
Coal density (ρ_{coal})	1366.9	kg/m^3
Coal porosity (Φ_{coal})	0.08	-
Coal MW (M_{coal})	15.03	kg/kmol

2.5. General approach

Based on the definition of exergy, a system that has a different temperature, pressure, or composition from the dead state can be used as an exergy source. Fossil fuels are chemical resources with a different composition, i.e., mainly hydrocarbons. To extract/convert the exergy available in fossil fuel resources, different processes can be devised. Each process needs streams of material and exergy to extract or convert the targeted resource (Fig. 2.5). To investigate the effectiveness of a particular process, one needs to quantify the streams depicted in Figs. 2.5 and 2.6.

Every process produces desirable and undesirable products. The cumulative exergetic efficiency of a process shows the desirable exergy output as a fraction of total exergy that goes into the process in the form of energy and material streams [46]. The exergetic efficiency is defined as

$$\Psi = \frac{Ex_{prod}}{\sum Ex_i + \sum \widetilde{Ex}_{M_i}}, \tag{2.14}$$

where Ex_{prod} [J/s] is the exergy of the final desirable product, Ex_i [J/s] are the input exergy streams to the process, and $\widetilde{Ex}_{M_i}$ [J/s] are the exergy requirement in the production of material streams M_i. When the conversion of material to a certain

product is the most important aim of the process, it is possible to use the exergetic efficiency to compare alternative processes.
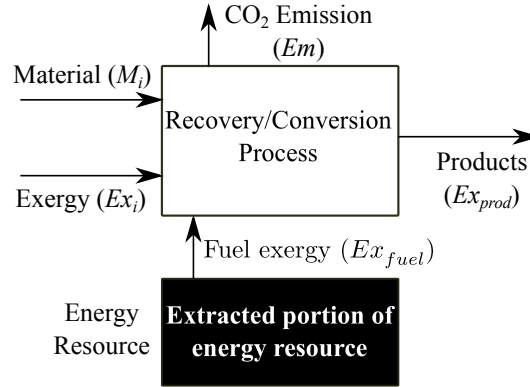
Figure 2.5.: A schematic view of the inputs/outputs of the energy recovery/conversion process; the product represents a certain amount of exergy. Part of the exergy is lost in the process.

For an energy conversion or recovery process, the exergy value of the energy resource can be considered separately from other input exergy streams as depicted in Fig. 2.5. Therefore, Eq. (2.14) can be rearranged to

$$\Psi = \frac{Ex_{prod}}{\sum Ex_i + \sum Ex_{M_i} + Ex_{fuel}}, \tag{2.15}$$

where $\sum Ex_{M_i}$ is the sum of the exergy values of all the material streams M_i except for the energy resource; Ex_{fuel} [J/s] is the exergy value of the extracted energy resource. In the energy conversion processes, producing a desirable mass stream of fuel does not guarantee the feasibility. The main goal is to extract or convert the exergy available in an energy resource by investing a lower amount of exergy in the form of material and exergy streams. It makes the net extracted or recovered exergy the most important factor in the feasibility of an energy conversion or extraction process. The net recovered or extracted exergy Ex_{net} [J/s] of an energy source can be defined as

$$Ex_{net} = Ex_{prod} - \left(\sum Ex_i + \sum Ex_{M_i} \right). \tag{2.16}$$

The exergetic efficiency (Ψ) is modified by including the net recovered exergy to define the recovery factor (R) for an energy conversion process as

$$\text{R} = \frac{Ex_{net}}{Ex_{fuel}} = \frac{Ex_{prod} - (\sum Ex_i + \sum Ex_{M_i})}{Ex_{fuel}}. \tag{2.17}$$

In the following sections, the calculation procedure for the material (Ex_{M_i}) and exergy (Ex_i) streams will be discussed.

2.5.1. Material streams

Every material stream (M_i) flowing into the process (P_i) can have been produced in another process/processes (P_{M_i}) by using feed streams (F_{M_i} [mol/s]) and the cumulative exergy streams ($CExC_{M_i}$ [J/mol]). The production process also emits CO_2 expressed in kg per mole of M_i, i.e., Em_{M_i} [kg/mol] (see Fig. 2.6). The cumulated exergy consumption has been calculated by Szargut for some materials [154, 156]. 2.6.5 explains how to attain the minimum cumulative exergy consumption ($CExC_{M_i,min}$) for producing material (M_i) from the dead state, which is equal to the chemical exergy of material M_i, i.e., $Ex_{M_i}^{ch}$ [J/mol]. In practice one will find $CExC_{M_i}$ to be higher than the minimum or theoretical value $Ex_{M_i}^{ch}$. The production efficiency for material stream M_i at standard conditions is defined by

$$\eta_{M_i}^{P_{M_i}} = \frac{Ex_{M_i}^{ch}}{CExC_{M_i}}. \tag{2.18}$$

Szargut used the term cumulative degree of perfection (CDP) for the production efficiency $\eta_{M_i}^{P_{M_i}}$ [156].

Due to the increasing interest in the low-emission and zero-emission energy supplies, the total amount of CO_2 associated with the production of M_i is quantified. The CO_2 emission in kg per mole of M_i in the production of M_i is the sum of the CO_2 emission related to the exergy consumption during the process and the CO_2 produced as byproduct, e.g., CO_2 produced during the production of CaO from $CaCO_3$. It is shown that the preparation step related to the coal feed stream F_{M_i} can be neglected and consequently there is no CO_2 emission associated with F_{M_i}. In practice, CO_2 emission in the production of a material M_i is calculated using the emission factors. Here, to estimate the CO_2 emission associated with material M_i, it is confined to multiplying the $CExC_{M_i}$ [J/mole M_i] by the emission factor of the fossil fuel that is used to provide exergy for the production of M_i.

$$Em_{M_i} = e_{fuel}CExC_{M_i} + Em_{byproduct}, \tag{2.19}$$

where e_{fuel} is the amount of CO_2 generated, expressed in kg per unit exergy of the fossil fuels considered (after combustion) [kg CO_2/J] and $Em_{byproduct}$ is the mass of CO_2 produced as a byproduct in the process per unit mole of M_i.

The calculation of Ex_{M_i} is done in three steps. First, it is assumed that the efficiency $\eta_{M_i}^{P_{M_i}}$ is equal to one and it is called the theoretical exergy requirement for the production of material stream M_i, i.e.,

$$Ex_{M_i}^{th} = Ex_{M_i}^{ch}. \tag{2.20}$$

In the second step the state of the art exergetic efficiency of production of M_i is taken into account, i.e., the practical exergy requirement for the production of material

M_i is

$$Ex^{pr}_{M_i} = \frac{Ex^{ch}_{M_i}}{\eta^{P_i}_{M_i}}. \tag{2.21}$$

Finally, in the zero-emission step, the exergy required in the capture and sequestration of CO_2 emitted during the production of material M_i in the state of the art process P_i is added to the practical value, i.e.,

$$Ex^{ze}_{M_i} = Ex^{pr}_{M_i} + Em_{M_i}Ex_{CCS}. \tag{2.22}$$

Here, Ex_{CCS} [J/kg] is the exergy requirement for the capturing and sequestration processes per unit mass of carbon dioxide, which is reported in 2.6.7 and 2.6.8.
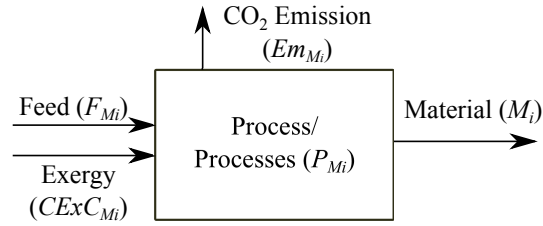
Figure 2.6.: Exergy and material streams and CO_2 emission in the production of material stream M_i, an input stream in Fig. 2.5

2.5.2. Exergy streams: heat and power

In general, the exergy requirement in a process can be expressed in terms of heat (per unit time) and power. A process needs exergy to be used in thermal units, e.g., heat exchangers, to provide heat and in mechanical units, e.g., compressors, to provide work. Here the exergy requirement is quantified by assuming that a fossil fuel, i.e., methane is used to provide all these exergy requirements.

2.5.2.1. Heat

First it is assumed that $\dot{Q}_i$ [J/s] of heat is required in a device which functions at temperature $T_{h,i}$. To use the theoretical, practical, and zero-emission steps, the following procedure is used:

$Ex^{th}_{i,heat}$ is defined as the minimum amount of exergy that needs to be consumed to provide $\dot{Q}_i$ units of heat per unit time at temperature $T_{h,i}$. Heat can be extracted from the surrounding environment at temperature $T_{0,i}$ using an ideal heat pump to provide $\dot{Q}_i$ at temperature $T_{h,i}$, which gives

$$Ex^{th}_{i,heat} = \dot{Q}_i \left(1 - \frac{T_{0,i}}{T_{h,i}}\right). \tag{2.23}$$

For the calculation of the practical exergy requirement for providing the heat stream $\dot{Q}_i$, the same approach as the practical exergy of material stream can be followed, i.e., the cumulative exergy consumption of heat is calculated by dividing the theoretical exergy of heat ($Ex^{th}_{i,heat}$) by the efficiency factor (η_{Q_i}) of the considered state of the art heat generator. The equation reads,

$$Ex^{pr}_{i,heat} = CExC_{i,heat} = \frac{Ex^{th}_{i,heat}}{\eta_{Q_i}}. \tag{2.24}$$

The cumulative exergy of heat is reported in the literature [156, 46]. Here, to obtain the cumulative exergy of a heat stream, a simplified calculation procedure can be used by assuming that the chemical exergy of a fossil fuel is directly converted to heat by a combustion process in a heat generator with the efficiency η_{Q_i}. This efficiency accounts for the production of fossil fuels (η_{fuel}), the exergy loss in the conversion of chemical exergy to heat at $T_{h,i}$ and transfer of heat to combustion products ($\frac{ex^{ch}_{fuel}}{LHV_{fuel}}(1 - T_{0,i}/T_{h,i})$), and the heat loss in the heat generator ($\eta_{generator}$), i.e.,

$$\eta_{Q_i} = \eta_{fuel}\eta_{generator}\frac{ex^{ch}_{fuel}}{LHV_{fuel}}\left(1 - \frac{T_{0,i}}{T_{h,i}}\right), \tag{2.25}$$

where LHV_{fuel} is the lower heating value of the fossil fuel. Here it is assumed that the fossil fuel is methane and disregard the production efficiency of methane (η_{CH_4}) and the heat loss in the heat generator ($\eta_{generator}$). By substituting Eq. (2.23) and Eq. (2.25) in Eq. (2.24), one obtains

$$Ex^{pr}_{i,heat} = \dot{Q}_i \times \frac{ex^{ch}_{CH_4}}{LHV_{CH_4}}, \tag{2.26}$$

where $ex^{ch}_{CH_4}$ [J/mol] is the chemical exergy of methane, and LHV_{CH_4} is the lower heating value of methane [J/mol]. The exergy to heating value ratio of a fossil fuel is nearly equal to one and can be assumed to be one. Finally, the zero-emission exergy requirement is

$$Ex^{ze}_{i,heat} = \dot{Q}_i \left(\frac{ex^{ch}_{CH_4}}{LHV_{CH_4}} + \frac{em_{CH_4}ex_{CCS}}{LHV_{CH_4}}\right), \tag{2.27}$$

where em_{CH_4} is the CO_2 emission due to methane consumption [kg CO_2/mol CH_4], and ex_{CCS} is the carbon capture and storage exergy requirement [J/kg CO_2].

2.5.2.2. Power

The minimum exergy requirement to drive a mechanical unit operation is equal to W^{rev}_i which is the minimum amount of work required in a reversible process, i.e.,

$Ex_{i,power}^{th} = W_i^{rev}$. For the practical case, the cumulative exergy ($CExC_{i,power}$) and the cumulative degree of perfection of a power generation process (η_W) are reported in the literature [156, 46]. The practical exergy of power is calculated by

$$Ex_{i,power}^{pr} = CExC_{i,power} = \frac{Ex_{i,power}^{th}}{\eta_W}, \qquad (2.28)$$

where η_W accounts for all the exergy losses during the conversion of an energy source to power. Here, for more clarification, it is assumed that in a power production process, chemical exergy of a fossil fuel is converted to electricity with efficiency η_{elec} and subsequently is converted to work with an electrical driver with efficiency η_{driver}. Then it drives a mechanical device that has an efficiency of $\eta_{device,i}$. Therefore, the cumulative degree of perfection for the conversion of fossil fuels is calculated as

$$\eta_W = \eta_{fuel}\eta_{device,i}\eta_{elec}\eta_{driver}, \qquad (2.29)$$

where η_{fuel} is the efficiency of the considered fossil fuel production. By replacing the value of $Ex_{i,power}^{th}$ and η_W in Eq. (2.28) and by neglecting the fuel production efficiency (here methane), one obtains

$$Ex_{i,power}^{pr} = \frac{W_i^{rev}}{\eta_{device,i}\eta_{elec}\eta_{driver}}. \qquad (2.30)$$

The CCS exergy of methane is added to $Ex_{i,power}^{pr}$ to calculate zero-emission exergy requirement, i.e.,

$$Ex_{i,power}^{ze} = \frac{W_i^{rev}}{\eta_{device,i}\eta_{elec}\eta_{driver}} \left(1 + \frac{em_{CH_4}ex_{CCS}}{ex_{CH_4}^{ch}} \right). \qquad (2.31)$$

2.5.3. Analysis of the energy recovery/conversion process

For a reversible energy conversion process, the exergy loss is zero and the exergetic efficiency (Ψ) is equal to 100 %. For an energy conversion process, when only the products wanted (here H_2, CO, and CH_4) are formed from all exergy input streams then this leads also to a recovery factor of 100 %, that has been indicated as the upper horizontal dot line in Fig. 2.7. In the more general case the products wanted and other byproducts are produced and consequently the theoretical recovery factor will be smaller than one. This is shown in Fig. 2.7 with the dash dot curve. However, in reality, exergy is lost in every step of an energy conversion process such as pumps, compressors, reactors, separation and heat transfer units. This exergy loss can be due to the physical limitations, e.g., separation efficiency and/or other state of the art technology limitations. Usually, in the exergy analysis, the exergy losses for all process steps are quantified and compared to the reversible process. It helps to identify the process steps that have the highest contribution to the exergy loss

and have the highest priority to be improved or to be replaced with more effective alternatives.

In the exergy analysis method proposed here, the details of every process step is not analyze. Instead, all the material and exergy streams entering the process are first identifed. Then the calculation procedure explained in section 2.5.2 is followed to calculate the theoretical, practical, and zero-emission exergy value of each stream. The state and composition of the output product is quantified by the phase and chemical equilibrium assumption in the reactors and separation units. The chemical and phase equilibrium assumptions in the reactors and separators, give the maximum possible conversion and separation efficiency for a given design. It means that the recovery factor can be over-estimated. However, the recovery factor calculated by using the equilibrium assumption combined with the theoretical exergy values of the material and exergy streams in Eq. (2.17) represents the maximum achievable recovery factor for a given overall process design, which here is called the *theoretical recovery factor* (R^{th}). The theoretical recovery factor is a function of process parameters, e.g., flow rate of material streams. Therefore, it is possible to calculate the theoretical recovery factor for a range of process parameters, which gives the upper limit of the recovery factor for a process, as depicted schematically in Fig. 2.7 with the dash dot line.

By using the practical exergy values of material and exergy streams in Eq. (2.17), the *practical recovery factor* (R^{pr}) is calculated shown schematically in Fig. 2.7 as a drawn line. The gap between the practical and theoretical curve shows the exergy loss in a process due to the state of the art technology limitations, i.e., low exergetic efficiency (Ψ) of the chemical, the separation, the mechanical, and the thermal devices.

The *zero-emission recovery factor* (R^{ze}) is calculated by using the zero-emission exergy values of material and exergy streams. It means that all the CO_2 emissions associated with the preparation of material M_i and exergy streams Ex_i are captured and stored. By including the exergy required to capture and store the CO_2 that will be generated after the combustion of produced fuel, Eq. (2.17) is modified to

$$R^{ze} = \frac{Ex_{net}}{Ex_{fuel}} = \frac{Ex_{prod} - \left(\sum Ex_i^{ze} + \sum Ex_{M_i}^{ze}\right) - Ex_{CCS}^{prod}}{Ex_{fuel}}. \qquad (2.32)$$

Here, Ex_{CCS}^{prod} can be calculated as

$$Ex_{CCS}^{prod} = e_{prod} Ex_{prod} ex_{CCS}, \qquad (2.33)$$

where e_{prod} is the CO_2 emission per unit product exergy [kg CO_2/J]. The exergy requirement for the capturing and sequestration per kg of CO_2 (Ex_{CCS}) depends on the type of capturing and sequestration process. The space between the zero-emission recovery curve, shown as a dashed curve in Fig. 2.7, and the practical recovery curve shows the state of the art additional exergy requirement for carbon

capture and storage.

The major difference between the exergetic efficiency (Ψ) and recovery factor (R) is that the exergetic efficiency always has a positive value ($0 \leq \Psi \leq 1$), but the recovery factor can be negative. A negative value for the recovery factor can be interpreted in the following way:

1. The theoretical recovery factor is negative i.e., $R^{th} < 0$; the proposed energy conversion process is not and will never be exergetically reasonable. In other words, the total input exergy to the process (excluding the exergy of fuel Ex_{fuel}) is always higher than the exergy content of the output products.

2. The theoretical recovery factor is positive, i.e., $R^{th} > 0$, but the practical recovery factor is negative, i.e., $R^{pr} < 0$; The process is not exergetically reasonable with the current state of technology. With higher efficiency in the production of material streams and thermal and mechanical devices, it is possible to improve R^{pr}. If this is achieved the process is exergetically reasonable.

3. The theoretical and practical recovery factors are positive, i.e., $R^{th} > 0$ and $R^{pr} > 0$, but the zero-emission recovery factor is negative, i.e., $R^{ze} < 0$; The energy conversion process is exergetically reasonable, but with the current state of CCS technology, the zero-emission process is not exergetically viable. Further improvement in the CCS technology can make the zero-emission process exergetically reasonable.

In the next section, the explained procedure will be applied to the underground coal gasification with the simultaneous capture of CO_2.
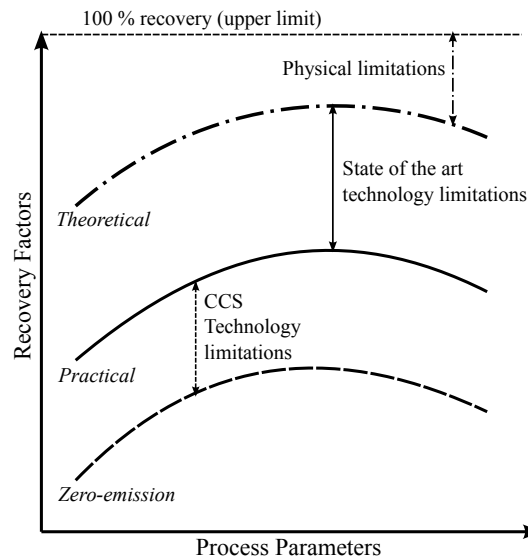
Figure 2.7.: Schematic representation of theoretical, practical, and zero-emission recovery factors as a function of process parameters for an energy conversion process

2.5.4. Exergy analysis of the UCG process

Here, the chemical equilibrium model of section 2.2 is used to represent the UCG process. A mixture of O_2, H_2O, and N_2 reacts with coal (CH_aO_b) to produce CO_2, CO, H_2, and CH_4. The process parameters are the water/oxygen molar ratio in the feed streams, the mole fraction of oxygen in the air/oxygen feed stream, and the pressure in the cavity. The possibility of methane formation in the analysis is also included. The same chemical equilibrium model is used for the theoretical, practical, and zero-emission steps, i.e., the product composition is the same.

The exergy of produced fuel gas (Ex_{prod}) can be written as

$$Ex_{prod,UCG} = Ex_{prod}^{ch} + Ex_{prod}^{ph} + Ex_{prod}^{mix}, \tag{2.34}$$

where $Ex_{prod,UCG}$ is the exergy of the UCG product gas. It can be divided into the chemical exergy Ex_{prod}^{ch}, a function of the number of moles of each of the substances present in the gas multiplied with their respective molar chemical exergy values, the physical exergy Ex_{prod}^{ph}, which takes into account the elevated temperature and pressure of the output gas, and the exergy of mixing Ex_{prod}^{mix}.

The process exergy requirement, i.e., $\sum Ex_i$ and $\sum Ex_{M_i}$, are calculated for theoretical, practical, and zero-emission cases by following the instructions given in sections 2.5.1 and 2.5.2. The theoretical input streams of exergy and material for the process flow diagram shown in Fig. 3.14-a are calculated as

$$\sum Ex_{i,UCG}^{th} = W_{pump}^{rev} + W_{comp}^{rev} + W_{grind}^{rev}, \tag{2.35}$$

$$\sum Ex_{M_i,UCG}^{th} = Ex_{CaO}^{ch} + Ex_{water}^{ch} + Ex_{O_2}^{ch}, \tag{2.36}$$

where W_{pump}^{rev}, W_{comp}^{rev}, and W_{grind}^{rev} are the reversible work required to drive pump, compressor, and crusher, respectively. Moreover, Ex_i^{ch} denotes the chemical exergy of component i, viz. calcium oxide, water, and oxygen.

Practical input exergy streams to the UCG process ($\sum Ex_{i,UCG}^{pr}$), and the cumulative exergy value of input material streams ($\sum Ex_{M_i,UCG}^{pr}$) are calculated by incorporating the efficiency factors to Eq. (2.35) and Eq. (2.36), i.e.,

$$\sum Ex_{i,UCG}^{pr} = \frac{W_{pump}^{rev}}{\eta_{pump}\eta_{driver}\eta_{elec}} + \frac{W_{comp}^{rev}}{\eta_{comp}\eta_{driver}\eta_{elec}} + \frac{W_{grind}^{rev}}{\eta_{grind}\eta_{driver}\eta_{elec}}, \tag{2.37}$$

$$\sum Ex_{M_i,UCG}^{pr} = \frac{Ex_{CaO}^{ch}}{\eta_{CaO}^{prod}} + \frac{Ex_{water}^{ch}}{\eta_{water}^{prod}} + \frac{Ex_{O_2}^{ch}}{\eta_{O_2}^{prod}}, \tag{2.38}$$

where η_{pump}, η_{comp}, and η_{grind} denote the mechanical efficiencies of pump, compres-

sor, and grinding device, respectively. Moreover, η_{CaO}^{prod}, η_{water}^{prod}, and $\eta_{O_2}^{prod}$ denote the exergetic efficiencies for the production of calcium oxide, water, and oxygen, respectively. In addition, η_{elec} denotes the efficiency of electricity generation in a natural gas power plant.

For the zero-emission exergy and material streams, the practical values calculated by Eq. (2.37) and Eq. (2.38) are modified as

$$\sum Ex_{i,UCG}^{ze} = \sum Ex_{i,UCG}^{pr} \left(1 + \frac{em_{CH_4}ex_{CCS}}{ex_{CH_4}^{ch}} \right), \tag{2.39}$$

$$\sum Ex_{M_i,UCG}^{ze} = \sum Ex_{M_i,UCG}^{pr} \left(1 + \frac{em_{CH_4}ex_{CCS}}{ex_{CH_4}^{ch}} \right). \tag{2.40}$$

In summary, for the theoretical case all of the efficiencies in Eq. (2.37) are equal to one, while for the practical case, current state of technology exergetic efficiencies for mechanical devices and production of materials are used. For the zero-emission case, here it is assumed that methane is used to cover all the exergy requirement (material and exergy streams) and add an extra term to consider the exergy requirement in capturing and sequestration of CO_2 generated by methane combustion, as discussed in sections 2.5.1 and 2.5.2.

For the UCG process, it is convenient to write Eq. (2.17) as

$$\text{R}_{coal} = \frac{Ex_{prod,UCG} - \left(\sum Ex_{i,UCG} + \sum Ex_{M_i,UCG} \right)}{Ex_{coal}^{ch}}, \tag{2.41}$$

where the term $\left(\sum Ex_{i,UCG} + \sum Ex_{M_i,UCG} \right)$ represents all the exergy streams into the UCG process except for the chemical exergy of coal. Eq. (2.41) can be used for the calculation of theoretical and practical recovery factors. For the calculation of zero-emission coal recovery factor in the UCG process, one can write

$$\text{R}_{coal}^{ze} = \frac{Ex_{prod,UCG} - \left(\sum Ex_{i,UCG}^{ze} + \sum Ex_{M_i,UCG}^{ze} \right) - e_{prod,UCG}Ex_{prod,UCG}ex_{CCS}}{Ex_{coal}^{ch}},$$
$$\tag{2.42}$$

where $e_{prod,UCG}$ is the CO_2 emission per unit exergy of UCG product [kg/J], which can be calculated as

$$e_{prod,UCG} = \frac{\left(y_{CO_2} + y_{CO} + y_{CH_4} \right) MW_{CO_2}}{\sum_i y_i Ex_i^{ch}}, \tag{2.43}$$

where y_i are the mole fractions of UCG product gas, MW_{CO_2} is the molecular weight of CO_2, i.e., 0.044 kg/mol, and Ex_i^{ch} is the chemical exergy of component i.

One other factor that will be discussed in the next section is the total CO_2 emission

per unit net recovered exergy, i.e.,

$$C_{prod} = \frac{\left(\sum Ex_{i,UCG}^{pr} + \sum Ex_{M_i,UCG}^{pr}\right) e_{CH_4} + Ex_{prod,UCG} e_{prod,UCG}}{Ex_{prod,UCG} - \left(\sum Ex_{i,UCG}^{pr} + \sum Ex_{M_i,UCG}^{pr}\right)}. \tag{2.44}$$

2.6. Calculation procedure and data

2.6.1. Compression exergy

Fig. 2.8 shows an isentropic compressor. A gas stream at a known temperature and pressure of T_1 and P_1 enters the unit and leaves it at elevated temperature T_2 and pressure P_2. The entropy of the stream does not change in an isentropic compressor and P_2 is specified as the output pressure of the compressor. No composition change is considered. The calculation can be performed using a thermodynamic model for the quantification of the physical properties of the gas, e.g., an equation of state (Peng-Robinson). The exergy requirement of this process is the enthalpy difference between output and input streams. The typical mechanical efficiency of the compressor, electrical driver, and electricity production power plant were considered in the evaluation of compression exergy. This assumption allows the calculation of the CO_2 emission from the overall process using the widely available emission data for power generation plants. The compression exergy Ex_{comp} is given by

$$Ex_{comp} = \frac{H_2\left(S_1\left(T_1, P_1\right), P_2\right) - H_1\left(T_1, P_1\right)}{\eta_{comp}\eta_{driver}\eta_{power}} = \frac{W_{comp}}{\eta_{comp}\eta_{driver}\eta_{power}}, \tag{2.45}$$

where W_{comp} is the mechanical energy requirement of the compressor as shown in Fig. 2.8, η_{comp} is the compressor mechanical efficiency, η_{driver} is the electrical driver efficiency, and η_{power} is the efficiency of power plant. Here it is assumed that the electricity is generated in a natural gas combined cycle power plant. The related CO_2 emission is calculated as

$$Em_{comp} = Ex_{comp} e_{CH_4}, \tag{2.46}$$

where e_{CH_4} is the CO_2 emission per unit exergy of methane [kg CO_2/kJ]. Indeed, here it is assumed that natural gas is pure methane.
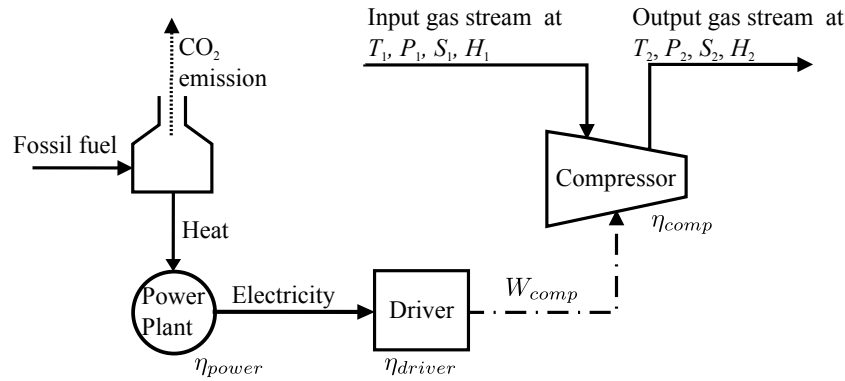
Figure 2.8.: Input and output of an isentropic compression unit

Here the following procedure is used in the calculation of compression exergy for a compressor:

1. For stream 1, the values of enthalpy and entropy are calculated using the Peng-Robinson equation of state.

2. For isentropic compression, the input entropy S_1 and output entropy S_2 are equal.

3. For the calculation of the theoretical compression exergy, a single stage compressor is considered. For the practical case, a multistage compressor with inter-stage cooling is considered where the pressure of the output stream from each stage is calculated using pressure ratio of typical compression processes ($\frac{P_2}{P_1} = 3.0 - 4.5$ for a centrifugal compressor [36]). The input temperature to each stage is assumed to be T_1.

4. The temperature and enthalpy of stream 2 can be calculated implicitly from the known pressure P_2 and entropy $S_2 = S_1$.

5. The amount of isentropic compression work is calculated as the enthalpy difference between the input and output streams $H_2 - H_1$.

6. After each compression stage, the gas is cooled down at constant pressure to its initial temperature T_1 and enters the next compression step, at temperature T_1 and pressure P_2 (the output pressure of the previous stage).

7. Using typical values for a centrifugal compressor and for power generation efficiencies, the values of the exergy requirements of a compressor such as used in the main text can be computed.

2.6.2. Well exergy

The exergy input to produce a well includes both drilling exergy, e.g., rotary drilling, and material consumption for piping and casing, e.g., steel and cement. Drilling

power input H_{rp} (horsepower) can be calculated by the empirical relation [6]

$$H_{rp} = FN, \tag{2.47}$$

where F is the torque factor and is equal to 1.5±1.75 for shallow holes less than 3,000 m with a light drill string and N is the bit rotational speed (rpm). The rate of penetration ROP [ft/hr] in the rotary drilling can be estimated using the empirical formula [139]

$$ROP = K_f \left(\frac{W}{4d_b}\right)^{a_1} \left(\frac{N}{100}\right)^{a_2}, \tag{2.48}$$

where a_1 and a_2 are empirical constants, K_f is the formation drillability factor in ft/hr, d_b is the bit diameter in inch, and W is the weight on the bit in klb_f. Note that this equation does not use a consistent unit system and only works with the suggested field unit system. Using the values in Table 2.4 for the parameters, the drilling power consumption will be 121 kW and the penetration rate will be 0.0018 m/s. The ratio between power consumption and ROP gives the power consumption of 68.8 MJ per meter drilled. For a 800 meter deep well, the total drilling power requirement excluding the steel and cement consumption is around 55,000 MJ excluding the power production and mechanical driver efficiencies.

Table 2.4.: Parameters used in the calculation of drilling power consumption and ROP [6, 139]

Parameter	Value	Unit
F	1.5+1.75	hp/min
N	50	rpm
K_f	110	ft/hr
W	10	klb_f
d_b	$6\frac{1}{4}$	inch
a_1	1.25	-
a_2	0.75	-

The steel and cement exergy value per unit mass has been reported in Table 2.5.

Table 2.5.: Exergy value of steel and cement [156]

Material	Exergy (kJ/kg)
Steel tube	58667
Cement	6165

Assuming that the casing steel pipe has an inside diameter of 200 mm with a thickness of 6.4 mm and 15 mm of space between the pipe and the hole wall that is

to be filled with cement, the values of exergy consumption for a 800 m deep well are reported in table 2.6. The results show that the drilling and cementing exergy consumption account for 14.34 % of the total exergy consumption of a well. The steel pipe with 85.66 % is the main contributor of the well exergy requirement.

Table 2.6.: The exergy consumption in drilling and completion of a 800 m deep injection well

Exergy consumption step	Exergy value (kJ)	Percent
Drilling	1.52×10^8	8.57
Piping	1.53×10^9	85.66
Cementing	1.03×10^8	5.77
Total	1.78×10^9	100.00

The well exergy contribution in a 5 MW underground coal gasification process with a lifetime of 10 years is 0.23 % which is neglected in the calculation of recovery factors.

2.6.3. Chemical Equilibrium

To calculate the equilibrium concentrations for the coal/O_2/H_2O/CaO system standard procedures are used. The equilibrium condition for reaction j can be written as

$$\sum_i \nu_{i,j} \mu_i = 0, \tag{2.49}$$

where $\nu_{i,j}$ is the stoichiometric coefficient of component i in reaction j and μ_i is the chemical potential of component i in the stable phase at the temperature and pressure considered.

For the chemical potential μ_i, the thermodynamic relation

$$\mu_i = \mu_i^o(T) + RT \ln \frac{\hat{f}_i}{f_i^o}, \tag{2.50}$$

is used where μ_i is the chemical potential of component i in its stable phase at T, P, and the composition of that phase, $\mu_i^o(T)$ is the chemical potential of pure component i in the same phase at T and the standard pressure P^0, $\hat{f}_i$ is the fugacity of component i in its stable phase at T, P, and the composition of that phase and f_i^o is the fugacity of the pure component i in the same phase at standard pressure P^o and temperature T. The phase in the standard state is not necessarily the same

for all components, but for each component i, the standard state for $\mu_i^o(T)$ and f_i^o must be the same.

Substitution of Eq. (2.50) in the equilibrium equation gives, after rearrangement, the following expression

$$\ln \prod_i \left(\frac{\hat{f_i}}{f_i^o} \right)^{\nu_{ij}} = \ln K_j = \frac{-\sum_i \nu_{ij} \mu_i^o}{RT} = \frac{-\Delta_r g_j^o}{RT}. \tag{2.51}$$

For component i in the gas phase and with the ideal gas state as reference state the quotient of the fugacities can be expressed as

$$\left(\frac{\hat{f_i}}{f_i^0} \right) = \frac{y_i \hat{\phi_i} P}{P^0}. \tag{2.52}$$

For component k as a pure solid phase the quotient of the fugacities can be expressed as

$$\left(\frac{\hat{f_k}}{f_k^0} \right) = \exp \left(\frac{\int_{P^0}^{P} v_k dP}{RT} \right), \tag{2.53}$$

where v_k is the molar volume of pure solid component k. When this molar volume can be considered constant to a reasonable approximation, the integral can be simplified, and the quotient of the fugacity coefficients becomes

$$\left(\frac{\hat{f_k}}{f_k^0} \right) = \exp \left(\frac{v_k (P - P^0)}{RT} \right). \tag{2.54}$$

Substitution of these expressions in Eq. (2.51) leads then finally to

$$\left(\sum_k \frac{\nu_{k,j} v_k (P - P^0)}{RT} \right) + \ln \prod_i \left(\frac{y_i \hat{\phi_i} P}{P^0} \right)^{\nu_{i,j}} = \ln K_j = \frac{-\Delta_r g_j^o}{RT}. \tag{2.55}$$

After introduction of the reaction coordinate ε_j for reaction j which is defined by

$$\mathrm{d} n_i = \nu_{ij} \mathrm{d} \varepsilon_j, \tag{2.56}$$

and $\varepsilon_j = 0$ at the beginning of the reaction. All mole fractions in the gas phase can be expressed as a function of the initial number of moles present, the stoichiometric coefficients, and the reaction coordinates, e.g.,

$$y_i = \frac{n_{i0} + \sum_j \nu_{ij}\varepsilon_j}{n_0 + \sum_j \nu_j\varepsilon_j}. \tag{2.57}$$

Here, n_0 is the total number of moles originally present, and the summation is over all independent chemical reactions taking place in the system considered. In this way there is one unknown variable per independent chemical reaction: the reaction coordinate ε_j.

A cubic equation of state (Peng-Robinson [118]) was used to calculate the fugacity coefficients for different pressures, temperatures and compositions.

The change in the molar Gibbs energy $\Delta g^o(T)$ is equal to $\Delta h^o(T) - T\Delta s^o(T)$. The enthalpy and entropy at temperature T can be found from the Eq. (2.58) and Eq. (2.59) [146].

$$\Delta_r h_j^o = \Delta h_{0,j}^o + R \int_{T_0}^T \frac{\Delta_r c_{p,j}^o}{R} \mathrm{d}T, \tag{2.58}$$

$$\Delta_r s_j^o = \Delta s_{0,j}^o + R \int_{T_0}^T \frac{\Delta_r c_{p,j}^o}{R} \frac{\mathrm{d}T}{T}. \tag{2.59}$$

Where $\Delta_r h_{0,j}^o$, $\Delta_r s_{0,j}^o$, and $\Delta_r c_{p,j}^o$ are molar values for each reaction and can be calculated using equations Eq. (2.60), Eq. (2.61), and Eq. (2.62) respectively.

$$\Delta_r h_{0,j}^o = \sum_i \nu_{i,j} \Delta h_{0,i}^o, \tag{2.60}$$

$$\Delta_r s_{0,j}^o = \sum_i \nu_{i,j} \Delta s_{0,i}^o, \tag{2.61}$$

$$\Delta_r c_{p0,j}^o = \sum_i \nu_{i,j} c_{p0,i}^o. \tag{2.62}$$

Values of $\Delta h_{0,i}^o$ and $\Delta g_{0,i}^o$ are enthalpy of formation and Gibbs energy of formation of component i at standard pressure, e.g., 1 bar and reference temperature of T_0, which is often 298 K. Moreover, $c_{p0,i}^o$ is the heat capacity of component i at standard pressure and has been reported in the literature [146, 122]. To find $\Delta s_{0,i}^o$ the following

thermodynamic relation can be applied.

$$\Delta s_{0,i}^o = \frac{\Delta h_{0,i}^o - \Delta g_{0,i}^o}{T_0}. \tag{2.63}$$

2.6.4. Physical parameters

Table 2.7 shows the values of $c_{p,i}^o$, $\Delta h_{0,i}^o$, and $\Delta g_{0,i}^o$ for gas species at standard pressure $P^o = 1$ bar.

Table 2.7.: Molar heat capacity $(C_{p,i}^o/R = c_1 + c_2 T + c_3 T^2 + c_4/T)$, standard enthalpy and Gibbs energies of formation for the gaseous species ([146])

Component	c_1	$c_2 \times 10^3$	$c_3 \times 10^6$	$c_4 \times 10^{-5}$	$\Delta H_{0,i}^o$ (J/mol)	$\Delta G_{0,i}^o$ (J/mol)
CO_2	5.457	1.045	0.0	-1.157	-393509	-394359
CO	3.376	0.557	0.0	-0.031	-110525	-137169
H_2	3.249	0.422	0.0	0.083	0.0	0.0
H_2O	3.470	1.450	0.0	0.121	-241818	-228572
CH_4	1.702	9.081	-2.164	0.0	-74520	-50460
N_2	3.2733	0.504	0.0	0.0	0.0	0.0
O_2	4.1646	0.1299	0.0	-0.9452	0.0	0.0

Thermodynamic properties of coal are estimated with the empirical equations in reference [53] using the ultimate analysis data of Barbara coal (see Table 2.8).

Table 2.8.: The Barbara coal ultimate analysis data; Using these information, the coal formula will be $CH_{0.6694}O_{0.1265}N_{0.0166}S_{0.0030}$. The moisture content of the coal is 9.1 wt% as received.

Ultimate analysis	Dry (wt%)
Ash	1.61
Carbon	78.58
Hydrogen	4.41
Nitrogen	1.52
Chlorine	0
Sulfur	0.64
Oxygen	13.24

2.6.5. Calculation of exergy values

In this section the lines of derivation which are required to clarify the concept of exergy analysis are sketched. The exergy calculation procedure below is based on the

book of De Swaan-Arons, Van der Kooi, and Sankaranarayanan [43] and repeated here for the easier reference. The calculation procedure can be split up in 5 different steps, the first 2 steps generate the basic data, the molar exergy values of the elements in the dead state, necessary to calculate exergy values. First a dead state is defined in which all substances present in the air, the seas and the upper crust of the earth are assumed to react and undergo phase transitions at the pressure and temperature of the dead state until complete (chemical and phase) equilibrium is achieved, without any kinetic limitation. The exergy values in this dead state are to be defined as zero. Then the molar exergy values of the elements are calculated from these zero exergy values and appropriate Gibbs energy of reaction (formation) values at the pressure and temperature value of the dead state. In the further 3 steps the exergy values wanted are determined. For the first two steps and the exergy values of the elements in their stable phase, e.g., the book of Szargut can be consulted [157]. These data were used by us too.

Step 1 starts with the consideration of the definition of the exergy concept. The exergy of a system in a given state 1 (temperature T_1, pressure P_1, and mole fraction Z_1) is defined as the maximum amount of work that can be extracted when it goes to the dead state (temperature $T_{ex,0}$, pressure $P_{ex,0}$, mole fraction $Z_{ex,0}$) in a reversible process (with only heat exchange at the temperature of the dead state). The "dead state" can be defined as the average composition ($Z_{ex,0}$), temperature ($T_{ex,0}$), and pressure ($P_{ex,0}$) of the environment after having reached the most stable state(s). The environment may be considered as a combination of the earth's crust, rivers, seas, oceans, and the atmosphere. The exergy value of each component depends on the selection of this dead state. In the case of a process stream the molar exergy ex_{P_1,T_1} of that stream in state 1 can be expressed quantitatively as

$$ex_{P_1,T_1} = \left(h_{P_1,T_1,Z_1} - h_{P_{ex,0},T_{ex,0},Z_{ex,0}} \right) - T_{ex,0} \left(s_{P_1,T_1,Z_1} - s_{P_{ex,0},T_{ex,0},Z_{ex,0}} \right), \quad (2.64)$$

where h_{P_1,T_1,Z_1} and s_{P_1,T_1,Z_1} are the molar enthalpy and entropy of the system at temperature T_1, pressure P_1, and composition Z_1, respectively. $h_{P_{ex,0},T_{ex,0}}$ and $s_{P_{ex,0},T_{ex,0}}$ are the molar enthalpy and entropy of the system at the dead state, and $T_{ex,0}$ is the dead state temperature. In general the stream in the initial state can have work forms that can be converted via reversible processes in the same amount of other forms of work, e.g., kinetic and potential energy. All work forms in the stream must be added to the right hand side of Eq. (2.64). Because often these contributions are small compared to the molar exergy values without these work forms, these contributions are not indicated further.

In order to determine the molar entropy and enthalpy values in the dead state one can start with a mixture, e.g., air in the dead state. The molar exergy values of the components in this mixture, e.g., O_2, N_2, and CO_2 are defined to be zero. From the properties of this mixture the exergy value of the pure substances at the pressure and temperature of the dead state can be calculated. For the elements, e.g.,O_2 and N_2 these values are their molar exergy values in the dead state. This procedure

is shown in general in the first 2 steps of Fig. 2.9. The calculation procedure starts from the identification of the reference state, i.e., the average temperature, pressure, and composition [155]. Then the mixture is separated into the individual components. The exergy needed for going from step 1 to step 2 is $-\Delta g^{mix}_{T_{ex,0},P_{ex,0}}$ and can be obtained as

$$-\Delta g^{mix}_{T_{ex,0},P_{ex,0}} = -\left(\Delta h^{mix}_{T_{ex,0},P_{ex,0}} - T_{ex,0}\Delta s^{mix}_{T_{ex,0},P_{ex,0}}\right), \tag{2.65}$$

which describes the demixing Gibbs energy of the mixture into its individual components. Then the components C_j decompose into their elements e_j at a constant temperature and pressure of $T_{ex,0}$ and $P_{ex,0}$. The decomposition requires the amount of Gibbs energy $\Delta g^0_{f_j}$ for each component. These two steps are referred to as the calculation of chemical exergy of elements and has been investigated by other investigators [155]. They have reported the results in the form of standard chemical exergies of the elements. For the exergy change in step 3, which is the chemical exergy of each component M_i at $T_{ex,0}$ and $P_{ex,0}$, one can write

$$\sum_j \upsilon^j_{M_i} e_j \longrightarrow M_i \ , \tag{2.66}$$

where $\upsilon^j_{M_i}$ are the number of elements e_j in component M_i. With the standard molar chemical exergy $ex^{ch}_{j,P_{ex,0},T_{ex,0}}$ of each element e_j and the standard molar Gibbs energy of formation $\Delta g^0_{f_i}$ for component i, the chemical exergy of component i can be calculated by

$$ex^{ch}_{i,P_{ex,0},T_{ex,0}} = \Delta g^0_{f_i} - \sum_j \upsilon_j ex^{ch}_{j,P_{ex,0},T_{ex,0}}. \tag{2.67}$$

The exergy of the system after step 3 is equal to the summation of the chemical exergy of all the components at $P_{ex,0}$ and $T_{ex,0}$, i.e.,

$$ex_{P_{ex,0},T_{ex,0}} = \sum_i x_i ex^{ch}_{i,P_{ex,0},T_{ex,0}}. \tag{2.68}$$

It can be that the actual reference temperature and pressure are P_0 and T_0 which are different from the pressure and temperature in the dead state. In this case heat capacity at constant pressure data and appropriate equations of state are needed to take these differences into account. The temperature and pressure of the system change from $T_{ex,0}$ and $P_{ex,0}$ to T and P in step 4. The exergy change is equal to the physical exergy

$$ex^{ph}_{P,T} = \sum_i x_i ex^{ph}_{i,P,T} = \sum_i x^p_i \left(h^p_{i,P,T} - h^p_{i,P_{ex,0},T_{ex,0}}\right) - T_{ex,0}\sum_i x^p_i \left(s^p_{i,P,T} - s^p_{i,P_{ex,0},T_{ex,0}}\right), \tag{2.69}$$

where x^p_i denotes the mole fraction of species i of phase p. It must be calculated

using heat capacity at constant pressure data and an equation of state. $h^p_{i,T,P}$ and $s^p_{i,P,T}$ are the molar enthalpy and molar entropy of the pure component i in phase p at temperature T and pressure P. The total exergy value after the step 4 is $\sum_i x_i ex^{ch}_{i,P_{ex,0},T_{ex,0}} + \sum_i x_i ex^{ph}_{i,P,T}$.

To obtain the exergy value of the mixture the effect of mixing on the exergy value must be considered, in step 5 the components M_i are mixed at constant temperature T and pressure P to form the final mixture. The exergy change can be quantified with this equation

$$\Delta ex^{mix}_{T,P} = \Delta h^{mix}_{T,P} - T_{ex,0}\Delta s^{mix}_{T,P}. \tag{2.70}$$

$\Delta h^{mix}_{T,P}$ and $\Delta s^{mix}_{T,P}$ are the enthalpy and entropy change of mixing at T and P. Appropriate thermodynamic models must be chosen to calculate both changes. The exergy value of the mixture at T and P can be calculated by application of the following equation

$$ex_{P,T} = \sum_i x_i ex^{ch}_{i,P_{ex,0},T_{ex,0}} + \sum_i x_i ex^{ph}_{i,P,T} + \Delta ex^{mix}_{T,P}. \tag{2.71}$$
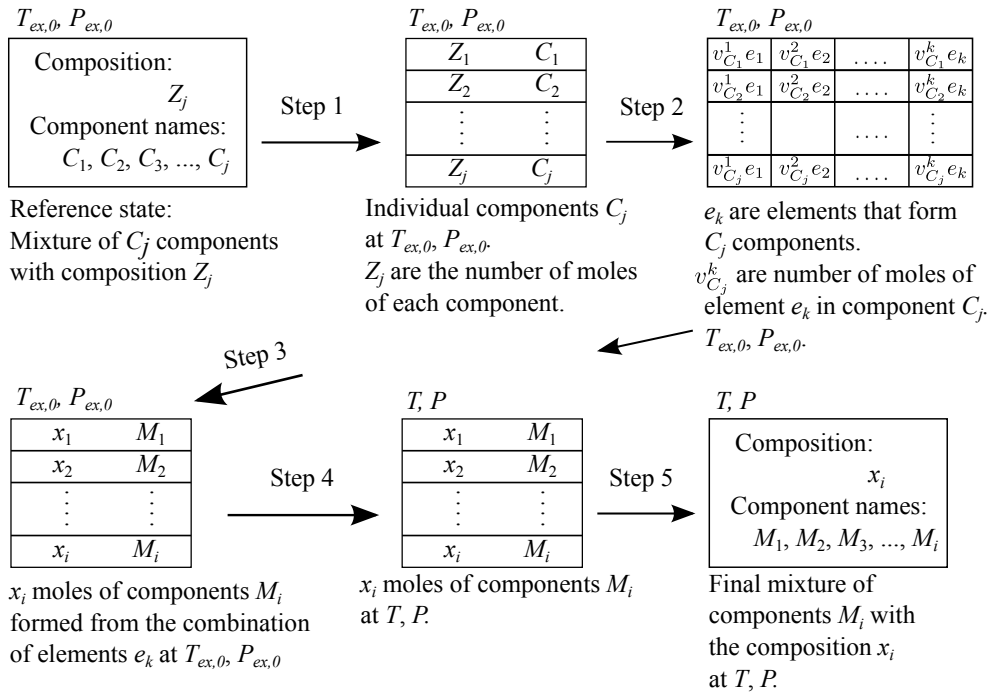

Figure 2.9.: Step by step calculation of exergy value

2.6.6. Grinding exergy

To calculate the energy required for grinding adsorbent minerals, the well-known equation of Bond [24] was used. Bond's equation is based on a differential equation [167] proposed by Walker et. al. [105], i.e.,

$$dE = -C\frac{dx}{x^n},$$
(2.72)

where E is the net required energy per unit weight of mineral, x is the size of a hole in the sieve that allows passing a given percentage (e.g., 80%) of the crushed mineral and C depends on its properties. The exponent n is an exponent that shows the order of the process; in Bond's law it is equal to 1.5. By integration of Eq. (2.72) the energy required to grind the material from passing size x_1 to x_2 is given by

$$E_{1-2} = C\left(\frac{1}{\sqrt{x_2}} - \frac{1}{\sqrt{x_1}}\right).$$
(2.73)

In this work the Bond equation

$$W = W_i\left(\frac{10}{\sqrt{P}} - \frac{10}{\sqrt{F}}\right)$$
(2.74)

is applied, where W is the specific energy of grinding per unit mass of a feed with 80% passing size of F micrometer to a product with 80% passing size of P micrometer. W_i is the Bond work index and is equal to the work required to reduce a unit weight of infinite size particle to the 80% passing size of 100 μm. It should be measured using experimental or plant data [105]. Ref. [122] has reported W_i values for some materials, of which the relevant values are given in Table 2.9.

Table 2.9.: Bond index for relevant minerals [122, 82]

Component	Bond index [kWh/ton]
Limestone	10.18
Wollastonite	14

2.6.7. Separation of CO_2 from flue gas

Flue gas is a mixture of nitrogen, water, CO_2, oxygen, and some other minor components. Separation of CO_2 from the flue gas is a very energy intensive process. The CO_2 capture technologies including chemical absorption, physical absorption/adsorption, membrane technologies, and cryogenic separation have been reviewed by many investigators [29, 33, 61, 70, 81, 99, 103, 113, 124, 173]. In spite of a tremendous ongoing research to improve the CO_2 capturing methods with respect to the energy consumption, these processes still consume a large magnitude of

energy. Currently, the chemical absorption using aqueous solution of MEA (mono-ethanol-amine) is the predominant technology. Table 2.10 shows the energy required to capture CO_2 for different processes according to different references. Here, an average CO_2 separation cost of 4000 kJ/kg CO_2 is used.

Table 2.10.: Practical exergy requirement in the CO_2 capture processes

Process	Exergy consumption (MJ/kg CO_2)	Note	Ref.
Aqueous MEA	3.0-7.0	Only stripping column reboiler	[113]
Chemical absorption	4.0-6.0	General review	[29]
MEA	3.7	-	[103]
MEA	4.2	Steam consumption	[33]
KS-2	2.9	Commercial solvent	[103]
Membrane system	0.5-6.0	Not yet feasible	[29]
Cryogenic	6.0-10.0	-	[29]
Wet mineral carbonation	3.6	Wollastonite, $\eta_{elec} = 0.40$	[82]

2.6.8. Exergy of CO_2 sequestration

Here it is assumed that CO_2 is separated from the flue gas of a 1000 MW natural gas power plant. The efficiency of the electricity production is assumed to be 45%, which means the natural gas exergy requirement is 1000/0.45=2222 MJ/s. By multiplying the natural gas exergy consumption by the CH_4 emission factor ($e_{CH4} = 0.055$ kg CO_2/MJ), the total CO_2 emission from the power plant Em_{pp} can be calculated as

$$Em_{pp} = \frac{1000}{0.45} \times 0.055 = 122.2 \, \frac{\text{kg} \, CO_2}{s}. \tag{2.75}$$

Here it is assumed that 122.2 kg/s CO_2 is transported to a sequestration aquifer via a 150 km pipeline to be injected at supercritical state, e.g., 100 bar and 35°C, at a depth of 1000 m. Using the Weymouth equation [98] to estimate the pressure drop in a gas pipeline, it is found that a pipeline with an inside diameter of 19 inch gives a pressure drop of 90 bar and an average gas velocity of 24 ft/s. The theoretical exergy consumption for the compression of CO_2 (Ex_{comp}) was calculated with the method explained in 2.6.1 and using the parameters in Table 2.11. The practical

exergy consumption of CO_2 transport can be calculated from the compression exergy requirement by

$$Ex_{transport} = \frac{Ex_{comp}^{th}}{\eta_{comp}\eta_{driver}\eta_{pp}}, \tag{2.76}$$

where η_{comp}, η_{driver}, and η_{pp} are the mechanical efficiencies of the compressor, electrical driver, and power plant. Here it is assumed that the gas compression is done in a multi-stage compressor with a maximum pressure ratio of three. The CO_2 stream leaves the pipeline at 10 bar and enters the injection multistage compressor station where the pressure increases to 100 bar before aquifer injection. The results of the compression exergy requirement in the transport and injection compressors are shown in Table 2.12. Here, an average value of 1000 kJ/kg CO_2 for the transport and injection costs is used.

Table 2.11.: CO_2 transport pipeline specification for a 1000 MW power plant

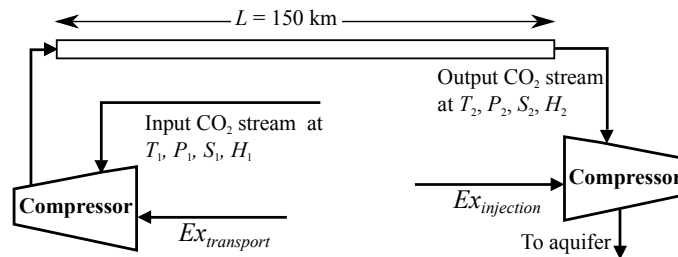| Pipeline Parameters	Value	Unit
Length	150	km
Inside diameter	19	inch
Input pressure	100	bar
Output pressure	10	bar
Mass flow rate	122.2	kg/s
Standard volumetric flow rate	201.6	MMSCFD
Average gas velocity	24	ft/s

Figure 2.10.: Transport of CO_2 via a 150 km pipeline and aquifer injection

Table 2.12.: Parameters and results for compression exergy in the transport and injection of CO_2

Compressor	Transport	Injection	Unit
Input pressure (P_{in})	1	10	bar
Output pressure (P_{out})	100	100	bar
Max pressure ratio ($\frac{P_{out}}{P_{in}}$)	3.0	3.0	-
η_{comp}	0.8	0.8	-
η_{driver}	0.9	0.9	-
η_{elec}	0.45	0.45	-
Ex_{comp}^{th}	288	142	kJ/kg CO_2
Ex_{comp}^{pr}	890	437	kJ/kg CO_2
Sequestration Exergy	1327		kJ/kg CO_2

2.7. Results and discussion

This section discusses three scenarios of UCG, i.e., (a) conventional air/water UCG, (b) using synthetic calcium oxide for insitu upgrading of the gas, and (c) using ex-situ wollastonite packed-bed for the conventional UCG product gas upgrading. In each scenario, maximizing the hydrogen content and minimizing the carbon content of the produced gas are the objectives. The scenarios can be distinguished according to the method of carbon capturing, i.e., (1) the conventional method using amine, (2) carbon capturing with synthetic minerals, i.e., calcium oxide and (3) carbon capturing with naturally occurring minerals. The results are presented in terms of gas compositions, recovery factors, and carbon dioxide produced per unit exergy of product gas.

2.7.1. Base case: air (oxygen)/water UCG

The base case considers conventional underground coal gasification with conventional carbon capture and sequestration, i.e., amine capturing and aquifer storage. It must be noted that throughout this book, the injection of "air/water" or "oxygen/water" is frequently repeated. It means that for the oxidizing agent in the feed stream, either oxygen or air is used. All results are presented as a function of the injected water/O_2 molar ratio for deep coal UCG at a pressure of 80 bar, which is the hydrostatic pressure for a 800 m deep coal layer.

The input exergy contains all contributions to generate the input materials. Indeed, when oxygen is used, it is necessary to calculate the exergy needed to separate O_2 from N_2. The exergy requirement in the production of oxygen is shown in Table 2.13. The air (oxygen) compressor, and water pump are the mechanical devices that need an exergy input; the exergy requirement of the water pump is neglected as in

many practical cases underground water flows into the UCG cavity by adjusting the pressure at the well head. The exergy consumption of the input streams has been calculated using the procedures explained in 2.6.1, 2.6.5, and 2.6.6 based on the specifications shown in Table 2.2. The exergy of the produced gas has been calculated using the procedure of 2.6.5. An in-house developed Matlab code is used to perform the computations. The reader can use the described model or a commercial process simulator, e.g., Aspen Plus to reproduce the result.
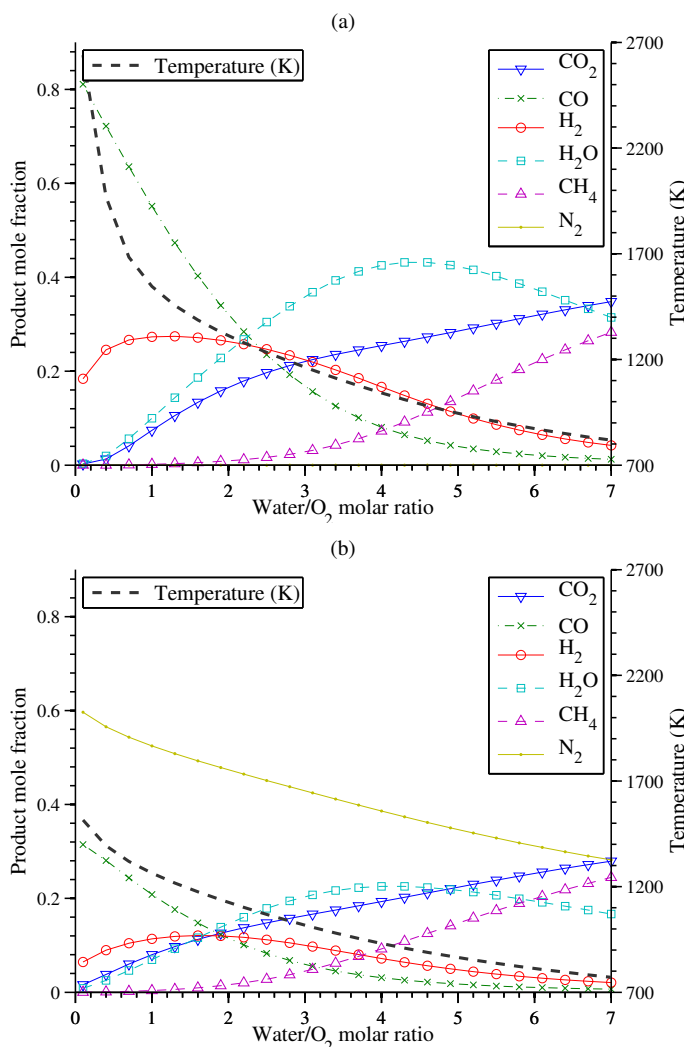

Figure 2.11.: Product composition profile for the conventional coal gasification at a pressure of 80 bar; a) pure oxygen b) N_2/O_2 ratio of 3.77 (air); the equilibrium model is considered to be valid above 1000 K.

Table 2.13.: Feed streams chemical exergy and CO_2 emission

Component	Chemical Exergy (kJ/kmol)	Production efficiency	Practical Exergy (kJ/kmol)	Production CO_2 emission (kg/kmol)	Ref.
CaO	135000	0.20	675000	73.7	[156]
O_2	3970	0.04	99250	5.5	[156]
H_2O	9490	1.0	9490	0	-

Fig. 2.11-a shows the product composition for oxygen gasification. A temperature of 1000 K is attained for a water/O_2 molar ratio of 4.2. The hydrogen concentration shows a maximum for a water/O_2 ratio of one, but it shows only a weak dependence for water/O_2 ratios below three. The methane concentration becomes significant above a water/O_2 of three, but it can be expected that high methane concentrations at high water/O_2 ratios will not be attained due to slow kinetics below a temperature of 1000 K [84, 104].

Fig. 2.11-b shows the product composition for air injection. Again the temperature decreases for increasing water/O_2 ratio. A temperature of 1000 K is attained for a water/O_2 molar ratio of three.
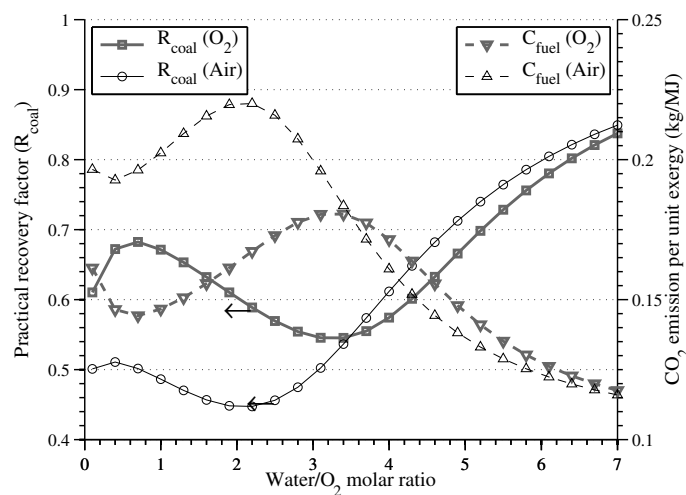
Figure 2.12.: Practical recovery factor of coal, Eq. (2.41), and CO_2 emission per unit net exergy of product gas for oxygen and air gasification at 80 bar; thick lines (∇, $\square$) show the result for a N_2/O_2 ratio of zero; thin lines ($\triangle$, $\circ$) show the results for a N_2/O_2 ratio of 3.77 (air).

Here, the carbon dioxide produced per unit net exergy, denoted by C_{fuel} [kg CO_2/MJ], is used as a measure of the CO_2 emission of the considered fuel. This will be shown in Fig. 2.12, which compares oxygen and air performances as oxidizing agents in UCG. At a water/O_2 ratio of zero the temperature in the cavity is very high (1500

K for air injection and 2600 K for oxygen injection, see Fig. 2.11) which shifts the Boudouard reaction Eq. (3.2) to the right side and results in a higher composition of CO. By increasing the water/O_2 ratio, more hydrogen is produced and the practical recovery factor increases due to the conversion of water with a low chemical exergy value to H_2 with a high chemical exergy value. This also increases the chemical exergy of the product without increasing its carbon content, which leads to a decline in CO_2 emission per unit exergy of product. However, the rate of increase of the H_2 composition becomes lower and it finally reaches a maximum, which causes the recovery factor to reach a maximum as well. At a water/O_2 ratios beyond 4.0 for oxygen injection and 2.5 for air injection the temperature drops below 1000 K, which gives a boost to the production of methane according to the chemical equilibrium model and the composition of methane significantly increases the chemical exergy of the product, which leads to an increasing recovery factor and a decreasing CO_2 emission per unit exergy at higher water/O_2 ratios. This temperature (1000 K) is chosen as an arbitrary marker below which the reaction rates are considered to be too slow for the process to be practically relevant particularly for the production of methane. In other words, only above 1000 K an equilibrium model is considered applicable. Within this range, the maximum recovery factor for air injection is around 52 % at a water/O_2 ratio of 0.4. The maximum practical recovery factor for oxygen injection is around 68 % for a water/O_2 ratio of 0.8. It shows that with oxygen injection it is possible to convert more water into fuel. The minimum carbon dioxide emission expressed in CO_2 emission per unit net exergy of product gas occurs at 0.19 kg CO_2/MJ for air injection and 0.14 kg CO_2/MJ for oxygen gasification at a water/O_2 ratio of 0.8 and a water/O_2 ratio of 0.4, respectively. In Fig. 2.13 where the methanation reaction has been disregarded, the optimum points can be observed more clearly. The model shows that oxygen gasification is the preferred method with a higher recovery factor and a lower CO_2 emission per unit net exergy, assuming that the thermodynamic model is adequate for these conditions.
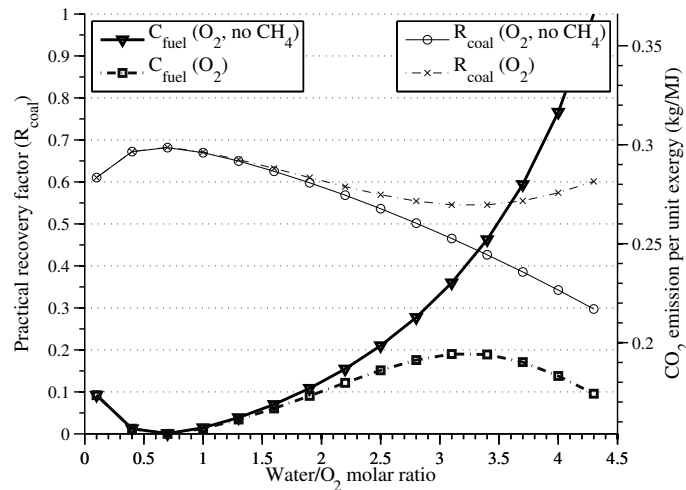
Figure 2.13.: Practical recovery factor (thin lines) and CO_2 emission per unit net
exergy of product gas (thick lines) for the oxygen gasification case as a function of
water/O_2 molar ratio; by eliminating methane formation reaction from the model
a single optimum point is found for this system.

For other types of coal or pressure the optimal water/O_2 ratio for the recovery factor
and CO_2 emission ratios varies. Depending on the situation oxygen or air injection
may be preferred.

The next steps are to show the effect of the current state of technology efficiency
factors (practical case) and the effect of carbon capture and sequestration (zero-
emission case) on the maximum recovery factor for oxygen and air gasification. Fig.
2.14 compares the theoretical case and practical case to the zero-emission case. All
the curves show a local maximum at low water/O_2 ratio, which similar to Fig. 2.12
can be explained by the conversion of water to H_2 at higher temperatures. The
local minimum in the recovery factors is a direct consequence of the increase in
composition of methane with increasing water/O_2 ratio. As discussed before, the
methanation reaction at this water/O_2 ratio is to slow to be practical. Indeed the
zero-emission recovery factor drops to 15% for oxygen injection and drops below zero
for air injection. If, as opposed to amine capture, optimized membrane separation
techniques could be used, the zero-emission recovery would be around 40%. Unfor-
tunately, for the current state of the art, membrane techniques are not efficient and
do not have sufficient capacity for practical applications and the efficiency for future
high capacity membranes is as yet not certain. It is concluded that underground
coal gasification with zero-emission greenhouse gases at the current state of the art
is not feasible.

Figure 2.14.: Theoretical (R^{th}), practical (R^{pr}), and zero emission (R^{ze}) recovery factors for (a) oxygen and (b) air gasification at 80 bar considering methane formation

Fig. 2.15 shows recovery factors for the base case in the absence of the methane formation reaction in the chemical equilibrium model; the recovery factor decreases at increasing water/O_2 ratios. Consequently, the calculation shows only one optimum water/O_2 ratio.
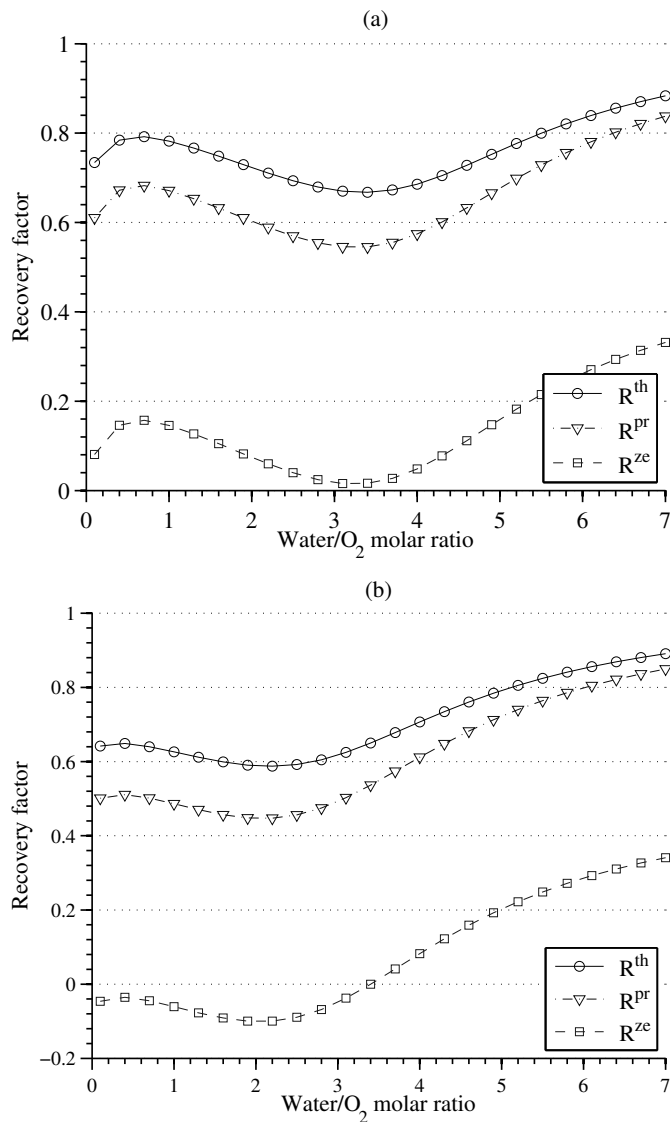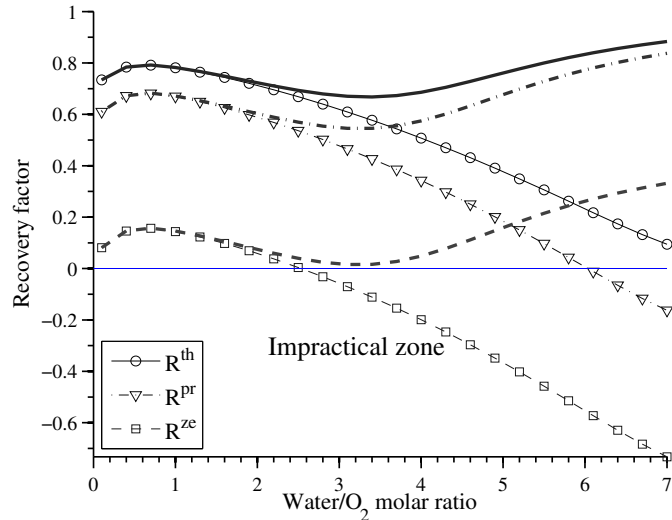
Figure 2.15.: Theoretical (R^{th}), practical (R^{pr}), and zero emission (R^{ze}) recovery factors for oxygen gasification at 80 bar with and without methane formation; Thick lines show the result of the equilibrium calculation with formation of methane. Thin lines with markers show the case with no methane formation; the area below the horizontal line shows the impractical zone, i.e., negative recovery factors.

2.7.2. Scenario 1: insitu usage of CaO

Scenario 1 considers the case of using insitu CO_2 capturing with CaO (see Fig 3.14-a). In this case one needs the exergy requirement in the production and preparation of CaO in addition to other exergy requirements considered in the base case. Therefore, the cumulative exergy consumption of CaO and the crusher are considered. These exergy contributions can be added to the exergy requirements of the input stream considered in the base case described above. Due to the fact that the volume limitation prevents the complete capture of CO_2 with insitu carbonation of CaO, the CCS procedure is implemented to capture and sequester the remaining CO_2 as described in the base case, i.e., amine capturing and aquifer injection.

Without loss of generality, a constant oxygen injection rate is chosen to burn 1 m^3 of coal per unit time. The CaO flow rate is calculated so that the volume of coal combusted and gasified is equal to the volume of $CaCO_3$ formed plus the volume of unreacted CaO (see Fig. 2.2). The temperature is constrained to be below the temperature at which $CaCO_3$ decomposes. Again it is assumed that at high temperatures, there is no reaction rate limitations. The temperature decreases as the flow of water increases as shown in Fig. 2.16; the water to oxygen ratio should be above 2.5 to avoid that $CaCO_3$ dissociates into CaO and CO_2 (see Fig. 2.16). Due to the volume constraint the fraction of carbon sequestered into $CaCO_3$ is constant, i.e., 0.36 mole CO_2/mole of converted coal. It turns out that the carbon content of

the product gas stream remains relatively constant as the water/O_2 ratio increases. The carbon content of the produced gas is lower than for the base case. Indeed, it results in the production of a gas fuel with a higher hydrogen to carbon ratio compared to the base case.
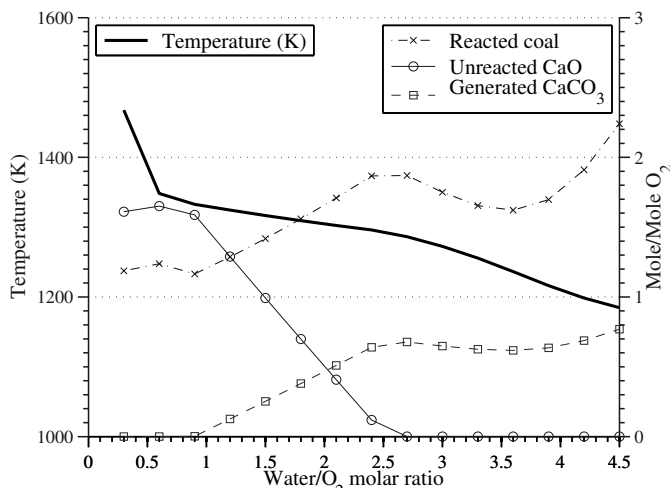
Figure 2.16.: Conversion of coal and CaO and temperature profile as a function of water/oxygen ratio for oxygen gasification at 80 bar; the calculated amounts of reacted coal, unreacted CaO, and generated $CaCO_3$ in the gasification cavity are reported as the number of moles divided by the number of moles of injected O_2.

The composition of the product gas is shown in Fig. 2.17. The main feature shown in the figure is that the hydrogen concentration is highest at water to oxygen molar ratio of 2.4 and decreases at the expense of methane formation. With respect to the composition obtained without CaO shown in Fig. 2.11-b, more methane and hydrogen and smaller amounts of CO_2 are produced when CaO is included; in this case more water is converted to fuel.
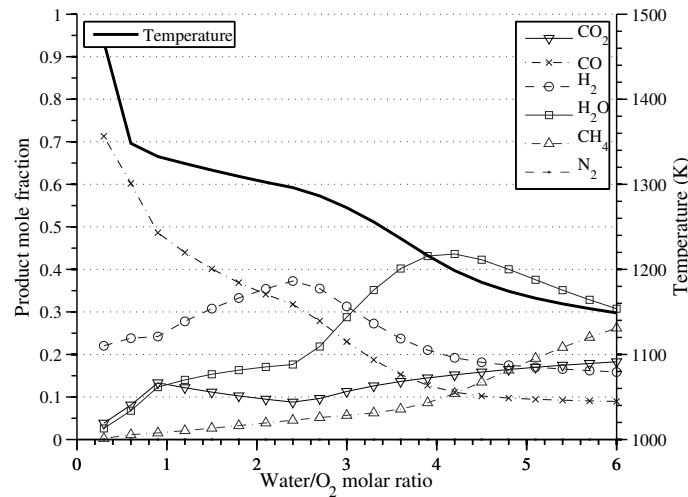
Figure 2.17.: Composition of final product as a function of water to oxygen ratio for oxygen gasification at 80 bar.

Also with the use of CaO, the final product is not carbon-free and one needs to consider again the exergy requirement for removal and sequestration of CO_2 after the combustion of the product gas. The results of the exergy recovery have been shown in Fig. 2.18. As discussed in section 2.5, the results are expressed in theoretical, practical, and zero-emission exergy recoveries as explained in the previous section. For a water/O_2 ratio below one, part of the initial CaO remains unreacted, which has a negative effect on the recovery factor by increasing the input exergy to the process and not performing its duty of removing CO_2 from the product. By increasing the water/O_2 ratio, the temperature drops and as a result more CaO reacts with CO_2 which improves the quality of product by shifting the shift reaction Eq. (3.3) towards production of more hydrogen. It also increases the recovery factor of the process. The recovery factor keeps increasing until the process reaches the volume constraint where no more CaO can be injected, which appears as a local maximum in Fig. 2.18. After this point, by increasing the water/O_2 ratio, temperature drops and the CO_2 content in the product increases, which causes a decline in the chemical exergy of the product and the recovery factor of the process. As explained before, by increasing the water/O_2 ratio the temperature drops, which results in the production of methane with a high exergy value, which can increase the recovery factor to a new maximum. But the slow rate of the methanation reaction does not allow this process to be practical at high water/O_2 ratios. From a theoretical point of view in principle more than 80% of exergy available in coal can be recovered. In practice, considering the present state of the art technology but without the removal of carbon emission only around 30% of the coal exergy can be recovered. Including removal of the carbon emission, the coal exergy recovery is negative meaning that the input exergy exceeds the output exergy. In other words the amount of energy gained from the coal is lower than the input exergy streams inclusive the exergy required for the

capture and sequestration.

Again the right half of the figure is ignored due to the reaction rate constraints. At temperatures higher than the stability temperature of $CaCO_3$, which occurs at water/O_2 injection ratios below 1.8 the practical and zero-emission recovery factors are low. It turns out that the CO_2 emission per unit net exergy is higher than the gasification without CaO addition (see Fig. 2.13). The zero emission curve with CaO addition is even more negative than the conventional case (see Fig. 2.12). It is concluded that the application of synthetic CaO does not lead to any advantages with respect to conventional gasification neither for the practical case nor for the zero emission case.
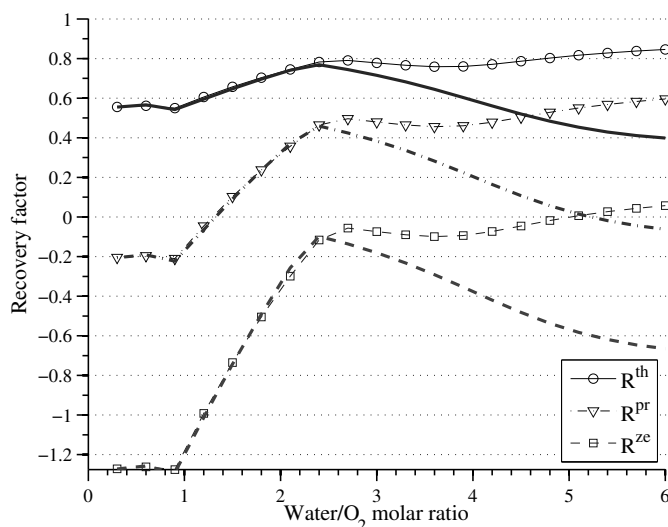
Figure 2.18.: Coal theoretical (R^{th}), practical (R^{pr}), and zero-emission (R^{ze}) exergy recovery for air gasification at 80 bar for different water to oxygen ratios. The thick drawn, dash-dot and dashed lines show the result of gasification model without the formation of methane.

Fig. 2.19 shows the effect of the CO_2 capturing process on the zero-emission recovery factor using membrane separation of CO_2 with average exergy consumption of 1000 kJ/kg CO_2, Amine separation with 4000 kJ/kg CO_2, and cryogenic separation with 8000 kJ/kg CO_2. The result shows that by advancing the CO_2 separation technology towards lower exergy consumption per unit mass of captured CO_2, the zero-emission recovery curve shifts upwards to narrow the wide gap between the zero-emission and practical recovery of the energy resource. Only with membrane technology, a positive zero-emission recovery is possible.

61
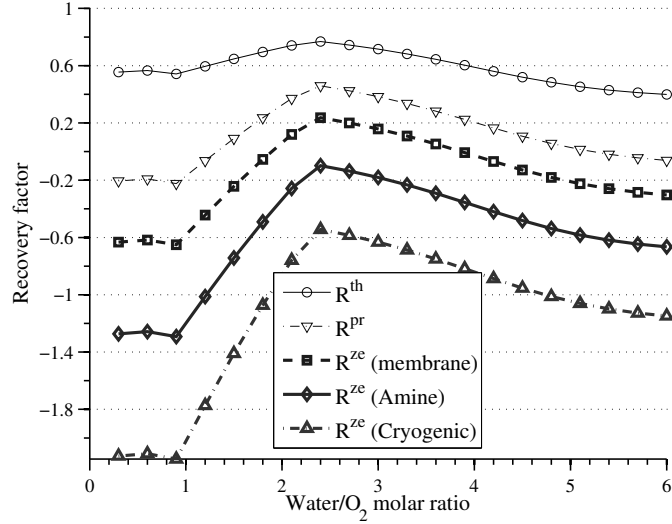
Figure 2.19.: Effect of CO_2 capture method on the zero emission (R^{ze}) recovery factor (thick lines); membrane ($\square$), amine ($\lozenge$), and cryogenic ($\triangle$) separation of CO_2 from the flue gas.

2.7.3. Scenario 2: ex-situ upgrading with wollastonite

In the second scenario the same conditions as in the base case are used, except that the step of wet mineral carbonization is added (see Fig. 3.14-b). In mineral carbonization, the CO_2 is removed ex-situ through the reaction [81]:

$$CaSiO_3 + CO_2 \rightarrow CaCO_3 + SiO_2. \tag{2.77}$$

The mineral carbonization is used to adsorb CO_2 from the gas produced in a conventional underground coal gasifier (Fig. 2.11-a,b) and upgrade the gas by promoting the shift reaction, i.e.,

$$CO + H_2O \rightleftharpoons CO_2 + H_2. \tag{2.78}$$

The advantage of using wollastonite is that it can be found in nature [67]. In addition, 38 μm particles of wet wollastonite in reaction with CO_2 at 200^oC and 20 bar can reach a maximum conversion of 70 % in 15 minutes[80], which is an acceptable reaction rate for this application. Fig. 2.20, which has been generated using the same approach as described in section 2.3, shows the effect of temperature and pressure on the equilibrium conversion of wollastonite. Based on the partial pressure of CO_2 in the gasification product, the temperature of the ex-situ reactor must be controlled to reach the maximum conversion of wollastonite (500 K in Fig. 2.20).
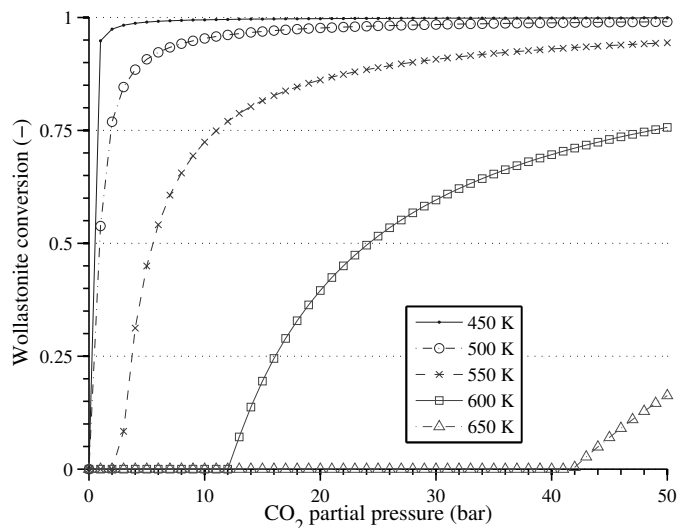
Figure 2.20.: Equilibrium conversion of wollastonite in contact with stoichiometric amount of CO_2 at different pressures and temperature. In this work, a temperature of 500 K is chosen for the ex-situ reactor.

In the exergy analysis, the exergy requirement for crushing the calcium silicate is considered. However, exergy connected to transport of wollastonite (calcium silicate) is disregarded. It should be noted that the exergy requirement for transport of solid materials over great distances can be very large and must be included in the analysis. The computations confirm that the net recovered exergy of coal strongly depends on the crushing size [82]. Fig. 2.21 shows the upgraded product gas composition. The optimal composition of hydrogen is reached at a water/O_2 ratio of 2.2. At this point all the carbon monoxide is consumed in the ex-situ reactor and is converted to H_2 and CO_2, where CO_2 reacts with the wollastonite. If the reaction rate at the ex-situ reactor operating condition, i.e., 500 K and 80 bar, is high enough then the reactor can produce pure hydrogen. By increasing the water/O_2 ratio above 2.2, no more hydrogen can be produced because there is no CO left to react with steam.

The recovery factors of the ex-situ upgrading scenario, shown in Fig. 2.22, looks counter intuitive as the maximum recovery value does not appear at the pure hydrogen production but appears at the water/O_2 ratio of 0.5, where the product gas consists of 70% CO and 30% H_2. This effect is due to the higher chemical exergy of CO with 283.0 kJ/mol than H_2 with 236.1 kJ/mol. At this point, the maximum theoretical and practical recovery factors are 76% and 64%, respectively. But when capturing and sequestration of CO_2 is considered, the product gas with a lower carbon content per unit exergy becomes more attractive and shows the highest zero emission recovery factor of 38% at a water/O_2 ratio of 2.2.

Fig. 2.23 shows the practical and zero emission recovery factors of the UCG process with ex-situ upgrading of the product and the CO_2 emission per unit net exergy (thick line). Without environmental concerns, the optimum that gives the highest
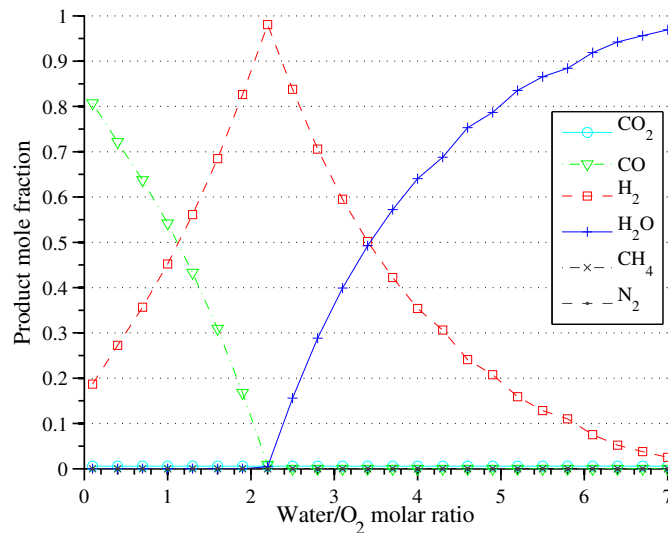
Figure 2.21.: Product composition of the UCG process- second scenario; the CO_2 is adsorbed by the wollastonite. theoretically, nearly pure hydrogen can be produced at water to oxygen ratio of 2.2. The temperature is constant at 500 K and the pressure is 80 bar. The methanation reaction has been disregarded.

practical exergy recovery, i.e., point *a* in Fig. 2.23, shows a practical recovery factor of 67 % with a CO_2 emission of 0.174 kg/MJ. On the other hand, at point *b* in Fig. 2.23, the CO_2 emission has a minimum value of 0.022 kg/MJ but with a lower recovery factor of 47 %. There is a sharp decline in both recovery factor and CO_2 emission curves from point *a* to point *b*. Based on these results, shown in Fig. 2.23, three criteria can be defined to choose the optimum process parameter, i.e., water/O_2 ratio:

1. If CO_2 emission is not a criterion, the optimum process parameter is the value that maximizes the practical recovery factor, i.e., point *a* with 67 % practical recovery.

2. If CO_2 emission is a criterion, but the CO_2 capture and sequestration is not an option, then any point between *a* and *b* that gives a feasible recovery factor and an acceptable level of CO_2 emission can be considered as the optimum. For instance, water/O_2 ratio of 1.6 gives a practical recovery factor of 57 % while the total CO_2 emission is 0.083 kg/MJ which is only 1.5 times higher than one would obtain by combustion of methane with a CO_2 emission of 0.055 kg/MJ.

3. If CO_2 emission is a criterion and CO_2 capturing and sequestration is an option, the optimum process parameter is the value that maximizes the zero-emission recovery factor, i.e., point *b* with 42 % zero-emission recovery. Hence, for a water/O_2 molar ratio of 2.2, CO_2 emission is minimal and zero-emission recovery factor is maximal. This behavior is coincidental.
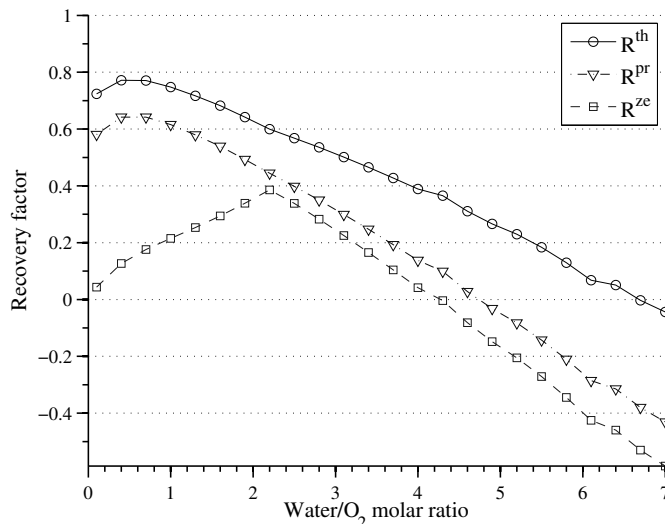
Figure 2.22.: Theoretical, practical, and zero-emission recovery factors for the ex-situ upgrading of conventional gasification products in an ex-situ wollastonite packed bed.

2.8. Conclusions

- The theoretical, practical, and zero-emission recovery factors for UCG are fully analyzed, which can serve as template for the analysis of any other energy recovery/conversion processes.

- Conventional underground coal gasification with oxygen has a higher recovery factor than air gasification.

- Practical oxygen gasification has a carbon emission of 0.14 kg CO_2/MJ exergy, which can be compared to combustion of methane with a carbon emission of 0.055 kg CO_2/MJ, i.e., three times larger.

- Zero-emission recovery factors of deep UCG using the state of the art technology, i.e., amine separation, are small or negative. More efficient CO_2 capture technology, e.g., membranes, have as yet not sufficient capacity to be practical.

- It is concluded that UCG with zero greenhouse gases emission with the current state of the art is not yet feasible, mainly due to the low efficiency of the CO_2 capturing processes.

- The use of synthetic CaO to reduce the carbon emission is counterproductive in reducing the greenhouse gas emission. Zero-emission/practical recovery factors are negative for practical water/O_2 injection ratios.

- Use of calcium silicates to reduce the greenhouse gas emission would perform better than CaO. Recent literature, however, shows that the reaction rates to convert wollastonite to calcium carbonate is too slow to lead to a practical technology.

Figure 2.23.: Practical and zero-emission recovery (left axis) and CO_2 emission per unit net exergy (right axis) of the UCG with ex-situ upgrading of product gas with wollastonite as a function of water/O_2 ratio; Letter a shows the maximum practical recovery factor with no concern on CO_2 emission and letter b shows the maximum practical recovery factor with the lowest CO_2 emission. In this figure reaction rate aspects are not considered (see text).

- The type of analysis proposed in this paper can be applied to any other energy conversion processes and shows where it has to be improved to increase the overall recovery factor.

- The main weak point of the use of zero-emission UCG with the current state of the art technology are the exergy-intensive CO_2 capturing methods. Theory indicates that less exergy-intensive processes can be developed.

- If CO_2 emission is not a criterion, the optimum process parameter is the value that maximizes the practical recovery factor.

- If CO_2 emission is a criterion, but the CO_2 capture and sequestration is not an option, then any value of the process parameters that gives a positive practical recovery factor and an acceptable level of CO_2 emission can be considered as the optimum.

- If CO_2 emission is a criterion and CO_2 capturing and sequestration is an option, the optimum process parameter is the value that maximizes the zero-emission recovery factor.

3. Alternating injection of oxygen and steam in underground coal gasification: mathematical modeling and exergy analysis

Things get worse under pressure.

Murphy's Law of Thermodynamics

Abstract

Recent successful low-pressure underground coal gasification pilot experiments that uses alternating injection of oxygen (or air)[1] and steam has shown potential in large scale hydrogen production. This chapter extends an existing steady state model to a transient model that can describe an alternating injection of oxygen (or air) and steam for deep thin coal layers. The model includes transient heat conduction, where the produced heat during the oxygen (or air) injection stage is stored in the coal and surrounding strata. The stored heat is used in the endothermic gasification reactions during the steam injection.

The results show that product composition and temperature oscillation can be predicted with a reasonable accuracy. The stored heat can deliver additional energy that can maintain the gasification during the steam injection period for a limited time. During the steam injection cycle, at low pressure the volumetric flow and the hydrogen content of the product gas are both high, but at higher pressures while the hydrogen composition is still high the coal conversion decreases considerably. Exergy analysis confirms that the alternating injection of oxygen (or air)/steam describes a practical process for UCG at low pressure. However, injecting a mixture of steam and oxygen results in a practical recovery factor of coal higher than the alternating injection process.

---

[1]The oxidizing agent can be either air (with natural oxygen content of 21 mole percent) or pure oxygen. In the modeling section, the composition of the injected oxidizing agent that is used for each simulation is explicitly given.

3.1. Introduction

The reserves of easily extractable oil and gas are decreasing [3, 18, 112]. Consequently, there is an increasing interest for coal utilization. Societal concern about global warming make that the use of coal, with on average only one atom of hydrogen per atom of carbon (CH), is considered less attractive than oil (two hydrogen/carbon, CH_2) or methane (four hydrogen per carbon, CH_4). Therefore it has been suggested to investigate whether it is possible to reduce the carbon foot print of coal if coal is utilized via underground coal gasification (UCG). In European countries like Belgium, the Netherlands, Poland and Great Britain coal is deposited in relatively thin (1-3 m) and deep layers (1000-2000 m) [20]. Moreover issues regarding the carbon foot print are high on the agenda in Europe. Moreover, developed technology can be exported to the BRICS (Brazil, Russia, India, China, and South Africa) countries [85].

Recent field trials in China and Poland suggested alternating injection of air and steam, where the air injection period serves to heat up the coal and surrounding strata, and the steam injection period serves to produce high quality gas recuperating the heat from the surrounding strata [174]. Stańczyk et al. [151, 152, 150] gasified the hard coal in a pilot underground gasifier in the Główny Instytut Górnictwa (GIG), Katowice, Poland with alternating injection of oxygen and steam. They successfully produced a fuel gas with more than 50 % hydrogen during the steam cycle. Both trials were done at atmospheric pressure. However, in the gasification of deep coal seams, with the coal connected to an aquifer system the pressure should be kept high, i.e., slightly higher than the hydrostatic pressure, to avoid underground water flow into the gasification cavity. If successful, this alternating injection procedure would allow to separate production periods with high CO_2 and nitrogen content from periods with mainly hydrogen content. If the gas of the first period can be sequestered separately the hydrogen/carbon ratio can be improved.

To be able to study the alternating injection UCG process, a dynamic model is needed, which can predict the composition of gaseous product, the rate of coal consumption, and the heat transfer to the coal layer and the surrounding strata. There is an extensive literature on coal gasification models that can predict product gas composition and the rate of cavity growth [28, 119, 120, 161, 115, 47, 21]. Some models use only chemical equilibria on the coal surface to predict the product gas composition [50]. However this assumption results in an overprediction of the carbon monoxide concentration and an underestimation of the CO_2 content in the product gas.

A model for the chemical reaction of a coal block with air or a mixture of oxygen and steam was developed by Perkins and Sahajwalla [119], which can be applied to underground coal gasification problems for the prediction of the coal consumption rate and the composition of the product gas. The model considers multi-component diffusion, coal drying, pyrolysis, and char/gas chemical reactions. In another paper

Perkins and Sahajwalla [120] studied the effect of various parameters, e.g., pressure, temperature, water influx, and coal properties on the rate of cavity growth and product gas quality. However, to find a numerical solution to their highly nonlinear model, they assume that the bulk gas composition is known.

A cavity growth model developed by Biezen et al. [21] describes cavity development in these coal layers and reasonable agreement with the Pricetown field trial was found, although the model is not developed to predict the product gas composition.

A mathematical model for the cavity growth applicable to UCG in shrinking coal was written by Britten and Thorsness [28]. It assumes a fixed low injection point and an axisymmetric cavity around it, well mixed bulk gas, radiation dominated heat transfer, and the spreading of the injected gas through the accumulated rubble on the cavity floor. The model predictions were in agreement with the process data from two UCG field tests [28, 161].

A quasi-steady state model developed by Van Batenburg et al. [161] based on the above mentioned model of Britten and Thorsness, was able to describe the product gas composition in the Pricetown field trial. It is, however, not suitable for alternating injection because it does not consider a time dependent heat conduction module. This study extends the previous quasi-steady-state model of Van Batenburg to account for heat accumulation and recuperation from the surrounding strata.

In a conventional underground coal gasification process, oxygen and steam are injected simultaneously into a coal layer. The idea behind this process is that oxygen reacts with coal in an exothermic reaction to produce heat, i.e.,

$$CH_aO_b + \left(1 - \frac{b}{2} + \frac{a}{4}\right) O_2 \rightarrow CO_2 + \frac{a}{2}H_2O. \tag{3.1}$$
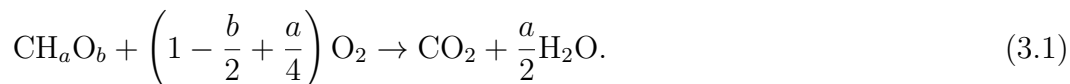
Then the injected steam and produced CO_2 reacts with coal to produce H_2 and CO due to the endothermic Boudouard and shift reactions, i.e.,

$$CH_aO_b\,(s) + (1 - b)\,CO_2 \rightleftharpoons (2 - b)\,CO + \frac{a}{2}H_2, \tag{3.2}$$

$$CH_aO_b + (1 - b)\,H_2O \rightleftharpoons CO + (1 - b + \frac{a}{2})H_2. \tag{3.3}$$
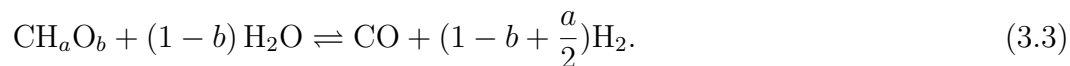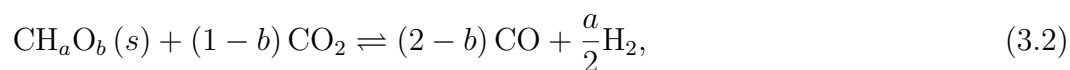
The heat required for the Bouduard and shift reactions is provided by the combustion reaction. However in practice injected oxygen reacts instantaneously with the combustible H_2 and CO in the cavity and subsequently the hot gases react with coal. The overall composition of the produced gas is reported in Table 3.1. It shows that the gas contains 56 % N_2 and 18 % CO_2, and consequently the fuel gas heating value is low. Downstream separation of N_2 and CO_2 to increase the quality of gas is not practical with the current state of technology.

Table 3.1.: A typical composition of UCG product gas; average values from the
   compositions reported in [85]

Component	CO_2	CO	H_2	CH_4	N_2	Other
Mole percent	18.3	7.4	14.9	2.1	55.9	1.4

The alternating injection of air and steam is an alternative procedure that separates
the combustion and gasification reactions. First air is injected to react with coal and
produce heat. It is assumed that the generated heat is stored in the coal and roof
layers. The gas produced in this cycle is mainly N_2 and CO_2. Some carbon monoxide
and hydrogen can also be produced depending on the composition and water content
of the coal. Then air injection is stopped and steam is injected. Steam reacts with
the hot coal layer, consumes the heat in the endothermic reactions, and produces
a gas with high hydrogen content. Effectiveness of this step highly depends on the
pressure. Low pressure is a more favorable condition for this reaction as equilibrium
reactions Eqs. (3.2 & 3.3) shift to the right side to produce more hydrogen and
carbon monoxide.

To illustrate these ideas an extended model is applied to low pressure alternating
injection underground coal gasification. This model can reproduce the results from
the GIG trial, which can also be used as a validation of the model. However, most of
the coal layers in Europe appear in deep layers and therefore the gasification must
be done at high pressure. Hence, the effect of pressure on the product quality of
deep UCG is investigated. Apart from pressure, the length of oxygen and steam
injection cycles, the time cycle ratio, and the steam/oxygen flow ratio are other
important parameters that affect the process and will be studied. Depending on the
volume of the cavity and steam/oxygen flow rates, the produced gas in each stage
can be mixed with the product of the previous and/or the next stage. In this case,
the average composition of the product gas of the alternating injection gasifier is
compared with the gasification product of a gasifier, which opposed to alternating
injection, uses a continuous injection of a feed stream of a mixture of oxygen and
steam.

The organization of the chapter is as follows: Section 3.2 describes the basic assump-
tions of the model. In Section 3.2.1 the multi-component mass transfer model and
the chemical equilibrium of char/gas are explained. Section 3.2.2 derives the heat
balance equations that include conductive heat loss or gain and radiation between
the cavity surfaces. Section 3.2.3 shows the relation for the calculation of the bound-
ary layer thickness for natural convection dominated flow inside the cavity. Then
an algorithm is described to solve the system of nonlinear differential and algebraic
equations in Section 3.3. Section 3.4 describes a model that shows the possibility
of mixing between cycles. In section 3.5.1, the results of the model are compared
with a chemical equilibrium model to show the importance of mass transfer limita-
tions in UCG reactions. Section 3.5.2 compares the results of the GIG field trial to
validate the mathematical model. Then, in section 3.5.3 the effect of the duration

of feed injection and the pressure of the gasifier on the quality of the UCG product are studied. In addition, the effect of steam/O_2 ratio on the UCG product quality for the injection of a mixture of oxygen and steam is analyzed. An exergy analysis is performed on the overall process and calculate the practical and zero-emission recovery factors of coal. Finally, the chapter ends with some conclusions.

3.2. Mathematical model

A schematic representation of the UCG process is shown in the left side of Fig. 3.1. It includes a vertical injection and production well into a coal layer. The bottom of the wells are interconnected through the coal layer by one of the linking methods [69], e.g., a horizontal well. Depending on the feed injection plan, oxygen (air) or water (steam) or a mixture of them is injected through the injection well. The combustion/gasification process is triggered near the production well by providing heat, for instance, by using a propane burner. The initial cross section (perpendicular to the horizontal well) of the coal layer and the roof rock above it is shown in Fig. 3.1-a. The combustion/gasification reactions consume coal leading to cavity formation. As the gasification proceeds the cavity will expand (Fig. 3.1-b); after some time the cavity reaches the roof rock and the roof begins to subside (Fig. 3.1-c). After that, depending on the constitution of the roof negligible collapse, complete collapse or partial collapse can occur. With negligible collapse an open channel remains. For complete collapse the coal layer is buried in the roof rock debris. For partial collapse two open channels remain on both sides of the coal face, as shown in Fig. 3.1-d. In this chapter, the author's interest is confined to the partial collapse case. The channel is bounded by three faces, viz. the coal face, the roof face, and the rubble face, where the injected oxygen penetrates through the rubble zone and reacts with the combustible gases as soon as it enters the cavity and before reaching the coal face. The heat and products of the combustion reaction reach the coal face, where they are converted to gaseous products. The goal is to write a mathematical model that describes this heat and mass transfer inside the cavity. The exothermic combustion reaction on the rubble face and the endothermic gasification reactions on the coal face cause a temperature difference between the cavity walls, which triggers a temperature and composition driven natural convection flow inside the cavity. Here it is assumed that the circulation of gas inside the cavity makes a uniform gaseous mixture, which is called the bulk gas. The bulk gas species diffuse through a boundary layer to the coal face and react with coal. Due to the high temperature of the surfaces, the heat transfer mechanism is radiation-dominated. The radiation from the rubble hot face (where the highly exothermic combustion reaction occurs) heats up the coal and the roof faces. On the coal face, part of the heat received by radiation is consumed in the endothermic gasification reactions between the coal and bulk gas. Part of the heat also diffuses into the coal and roof layers where it increases the temperature; for the calculations, it is assumed that the coal and roof

are initially at the subsurface environmental temperature.

Referring to Fig. 3.1-d, one needs to establish the fluxes at the three faces of the cavity, to find the gas composition in the cavity, which is assumed to be the product composition. The following three faces are considered in the cavity. The cavity/rubble interface through which the injected fluids, like oxygen, nitrogen and water enter the cavity. The oxygen that enters the cavity immediately reacts with the product gas in the cavity. It is assumed that a fraction ε_{CH_4}, ε_{CO}, ε_{H_2} of oxygen is reacting with methane, carbon monoxide, and hydrogen respectively where $\varepsilon_{CH_4}+\varepsilon_{CO}+\varepsilon_{H_2}=1$. In the calculations it is assumed that 50 % of the oxygen reacts with CO in the produced gas to form CO_2 and 50 % of the oxygen reacts with H_2 to form H_2O.
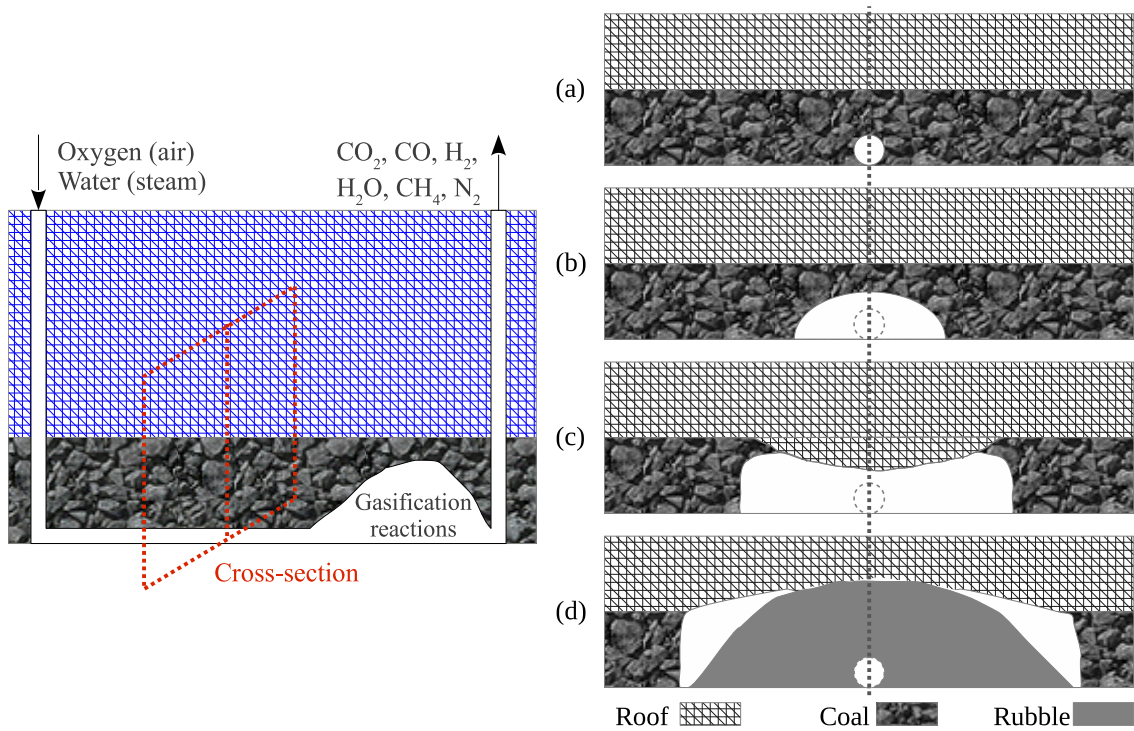
Figure 3.1.: Schematic flow diagram of underground coal gasification (left) and the cavity growth and partial roof collapse in a cross section perpendicular to the injection line (right).

In the partial collapse case, for the fluxes slightly downstream of the rubble cavity interface the following expressions are obtained (see Fig. 3.2):

$$N_{CH_4}^{rubble} = -\frac{1}{2}\varepsilon_{CH_4}\overline{N}_{O_2}^{rubble}, \tag{3.4}$$

$$N_{\text{H}_2}^{rubble} = -2\varepsilon_{\text{H}_2}\overline{N}_{\text{O}_2}^{rubble}, \tag{3.5}$$

$$N_{\text{CO}}^{rubble} = -2\varepsilon_{\text{CO}}\overline{N}_{\text{O}_2}^{rubble}, \tag{3.6}$$

$$N_{\text{H}_2\text{O}}^{rubble} = \overline{N}_{\text{H}_2\text{O}}^{rubble} + 2\varepsilon_{\text{H}_2}\overline{N}_{\text{O}_2}^{rubble} + \varepsilon_{\text{CH}_4}\overline{N}_{\text{O}_2}^{rubble}, \tag{3.7}$$

$$N_{\text{CO}_2}^{rubble} = 2\varepsilon_{\text{CO}}\overline{N}_{\text{O}_2}^{rubble} + \frac{1}{2}\varepsilon_{\text{CH}_4}\overline{N}_{\text{O}_2}^{rubble}, \tag{3.8}$$

$$N_{\text{N}_2}^{rubble} = \overline{N}_{\text{N}_2}^{rubble}. \tag{3.9}$$

The boundary fluxes are different from the surface fluxes due to the combustion reactions in the rubble zone. The symbols with the bar ($\overline{N}_i^{\alpha}$ [mol/(m².s)]) denote the injection boundary fluxes and the fluxes N_i^{rubble} (without the bar) [mol/(m².s)] denote the fluxes of component i after the combustion reaction through the rubble zone in case of a partially collapsed channel or through the upstream cross-section of the channel in the case of no collapse. For given values of $\varepsilon_{\text{CH}_4}$, ε_{CO}, ε_{H_2} [dimensionless], which are the fraction of injected oxygen that reacts with CH$_4$, CO, and H$_2$ all fluxes are specified. Fig. 3.2 shows the cavity and the fluxes from the coal and rubble zones.

3.2.1. Mass transfer

Adjacent to the coal/cavity interface is a laminar boundary layer through which the gases diffuse towards the coal. The laminar boundary layer has a thickness δ, which can be calculated using conventional correlations involving the Sherwood number. In this boundary layer the Stefan-Maxwell equations are applied, i.e.,

$$\frac{dx_i}{dz} = \frac{RT_c}{p}\sum_j \frac{x_i\left(z\right)N_j^c - x_j\left(z\right)N_i^c}{\mathcal{D}_{ij}}, \tag{3.10}$$

where N_i^c [mol/(m².s)] is the molar flux of component i from the coal surface to the cavity, $\mathcal{D}_{ij}$ [m²/s] is the Stefan-Maxwell diffusion coefficient, T_c [K] is the temperature on the coal surface, p [Pa] is the pressure, x_i is the mole fraction of component
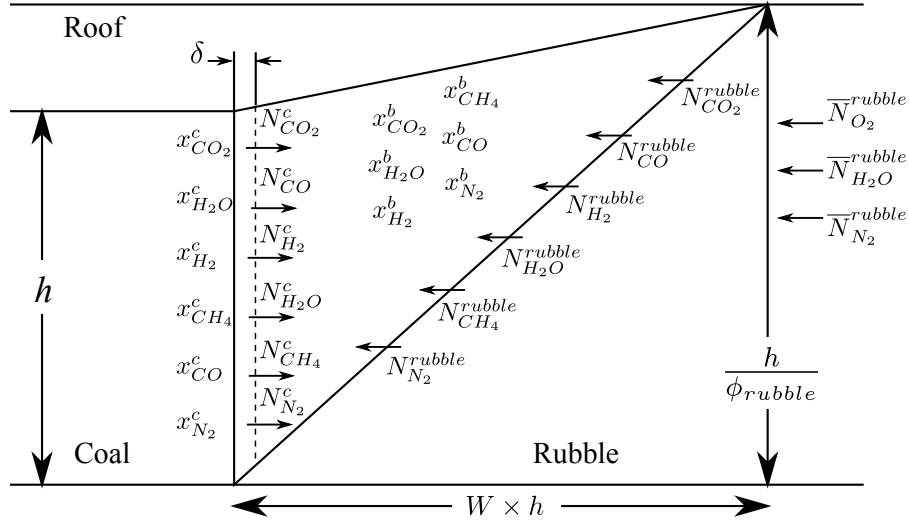
Figure 3.2.: Roof, coal, and rubble zones and fluxes from each surface to the cavity.

i in the boundary layer, and R [8.314 J/(mol.K)] is the gas constant. All together there are $\mathcal{N} - 1$ Stefan-Maxwell equations (3.10). Here it is assumed that the reactions occur at the coal face. Therefore at the coal face, forming one side of the laminar boundary layer using a carbon atom balance for the amount of reacted coal, one can write

$$\left(N_{\mathrm{CH_4}}^c + N_{\mathrm{CO}}^c + N_{\mathrm{CO_2}}^c \right) \mathrm{CH}_{\bar{a}}\mathrm{O}_{\bar{b}} \rightarrow$$
$$N_{\mathrm{CO_2}}^c \mathrm{CO_2} + N_{\mathrm{H_2O}}^c \mathrm{H_2O} + N_{\mathrm{CO}}^c \mathrm{CO} + N_{\mathrm{CH_4}}^c \mathrm{CH_4} + N_{\mathrm{H_2}}^c \mathrm{H_2}, \quad (3.11)$$
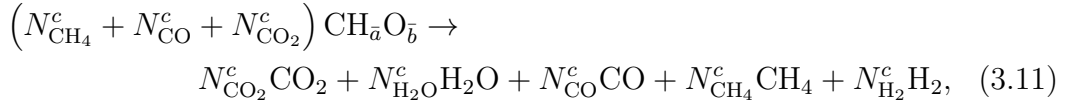
which is expressed in terms of net fluxes N_i^c from the coal face to the cavity. The fluxes in Eq. (3.11) are net fluxes, which consist of a part leaving the coal and a part moving towards the coal. A positive flux indicates a flux going from the coal into the cavity, whereas a negative flux denotes a flux going into the coal layer. Eq. (3.11) contains five unknown fluxes, but it is possible to relate the carbon monoxide flux and hydrogen flux to the other fluxes using mass balance considerations, i.e.,

$$N_{\mathrm{CO}}^c = \frac{-N_{\mathrm{H_2O}}^c + (\bar{b} - 2)N_{\mathrm{CO_2}}^c + \bar{b}N_{\mathrm{CH_4}}^c}{1 - \bar{b}} \tag{3.12}$$

and

$$N_{\mathrm{H_2}}^c = \frac{\bar{a}}{2}\left(N_{\mathrm{CH_4}}^c + N_{\mathrm{CO}}^c + N_{\mathrm{CO_2}}^c \right) - N_{\mathrm{H_2O}}^c - 2N_{\mathrm{CH_4}}^c . \tag{3.13}$$

Now three unknown fluxes are left, viz., $N_{\mathrm{CH_4}}^c$, $N_{\mathrm{CO_2}}^c$ and $N_{\mathrm{H_2O}}^c$.

Per unit volume of coal consumed, a certain amount of roof collapses into the hot cavity. It releases ζ moles of H_2O per mole of coal consumed. However, this shall be ignored as it can be lumped into the injected H_2O.

$$N_{H_2O}^{roof} = \zeta(N_{CH_4}^c + N_{CO}^c + N_{CO_2}^c) \tag{3.14}$$

It is assumed that the cavity moves perpendicular to the injection production line at a constant velocity dictated by the coal consumption rate. This velocity is calculated by

$$v_{coal} = \frac{\left(N_{CO_2}^c + N_{CO}^c + N_{CH_4}^c\right) M_{coal}}{\rho_{coal}}, \tag{3.15}$$

where M_{coal} [kg/mol] is the coal molecular weight and ρ_{coal} [kg/m^3] is the density of coal. Even if a transient heat conduction problem (see below) is attached to this problem, the quasi-steady state assumption for the composition will be maintained. This leads to the following expression for the mole fraction of a component $i = CO_2$, CO, H_2, H_2O, CH_4, N_2 in the cavity:

$$x_i^{bulk} = \frac{\sum_\alpha N_i^\alpha}{\sum_\alpha \sum_i N_i^\alpha}. \tag{3.16}$$

At the coal face it is assumed that all components are in equilibrium with the pyrolyzed coal (char) CH_aO_b (and not with the original coal $CH_{\bar{a}}O_{\bar{b}}$). Three equilibrium reactions are considered, involving pyrolyzed coal and all of the components. The equilibrium constant of reaction-1, i.e., char + carbon dioxide gives carbon monoxide and water is given by

$$K_1 = \frac{p_{CO}^{2+\frac{a}{2}-b} p_{H_2O}^{\frac{a}{2}}}{p_{CO_2}^{1-b+\frac{a}{2}}} = \frac{(x_{CO}^c)^{2+\frac{a}{2}-b} \left(x_{H_2O}^c\right)^{\frac{a}{2}}}{\left(x_{CO_2}^c\right)^{1-b+\frac{a}{2}}} p^{1-\frac{a}{2}} . \tag{3.17}$$

The equilibrium constant for reaction-2, i.e., char + water gives hydrogen and carbon monoxide is given by

$$K_2 = \frac{p_{CO}p_{H_2}^{1-b+\frac{a}{2}}}{p_{H_2O}^{1-b}} = \frac{x_{CO}^c \left(x_{H_2}^c\right)^{1-b+\frac{a}{2}}}{\left(x_{H_2O}^c\right)^{1-b}} p^{1+\frac{a}{2}} . \tag{3.18}$$

Finally the equilibrium constant for reaction-3, i.e., char + hydrogen gives methane

and water is given by

$$K_3 = \frac{p_{\mathrm{CH_4}} p_{\mathrm{H_2O}}^b}{p_{\mathrm{H_2}}^{2+b-\frac{a}{2}}} = \frac{x_{\mathrm{CH_4}}^c \left(x_{\mathrm{H_2O}}^c\right)^b}{\left(x_{\mathrm{H_2}}^c\right)^{2+b-\frac{a}{2}}} p^{\frac{a}{2}-1} \ . \tag{3.19}$$

The mole fractions serve as boundary conditions for the Stefan-Maxwell equations to calculate the mole fractions at the coal surface. They must, however, satisfy the equilibrium conditions Eqs. (3.17, 3.18, 3.19). So the guessed fluxes are adapted until consistency is obtained. However this assumes that the temperature at the coal face is known. There are four unknown temperatures, viz. the temperature of the rubble zone, the roof, the coal and in the cavity. This requires four energy balance equations that will be treated in the next section.

3.2.2. Energy balance

The energy balance on each face of the cavity consists of the heat generated by the reactions near that face, the radiation heat exchange, the heating of the cold spalled roof-rock to hot rubble and finally the heat conducted into the formation behind the faces. Radiation is the dominant heat transfer mechanism in the cavity due to the high temperature, but the conduction heat is added to the coal and roof rock in the energy balance. The heat of conduction in the rubble zone is not considered because it is assumed that the injected gases sweep this heat immediately into the cavity. As the cavity moves with velocity v_{coal} [m/s], a moving coordinate is considered and the 1-D transient heat transfer equations are written for the coal and roof rock as

$$\rho_\beta c_\beta \frac{\partial T_\beta}{\partial t} - v_{coal} \rho_\beta c_\beta \frac{\partial T_\beta}{\partial x} = k_\beta \frac{\partial^2 T_\beta}{\partial x^2} \ , \quad \beta = \mathrm{roof, coal,} \tag{3.20}$$

where ρ_β [kg/m^3] is the solid density, c_β [J/(kg.K)] is the solid heat capacity, v_{coal} [m/s] is the velocity of the coal face, k_β [W/(m.K)] is the solid thermal conductivity, and the moving coordinate $x = \widetilde{x} - v_{coal}t$ where $\widetilde{x}$ is the fixed coordinate. Eq. (3.20) is rearranged by defining the reference time $t_R = \frac{L^2}{\bar{\alpha}_\beta}$ and the Peclet number as $\mathrm{Pe}_\beta = \frac{v_{coal}}{L} t_R$, where $\bar{\alpha}_\beta = \frac{k_\beta}{\rho_\beta c_\beta}$ is the thermal diffusivity and L is the length of solid. x is used to denote the distance from the surface both in the coal and the roof. Using the dimensionless time ($\tau = t/t_R$) and space ($X = x/L$) variables, Eq.

(3.20) can be rewritten as

$$\frac{L^2}{\bar{\alpha}_\beta t_R}\frac{\partial T_\beta}{\partial \tau} - \mathrm{Pe}_\beta\frac{\partial T_\beta}{\partial X} = \frac{\partial^2 T_\beta}{\partial X^2}. \tag{3.21}$$

The boundary conditions are

$$T_\beta(X = 0, \tau) = T_{\beta,s} \qquad \frac{\partial T_\beta(X = 1, \tau)}{\partial X} = 0 \ , \tag{3.22}$$

whereas the initial condition is

$$T_\beta(X, \tau = 0) = T_\beta^0(X) \qquad at \ t = 0, \ 0 < X \leq 1 \ , \tag{3.23}$$

where $T_\beta^0(X)$ is the initial temperature in the coal layer and the roof respectively.

3.2.2.1. Coal/cavity interface

The energy balance relation for the coal cavity interface is

$$\Delta H_{coal}A_{coal} + Q_{coal-roof} + Q_{coal-rubble} + q_{coal}A_{coal} = 0 \tag{3.24}$$

where ΔH_{coal} [J/(m^2.s)] is the heat of reaction, which can be related to the net fluxes from the coal face by

$$\Delta H_{coal} = N_{CO}^c h_{CO}\left(T_\alpha\right) + N_{CO_2}^c h_{CO_2}\left(T_\alpha\right) + N_{CH_4}^c h_{CH_4}\left(T_\alpha\right) +$$
$$+ N_{H_2}^c h_{H_2}\left(T_\alpha\right) + N_{H_2O}^c h\left(T_\alpha\right) - \left(N_{CO}^c + N_{CO_2}^c + N_{CH_4}^c\right) h_{char}\left(T_{coal,s}\right), \tag{3.25}$$

where the temperature T_α is defined as $T_\alpha = U\left(N_i^c\right)T_{coal,s} + \left(1 - U\left(N_i^c\right)\right)T_g$, and $h_i\left(T_\alpha\right)$ is the enthalpy of component i. The unit step function $U\left(x\right)$ is used to ensure that when the flux is negative it comes from the cavity, whereas positive fluxes are into the cavity. The enthalpy is calculated by

$$h_i\left(T_\alpha\right) = \Delta h_{0,i}^o + \int_{T_0}^{T_\alpha} c_{p,i}\left(T\right) dT. \tag{3.26}$$

Here $\Delta h_{0,i}^o$ [J/mol] is the enthalpy of formation at the standard temperature and pressure and $c_{p,i}(T)$ [J/(mol.K)] is the temperature-dependent ideal gas specific heat capacity of component i. Here the effect of pressure on the enthalpy of the components is disregarded.

The radiated heat Q_{1-2} between surface 1 and surface 2 is calculated [77] by using the following relation

$$Q_{1-2} = \frac{\epsilon_1 \epsilon_2 \sigma}{1 - F_{1-2}F_{2-1}\left(1 - \epsilon_1\right)\left(1 - \epsilon_2\right)} \left(A_1 F_{1-2} T_1^4 - A_2 F_{2-1} T_2^4\right), \qquad (3.27)$$

where ϵ_α and A_α [m^2] represent the emissivity and area of surface α, F_{1-2} denotes the view factor of surface 1 to surface 2, and $\sigma = 5.67 \times 10^{-8}$ [W/(m^2.K^4)] is the Stefan-Boltzmann constant.

The heat transfer by conduction to the coal layer q_{coal} [J/(m^2.s)] is calculated by

$$q_{coal} = \frac{-\frac{k_{coal}}{L} \int_{t=0}^{t=\Delta t} \frac{\partial T_{coal}}{\partial X} \mathrm{d}t}{\Delta t}, \qquad (3.28)$$

where Δt shows the time step for the numerical model (see section 3.3). The value of q_{coal} is estimated using numerical integration and differentiation as explained in Appendix A. L is chosen to be long enough to avoid that the conducted heat reaches the downstream boundary.

3.2.2.2. Roof/cavity interface

No chemical reaction occurs at the roof surface and the energy transfer from the roof to the coal and rubble zones is given by

$$Q_{roof-coal} + Q_{roof-rubble} + q_{roof} A_{roof} = 0, \qquad (3.29)$$

where $Q_{roof-coal}$ and $Q_{roof-rubble}$ are calculated by Eq. (3.27) and q_{roof} is calculated by Eq. (3.28).

3.2.2.3. Rubble/cavity interface

The reaction between the injected oxygen and the combustible gases and the evaporation of injected liquid water occur in the rubble zone. The energy balance for

this zone can be written as

$$Q_{rubble-coal} + Q_{rubble-roof} + \Delta H_{rubble} A_{coal} + Q_{rubble} = 0, \tag{3.30}$$

where the radiation heat transfer terms are calculated by Eq. (3.27). The net energy production near the rubble zone ΔH_{rubble} [J/(m^2.s)] is calculated by

$$\begin{aligned} \Delta H_{rubble} = {}& N_{CO_2}^{rubble} h_{CO_2}\left(T_{rubble}\right) + N_{CO}^{rubble} h_{CO}\left(T_g\right) + N_{N_2}^{rubble} h_{N_2}\left(T_{rubble}\right) + \\ & + N_{H_2O}^{rubble} h_{H_2O}\left(T_{rubble}\right) + N_{H_2}^{rubble} h_{H_2}\left(T_g\right) + N_{CH_4}^{rubble} h_{CH_4}\left(T_g\right) \\ & - \overline{N}_{N_2}^{rubble} h_{N_2}\left(T_a\right) - \overline{N}_{O_2}^{rubble} h_{O_2}\left(T_a\right) - \overline{N}_{H_2O}^{rubble}\left(h_{H_2O}\left(T_a\right) - \Delta h_{H_2O}^{vap}\right), \end{aligned} \tag{3.31}$$

where h_i [J/mol] is the enthalpy of component i in the *gas* phase, and if the species come from the rubble zone the enthalpies are calculated with T_{rubble} and if the species come from the cavity the enthalpies are calculated with T_g. The heat of vaporization of water $\Delta h_{H_2O}^{vap}$ [J/mol] is eliminated from the Eq. (3.31) when water is injected in the form of steam. The net flux is positive when the species originates from the rubble zone and negative when it originates from the cavity.

The value of Q_{rubble}, which represents the sensible heat of the rubble mass is calculated by

$$Q_{rubble} = \dot{m}_{rubble} \int_{T_{roof,s}}^{T_{rubble}} c_{roof} dT, \tag{3.32}$$

where $\dot{m}_{rubble}$ is proportional to the cavity growth rate v_{coal} and is calculated by

$$\dot{m}_{rubble} = v_{coal} A_{roof} \rho_{roof}, \tag{3.33}$$

where ρ_{roof} [kg/m^3] is the density of the roof rock (see Fig. 3.2).

3.2.2.4. Bulk gas energy balance

All the gas fluxes N_i^α (α = roof, coal, rubble, cavity) at their respective temperatures T_α from the cavity faces into the cavity are mixed to reach the average gas temperature T_g. The energy balance for this mixing process can be written as

$$\sum_i \sum_\alpha N_i^\alpha \left(h_i\left(T_\alpha\right) - h_i\left(T_g\right)\right) = 0, \tag{3.34}$$

where i is the component index (CO$_2$, CO, H$_2$, H$_2$O, CH$_4$, N$_2$), α is the interface or cavity index (roof, coal, rubble, cavity), and $h_i(T_\alpha)$ is the enthalpy of species i

at temperature T_α. As before, the temperature $T_\alpha = U\left(N_i^\alpha\right)T_{\beta,s} + \left(1 - U\left(N_i^\alpha\right)\right)T_g$, where positive fluxes are into the cavity, and T_g is the cavity temperature. Ideal mixing rule is assumed and the effect of pressure on the enthalpy of the gas is disregarded.

3.2.3. Boundary layer thickness

For natural convection dominated flow, the Sherwood number (Sh) can be calculated by

$$\mathrm{Sh} = 0.59\mathrm{Gr}^{\frac{1}{4}}\mathrm{Sc}^{\frac{1}{4}}, \qquad \mathrm{Gr} < 10^9, \tag{3.35}$$

$$\mathrm{Sh} = 0.13\mathrm{Gr}^{\frac{1}{3}}\mathrm{Sc}^{\frac{1}{3}}, \qquad \mathrm{Gr} > 10^9, \tag{3.36}$$

where Gr is the Grashof number, which is defined by

$$\mathrm{Gr} = \frac{h^3 g \Delta\rho}{\nu^2 \rho}, \tag{3.37}$$

where h is the coal layer thickness [m], g [m/s^2] is the acceleration due to gravity, $\Delta\rho = \left|\rho\left(x^b, T_g\right) - \rho\left(x^c, T_{coal,s}\right)\right|$ [kg/m^3] is the difference between the density of non-ideal gas at the coal surface and the cavity, and ρ [kg/m^3] is a reference density, which is taken to be the density $\rho\left(x^c, T_{coal,s}\right)$ at the coal surface, and $\nu = \mu/\rho$ [m^2/s] is the kinematic viscosity of the gas mixture [138] also at the coal surface. The gas density is calculated using the Peng-Robinson equation of state [118]. The Schmidt number is defined as

$$\mathrm{Sc} = \frac{\nu}{\mathcal{D}}, \tag{3.38}$$

where $\mathcal{D}$ [m^2/s] is the average diffusivity of the gas mixture at the coal surface. The binary diffusion coefficients $\mathcal{D}_{ij}$ are calculated according to Eq. (5) in reference [138]. It is a function of temperature, pressure, and concentration. The average diffusivity is strongly influenced by the presence of hydrogen. The following relation [22] is used to calculate the average diffusivity using the gas phase mole fraction x_i^c and Stefan-Maxwell diffusion coefficients $\mathcal{D}_{ij}$:

$$\mathcal{D} = 1/\sum_j \left(\frac{x_j^c}{1 - x_j^c}\sum_{i \neq j}\left(x_i^c/\mathcal{D}_{ij}\right)\right). \tag{3.39}$$

In this procedure the contribution due to forced convection is disregarded as Gr/Re^2 is around 4×10^4, i.e., Gr/Re^2>>1; therefore the flow is dominated by natural convection.

3.3. Numerical scheme

The following numerical algorithm is used to solve the equations and find the 10 unknown variables, viz. $N_{CO_2}^c$, $N_{H_2O}^c$, $N_{CH_4}^c$, $x_{H_2}^c$, $x_{H_2O}^c$, $T_{rubble,s}$, $T_{gas,s}$, $T_{coal,s}$, $T_{roof,s}$, and δ. The initial condition at $t = 0$ is $T_{coal}^0 = T_{roof}^0 = 308$ K and the time step Δt is 1800 seconds (0.5 hour). The symbols are defined in the nomenclature, at the end of the chapter.

1. First, initial estimates are assigned to all the unknowns

2. Eq. (3.12) and Eq. (3.13) are used to calculate the N_{CO}^c and $N_{H_2}^c$, respectively.

3. The equilibrium constants K_j are calculated at the estimated coal surface temperature $T_{c,s}$ using the procedure explained in Appendix B. Then using the initial estimate for $x_{H_2}^c$ and $x_{H_2O}^c$, Eq. (3.18) is used to calculate x_{CO}^c and after that Eq. (3.17) is used to calculate $x_{CO_2}^c$. For the calculation of $x_{CH_4}^c$, Eq. (3.19) is used during the oxygen injection cycle (with high enough temperatures), but it is assumed that $x_{CH_4}^c$ is zero during the steam injection cycle due to the very slow reaction rate of methane at low temperatures [84, 104]. The mole fraction of nitrogen $x_{N_2}^c$ is calculated using that the sum of the mole fractions is equal to one, i.e., $\sum_i x_i^c = 1$.

4. The roof flux $N_{H_2O}^{roof}$ is calculated using Eq. (3.14). Here, it is assumed that the roof collapse does not result in a water roof flux, i.e., $\zeta = 0$.

5. The bulk gas component mole fractions are calculated using Eq. (3.16).

6. The Stefan-Maxwell equations are solved analytically [5] with the boundary condition of $x_i = x_i^c$ at $z = 0$ (on the coal surface), i.e.,

$$x_i = x_i^c \exp\left(\lambda_i z\right) \tag{3.40}$$

where λ_i are the eigenvalues of the matrix M, which is given by

$$M_{ij} = \begin{cases} \frac{RT_{coal,s}}{P} \sum_{j \neq i} \frac{N_j^c}{\mathcal{D}_{ij}} & i = j \\ \frac{-RT_{coal,s}}{P} \frac{N_i^c}{\mathcal{D}_{ij}} & i \neq j \end{cases}. \tag{3.41}$$

7. The bulk gas composition calculated in step 5 must satisfy the solution of the Stefan-Maxwell Eq. (3.40) at $z = \delta$. Writing this equation for CO_2, CO, H_2, H_2O, and CH_4 gives five error values e_i:

$$x_i^{bulk} - x_i^c \exp\left(\lambda_i \delta\right) = e_i. \tag{3.42}$$

8. Using the estimated surface temperature of coal and roof, the conducted heat losses for coal and roof are calculated using the procedure described in Appendix A. Then the four energy balance equations (3.24), (3.29), (3.30), and (3.34) are used to calculate four error values e_l.

9. If the nine calculated values of e_i and e_l do not satisfy the convergence criteria $\sum_{i=1}^{5} |e_i| < \omega_1$ and $\sum_{l=1}^{4} |e_l| < \omega_2$ then the estimated values of $N_{CO_2}^c$, $N_{H_2O}^c$, $N_{CH_4}^c$, $x_{H_2}^c$, $x_{H_2O}^c$, $T_{rubble,s}$, $T_{gas,s}$, $T_{coal,s}$, and $T_{roof,s}$ are corrected using the Quasi-Newton method with a numerically calculated Jacobian matrix.

10. The Sherwood number is calculated using Eq. (3.35) or Eq. (3.36) and the new boundary layer thickness δ_{new} is calculated by

$$\delta_{new} = \frac{h}{\text{Sh}}. \tag{3.43}$$

   If this new value does not satisfy the convergence criterion $|\delta_{new} - \delta| < \omega_3$ then the new value of δ is calculated as $\delta_\kappa = 0.1\delta_{new} + 0.9\delta_{\kappa-1}$ until convergence is obtained. We observe that for this problem this weighted method is more stable even though slower than the direct substitution.

11. The values of the initial profiles T_{coal}^0 and T_{roof}^0 are replaced by the new temperature profiles in the coal $T_{coal,n}^m$ and roof $T_{roof,n}^m$ (see Appendix A). The procedure starts again from step 1 using the new values for the unknowns.

3.4. Mixing effect

One issue with the alternating injection is that the current product is always mixed with the products from the previous cycle. Hence, this section will quantify the degree of this mixing. One may recall that air/oxygen or steam are injected during selected periods. The injected fluids will percolate through a rubble layer until they reach the channel surrounding the rubble zone. In the rubble zone the injected oxygen reacts with the gases in the channel (the steam is only heated). The gases in the channel react at the coal face, which forms one boundary of the channel. The gases move in the channel towards the production well. It is important to estimate the residence time distribution of the injected gas and the ensuing product gases. It will be done by injecting an inert tracer in the injection well and showing its concentration profile thus ignoring any reactions and temperature effects. In other words the residence time distribution will be estimated with a numerical model where a tracer is injected in the central injection channel and its concentration is monitored at the production well. The produced concentration profile gives an estimate of the residence time distribution. The geometry is also simplified as shown in Fig. 3.3.

An incompressible continuity equation is solved with Darcy's law assuming the permeability distribution shown in Fig. 3.3. From this the velocity field is calculated. At the interface between the injection well and the rubble zone, a constant mass flux is specified. The second boundary condition is a zero diffusive flux condition at the outer boundary of the channel [40]. The pressure is fixed at 80 bar for the
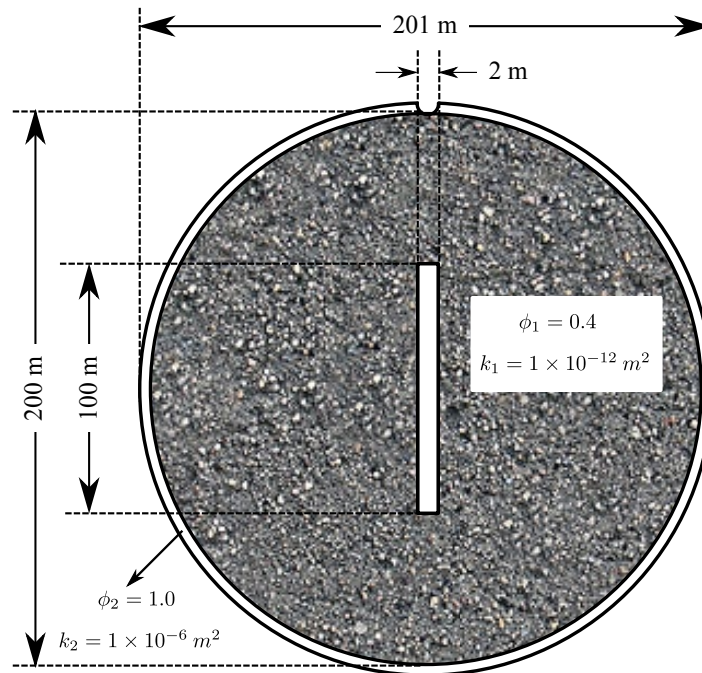
Figure 3.3.: Schematic representation of the geometry used for the calculation of residence time distribution; the gray area is the rubble zone with the permeability of 1×10^{-12} m² and the porosity of 0.4 which is connected to the production well (half circle with the diameter of 2 m) through a 1 m wide channel (white circle around the gray area)

production well. The velocity field is specified as an input to the convection diffusion equation. At the injection well a concentration $c = 1$ mol/m³ is assumed. At the production point it is assumed that the diffusion flux is zero. Everywhere else no flow boundary conditions are considered. The result is shown in Fig. 3.4. The concentration profile shows breakthrough at 0.9 pore volume (PV) and complete breakthrough occurs at 2.1 PV. The interpretation is that after switching between air and steam injection 1.2 PV of mixed products are produced. It means that to achieve separated production for a considerable period, around 10 PV's must be injected. This is possible at low pressures but at high pressures separate production is not practically achievable (see below).

3.5. Results and discussion

In this section, first the result of the extended model is compared with the result of a simple chemical equilibrium model. Then, the data of the GIG field trial [152]
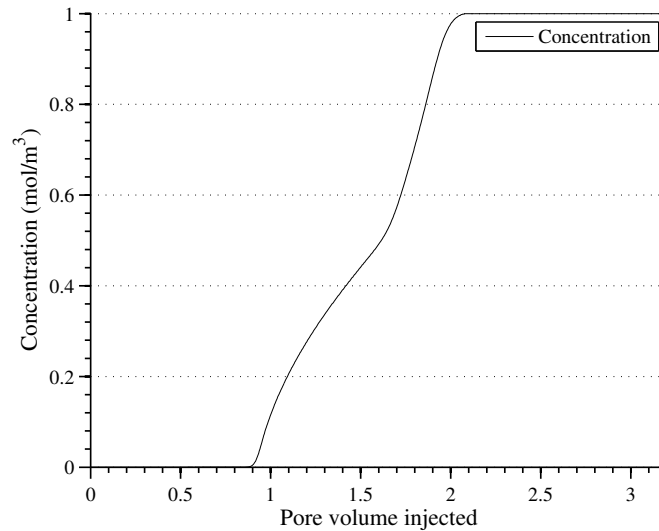
Figure 3.4.: The average concentration of tracer at the production well as a function of number of pore volumes of injected gas

are compared with the simulation results of the extended model. A few sensitivity analyses are performed by changing the practical process parameters, i.e., pressure, duration of oxygen (air) and steam injection cycles, and the flow rate of oxygen (air) and steam. The effect of each parameter on the coal conversion rate, gas production flow rate and gas composition will be discussed. Finally, an exergy analysis is performed and the practical and zero-emission recovery factors [52] are calculated to investigate the practicality of the process.

3.5.1. Comparison with chemical equilibrium model

To investigate the significance of considering mass transfer limitations in the model, the steady state results of the model are compared to the results obtained with a chemical equilibrium model [52]. Fig. 3.5-a shows the composition obtained previously [52] with a chemical equilibrium model and Fig. 3.5-b shows the composition of the UCG product gas predicted by the present model. In both cases, the pressure is 3 bar, the flux of oxygen is 0.1 mol/(m^2.s) and the flux of saturated steam (saturation temperature of 133°C at 3 bar [123]) is increased gradually from 0.05 mol/(m^2.s) to 0.45 mol/(m^2.s) corresponding to a water/O_2 ratio between 0.5-4.5. The comparison (Fig. 3.5-a, 3.5-b) shows a number of differences between the equilibrium model and the extended channel gasification model. First, it is observed that by increasing the water/O_2 ratio, the temperature decreases much faster for the equilibrium model than for the extended gasification model, which includes heat and mass transfer. This is attributed to the fact that in the equilibrium model the endothermic reactions play a more important role. For the same reason the Boudouard reaction (C + CO_2 = 2 CO) produces more CO and less CO_2. One

can also observe more H_2 production and more H_2O consumption in the equilibrium model, which shows that the rate of coal consumption is higher in the equilibrium model due to the lack of mass transfer resistances.
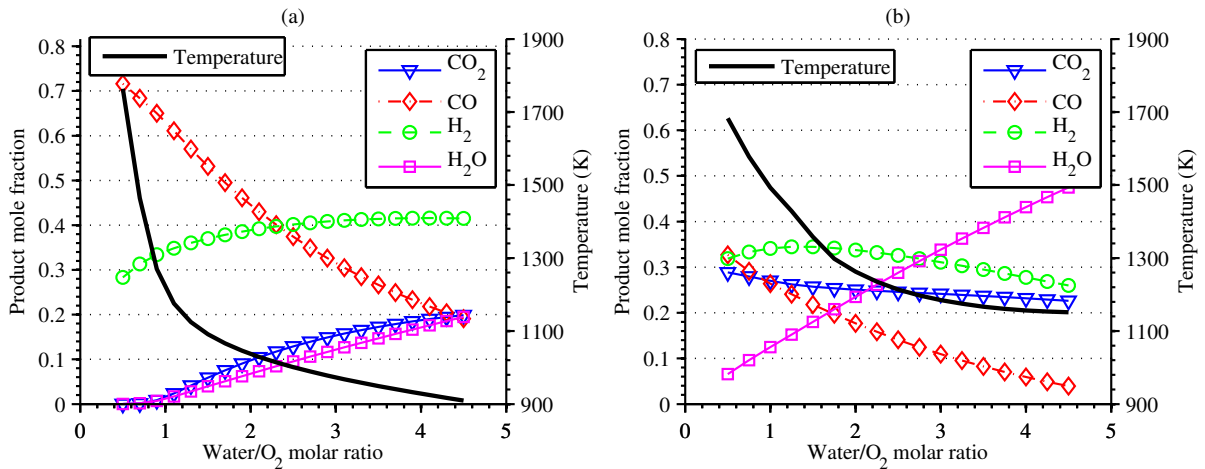
Figure 3.5.: Steady state composition of UCG product for (a) chemical equilibrium model without mass transfer limitations; (b) the extended model including mass transfer limitations.

3.5.2. Comparison with field experiments

In this section, first the result of related experimental work available in the literature are explained and subsequently is compared with the simulations. In a pilot scale gasification experiment, Stanczyk et al. gasified a coal block of $2.4 \times 0.6 \times 0.55$ m^3 (length×height×width) [152]. This experiment is referred to as the GIG field trial. The experiment was carried out in a geo-reactor, which was designed to simulate the underground coal gasification conditions. The injection channel is initially 2.4 m long with a diameter of 0.07 m at the bottom of the coal seam. First, oxygen was injected for 10 hours to initiate the process and heat up the coal seam. Then oxygen and steam are injected alternately for two hours and 1.0-1.5 hour, respectively for a period of 120 hours. The temperature in the channel and in the coal layer and the composition of dry gaseous product were recorded.

The model is used for the same oxygen and steam molar injection rate and the temperature and composition profiles predicted by the model are compared with the GIG field trial results. Approximately, the same injection rate and initial conditions as the GIG field trial are used, i.e., the same injection rate per unit area of coal, the same coal composition, and the same initial and injection temperature and pressure. The main difference between the model and the GIG field experiment is the existence of a nonreactive face (roof face) in the model while in the GIG field trial all the faces are reactive as they consist of coal. To model the GIG field

experiment, oxygen with a rate of 0.086 mol/(m^2.s) is injected for the first 10 hours. The flow rate per unit surface area of coal is estimated by dividing the reported value of the injection rate of oxygen [152] by the surface area of the injection channel (a diameter of 0.07 m). Any changes in the diameter of the injection channel during its operation is disregarded. Then the alternating injection is started by the injection of 0.077 mol/(m^2.s) steam for 2.0 hours, which is followed by the injection of 0.086 mol/(m^2.s) oxygen for 2.0 hours. The temperature of the steam corresponds to its saturation temperature at 12 bar. The simulation is continued for two oxygen and two steam injection cycles. Fig. 3.6 shows the temperature profile predicted by the model. For the first 10 hours, the temperature increases from the initial temperature of 308 K (not shown in the figure) to 1300 K on the coal face. This is in reasonable agreement with the value of 1373 K reported by Stańczyk et al. [152]. After 10 hours, when starting the steam cycle, the temperature drops very fast due to endothermic gasification reactions on the coal face to 990 K and then more gradually decreases to 800 K after 2 hours of steam injection. The observed temperature in the GIG field trial at the end of the first steam cycle is 700 K, which is 100 K lower than the model prediction. This difference can be explained by the fact that in the GIG field experiments, the endothermic gasification reaction occurs at all surfaces, while in the model, no reaction happens on the roof surface and consequently the calculated *temperature drop* due to the endothermic gasification reactions is lower than the observed value.
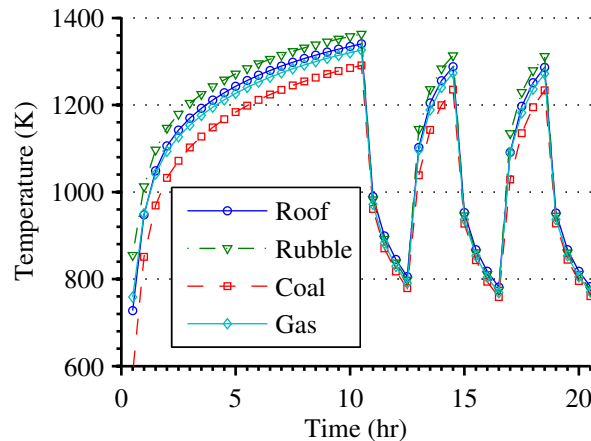
Figure 3.6.: Temperature history results of the model with the initial conditions of the GIG field experiments [152].

Fig. 3.7 shows the composition history of the dry product gas predicted by the model for the simulation of the GIG field trial. The average composition during the initiation stage (first 10 hours) predicted by the model is 35 % CO_2, 49 % CO, and 16 % H_2 which is different from the composition of product obtained in the GIG field trial, i.e., 25 % CO_2, 36 % CO, 33 % H_2, and 2 % CH_4. The formation of methane is ignored in the model because the equilibrium constant of the methanation

reaction at high temperature (above 1000 K) is low and the reaction rates at low temperature (below 1000 K) are too slow to reach equilibrium. The differences between the results of the model and the GIG field trial are a consequence of the author's assumption that the injected oxygen reacts with dry coal. During the pure oxygen injection stage, the average composition of the product gas in the GIG field trial is 57 % (36 %) CO_2, 18 % (49 %) CO, 15 % (15 %) H_2, and 3 % (0 %) CH_4. The numbers in brackets show the results of the simulation under the same condition. It shows that while the model predicts the mole fraction of H_2 in the product gas with reasonable accuracy, it overestimates the composition of CO and underestimates the composition of CO_2. This discrepancy can be a consequence of the fact that chemical equilibrium is assumed instead of finite reaction rates on the coal surface [75].

For the steam injection stage, the product gas composition is 14 % (20 %) CO_2, 16 % (16 %) CO, 54 % (63 %) H_2, and 10 % (0 %) CH_4, which is in good agreement with the simulation results, except for the mole fraction of methane. Considering the very low reaction rate of methane formation, this high percentage of methane (10 %) observed in the field trial is probably not a consequence of the gasification reaction but a result of pyrolysis, which is not considered in the model.
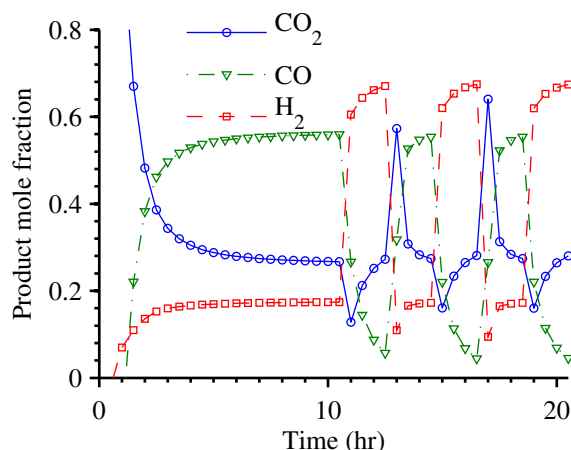
Figure 3.7.: Composition history of the dry product predicted by the model with the initial conditions of the GIG field trial

In spite of the discrepancies, the model grasps the qualitative features of alternating injection of oxygen and steam in UCG.

3.5.3. Sensitivity analysis

In this section, the effect of the length of the time cycles of the oxygen and steam injection stages, the injection rate of oxygen and steam (and the ensuing steam/O_2 ratio), and the effect of pressure on the average composition and the rate of coal consumption are analyzed.

3.5.3.1. Duration of steam/O_2 injection stages

The purpose of the oxygen injection stage (cycle) is to store the heat of combustion of coal and combustible gases in the coal and roof rock, which will be recuperated subsequently during the steam injection stage to be consumed in the endothermic gasification reactions. During the injection of oxygen, in addition to heat, a low value product gas is also generated. The amount of heat that is stored in the coal and roof is increased by increasing the length of the oxygen injection cycle, which at the same time increases the amount of the low quality combustion products. By storing more heat in the coal and roof layers, the subsequent steam injection cycle, which produces the high quality product gas, can go on for a longer period of time. In other words, a longer oxygen injection time has the benefit of extending the subsequent steam injection stage. However, the disadvantage is that more coal is converted to a low value product. According to references [152, 174] the steam injection period can continue until the temperature on the coal surface drops to 1000 K. Here, the model is used with various oxygen injection time periods to quantify the length of the subsequent oxygen injection cycle before the temperature drops to 1000 K or 900 K (see Fig. 3.8). It is a matter of choice whether one chooses 1000 K or 900 K as the criterion to switch from steam injection to oxygen injection.

All the conditions are kept the same as in the GIG field trial. Every simulation starts with a 10 hour start up period of oxygen injection with a rate of 0.086 mol/(m^2.s) followed by a two hour period of steam injection with a rate of 0.077 mol/(m^2.s). The coal and roof temperature profiles after these two hours are used as the initial condition to perform four different simulations. Each simulation starts with an oxygen injection stage with time periods of 2, 4, 7, and 10 hours. Afterwards, each simulation continues by a steam injection stage, which goes on until the coal surface temperature goes below 900 K. Then steam injection is stopped and another oxygen injection step starts. Fig. 3.8 shows the values of steam/O_2 time cycle ratios for different O_2 injection times. The figure can be used as follows: first an oxygen injection time is chosen. This oxygen injection stage will be followed by a steam injection stage, which will be continued until the temperature on the coal face drops below the chosen temperature criterion, e.g. 1000 K. The steam/O_2 time cycle ratio on the vertical axis is read, which corresponds to the oxygen injection time on the horizontal axis using the solid (or dashed) curve of Fig. 3.8 and it is multipled by the oxygen injection time, which gives the length of the steam injection stage. For instance, if the duration of the oxygen injection stage is 4.0 hours, the subsequent steam injection stage can be continued for 2.0 hours before the temperature on the coal surface drops slightly below 1000 K or it can be continued for 4.0 hours before the temperature drops slightly below 900 K.

Of the two different gas compositions that are produced during the oxygen and steam injection stages, the product of the steam injection has a higher quality, i.e., a higher heating value/carbon content ratio. Therefore, it is rational to adjust the process parameters to extend the time of the steam injection stage and shorten the time

of the oxygen injection stage, or in other words, maximize the steam/O_2 injection time ratio. Fig. 3.8 shows that the steam/O_2 injection time ratio is increased by decreasing the oxygen injection duration. However, for practical reasons, in a field scale trial it is not viable to switch between oxygen and steam injection very frequently, e.g., every hour. Here, it is assumed that the oxygen injection time should be at least two hours long, which gives the best injection scenario with a subsequent steam injection time of around two hours for a coal surface temperature of 1000 K (around four hours for 900 K).
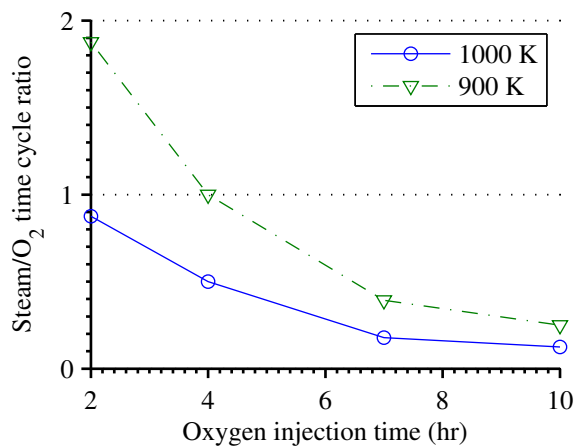
Figure 3.8.: Steam/O_2 time cycle ratios for various O_2 injection time cycles. The solid line with circle markers shows the steam injection time period before the temperature on the coal face reaches 1000 K. The dashed line with triangular markers shows the steam injection time period before the temperature reaches 900 K. For example, if the length of oxygen injection stage is 4.0 hours (horizontal axis), the subsequent steam injection stage can be continued for 2.0 hours (0.5×4.0) before the coal surface drops to 1000 K or it can be continued for 4.0 hours (1.0×4.0) before the temperature drops to 900 K.

3.5.3.2. Pressure

The pressure of the cavity in the UCG process is usually maintained above the hydrostatic pressure. Here, the same geo-reactor configuration and feed injection rates as the GIG field trial are used and the extended channel gasification model is used with four different pressures, i.e., 3 bar, 20, bar, 40 bar, and 80 bar.

Fig. 3.9 shows the effect of pressure on the product composition and the product molar flux of the steam injection stage. The mole fractions of CO and CO_2 do not change considerably. However, at high pressures, the equilibrium reaction between steam and carbon, i.e.,

$$C + H_2O \rightleftharpoons H_2 + CO, \tag{3.44}$$

shifts to the left side, more H_2O and less H_2.
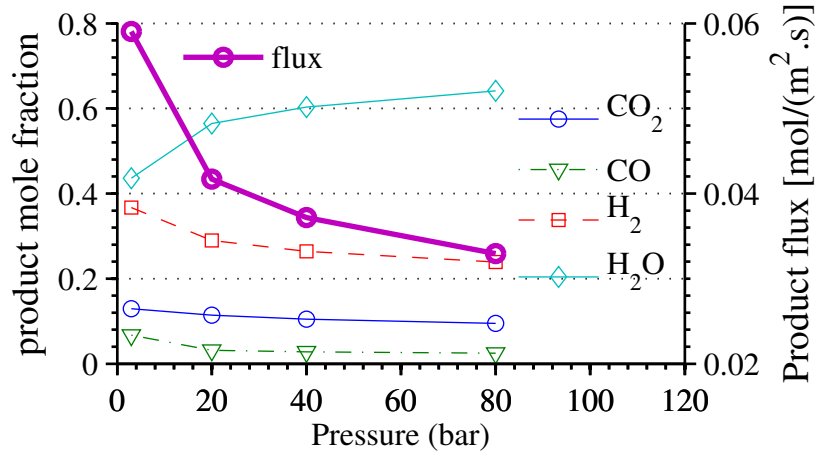
Figure 3.9.: Effect of pressure on the product composition and the product flux of the steam injection stage; the thick line with ∘ markers shows the total flux of the dry gas product (without H_2O).

To explain the lower production rate at high pressure, the mass transfer coefficient and the mass flux from the coal surface to the cavity (N_i^c) are plotted at different pressures. The relation between the mass flux and the mass transfer coefficient is shown by

$$N_i^c = k' \left(x_i^c - x_i^{bulk} \right), \tag{3.45}$$

where the mass transfer coefficient k' [mol/(m^2.s)] is calculated by

$$k' = \mathcal{D}C/\delta, \tag{3.46}$$

where δ [m] is the boundary layer thickness, C [mol/m^3] is the average total concentration of the gas phase and $\mathcal{D}$ [m^2/s] is the molecular diffusivity estimated by Eq. (3.39). The result is shown in Fig. 3.10. The mass transfer coefficient increases with increasing pressure, from 0.4 mol/(m^2.s) at 3 bar to 1.8 mol/(m^2.s) at 80 bar. The molecular diffusivity ($\mathcal{D}$) is inversely proportional to pressure and the total concentration is proportional to pressure, and therefore $\mathcal{D}C$ does not change with pressure. Therefore, the boundary layer thickness decreases with increasing pressure, which leads to a lower mass transfer resistance. However, this lower mass transfer resistance at higher pressure does not increase the rate of conversion, which is shown in Fig. 3.10 by the net molar flux of the component from the coal face to the cavity. The rate of production of H_2 shows a 50 % decline by increasing the pressure, i.e., it drops from 0.04 mol/(m^2.s) at 3 bar to 0.02 mol/(m^2.s) at 80 bar. The same behavior is observed for the rate of *consumption* of water, which is shown by the negative values in Fig. 3.10. The production rate decline of CO and CO_2 is almost negligible. This behavior can be explained by the chemical reaction of Eq.

(3.18), which can be simplified to

$$C + H_2O \rightleftharpoons CO + H_2. \tag{3.47}$$

By increasing the pressure, the equilibrium reaction shifts towards the left side, i.e., lower amount of H_2 and CO, and higher amount of water. This increases the amount of water on the coal face ($x_{H_2O}^c$). The composition of water in the cavity ($x_{H_2O}^{bulk}$) is also high due to the injection of steam. Therefore, the driving force term in Eq. (3.45), i.e., $\left(x_{H_2O}^c - x_{H_2O}^{bulk} \right)$ decreases which results in a lower gas flux and production rate.
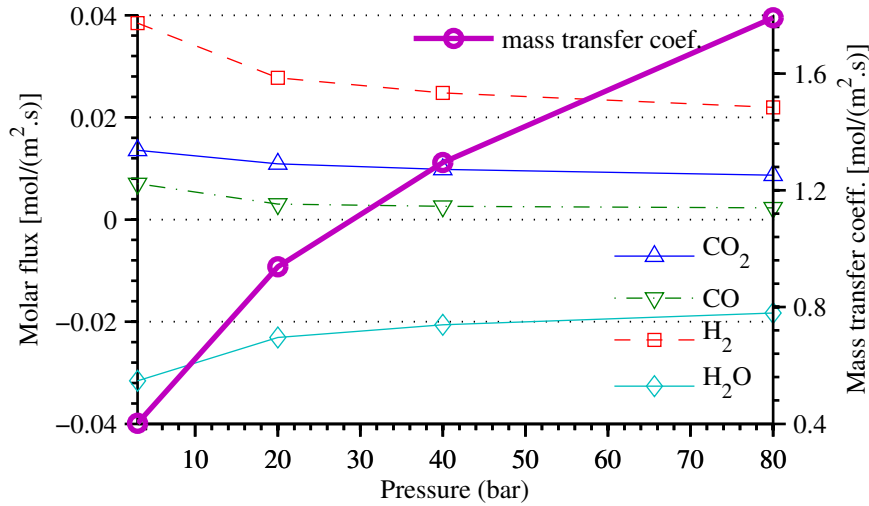
Figure 3.10.: Effect of pressure on the mass transfer coefficient and the net molar fluxes from the coal face

The effect of pressure on the average chemical exergy (see section 3.5.5) of the product of the steam injection stage and the oxygen injection stage are shown in Fig. 3.11. The chemical exergy of the oxygen injection first drops from around 190 kJ/mol at 3 bar to around 180 kJ/mol at 20 bar, but for the pressure above 20 bar stays almost constant at 180 kJ/mol. This behavior is in agreement with the composition of the *dry* product gas of the steam injection stage, that does not change by increasing the pressure above 20 bar. However, for the steam injection stage, the chemical exergy drops from around 170 kJ/mol at 20 bar to around 150 kJ/mol at 80 bar. It can be explained by the Boudouard reaction, i.e.,

$$C + CO_2 \rightleftharpoons 2CO, \tag{3.48}$$

which shifts to the left side at high pressures and produces more CO_2 and decreases the amount of CO in the final product.

To summarize, by increasing the UCG pressure, the quality and flow rate of the gaseous product (rate of conversion of coal) decline, which suggests that high pres-
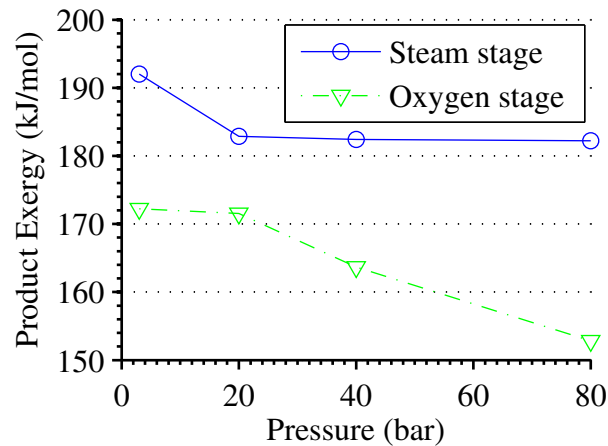
Figure 3.11.: The average chemical exergy of the *dry* gas product in the steam injection stage (∘ markers) and in the oxygen injection stage (∇ markers) for the same conditions as of the GIG field trial but at different pressures. The GIG field trial was carried out at atmospheric pressure.

sure is not a favorable condition for underground coal gasification. This observation will be discussed quantitatively in section 3.5.5.

3.5.4. Steady state results

In section 3.5.3.1 it was shown that to have an effective alternating injection UCG process, the duration of steam and oxygen injection stages must be in the order of a few hours. e.g., 2.0-5.0 hours. In a pilot scale trial, i.e., to gasify a few cubic meters of coal, it is possible to switch frequently between oxygen and steam injection. However, at the field scale, i.e., to gasify a few thousands cubic meters of coal, it is not practical to switch between oxygen and steam every few hours. In addition as discussed in section 3.4, the high quality product of the steam stage will be mixed with the rather low quality product of the oxygen stage, which is counterproductive to the goal of producing separate products. In this subsection, the co-injection of steam and oxygen and its effect on the quality of the UCG product is analyzed. The heat loss to the surrounding strata is ignored, which converts the model to a steady-state model. The effect of steam/O_2 ratio on the temperature profile and the quality of the product at low and high pressures is studied, and the result is used to perform an exergy analysis of the overall process.

3.5.4.1. Steam/O_2 ratio

The extended gasification model is applied in steady state mode, i.e., by ignoring the heat loss to the coal and roof layers, to underground gasification of Barbara coal

(Poland [20, 151]). Oxygen is injected with a constant flux of 0.1 mol/(m^2.s) and the injection flux of steam is varied between 0.05-0.45 mol/(m^2.s) to obtain a water/O_2 ratio that varies between 0.5 to 4.5. Fig. 3.12 shows the temperature profile on the roof, rubble, and coal faces and the average temperature of the product gas at two different pressures, i.e., 3 bar and 80 bar. In general, the highest temperature is observed on the rubble face, where the combustible gas reacts with the injected oxygen and generates heat. The lowest temperature is observed on the coal face, where the endothermic gasification reactions occur. The temperature on the coal and the roof face are between the temperature of the coal and the rubble faces. At a low pressure (3 bar), the average temperature in the cavity is around 1700 K for a steam/O_2 ratio of 0.5 (see Fig. 3.12-a), which drops linearly to 1300 K by increasing the steam/O_2 ratio to 2.0. At the same time, the rate of conversion of coal to combustible gases increases from 0.17 m/day to a maximum value of 0.20 m/day at a steam/O_2 ratio of 2.25. Then, by increasing the steam/O_2 ratio from 2.0 to 4.5, the rate at which the temperature drops slows down and the temperature linearly drops from 1300 K to 1200 K, which is above the lower temperature limit of 1000 K to achieve practical gasification reaction rates [161]. The rate of conversion of coal starts decreasing by going above the steam/O_2 ratio of 2.25. Fig. 3.12-b shows the temperature profile in the cavity and the rate of conversion of coal as a function of the injected steam/O_2 ratio at 80 bar. Similar to the low pressure case, the temperature is high (1600 K) at low steam/O_2 ratio and gradually drops to a lower value of 1300 K by increasing the steam/O_2 ratio to 4.5. Again, a maximum is observed for the rate of coal conversion at a steam/O_2 ratio of around 2.0. Up to this steam/O_2 ratio, the temperature drops faster than above this value (see Fig. 3.12). As discussed in section 3.5.3.2, the mass transfer rate from the coal surface declines with increasing pressure, which subsequently decreases the endothermic conversion of coal to a gaseous product. As a result, at high pressure, the temperature drops more slowly by increasing the steam/O_2 ratio compared to low pressure gasification.

(a)

(b)
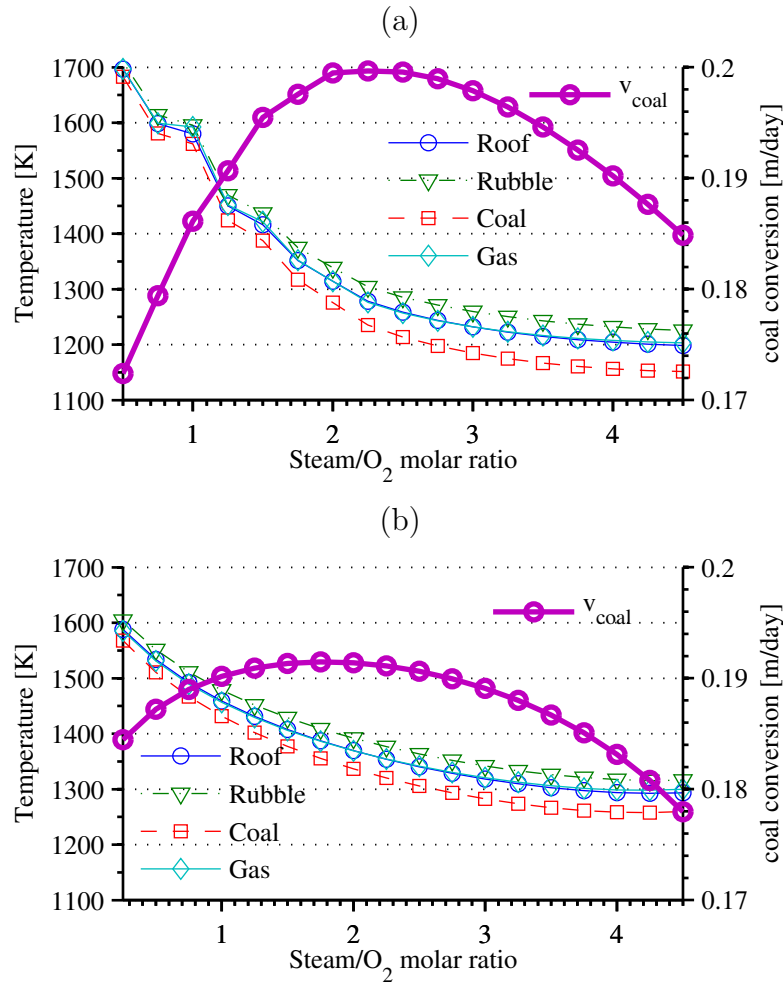
Figure 3.12.: Steady state temperature profile at (a) 3 bar; (b) 80 bar. The oxygen (O_2) injection rate is constant at 0.1 mol/(m^2.s) and the steam injection rate is altered to investigate the effect of various steam/O_2 ratios.

Fig. 3.13-a and Fig. 3.13-b show the composition of the gasification product of the co-injection of oxygen and steam in a coal layer at 3 bar and 80 bar, respectively. As to the composition of the gas at both low and high pressures, the molar composition of water in the product increases by increasing the steam/O_2 ratio, which means that the total amount of injected steam cannot be converted to a gaseous product and its conversion declines. This decline in the conversion of steam is slightly higher at higher pressure. The other observation is that at low pressure, the CO and H_2, i.e., the combustible or valuable products, show a higher mole fraction at lower pressure while the mole fraction of H_2 shows a maximum at a steam/O_2 ratio of around 1.5. By increasing steam/O_2 ratio, the mole fraction of CO decreases and the mole fraction of CO_2 increases, which can be explained by the endothermic Boudouard reaction, i.e., Eq. (3.48), which shifts to the left side (production of more CO_2) at lower temperatures (see Fig. 3.12-a). These numbers suggest that

an optimum steam/O_2 ratio can probably be found in the range between 0.5 to 1.5. The optimum value can be obtained by performing an exergy analysis (see section 3.5.5). Similarly, at 80 bar (see Fig. 3.13-b) the optimum water/O_2 ratio can be expected to fall in the range between 0.5 to 1.8, considering the maximum mole fraction of hydrogen, which is observed at a steam/O_2 ratio of around 1.8.
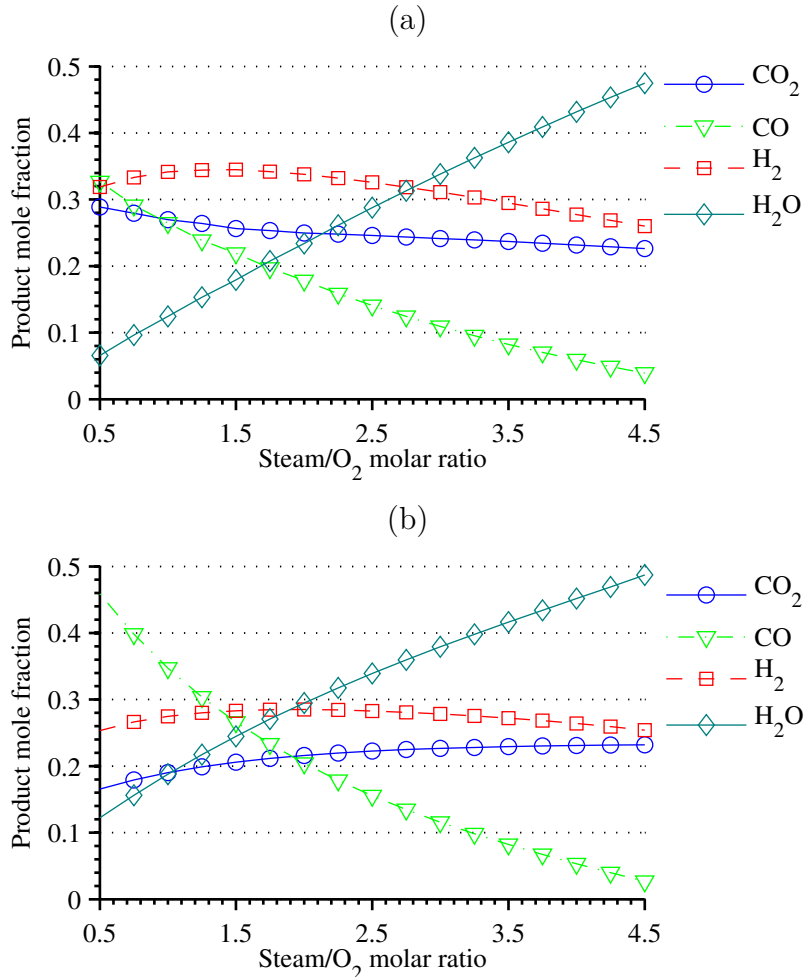
Figure 3.13.: Steady state composition profile as a function of water/O_2 ratio at (a) 3 bar; (b) 80 bar. The O_2 injection rate is 0.1 mol/(m^2.s)

To summarize, the important practical parameters that are sensitive to the change of the steam/O_2 ratio are the rate of conversion of coal, and the mole fraction of CO and H_2. Rationally, one is interested in high temperatures (which keeps the reaction rates high), a high steam/O_2 ratio (which can potentially convert more steam to combustible gases), a high hydrogen mole fraction (which is a fossil fuel with zero carbon emission), and a high CO mole fraction (which increases the heating value of the UCG product). It is observe that a single optimum value of steam/O_2 ratio that optimizes all the mentioned practical parameters cannot be found. In the next

section, all these criteria will be combined to find the optimum value of the steam/O_2 ratio by performing an exergy analysis.

3.5.5. Exergy analysis

This section deals with the exergy analysis of both the steady state and dynamic cases. The procedure explained in reference [52] is followed to calculate the practical and zero emission recovery factors of the UCG process with cyclic and mixed injection of oxygen and steam.

Fig. 3.14 shows the process flow diagram of the UCG process. Water is pumped to a steam generator by a centrifugal pump with a mechanical efficiency of 80 % and is converted to high pressure superheated steam. It is assumed that the steam generator works at a pressure of 10 bar above the injection pressure. The fuel for the steam generator is methane and the heat loss of the steam generation process is disregarded. However, considering the length of the injection well and the volumetric flow rate of the steam, a 30 % heat loss in the injection well is assumed for the high pressure (80 bar, 800 m deep) UCG and 10 % heat loss is assumed for the low pressure (3 bar, 30 m deep) UCG [134]. High pressure superheated steam is injected into the underground cavity through a well. It is assumed that the pressure of the reaction zone is equal to the hydrostatic pressure. Air or oxygen is compressed in a centrifugal compressor with a mechanical efficiency of 80 %. The compressor is driven by an electrical motor with an efficiency of 90 %. The electricity is produced in a natural gas combined cycle power plant with an efficiency of 40 %. In the case of oxygen injection, one needs to consider the production exergy of oxygen in a cryogenic air separation unit with an exergy consumption of 100 kJ/mol O_2 [52]. The exergy of the gasification product (Ex_p) is extracted and the exhaust gas is transferred to a carbon capture and storage plant. Two different CO_2 separation processes are distinguished, viz. amine chemisorption and membrane separation with average exergy requirements of 4000 kJ/kg CO_2 and 1000 kJ/kg CO_2, respectively. The separated CO_2 is transferred to an aquifer via a 100 km pipeline and subsequently injected into a 1000 m deep aquifer, which requires an additional amount of exergy of 1000 kJ/kg CO_2 [52].

Following Eftekhari et al. [52], the practical and zero emission recovery factors are defined by

$$\text{R}^{pr} = \frac{Ex_{net}}{Ex_{coal}} \quad \text{and} \quad \text{R}^{ze} = \frac{Ex_{net} - Ex_{CCS}}{Ex_{coal}}, \tag{3.49}$$

where R^{pr} is the practical recovery factor, R^{ze} is the zero emission recovery factor, Ex_{coal} [J/(m^2.s)] is the chemical exergy of converted coal per unit surface area of coal face, and Ex_{CCS} [J/(m^2.s)] is the exergy requirement for the capture and storage of all the CO_2 emission sources of the process shown in Fig. 3.14. The net recovered

exergy Ex_{net} is calculated by

$$Ex_{net} = Ex_p - (Ex_{pump} + Ex_{steam} + Ex_{O_2} + Ex_{comp}), \qquad (3.50)$$

where Ex_p [J/(m^2.s)] is the exergy value of the UCG product, Ex_{pump} [J/(m^2.s)] is the exergy consumption of pump, Ex_{steam} [J/(m^2.s)] is the exergy requirement of the steam generator, Ex_{O_2} [J/(m^2.s)] is the cumulative exergy consumption [154, 156, 157] of oxygen flux, and Ex_{comp} [J/(m^2.s)] is the exergy consumption of the compressor.

One other factor, which can be used to compare different fossil fuels with respect to their CO_2 emission is the total carbon emission per unit exergy of the final product (C_{fuel}). Using the above mentioned notations, it is calculated by

$$C_{fuel} = \frac{N_C^t M_{CO_2} + (Ex_{pump} + Ex_{steam} + Ex_{O_2} + Ex_{comp})\, e_{CH_4}}{Ex_p}, \qquad (3.51)$$

where e_{CH_4} [5.5×10^{-8} kg/J] is the emission factor of methane (see the assumptions at the beginning of this section), M_{CO_2} [kg/mol] is the molecular mass of CO_2, and N_C^t [mol/(m^2.s)] is the molar flux of carbon in the final gaseous product, which is calculated by

$$N_C^t = \sum_\alpha \left(N_{CO_2}^\alpha + N_{CO}^\alpha + N_{CH_4}^\alpha \right), \quad \alpha = c,\ roof,\ rubble. \qquad (3.52)$$
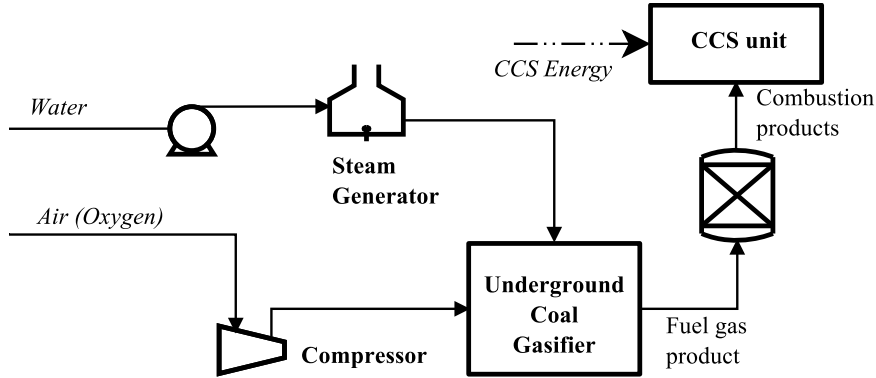
Figure 3.14.: Process flow diagram of the UCG process

It was shown that the optimum condition is the one that maximizes the rate of conversion of coal and steam, the mole fractions of hydrogen and carbon monoxide, and minimizes the carbon content per unit exergy of the final gaseous product. It was previously shown that one cannot find a single set of process parameters that satisfies simultaneously all the mentioned conditions. Therefore, the exergy analysis is used to find the optimum process parameters.
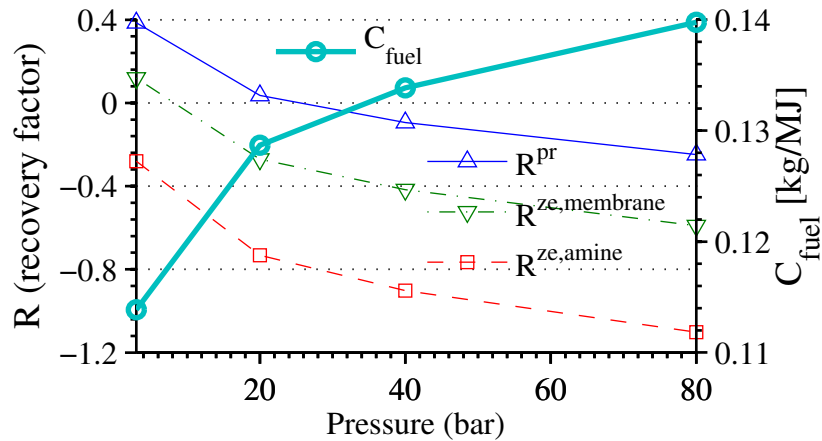
Figure 3.15.: Recovery factors and CO_2 emission of UCG with alternating injection of oxygen and steam at different pressures; the simulation results of section 3.5.3.2 are used for the calculation of practical and zero-emission (amine chemisorption, membrane capturing) recovery factors and CO_2 emission per unit exergy of products.

Fig. 3.15 shows the values of practical and zero-emission recovery factors for the simulation results of the GIG field trial at different pressures. At 3 bar, the practical recovery factor for an alternating injection of oxygen and steam is equal to 39 %, which means that a net amount of 39 % of the converted coal is extracted in the form of a gaseous product with a net emission factor of 0.11 kg CO_2/MJ. This emission factor is only two times higher than the emission factor of methane, which is the cleanest fossil fuel in terms of CO_2 emission. However, the zero-emission recovery factor is only 12 % for membrane CO_2 separation technology (which is not yet proven for large scale applications [29]). The zero emission recovery factor drops to -28 % for amine separation of CO_2 (current state of technology), which shows that a fully zero emission UCG process with alternating injection of Oxygen and CO_2 is not viable. The recovery factors decreases rapidly with increasing pressure. For pressures above 20 bar, the practical recovery factor becomes negative. It means that with the current state of technology, the UCG process with alternating injection of oxygen and steam is not a practical choice for high pressure conversion of deep coal layers. However, for low pressure gasification, the practical recovery factor is acceptable although the zero emission UCG process with the current state of technology is not practical for the alternating injection process.

Fig. 3.16 shows the result of exergy analysis obtained from applying the extended gasification model to low and high pressure underground gasification of Barbara coal. The values of the practical recovery factor, zero emission recovery factor with amine separation of CO_2, and zero-emission recovery factor for membrane separation of CO_2, and the CO_2 emission per unit exergy of product are shown in Fig. 3.16-a for UCG at 3 bar (low pressure) and in Fig. 3.16-b for UCG at 80 bar (high

pressure). At low pressure (Fig. 3.16-a) the practical recovery factor is 41 % at a steam/O_2 ratio of 0.5 and gradually increases with increasing steam/O_2 ratio to reach a maximum value of 45 % at a steam/O_2 ratio of 1.5. At the same time, the value of C_{fuel} (total carbon emission per unit exergy of product) decreases from 0.17 kg CO_2/MJ at a steam/O_2 ratio of 0.5 to 0.156 at a steam/O_2 ratio of 1.5, which is close to its minimum value of 0.155 at a steam/O_2 ratio of 2.0. The recovery factor follows a decreasing trend above a steam/O_2 ratio of 1.5. By applying an amine capturing technique to all the CO_2 emission sources the process can become a zero-emission process. However, the value of zero-emission recovery factor ($R^{ze,amine}$) showed in Fig. 3.16-a is always negative, which suggests that the zero-emission UCG process with the current state of technology is not yet practical. Using emerging technologies such as membrane separation can improve the recovery factor, as shown in Fig 3.16-a by $R^{ze,membrane}$. The zero-emission recovery factor reaches a maximum value of 24 % at a steam/O_2 ratio of 1.5, which means that only 24 % of the converted coal can be extracted. The economical feasibility of the process with this recovery factor is outside the scope of this work. Fig. 3.16-b shows the exergy analysis result at pressure of 80 bar (deep coal layer). A lower limit of 0.25 for the steam/O_2 ratio is used for practical purposes, because below this value the temperature in the cavity becomes too high (see Fig. 3.12-b). At a steam/O_2 ratio of 0.25, the practical recovery attains its maximum value of 46 %, which gradually decreases to a value of 12 % by increasing steam/O_2 ratio to 4.5, while the total CO_2 emission per unit product exergy increases from a minimum value of 0.16 kg/MJ to 0.19 kg/MJ. Again, similar to the low pressure case in Fig. 3.16-a, the zero emission recovery factor, using the state of the art CO_2 capturing technology (amine separation), is negative for the whole range of steam/O_2 ratios, which shows that the zero-emission process is not viable. However, by using membrane separation of CO_2, the zero-emission recovery factor can reach a maximum value of 26 % at a steam/O_2 ratio of 0.25.

Figure 3.16.: Exergy analysis of channel gasification of thin coal for injection of a steam/O_2 mixture with various compositions at (a) 3 bar and (b) 80 bar; Practical and zero emission recovery factors and product gas CO_2 emission per unit exergy of product are shown.

In the simulation of the mixed injection of steam/O_2 (Fig. 3.16), it is assumed that only a fraction of heat is lost during steam injection. However, in practice, for long injection wells at low injection rates, up to 90 % of heat can be lost, which causes the condensation of steam [134]. To avoid this heat loss, one can inject liquid water (or allow underground water influx into the cavity by adjusting the pressure) and vaporize it in the rubble zone by using the heat of reaction of the injected oxygen with combustible gases. In the model, this can be implemented by assigning the heat of vaporization of water to the parameter $\Delta h_{H_2O}^{vap}$ in Eq. (3.31). Fig. 3.17 shows the exergy analysis results for the UCG with the co-injection of *water* and oxygen. The general behavior of the recovery factors and CO_2 emission is similar to the co-injection of *steam* and oxygen (Fig. 3.16). There are however a few differences in the optimum values of recovery factors and the value of a water/O_2

ratio that maximizes the recovery factor and minimizes the total CO_2 emission per unit exergy of product. At 3 bar, as shown in Fig. 3.17-a, the maximum practical recovery factor is equal to 50 % (45 % for the steam injection) and the total CO_2 emission per unit exergy of product is equal to 0.156 kg/MJ (same value for the steam injection) at a water/O_2 ratio of 1.25 (steam/O_2 ratio of 1.5). Here any practical complications of gravity segregation are ignored. The 5 % higher practical recovery factor for the water injection compared to steam injection is a direct result of avoiding the heat loss that occurs during the injection of steam. On the downside, the optimum value is reached at a lower water/O_2 ratio, which means that a lower amount of water is converted to combustible products. Also, the rate of conversion of the coal layer for the water injection case (not shown in the figures) is 1 cm/day lower than the steam injection case (Fig. 3.12). Unlike the steam injection case, the zero-emission recovery factor with the state of the art CO_2 capturing technology (amine chemisorption) is not always negative and indeed it reaches a maximum value of 1.5 % at a water/O_2 ratio of 1.25, which is however too low to make the zero-emission process a practical option. By using a membrane separation process for CO_2 capturing, the zero emission recovery factor can be improved up to a maximum value of 30 % at a water/O_2 ratio of 1.25. Fig. 3.17-b shows the exergy analysis result and total CO_2 emission per unit exergy of product for deep UCG at 80 bar with the co-injection of *water* and oxygen. Compared to the high pressure UCG with steam injection (Fig. 3.16-b), the maximum recovery factor is 46 % (same value for steam injection, see Fig. 3.16-b) and the minimum CO_2 emission per unit exergy is 0.16 kg/MJ (the same value as for steam injection) both at a water/O_2 ratio of 0.25. However, the rate of conversion of coal is around 1 cm/day lower than the steam injection case (Fig. 3.12). The other difference with the steam injection case is that by increasing the water/O_2 ratio, the value of CO_2 emission increases much faster for the water injection case, whereas it increases from its minimum value at a water/O_2 ratio of 0.25 to a value of 0.32 at a water/O_2 ratio of 4.5. Similar to the high pressure UCG with steam injection, the zero-emission recovery factor with amine capturing technique is not viable with a negative recovery factor for the whole range of water/O_2 ratios. However, the zero-emission recovery factor can be increased up to 26 % by using a membrane CO_2 capturing method.

The exergy analysis results can be summarized as follows:

- The alternating injection of oxygen and steam is only practical for low pressure UCG, i.e., shallow coal layers, with a recovery factor of around 40 %. The total CO_2 emission per unit exergy of the final product is only twice as large as the emission factor of methane. The zero emission recovery of coal with alternating injection of oxygen and steam is not practical with the current state of technology.

- The conversion of coal with the co-injection of steam (or water) and oxygen is a more attractive option compared to the alternating injection. The practical recovery factor is around 50 %, which is 10 % higher than the alternating injection process. However, the total CO_2 emission per unit exergy of product

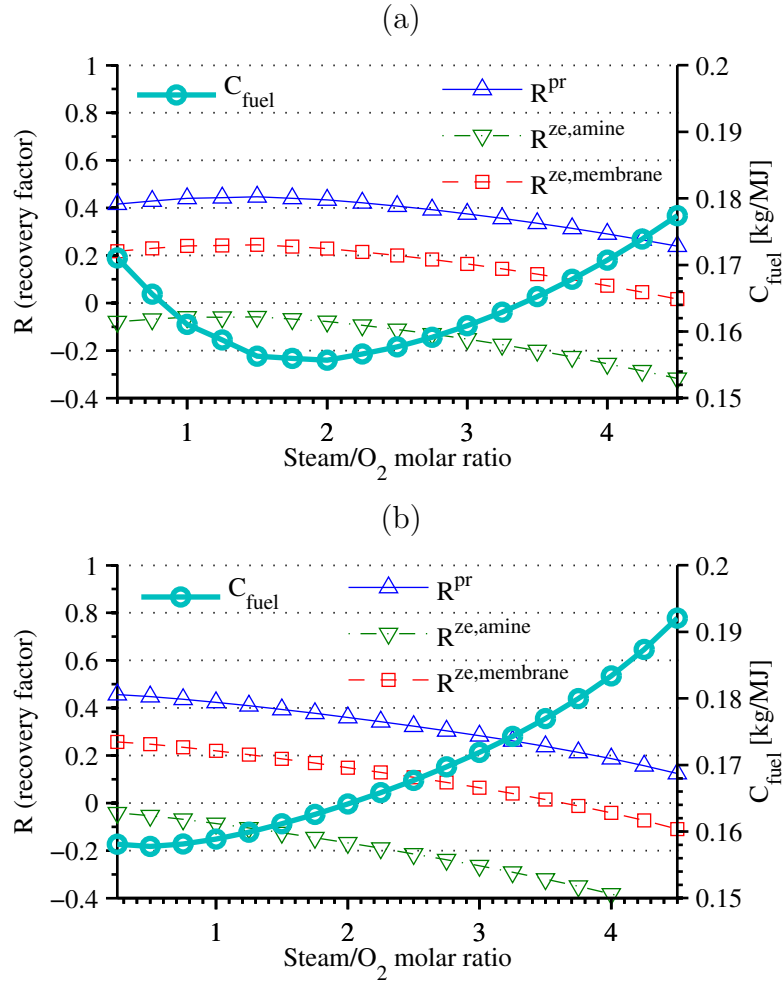is 30 % higher than the alternating injection scenario.

(a)

(b)
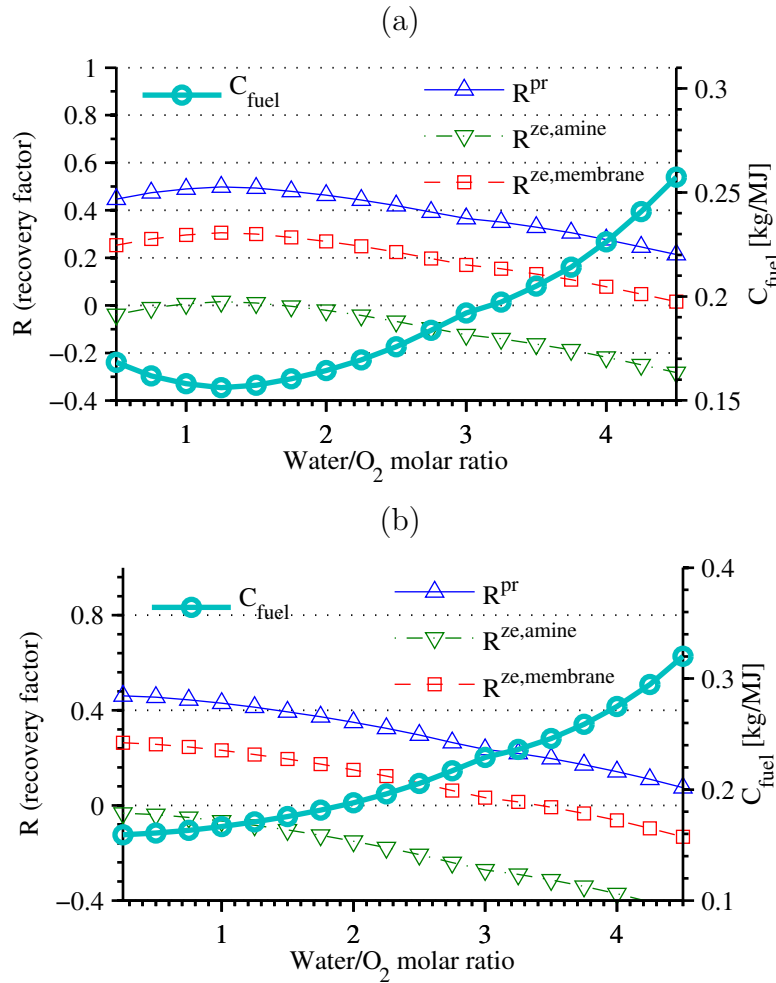
Figure 3.17.: Exergy analysis of channel gasification of thin coal for injection of a water/O_2 mixture with various compositions at (a) 3 bar and (b) 80 bar; Practical and zero emission recovery factors and product gas CO_2 emission per unit exergy of product are shown.

- Low pressure is the favorable condition for UCG, with the possibility of conversion of larger amounts of water to combustible gases.

- With the current state of technology, zero emission UCG is not a practical option with a recovery factor which is negative or very low.

- Exergy analysis suggests that the development of a less energy intensive CO_2 capturing method, e.g., membrane separation, gives a positive recovery factor. However, the economical feasibility of those methods are outside the scope of this work.

- In UCG with the co-injection of steam or water and oxygen, the injection of water is the preferred technique with a higher recovery factor. Injection of

water instead of steam avoids the high heat loss that otherwise can happen during the steam injection.

3.6. Conclusions

- This study investigated whether it is possible that underground coal gasification can be used to utilize the coal energy with a reduced carbon foot print.

- There are three scenarios for UCG depending on roof stability, i.e., no collapse, partial collapse and total collapse. The partial collapse case is amenable for simple modeling. The model consists of alternating injection of reactive gases (oxygen and steam) in a rubble zone, which react with the combustible gas in the channel and with coal on the coal face. It is possible to reach quasi-steady state conditions for the channel during the gasification process. However, it is also possible to incorporate transient heat conduction effects.

- The reduced carbon footprint can be brought about by first injection of mainly oxygen to heat up the formation and subsequently injection of pure water or steam. In the first period a gas with a high CO_2 content is produced. After switching to pure water or steam injection thermodynamic calculations suggest that a gas with a relatively low carbon dioxide content, but high hydrogen content can be produced. The result shows a reasonable agreement with a recent field trial in Katowice, Poland.

- The process can become sustainable if a mixture of steam and oxygen is injected. The product gas contains some carbon dioxide.

4. Application of the negative saturation method to model salt precipitation in the injection of CO$_2$ into aquifers

The Ghost of Sir Felix Finch whines, "But it's been done a hundred times before!"–as if there could be anything *not* done a hundred *thousand* times between Aristophanes and Andrew Void-Webber! As if Art is the *What*, not the *How*!

David Mitchel, Cloud Atlas

Abstract

The negative saturation (NegSat) method, which is a combination of negative flash and multicomponent single/two-phase flow in porous media, has been shown to be beneficial in numerical simulations of phase appearance/disappearance for mixtures that consist of volatile components, i.e., components that appear in both liquid and gas phases. The method is extended to a three phase system of CO$_2$-water-NaCl, in which NaCl appears as a nonvolatile dissolved component (NaCl) and as an immobile precipitated solid phase. A detailed thermodynamical analysis of the NegSat method is given and the possibility to extend it to injection in brine aquifers is demonstrated. Precipitation of salt occurs due to evaporation of water into supercritical CO$_2$. Precipitation decreases the permeability near the injection well forming a dry-out zone. With this permeability change, the injection pressure needs to be increased to maintain the CO$_2$ injection rate, which requires more compression energy. To address this issue, first a thermodynamic model is optimized to predict the phase behavior of the CO$_2$-water-NaCl system with reasonable accuracy. Then the NegSat method is modified for two-phase flow to include salt precipitation. The

model is solved to analyze the effect of various physical parameters on the injectivity of CO_2. Finally an exergy analysis is performed to quantify the effect of salt precipitation on the compression power requirement for CO_2 injection into high pressure-temperature-salinity aquifers.

4.1. Introduction

The Negative Saturation (NegSat) method is a useful combination of the *negative flash* [169] concept from fluid phase equilibria with the classic equation of multi-component two-phase flow in porous media [14]. Negative flash refers to a nontrivial solution of vapor-liquid equilibrium for a single phase multi-component system, which gives rise to positive values for the vapor and liquid equilibrium compositions and satisfies mass balance and equality of fugacities [169], but yields a non-physical value for the molar phase fraction, i.e., lower than zero or higher than one. When the gas phase fractionis higher than one, the gas phase is stable and the liquid phase is meta stable. When the gas phase fraction is negative the liquid phase is stable and the gas phase is meta stable. Negative flash is not the usual description in thermodynamics. The NegSat method takes advantage of the negative flash to convert the single phase flow to a pseudo two-phase flow, which, similarly to the negative flash, satisfies the mass balance and equilibrium conditions. The NegSat method was first proposed by Abadpour and Panfilov [1] for isothermal multi-component two-phase flow in porous media and then extended by Panfilov and Rasoulzadeh [114] to include diffusion and capillarity. Salimi et al. extended the original NegSat method to include the energy balance equation for non-isothermal flow [142].

In this chapter the possibility of injection of CO_2 into an aquifer near an oil reservoir is considered, which is applicable to the "pre-salt" reservoir that extends over 800 km off the Brazilian coast, from the state of Espírito Santo to Santa Catarina, below a thick salt layer that covers the sedimentary basins [30]. The high content of carbon dioxide extracted along with oil, over 20% in the case of some reservoirs, deserves special attention. Estimates [16, 4] suggest that just in two areas bounded by the Tupi and Iara reservoirs, where there is an accumulation of up to 12 billion barrels of oil and gas, there are 3.1 billion tons of CO_2. It is proposed to reinject the CO_2 into the wells or nearby aquifers. Therefore it is important to model accurately the gas injection in brine layers at high pressures and temperatures. Conventional high pressure gas injection occurs between 100-300 bars. In this case one deals with pressures of more than 700 bars. Therefore the equation of state (EOS) needs to be optimized using experimental data at high pressures. Many data for the phase behavior of the CO_2-brine system do exist [55, 158, 66], which can be used to calibrate the EOS at high pressures for different temperatures and salt concentrations. Here the PRSV (Peng-Robinson-Strijek-Vera) EOS [153] is used. The force parameter and the volume parameter in this equation are obtained by using the NRTL (Non-random two liquid) [135] based MHV2 (modified Huron-Vidal second order)

mixing rule [39, 102]. It will be shown that this EOS and mixing rule give the best fit to experimental data in the pressure range of interest to us. The purpose of this work is to show their validity in the high pressure range prevailing in the pre-salt reservoirs. For this validation experimental results are used that are available in the literature [48]. Then the available experimental data on the density of the CO_2-water-NaCl mixture are used [73, 109] to optimize the volume shift parameters [117] for accurate prediction of the density of the liquid mixture. In the literature, there are numerous dedicated models for the calculation of thermodynamic and transport properties of CO_2-water and CO_2-water-NaCl mixtures [34, 44, 48, 71, 94, 149], of which the models of Duan and Sun [48] and Spycher et al. [129, 149] are applicable to a wide range of pressure and temperature with high accuracy. The model, which is a combination of standard equation of state and activity coefficient models, is more general, which allows it to be easily extendable to other multi-component mixtures, e.g. hydrocarbons. However, it is not as accurate as the above mentioned dedicated models.

The optimized thermodynamic model is used to calculate the thermodynamics and transport properties of the CO_2-water-NaCl mixture that are required in the simulation of the injection of supercritical CO_2 into an aquifer filled with saturated brine. In the aquifer injection process, supercritical CO_2 extracts water from the brine (CO_2+water mixture), increasing the concentration of NaCl. If this concentration increases above the solubility of NaCl in water, solid NaCl precipitates. By continuing the injection of supercritical CO_2, irreducible water saturation is decreased (through evaporation) by supercritical CO_2, which eventually leads to the evaporation of all the water and the precipitation of all the dissolved NaCl that is not transported away. The total evaporation of water (total precipitation of salt), which is called formation dry-out, impairs the permeability and porosity of the aquifer, is most important near the injection well [131, 130]. With this reduced permeability near the injection well, the injection pressure must be increased to keep a constant injection rate. The higher injection pressure increases the compression energy for CO_2 and consequently increases the energy cost of the project [106].

The formation dry-out effect with precipitation of salt has been investigated previously by other researchers, theoretically and experimentally. Giorgis et al. [68] performed a 2D simulation of the injection of dry CO_2 in a depleted gas reservoir. Their results show that if the liquid relative permeability is low or if the capillary pressure effect is ignored, the salt precipitation near the injection well has little effect on the permeability. However, for a high mobility brine, the capillary-driven brine backflow can refill the dried area near the injection point, with consequent creation of an area with a high solid saturation. This capillary pressure effect near the injection well can have a deleterious effect on the CO_2 injectivity [68] and emphasizes the effect of gravity override, as explained in [131]. The same results were obtained in the experimental investigation of Ott et al. [111] and Bacci et al. [8, 7] , the 2D numerical simulations of Pruess and Muller [131], Kim et al. [89], Muller et al. [106], and the 3D simulations of Naderi Beni et al. [17].

In addition, analytical solutions for simplified one-dimensional models of salt precipitation during injection of CO$_2$ in a brine aquifer have been proposed by Pruess [130] and Zeidouni et al. [175]. These simple (yet accurate) models and analytical solutions are extremely useful in the validation of numerical procedures.

Here, by applying the NegSat method to the salt precipitation in the aquifer due to injection of supercritical CO$_2$, three main objectives are being pursued.

First, a general simplified model for CO$_2$-water-salt is tuned, which is easily extendable and fairly accurate. In the development of this model, well-known standard cubic equations of state and mixing rules are used, which makes the model suitable for applications in other areas, e.g., phase equilibria of mixtures that include hydrocarbons. Secondly, the two-phase NegSat method is extended to a three-phase system with one immobile phase and one nonvolatile component to stress the limitations in the application of the current NegSat method, as will be explained in the numerical solution section. Thirdly, the procedure for coupling fluid phase equilibria and single/two phase flow in porous media is explained, especially for the simple case of a binary mixture.

4.2. Phase equilibrium model

Many experimental data of vapor-liquid and liquid-liquid equilibrium (VLE and LLE) of CO$_2$ with electrolyte solutions can be found in the literature [55, 66, 158]. For a good review, see [48]. In addition, efforts have been undertaken to find a comprehensive model that can predict accurately the equilibrium composition and density of the different phases for a wide range of temperatures, pressures and NaCl concentrations [49, 48, 132]. In addition to accuracy, the numerical implementation of these models should have a relatively fast convergence rate in order to be practical in numerical simulations. Cubic equations of state are reasonably fast in numerical multicomponent phase equilibrium (flash) calculations. To use an equation of state for the highly non-ideal CO$_2$-brine system, an appropriate mixing rule must be implemented. Here different mixing rules for four different equations of state were compared, i.e., Peng-Robinson (PR) [118], Soave-Redlich-Kwong (SRK) [147], Peng-Robinson-Stryjek-Vera (PRSV) [153], and SRK-MC (Mathias-Copeman) [96] with the mixing rules of van der Waals, Huron-Vidal (HV) [83], Modified Huron-Vidal (MHV1, MHV2) [39, 102], and Predictive SRK (PSRK) in combination with Non-Random Two-Liquid (NRTL) [135] and UNIversal QUAsiChemical (UNIQUAC) [2] activity coefficient models. The PRSV equation of state with the MHV2 mixing rule that uses the NRTL activity coefficient model was selected as the most useful for this work's purposes. The mixing rules take the salt concentrations explicitly into account at a given temperature. The liquid density predicted by the PRSV equation was adjusted using the volume shift parameter [117]. The details of the equations and the calculation procedure are explained in the next sections.

4.3. Flash calculation

In the oil and gas industries, the term flash or flash evaporation refers to the separation of a multicomponent liquid mixture into a gas phase and a liquid phase in a flash drum [166]. In thermodynamics, however, this term refers to a general phase equilibrium calculation procedure. Here, first the parameters that are required for explaining the flash calculation procedure are defined. In the next section, the problem is formulated and a numerical method for solving the system of equations is presented.

4.3.1. Basic definitions

A mixture consisting of a certain amount of moles of different components is considered. The number of moles of each component in the mixture is written as n_i^t [mol], where i denotes the component and t denotes the overall mixture. Under equilibrium condition, this system separates into a few phases in equilibrium, with the component i distributed between these phases in a manner such that the total Gibbs energy (at constant p and T) of the system is minimized (equilibrium condition). The number of moles of component i in phase α is denoted by n_i^α [mol]. These notations can be used to write the mole balance for each component i in the system, i.e.,

$$n_i^t = \sum_\alpha n_i^\alpha, \text{ for all } i. \tag{4.1}$$

Generally, working with the mole fractions x_i^α is considered more convenient, which are defined as

$$x_i^\alpha = n_i^\alpha / \sum_\alpha n_i^\alpha. \tag{4.2}$$

For each phase α, another parameter, which is normally used in the formulation of flash calculation, is called the molar phase fraction Ψ^α, i.e., the total number of moles of components in phase α divided by the total number of moles of all components in the whole mixture:

$$\Psi^\alpha = \frac{\sum_i n_i^\alpha}{\sum_i \sum_\alpha n_i^\alpha}. \tag{4.3}$$

In flash calculation procedures, the volumetric parameters are not used. However, in the text they will be used in the formulation of fluid flow in porous media. For phase α, one variable is the volumetric phase fraction S^α, which is known as *saturation* in petroleum engineering. Saturation is defined as the total volume of phase α (V^α [m^3]) divided by the total volume of the mixture, i.e.,

$$S^\alpha = V^\alpha / \sum V^\alpha. \tag{4.4}$$

The relation between the molar properties and the volumetric properties requires another property, which is called molar concentration. The molar concentration of component i in phase α is denoted by c_i^α [mol/m³] and is defined by

$$c_i^\alpha = \frac{n_i^\alpha}{V^\alpha}. \tag{4.5}$$

The molar concentration can also be defined for a phase α, i.e., C^α [mol/m³]. It is the total number of moles in phase α divided by the volume of phase α:

$$C^\alpha = \sum_i c_i^\alpha. \tag{4.6}$$

The mole fraction can also be expressed in terms of molar concentrations, i.e.,

$$x_i^\alpha = c_i^\alpha / C^\alpha. \tag{4.7}$$

The above definitions can be combined to write two important relations, which will be used throughout the text. The ratio between the mole fraction of component i in the overall mixture (x_i^t) to the equilibrium mole fractions (x_i^α) and the molar phase fraction (Ψ^α) reads

$$x_i^t = \sum_\alpha x_i^\alpha \Psi^\alpha, \text{ for all } i. \tag{4.8}$$

The ratio between the molar concentration of component i in the overall mixture $(c_i^t$ [mol/m³]) and the concentration of component i in each equilibrium phase $(c_i^\alpha$ [mol/m³]) reads

$$c_i^t = \sum_\alpha c_i^\alpha S^\alpha = \sum_\alpha x_i^\alpha C^\alpha S^\alpha. \tag{4.9}$$

Fig. 4.1 shows a summary of these relations (Eqs. (4.1) to (4.9)) in general forms (as described in this section) and for a specific case of gas-liquid-solid equilibrium.

In the next section, the formulation of the flash calculation for a three phase system will be explained.

4.3.2. Vapor-liquid-solid flash calculation

In this section, the procedure for the calculation of vapor-liquid-solid equilibrium compositions and densities of the CO_2-water-NaCl system will be explained. First, the relation between the molar and volumetric properties of the system are described. Fig. 4.1 shows the definition of basic physical properties that are important in both the phase equilibria and the fluid flow. These notations will be used throughout this section (most of them are defined in more details in the previous section); superscripts g, l, s, and t denote the gas, liquid, solid, and total mixture, respectively.

Subscript i for the small letters denotes the component i. The equilibrium conditions are expressed in terms of chemical potentials, i.e. [126]

$$\hat{\mu}_i^g \left(p, T, x_i^g\right) = \hat{\mu}_i^l \left(p, T, x_i^l\right) = \hat{\mu}_i^s \left(p, T, x_i^s\right), \tag{4.10}$$

where $\hat{\mu}_i^\alpha$ [J/mol] ($\alpha = g, l, s$) is the chemical potential of component i in phase α. The hat sign on chemical potential is used to denote that the value of the chemical potential is calculated for component i in a mixture [145]. The mass balance equations read

$$x_i^t N^t = x_i^g N^g + x_i^l N^l + x_i^s N^s, \tag{4.11}$$

which can be rewritten as

$$x_i^t = \Psi^g x_i^g + \Psi^l x_i^l + \Psi^s x_i^s, \tag{4.12}$$

where N^t is the total number of moles in the system, Ψ^α ($\alpha = g$, l, or s) denotes the molar phase fraction of phase α (see Fig. 4.1) and is defined by Eq. (4.3), which can be rewritten as

$$\Psi^\alpha = \frac{N^\alpha}{N^t}. \tag{4.13}$$

For a component that is distributed between two phases in equilibrium, K-values are defined, which are the ratio between the equilibrium mole fraction of a component in one phase and the equilibrium mole fraction of the same component in liquid phase, as

$$K_i^{gl} = x_i^g / x_i^l \quad \text{and} \quad K_i^{sl} = x_i^s / x_i^l, \tag{4.14}$$

which can be rearranged as

$$x_i^g = K_i^{gl} x_i^l \quad \text{and} \quad x_i^s = K_i^{sl} x_i^l, \tag{4.15}$$

The summation equations, i.e., $\sum_{i=1}^{N_c} x_i^\alpha = 1$ can be rewritten as

$$\sum_{i=1}^{N_c} \left(x_i^g - x_i^l\right) = 0, \quad \sum_{i=1}^{N_c} \left(x_i^s - x_i^l\right) = 0. \tag{4.16}$$

Here, N_c is the number of components. One can replace x_i^g and x_i^s from Eq. (4.15) into Eq. (4.16), to obtain

$$\sum_{i=1}^{N_c} x_i^l \left(K_i^{gl} - 1\right) = 0, \quad \sum_{i=1}^{N_c} x_i^l \left(K_i^{sl} - 1\right) = 0. \tag{4.17}$$

Using Eq. (4.15) to replace x_i^g and x_i^s in Eq. (4.12), one obtains

$$x_i^t = \Psi^g K_i^{gl} x_i^l + \Psi^l x_i^l + \Psi^s K_i^{sl} x_i^l. \tag{4.18}$$

Substituting $\Psi^l = 1 - \Psi^g - \Psi^s$ in Eq. (4.18), one obtains x_i^l in terms of K-values and phase fractions, i.e.,

$$x_i^l = \frac{x_i^t}{1 + \Psi^g \left(K_i^{gl} - 1 \right) + \Psi^s \left(K_i^{sl} - 1 \right)}. \tag{4.19}$$

Then substituting x_i^l from Eq. (4.19) into Eq. (4.17), F_1 and F_2 are defined, i.e.,

$$F_1 \left(\Psi^g, \Psi^s \right) \equiv \sum_{i=1}^{N_c} \frac{x_i^t \left(K_i^{gl} - 1 \right)}{1 + \Psi^g \left(K_i^{gl} - 1 \right) + \Psi^s \left(K_i^{sl} - 1 \right)} = 0, \tag{4.20}$$

$$F_2 \left(\Psi^g, \Psi^s \right) \equiv \sum_{i=1}^{N_c} \frac{x_i^t \left(K_i^{sl} - 1 \right)}{1 + \Psi^g \left(K_i^{gl} - 1 \right) + \Psi^s \left(K_i^{sl} - 1 \right)} = 0. \tag{4.21}$$

Eqs. (4.20-4.21) are known as the Rachford-Rice [133] equations. To estimate the K-values, the definition of chemical potential can be used, i.e. [145]

$$\hat{\mu}_i - \mu_i^o = -RT \ln \frac{\hat{f}_i}{f_i^o}, \tag{4.22}$$

where the superscript "o" denotes standard pressure and temperature T. To rewrite Eq. (4.10) as the equality of fugacities, $\hat{f}_i^\alpha$, i.e,

$$\hat{f}_i^g = \hat{f}_i^l = \hat{f}_i^s, \text{ for all } i, \tag{4.23}$$

where the $\hat{f}_i^\alpha$ is the fugacity of component i in phase α, and the hat sign denotes that the fucacity is calculated for each component in a mixture (and not for the pure component i). The above equation can be expressed in terms of fugacity coefficients ($\hat{\Phi}_i^\alpha = \frac{\hat{f}_i^\alpha}{x_i^\alpha p}$), i.e.,

$$x_i^g \hat{\Phi}_i^g = x_i^l \hat{\Phi}_i^l = x_i^s \hat{\Phi}_i^s. \tag{4.24}$$

Fugacity coefficients $\hat{\Phi}_i^\alpha$ can be evaluated in terms of pressure, temperature, and mole fraction using a cubic equation of state, e.g. PRSV-MHV2 (see Section 4.4). The K-values are calculated in terms of fugacity coefficients by combining Eq. (4.14)

Phase	Volumetric phase fraction (saturation)	Molar phase fraction	Mole fraction	Molar concentration	Volume	Mole
Gas	$S^g = \frac{V^g}{V^t}$	$\Psi^g = \frac{N^g}{N^t}$	$x_i^g = \frac{n_i^g}{N^g}$ $\sum_i x_i^g = 1$	$c_i^g = \frac{n_i^g}{V^g}$ $C^g = \frac{N^g}{V^g}$	V^g	n_i^g $N^g = \sum_i n_i^g$
Liquid	$S^l = \frac{V^l}{V^t}$	$\Psi^l = \frac{N^l}{N^t}$	$x_i^l = \frac{n_i^l}{N^l}$ $\sum_i x_i^l = 1$	$c_i^l = \frac{n_i^l}{V^l}$ $C^g = \frac{N^g}{V^g}$	V^l	n_i^l $N^l = \sum_i n_i^l$
Solid	$S^s = \frac{V^s}{V^t}$	$\Psi^s = \frac{N^s}{N^t}$	$x_i^s = \frac{n_i^s}{N^s}$ $\sum_i x_i^s = 1$	$c_i^s = \frac{n_i^s}{V^s}$ $C^s = \frac{N^s}{V^s}$	V^s	n_i^s $N^s = \sum_i n_i^s$
Mixture	$\sum_\alpha S^\alpha = 1$	$\sum_\alpha \Psi^\alpha = 1$	$x_i^t = \frac{n_i^t}{N^t}$ $\sum_i x_i^t = 1$	$c_i^t = \frac{n_i^t}{V^t}$ $C^t = \frac{N^t}{V^t}$	$V^t = \sum_\alpha V^\alpha$	$n_i^t = \sum_\alpha n_i^\alpha$ $N^t = \sum_i n_i^t$

Figure 4.1.: Definition of basic physical properties in a three phase system based on number of moles and volume in a three phase vapor-liquid-solid mixture

and Eq. (4.24) to obtain

$$K_i^{gl} = \frac{x_i^g}{x_i^l} = \frac{\hat{\Phi}_i^l}{\hat{\Phi}_i^g} \quad \text{and} \quad K_i^{sl} = \frac{x_i^s}{x_i^l} = \frac{\hat{\Phi}_i^l}{\hat{\Phi}_i^s}. \tag{4.25}$$

The Rachford-Rice algorithm for the calculation of equilibrium composition of each phase at known temperature T, pressure p, and total composition x_i^t solves the non-linear equations (4.20), (4.21), (4.19), and (4.15) by means of an iterative procedure, which can be described in the following steps:

1. Initialize the K-values, K_i^{gl} and K_i^{sl}, by estimated values.

2. Solve the Rachford-Rice equations, i.e., Eqs. (4.20)-(4.21), for the unknowns Ψ^g and Ψ^s.

3. Calculate x_i^l from Eq. (4.19) and x_i^g and x_i^s from Eq. (4.15).

4. Check the convergence criteria, i.e., the equalities in Eq. (4.16), with a tolerance of, e.g., 1×10^{-6}. If the equilibrium mole fractions do not satisfy Eq. (4.16), use the mole fractions calculated in step 3 to calculate new K-values by means of Eq. (4.25). Go to Step 1.

In the next section, the detailed procedure of estimating the fugacity coefficients and K-values using the PRSV equation of state with MHV2 mixing rule will be explained.

4.4. Thermodynamic models

For the non-specialized reader the complete procedure for the calculation of the fugacity coefficient for each component in each phase is provided here. The fugacity coefficient is a function of composition, temperature and pressure. The compositions are denoted in terms of mole fractions x_i^l in the liquid phase and mole fractions x_i^g in the vapor phase. These will be obtained from an iterative flash calculation. The vapor-liquid phase equilibrium (flash) calculation is done using the well-known Rachford-Rice [133] algorithm of PT-flash, which can be found in many references [145, 166]. The algorithm calculates the molar fraction of each component in different phases at constant temperature and pressure using the mass balance equations and the following equilibrium conditions for each component i [166]

$$x_i^g \hat{\Phi}_i^g \left(p, T, x_i^g \right) = x_i^l \hat{\Phi}_i^l \left(p, T, x_i^l \right). \tag{4.26}$$

Superscripts g and l represent vapor and liquid phases respectively. The mole fraction of each component in the gas phase is written as x_i^g and in the liquid phase as x_i^l. The hat notation on fugacity coefficient, $\hat{\Phi}_i^\alpha$ denotes the value of fugacity coefficient of component i in a mixture.

4.4.1. The PRSV equation of state with the MHV2 mixing rule

The general form of the PR equation of state [118] is

$$p = \frac{RT}{v - b} - \frac{a}{v(v+b) + b(v-b)}, \tag{4.27}$$

where T [K] is the absolute temperature, p [Pa] is the absolute pressure, v [m^3/mol] is the specific volume of the fluid mixture, and R=8.314 Pa.m^3/(mol.K) is the ideal gas constant. The author's approach is to separate the salt from the water and consider its effect on the binary interaction parameters of CO_2-water. In other words the critical properties of the brine are assumed to be the same as the properties of water, except that another parameter is added, i.e., the salt mole fraction. The procedure to obtain the phase equilibrium properties is exactly the same as for the CO_2-water system [165]. The presence of salt is taken into account by assuming that the binary interaction parameters ΔG_{12}, ΔG_{21} in Eq. (4.40) are linear functions of the salt mole fraction and temperature. The procedure is modified for calculating the equilibrium properties of the CO_2-water system [165] for the user to be able to predict the phase behavior of the CO_2-brine system, by optimizing the quantities that determine the force parameter a [J/mol] using experimental data on the vapor-liquid equilibrium (VLE) of CO_2-brine (see below). The volume parameter b [m^3/mol] is left unchanged w.r.t. the carbon dioxide water system. In order to obtain a, b in Eq. (4.27) one can proceed as follows. The values of the force parameters a_i and the volume parameters b_i for each component i are calculated using

$$a_i = 0.457235 \frac{R^2 T_{c_i}^2}{P_{c_i}} \alpha_i(T), \quad b_i = 0.077796 \frac{RT_{c_i}}{P_{c_i}}, \tag{4.28}$$

where T_{c_i} [K] is the critical temperature and P_{c_i} [Pa] is the critical pressure of component i (see Table 4.1). The parameter $\alpha_i(T)$ [dimensionless] is a function of the vapor pressure for each component i and is calculated by the relation suggested by Stryjek and Vera [153]

$$\alpha_i(T) = \left[1 + \kappa_i\left(1 - \sqrt{T_{r_i}}\right)\right]^2, \quad \kappa_i = \kappa_{0_i} + \kappa_{1_i}\left(1 + \sqrt{T_{r_i}}\right)(0.7 - T_{r_i}), \tag{4.29}$$

with

$$\kappa_{0_i} = 0.378893 + 1.4897153\omega_i - 0.17131848\omega_i^2 + 0.0196554\omega_i^3, \tag{4.30}$$

where T_{r_i} are the reduced temperatures (T/T_{c_i}) and ω_i are the acentric factors of component i (see Table 4.1). Values of κ_{1_i} (see Table 4.1) are component-specific and are calculated using the vapor pressure data (for more details, see [110]). The MHV2 [38] is a modification of Huron and Vidal (HV) mixing rule [83]. For

parameter b in Eq. (4.27) one uses

$$b = \sum_{i}^{N_c} x_i b_i, \tag{4.31}$$

where x_i is the mole fraction of component i in the vapor or liquid mixture (here it is used without any superscript for convenience), and b_i [m^3/mol] is the volume parameter for pure component i and is calculated by Eq. (4.28). To find the force parameter a for the mixture, the following quadratic equation [110] must be solved for the variable ε

$$q_2 \varepsilon^2 + q_1 \varepsilon + q_0 = 0, \ q_0 \equiv -q_1 \sum_{i=1}^{N_c} x_i \varepsilon_i - q_2 \sum_{i=1}^{N_c} x_i \varepsilon_i^2 - \frac{g^E}{RT} - \sum_{i=1}^{N_c} x_i \ln \frac{b}{b_i} \tag{4.32}$$

On the RHS of the above equation, $\varepsilon_i = a_i / (b_i RT)$ (see Eq. (4.28)) and g^E [J/(mol.K)] are functions of T and x_i (see Eq. (4.36)). The mole fraction x_i belongs to the pseudo 2-component CO$_2$-brine system. The quantity g^E will be calculated using the NRTL activity coefficient model (see Eq. (4.36)). For the PRSV equation of state the MHV2 model parameters q_1 and q_2 are -0.4347 and -0.003654, respectively [78]. One can show that Eq. (4.32) has two roots, a positive and a negative one. The positive root must be chosen as ε is always positive by definition, i.e., $\varepsilon = a / (bRT)$. Parameter a in Eq. (4.27) can then be calculated using the definition $\varepsilon = a / (bRT)$.

To calculate the fugacity coefficient $\hat{\Phi}_i$ for each component i (the hat sign denotes the fugacity coefficient of component i in a mixture) one can use [110]

$$\ln \hat{\Phi}_i = \frac{b_i}{b} (Z - 1) - \ln (Z - b) - \frac{1}{2\sqrt{2}} \bar{\varepsilon}_i \ln \frac{Z + \left(1 + \sqrt{2}\right) B}{Z + \left(1 - \sqrt{2}\right) B}, \tag{4.33}$$

where [110]

$$\bar{\varepsilon}_i = \frac{q_1 \varepsilon_i + q_2 \left(\varepsilon^2 + \varepsilon_i^2\right) + \ln (b/b_i) + (b_i/b) - 1}{q_1 + 2 q_2 \varepsilon}, \tag{4.34}$$

and where $Z = pv / (RT)$ is the compressibility factor. The compressibility factor Z is a root of the following dimensionless form of the Peng-Robinson equation of state [110, 118]:

$$Z^3 - (1 - B) Z^2 + \left(A - 2B - 3B^2\right) Z - B \left(A - B - B^2\right) = 0, \tag{4.35}$$

where $A = ap / (RT)^2$ and $B = bp / (RT)$. The smallest positive root of the equation of state represents the liquid phase compressibility factor and the largest one represents the vapor phase compressibility factor. The value of $\hat{\Phi}_i$ for the smallest value of Z viz., $\hat{\Phi}_i^l$ and the value of $\hat{\Phi}_i$ for the largest value of Z viz., $\hat{\Phi}_i^g$ are used in

Eq. (4.26).

Table 4.1.: Critical properties of CO_2 and H_2O

Component	T_c [K]	P_c [Pa]	ω [-]	κ_1 (PRSV, Eq. (4.29))
CO_2 (1)	304.10	73.7	0.23894	0.04285
H_2O (2)	647.30	221.2	0.344	-0.06635

4.4.2. NRTL activity coefficient model for a binary mixture

The NRTL model [135] is implemented for the estimation of excess Gibbs energy g^E [126] of the solution and the activity coefficients γ_i [126] of the individual components ($i=1$ denotes CO_2 and $i=2$ denotes water) in Eq. (4.34), i.e.,

$$\frac{g^E}{RT} = x_1 x_2 \left(\frac{\tau_{21} G_{21}}{x_1 + x_2 G_{21}} + \frac{\tau_{12} G_{12}}{x_2 + x_1 G_{12}} \right), \tag{4.36}$$

$$\ln \gamma_1 = (x_2)^2 \left(\tau_{21} \left(\frac{G_{21}}{x_1 + x_2 G_{21}} \right)^2 + \frac{\tau_{12} G_{12}}{(x_2 + x_1 G_{12})^2} \right), \tag{4.37}$$

$$\ln \gamma_2 = (x_1)^2 \left(\tau_{12} \left(\frac{G_{12}}{x_2 + x_1 G_{12}} \right)^2 + \frac{\tau_{21} G_{21}}{(x_1 + x_2 G_{21})^2} \right), \tag{4.38}$$

where G_{ij} are the binary interaction parameters and are calculated as

$$G_{12} = \exp\left(-\alpha_{12} \tau_{21}\right), \, G_{21} = \exp\left(-\alpha_{12} \tau_{12}\right),$$
$$\tau_{12} = \Delta G_{12} / (RT), \, \tau_{21} = \Delta G_{21} / (RT). \tag{4.39}$$

In this work ΔG_{12} and ΔG_{21} are proposed to be linear functions of the temperature and salt mole fraction, i.e.,

$$\Delta G_{12} = \left(\Delta G_{12}^0 + \Delta G_{12}^1 x_{\text{salt}}\right) + \left(\Delta G_{12}^2 + \Delta G_{12}^3 x_{\text{salt}}\right) T,$$
$$\Delta G_{21} = \left(\Delta G_{21}^0 + \Delta G_{21}^1 x_{\text{salt}}\right) + \left(\Delta G_{21}^2 + \Delta G_{21}^3 x_{\text{salt}}\right) T, \tag{4.40}$$

where x_{salt} is the mole fraction of NaCl in the liquid phase. All ΔG_{ij}^k appearing above are free parameters in the optimization procedure (see Eq. (4.41)). In ΔG_{ij}, the subscripts $i, j=1$ denote carbon dioxide, whereas $i, j=2$ denote the pseudo-component brine, which is treated as a single component. For the VLE calculation the value of the nonrandomness parameter α_{12} in Eq. (4.39) is set to the constant value of 0.3 [136].

4.4.3. Objective function and optimization

All eight parameters ΔG_{ij} of the model are optimized by fitting the model to the experimental VLE data of CO$_2$-brine system. The Objective Function for the optimization of the NRTL parameters is defined as

$$OF\left(\Delta G_{12}^0, \Delta G_{21}^0, \Delta G_{12}^1, \Delta G_{21}^1, \Delta G_{12}^2, \Delta G_{21}^2, \Delta G_{12}^3, \Delta G_{21}^3\right) =$$

$$\frac{1}{N_d}\sum_{i=1}^{N_d}\frac{\left|x_{\mathrm{CO_2},i}^{exp} - x_{\mathrm{CO_2},i}^{cal}\right|}{x_{\mathrm{CO_2},i}^{exp}}. \quad (4.41)$$

Here $N_d = 161$ is the number of data points, $x_{\mathrm{CO_2}}$ is the mole fraction of CO$_2$ in the liquid phase. The superscripts '*exp*' and '*cal*' denote the experimental and calculated values, respectively. The experimental VLE data of the CO$_2$-water-NaCl system of references [141, 88, 10] were used in this study. The experimental data are within the temperature range of 278.22 K to 473.65 K and the pressure range of 4.65 bar to 709.28 bar.

4.4.4. Correction parameters of the liquid density

To make a correction to the liquid density predicted by the equation of state, generally the volume shift parameters are used [117], which are deined by the following equation

$$v^{exp} = v^{cal} + \sum_{i=1}^{N_c} x_i v_{c,i}, \quad (4.42)$$

where $v_{c,i}$ [m^3/mol] is the volume shift parameter of component i and must be obtained by fitting the above equation to the experimental data, v^{cal} [m^3/mol] is the specific volume of the mixture calculated by the equation of state, Eq. (4.27), and v^{exp} [m^3/mol] is the experimental specific volume. It is shown in [117] that adding shift parameters does not affect the phase equilibrium condition Eq. (4.26) and therefore optimization (4.41) leads to the same result for ΔG_{ij}^k. To calculate the volume shift parameters, the data published by Hebach et al. [73] are used, who report the density of liquid water in equilibrium with CO$_2$ in the temperature range of 283.01-333.02 K and pressure range of 10.9-306.6 bar. As the mole fraction of the aqueous phase is not reported by Hebach et al., first the mole fractions are calculated using the optimized thermodynamic model and then the liquid phase compositions are used to calculate the liquid compressibility factor at constant temperature and pressure. The specific volume of the liquid phase can be calculated as $v^{cal} = ZRT/p$.

The objective function for the optimization of the volume shift can be defined as

$$OF\left(v_{c,1}^0, v_{c,1}^1, v_{c,2}^0, v_{c,2}^1\right) =$$
$$\frac{1}{N_d}\sum_{i=1}^{N_d}\left(\left|\frac{x_{\text{CO}_2,i}M_{\text{CO}_2} + x_{\text{water},i}M_{\text{water}} + x_{\text{salt},i}M_{\text{salt}}}{v_i^{cal}} - \rho_i^{exp}\right|/\rho_i^{exp}\right). \quad (4.43)$$

It is assumed that $v_{c,i}$ in Eq. (4.42) are linear functions of the temperature $v_{c,1} = v_{c,1}^0 + v_{c,1}^1 T$ and $v_{c,2} = v_{c,2}^0 + v_{c,2}^1 T$. Moreover, M_{CO_2}, M_{water}, and M_{salt} [kg/mol] are the molecular weight of CO_2, water, and NaCl, respectively, x_{CO_2}, x_{water}, x_{salt} are the mole fractions of CO_2, water, and NaCl in the aqueous phase, respectively, and ρ_i^{exp} is the experimental value of the density in [kg/m3], $N_d = 203$ is the number of data points that are found in the literature. The four parameters obtained from minimizing Eq. (4.43) are denoted by c_i^0, c_i^1.

4.4.5. Equilibrium results

The procedure described above was implemented in Matlab. Table 4.1 gives the standard physical parameters of CO_2 and water. Table 4.2 gives the optimized values of the binary interaction parameters of NRTL based on the experimental results referenced above. Using these parameters one can predict the solubility of CO_2 in the pressure range of 0.98-101 bar, temperature range of 313.14-473.65 K and salt mole fraction range between 5.46×10^{-6} - 9.74×10^{-2}. Table 4.3 gives the optimized volume shift parameters, which are to be used in the calculation of the liquid molar concentrations and of the aqueous density. For the gas concentrations and density the volume shift parameters have only a negligible effect. For the pressure range 0.98-101 bar in the indicated temperature and concentration ranges the model is accurate within 4%. Figure 4.2 shows the CO_2 mole fraction in the brine as a function of NaCl mole fraction at 483 K and 700 bar. The drawn curve represents the calculations and the open circles represent data obtained by [48], which is expected to be close to experimental reality. Duan made a dedicated model and calibrated it against numerous experimental data for the carbon-dioxide-water-NaCl system. Duan's model is only valid for the calculation of the VLE of this carbon dioxide-water-NaCl system, but it is accurate. The agreement of CO_2 solubility between the described model and Duan's for a few data points at this higher pressure range is acceptable within 22%. The author believes that this model can be used as a first estimate with similar errors in the pressure range $600 - 800$ bar and a variety of temperatures and concentrations. The described methodology is more general, in the sense that it can also be used for other systems, e.g., for systems containing hydrocarbons. Figure 4.2 shows that the solubility of CO_2 decreases with increasing salt concentrations. Figure 4.3 plots the liquid phase density as a function of the salt concentration at 700 bar and 483 K. It can be observed that the liquid density increases together with salt concentration. The optimized volume shift values and the objective function value are given in Table 4.3.
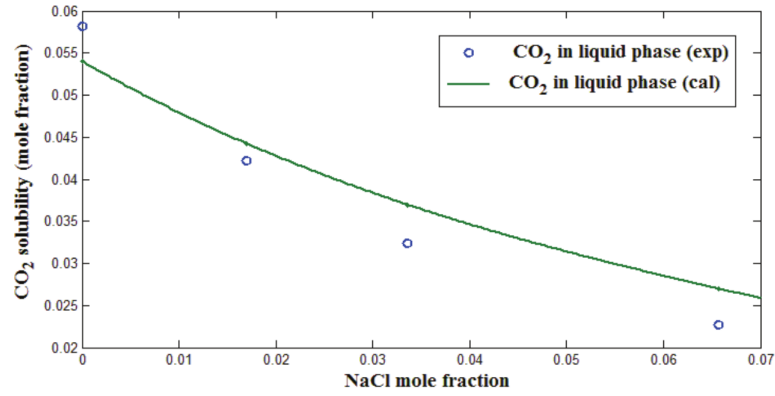
Figure 4.2.: Equilibrium mole fraction of CO_2 in the aqueous phase at 483 K and 700 bar. The drawn curve represents the calculations. The open circles are obtained from Duan's model.
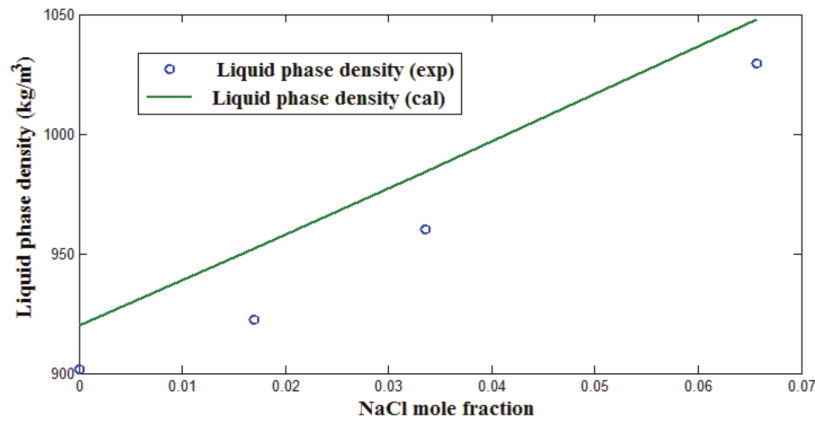
Figure 4.3.: Aqueous phase density at 483 K and 700 bar. The drawn curve represents the calculations. The open circles are obtained from Duan's model.

4.5. Negative flash for a gas-liquid system

To simplify the description of negative flash, in this section a two-phase gas-liquid system is considered. For gas-liquid equilibrium, Eq. (4.21) disappears because of the lack of a solid phase and Rachford-Rice equation (4.20) simplifies to

$$F\left(\Psi^g\right) \equiv \sum_{i=1}^{N_c} \frac{x_i^t\left(K_i - 1\right)}{1 + \Psi^g\left(K_i - 1\right)} = 0, \tag{4.44}$$

where $K_i = x_i^g/x_i^l = \hat{\Phi}_i^l/\hat{\Phi}_i^g$ originates from K_i^{gl} with superscript gl omitted (see Eq. (4.25)). Whitson and Michelsen [169] show that the only physical solution for Eq.

Table 4.2.: Fitted parameters of the NRTL model. Subscript 1 is for CO_2 and subscript 2 is for water

ΔG_{12}^0 [J/mol]	ΔG_{12}^1 [J/mol/K]	ΔG_{12}^2 [J/mol]	ΔG_{12}^3 [J/mol/K]	$\frac{100}{N} \sum_{i=1}^N \frac{\left| x_{CO_2,i}^{exp} - x_{CO_2,i}^{cal} \right|}{x_{CO_2,i}^{exp}}$
-7327.1	68.8	39.7	153.6	
ΔG_{21}^0 [J/mol]	ΔG_{21}^1 [J/mol]	ΔG_{21}^2 [J/mol]	ΔG_{21}^3 [J/mol]	4.04 %
7694.3	-159.5	-1.7	82.5	

Table 4.3.: Optimized volume shift values for CO_2 and water for the PRSV-MHV2 equation of state using CO_2-water and CO_2-brine mixture density data. Subscript 1 is for CO_2 and subscript 2 is for water

c_1^0 [m^3/mol]	c_1^1 [m^3/mol/K]	c_2^0 [m^3/mol]	c_2^1 [m^3/mol/K]	Minimized O.F. value
1.496×10^{-6}	4.706×10^{-9}	-1.072×10^{-7}	-1.012×10^{-8}	14.9 %

(4.44) lies between Ψ_{min}^g and Ψ_{max}^g, which are given by

$$\Psi_{min}^g = \frac{1}{1 - K_{i,max}} \text{ and } \Psi_{max}^g = \frac{1}{1 - K_{i,min}}. \tag{4.45}$$

The values of $K_{i,max}$ and $K_{i,min}$ are calculated in the flash calculation procedure described in the previous section. The plots of $F(\Psi^g)$ for CO_2-water mixture with three different overall molar fractions, i.e., (a) 50% CO_2, (b) 1% CO_2, and (c) 99% CO_2 are shown in Fig. 4.4. The value of the Rachford-Rice function for the equimolar mixture of CO_2 and water (dashed-dotted curve) is zero at $\Psi^g = 0.508$, which indicates that the system is in two phase equilibrium. For the mixture with 1% CO_2, the solution to $F(\Psi^g) = 0$ is $\Psi^g = -0.0145$, which is a negative value and therefore physically impossible, even though it satisfies the mass balance and equilibrium conditions. Another physically impossible solution is realized for the mixture with 99% CO_2 with $\Psi^g = 1.0312$, which is larger than one. In both cases, the system is in a single phase region; the negative value for the molar gas fraction, i.e., $\Psi^g < 0$ indicates a liquid phase and a value larger than one, i.e., $\Psi^g > 1$ indicates a gaseous phase. Consequently, the equilibrium mole fractions calculated from Eq. (4.19) and Eq. (4.15) for the liquid x_i^l and vapor x_i^g phase are not physically meaningful, even though the mass balance, i.e.,

$$x_i^t = \Psi^g x_i^g + (1 - \Psi^g) x_i^l, \tag{4.46}$$

is satisfied.
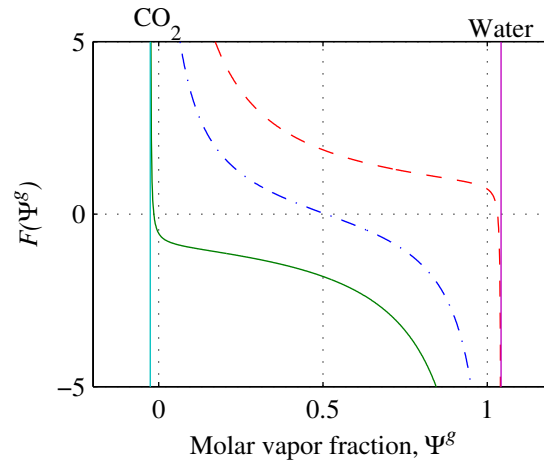
Figure 4.4.: Rachford-Rice function for a mixture of water and CO_2 at 483 K and 700 bar with the total molar composition of (a) 50% CO_2 in water shown in the dashed-dotted curve; (b) 1% CO_2 in water shown in the solid curve; (c) 99% CO_2 in water shown in the dashed curve. The vertical line on the right side shows Ψ^g_{max}, which corresponds to the water K-value K_{water}; the vertical line on the left side shows Ψ^g_{min}, which corresponds to the CO_2 K-value K_{CO_2}.

4.6. Molar and volumetric concentrations

In this section, the equations that give the volumetric properties as a function of molar phase fractions are derived, including of molar phase fractions less than zero or larger than one. The reader is advised to find the basic definition of the parameters in Fig. 4.1 and Section 4.3.

Using an equation of state (here PRSV), the molar concentration of each phase C^α is calculated by

$$C^\alpha (p, T, x_i^\alpha) = \frac{p}{Z^\alpha (p, T, x_i^\alpha) \, RT}, \tag{4.47}$$

where Z^α is the compressibility factor of phase α and is calculated as a function of pressure p, temperature T, and composition x_i^α using the equation of state, i.e., Eq. (4.35). Note that C^α is always positive. Starting from the definition of saturation, i.e., Eq. (4.4), (see also Fig. 4.1), one can write

$$S^\alpha = \frac{V^\alpha}{V^t}, \tag{4.48}$$

where $V^\alpha = N^\alpha / C^\alpha = \Psi^\alpha N^t / C^\alpha$ and $V^t = \sum_\alpha V^\alpha = N^t \sum_\alpha (\Psi^\alpha / C^\alpha)$, which are

replaced in the definition of S^α in Eq. (4.48) to obtain

$$S^\alpha = \frac{\Psi^\alpha / C^\alpha}{\sum_\alpha \left(\Psi^\alpha / C^\alpha \right)}. \tag{4.49}$$

For a two-phase vapor-liquid equilibrium, Eq. (4.49) can be simplified to

$$S^g = \frac{\Psi^g / C^g}{\Psi^g / C^g + (1 - \Psi^g) / C^l}. \tag{4.50}$$

It was shown in Section 4.5 that the flash calculation for a mixture in a single phase region sometimes converges to nonphysical values, i.e., to $\Psi^g < 0$ or to $\Psi^g > 1$. It must be pointed out that even though the flash scheme is mass conservative, the calculated hypothetical molar phase fraction (Ψ^α) and hypothetical vapor and liquid compositions (x_i^α) cannot be used in Eq. (4.49) for the calculation of volumetric phase fraction. This is so because these equations are only applicable to multiphase equilibrium mixtures within $0 \leq \Psi^\alpha \leq 1$. For a two-phase vapor-liquid system, when the calculated Ψ^g is negative or higher than one, it can be suggested [74] that the molar density in both hypothetical phases is equal to the molar density of the single phase $C^{t,\alpha}$, i.e.,

- $\Psi^g < 0$ or single liquid phase ($\alpha = l$); the molar density of the system is calculated as

$$C^g = C^l = C^{t,l} \left(p, T, x_i^t \right) = \frac{p}{Z^l \left(p, T, x_i^t \right) RT}, \tag{4.51}$$

    where Z^l is the single phase compressibility factor, which is calculated using the equation of sate, i.e., Eq (4.35).

- $\Psi^g > 1$ or single gas phase ($\alpha = g$); the molar density of the system is calculated as

$$C^g = C^l = C^{t,g} \left(p, T, x_i^t \right) = \frac{p}{Z^g \left(p, T, x_i^t \right) RT}, \tag{4.52}$$

    where in both cases the total mole fraction is calculated using Eq. (4.46).

Substituting the molar densities of Eqs. (4.51)-(4.52) in Eq. (4.50), one obtains

$$S^g = \begin{cases} \frac{\Psi^g / C^g}{\Psi^g / C^g + (1 - \Psi^g) / C^l}, & 0 \leq \Psi^\alpha \leq 1 \\ \Psi^g, & \Psi^g < 0 \text{ or } \Psi^g > 1. \end{cases} \tag{4.53}$$

Note that the second line of the above equation is obtained from Eq. (4.50) for the special case that $C^g = C^l$. Eq. (4.46) shows the total composition of the mixture as a function of equilibrium compositions and molar phase fractions (Ψ^α). However, to be able to use these thermodynamic relations in the formulation of two-phase fluid flow, one needs to have a relation that gives the total mole fraction of the mixture

in terms of the volumetric phase fractions (or saturation S^α). To obtain the total composition of the mixture (x_i^t) in terms of the volumetric phase fractions (S^α), one can start by writing the definition of the total composition (see Fig. 4.1), i.e.,

$$x_i^t = n_i^t / N^t = \left(\sum_\alpha n_i^\alpha \right) / \left(\sum_\alpha N^\alpha \right), \tag{4.54}$$

where $n_i^\alpha = x_i^\alpha C^\alpha V^\alpha$, $N^\alpha = C^\alpha V^\alpha$, and $V^\alpha = S^\alpha V^t$ can be substituted in Eq. (4.54) to obtain

$$x_i^t = \frac{\sum_\alpha x_i^\alpha C^\alpha S^\alpha}{\sum_\alpha C^\alpha S^\alpha}. \tag{4.55}$$

For a two-phase vapor-liquid equilibrium, Eq. (4.55) reduces to

$$x_i^t = \frac{x_i^g C^g S^g + x_i^l C^l (1 - S^g)}{C^g S^g + C^l (1 - S^g)}. \tag{4.56}$$

By combining Eqs. (4.46), (4.53), and (4.56), the total composition can be written as a function of S^g that is applicable in both single and two-phase regions:

$$x_i^t = \begin{cases} \frac{x_i^g C^g S^g + x_i^l C^l (1 - S^g)}{C^g S^g + C^l (1 - S^g)}, & 0 \leq S^g \leq 1 \\ S^g x_i^g + (1 - S^g) x_i^l & S^g < 0 \text{ or } S^g > 1 \end{cases}. \tag{4.57}$$

Note that the second line of Eq. (4.57) comes from the fact that in the single phase region, $C^l = C^g = C^{t,\alpha}$, where α is g when $S^g \geqslant 1$ or l when $S^g \leqslant 0$. Similarly, one can derive the following relation for c_i^t (the molar concentration of component i in the mixture):

$$c_i^t = x_i^g C^g S^g + x_i^l C^l (1 - S^g), \tag{4.58}$$

where

$$C^g = \begin{cases} \frac{p}{Z^l \left(p, T, x_i^t \right) RT}, & S^g \leq 0 \\ \frac{p}{Z^g \left(p, T, x_i^g \right) RT}, & S^g > 0 \end{cases},$$

and

$$C^l = \begin{cases} \frac{p}{Z^g \left(p, T, x_i^t \right) RT}, & S^g \geq 1 \\ \frac{p}{Z^l \left(p, T, x_i^l \right) RT}, & S^g < 1 \end{cases},$$

where x_i^g and x_i^l are the equilibrium compositions in the gas and liquid phases calculated in a negative flash procedure (see Section 4.5), respectively, and x_i^t is the total mole fraction of mixture calculated by Eq. (4.57).

4.7. Modeling two-phase flow

The two-phase flow equations are written as (for i between 1 and N_c)

$$\frac{\partial \left(\varphi c_i^t\right)}{\partial t} + \nabla . \left(\mathbf{u}^g x_i^g C^g + \mathbf{u}^l x_i^l C^l\right) + \nabla . \left(-\varphi \mathcal{D}_i^g S^g \nabla \left(x_i^g C^g\right) - \varphi \mathcal{D}_i^l \left(1 - S^g\right) \nabla \left(x_i^l C^l\right)\right) = 0, \tag{4.59}$$

where $c_i^t = x_i^g C^g S^g + x_i^l C^l \left(1 - S^g\right)$ [mol/m^3] is the molar concentration of component i in the overall mixture, φ is the porosity of the porous medium, $\mathbf{u}^\alpha$ [m/s] is the Darcy velocity vector of phase α $(\alpha = g, l)$, $\mathcal{D}_i^\alpha$ [m^2/s] is the Fickian diffusivity of component i in the phase α. The Darcy velocity is calculated as

$$\mathbf{u}^\alpha = -\frac{k k_{r\alpha}}{\mu^\alpha} \left(\nabla p^\alpha - \rho^\alpha \mathbf{g}\right), \tag{4.60}$$

where $k_{r\alpha}$ is the relative permeability of phase α and is usually a function of S^g, k [m^2] is the absolute permeability of the porous medium, μ^α [Pa.s] is the viscosity of phase α, p^α [Pa] is the pressure of phase α, ρ^α [kg/m^3] is the mass density of phase α, and $\mathbf{g}$ [m/s^2] is gravity acceleration vector. The difference between the gas phase and liquid phase pressure is the capillary pressure, which is usually a function of S^g, i.e.,

$$p_c = p_c \left(S^g\right) = p^g - p^l. \tag{4.61}$$

The equations for each single-phase region, i.e., $S^g < 0$ or $S^g > 1$ read (for i between 1 and N_c and α is either g or l)

$$\frac{\partial \left(\varphi c_i^t\right)}{\partial t} + \nabla . \left(\mathbf{u}^{t,\alpha} x_i^t C^{t,\alpha}\right) + \nabla . \left(-\varphi \mathcal{D}_i^\alpha \nabla \left(x_i^t C^{t,\alpha}\right)\right) = 0, \tag{4.62}$$

where $\mathbf{u}^{t,\alpha}$ [m/s] is the velocity of the single phase α and is calculated by

$$\mathbf{u}^{t,\alpha} = -\frac{k}{\mu^\alpha} \left(\nabla p^\alpha - \rho^\alpha \mathbf{g}\right), \tag{4.63}$$

and $C^{t,\alpha}$ [mol/m^3] is the molar density of the single phase and is calculated by

$$C^{t,\alpha} = \frac{p^\alpha}{Z^\alpha \left(p^\alpha, T, x_i^t\right) RT}, \quad \alpha = g, l. \tag{4.64}$$

By replacing x_i^t from Eq. (4.57) in Eq. (4.62), the latter reads

$$\frac{\partial \left(\varphi c_i^t\right)}{\partial t} + \nabla.\left(S^g \mathbf{u}^{t,\alpha} x_i^g C^{t,\alpha} + (1 - S^g)\, \mathbf{u}^{t,\alpha} x_i^l C^{t,\alpha}\right) =$$
$$\nabla.\left(\varphi \mathcal{D}_i^\alpha S^g \nabla \left(x_i^g C^{t,\alpha}\right) + \varphi \mathcal{D}_i^\alpha (1 - S^g) \nabla \left(x_i^l C^{t,\alpha}\right) + \varphi \mathcal{D}_i^\alpha C^{t,\alpha} \left(x_i^g - x_i^l\right) \nabla S^g\right),$$
$$(4.65)$$

with α being either g or l. By comparing the above equation with the two-phase flow equation, Eq. (4.59), it can be observed that the extended single phase flow equation is similar to the two phase flow equation [1, 114], and can be merged into one equation valid for the whole single and two phase regions. This merge will be explained in the next section.

4.7.1. Convective flux

The convective fluxes for the single- (Eq. (4.65)) and two-phase (Eq. (4.59)) flow equations read

$$\mathbf{F}_{sp}^{conv} = S^g \mathbf{u}^{t,\alpha} x_i^g C^{t,\alpha} + (1 - S^g)\, \mathbf{u}^{t,\alpha} x_i^l C^{t,\alpha}, \tag{4.66}$$

$$\mathbf{F}_{tp}^{conv} = \mathbf{u}^g x_i^g C^g + \mathbf{u}^l x_i^l C^l, \tag{4.67}$$

where subscripts sp and tp indicate single-phase and two-phase, respectively. The Darcy velocities (Eq. (4.60) and (4.63)) can be substituted to obtain

$$\mathbf{F}_{sp}^{conv} = -\frac{kS^g}{\mu^\alpha} \left(\nabla p^\alpha - \rho^\alpha \mathbf{g}\right) x_i^g C^{t,\alpha} - \frac{k\left(1 - S^g\right)}{\mu^\alpha} \left(\nabla p^\alpha - \rho^\alpha \mathbf{g}\right) x_i^l C^{t,\alpha}, \tag{4.68}$$

$$\mathbf{F}_{tp}^{conv} = -\frac{kk_{rg}}{\mu^g} \left(\nabla p^g - \rho^g \mathbf{g}\right) x_i^g C^g - \frac{kk_{rl}}{\mu^l} \left(\nabla p^l - \rho^l \mathbf{g}\right) x_i^l C^l. \tag{4.69}$$

By comparing the two equations, a general equation can be proposed for the convective flux for the single and two phase regions that reads

$$\mathbf{F}^{conv} = -\frac{k\hat{k}_{rg}}{\hat{\mu}^g} \left(\nabla \hat{p}^g - \hat{\rho}^g \mathbf{g}\right) x_i^g \hat{C}^g - \frac{k\hat{k}_{rl}}{\hat{\mu}^l} \left(\nabla \hat{p}^l - \hat{\rho}^l \mathbf{g}\right) x_i^l \hat{C}^l, \tag{4.70}$$

$$\hat{p}_c = \hat{p}^g - \hat{p}^l. \tag{4.71}$$

where the value of each parameter is shown in Table 4.4. The hat sign is used on top of the parameters that are a function of saturation (S^g). Indeed, with definitions of Table 4.4, Eq. (4.70) can be used for both single and two phase regions. This is the achievement of the NegSat method.

4.7.2. Diffusive flux

The diffusive fluxes for the single- (Eq. (4.65)) and two-phase (Eq. (4.59)) flow equations read

$$-\mathbf{F}_{sp}^{diff} = \varphi \mathcal{D}_i^\alpha S^g \nabla \left(x_i^g C^{t,\alpha} \right) + \varphi \mathcal{D}_i^\alpha \left(1 - S^g \right) \nabla \left(x_i^l C^{t,\alpha} \right) + \varphi \mathcal{D}_i^\alpha C^{t,\alpha} \left(x_i^g - x_i^l \right) \nabla S^g, \tag{4.72}$$

$$-\mathbf{F}_{tp}^{diff} = \varphi \mathcal{D}_i^g S^g \nabla \left(x_i^g C^g \right) + \varphi \mathcal{D}_i^l \left(1 - S^g \right) \nabla \left(x_i^l C^l \right). \tag{4.73}$$

Here there is an extra term with gas saturation gradient in the single phase diffusive flux which is called extra-diffusion by Panfilov [114] and is explained as the diffusion between the single-phase zone and the two-phase zone through the PT-interface (PT = phase transition). The following general term is proposed for the diffusive flux for both single and two-phase flow:

$$-\mathbf{F}^{diff} = \varphi \hat{\mathcal{D}}_i^g S^g \nabla \left(x_i^g \hat{C}^g \right) + \varphi \hat{\mathcal{D}}_i^l \left(1 - S^g \right) \nabla \left(x_i^l \hat{C}^l \right) + \varphi \hat{\mathcal{D}}_i^\alpha \hat{C}^{t,\alpha} \left(x_i^g - x_i^l \right) \nabla S^g, \tag{4.74}$$

where the parameters are shown in Table 4.4. Once again, $\alpha = g$ when $S^g \geq 1$ or $\alpha = l$ when $S^g \leq 0$. The value of S^g can be used with Eq. (4.57) to calculate the total composition. The values of $S^g > 1$ or $S^g < 0$ sometimes are considered unphysical while in fact they have a physical interpretation. The value $0 < S^g < 1$ in the two-phase region is interpreted as the saturation and in the single phase region, combined with the equilibrium composition obtained from the negative flash, ($S^g \geq 1$ or $S^g \leq 0$) is interpreted as a measure of total mole fraction of the single phase region (see Eq. (4.57)).

4.7.3. General formulation

By substituting the general convective and diffusive fluxes, i.e., Eqs. (4.70 & 4.74) in the mass conservation equation, i.e.,

$$\frac{\partial \left(\varphi c_i^t \right)}{\partial t} + \nabla \cdot \left(F^{conv} + F^{diff} \right) = 0, \tag{4.75}$$

the final equation, which is applicable to the whole domain, is written as

$$\frac{\partial}{\partial t}\left[\varphi\left(x_i^g C^g S^g + x_i^l C^l\left(1 - S^g\right)\right)\right] +$$

$$\nabla.\left(-\frac{\hat{k}_{rg}k}{\hat{\mu}^g}\left(\nabla\hat{p}^g - \hat{\rho}^g\mathbf{g}\right)x_i^g\hat{C}^g - \frac{\hat{k}_{rl}k}{\hat{\mu}^l}\left(\nabla\hat{p}^l - \hat{\rho}^l\mathbf{g}\right)x_i^l\hat{C}^l\right) +$$

$$-\nabla.\left(\varphi\hat{\mathcal{D}}_i^g S^g\nabla\left(x_i^g\hat{C}^g\right) + \varphi\hat{\mathcal{D}}_i^l\left(1 - S^g\right)\nabla\left(x_i^l\hat{C}^l\right) + \varphi\hat{\mathcal{D}}_i^\alpha\hat{C}^{t,\alpha}\left(x_i^g - x_i^l\right)\nabla S^g\right),$$

$$\tag{4.76}$$

where the parameters are clearly explained in Table 4.4.

Table 4.4.: Values of the parameters in the generalized convective and diffusive terms of the two phase flow equation. Note that x_i^t is a function of S^g and is calculated by Eq. (4.57)

Parameter	$S^g < 0$	$0 \leq S^g \leq 1$	$S^g > 1$
$\hat{k}_{rg}$	S^g	k_{rg}	S^g
$\hat{k}_{rl}$	$1 - S^g$	k_{rl}	$1 - S^g$
$\hat{p}^g$	p^l	p^g	p^g
$\hat{p}^l$	p^l	p^l	p^g
$\hat{\mu}^g$	μ^l	μ^g	μ^g
$\hat{\mu}^l$	μ^l	μ^l	μ^g
$\hat{C}^g$	$\frac{p^l}{Z^l\left(p^l,T,x_i^t\right)RT}$	$\frac{p^g}{Z^g\left(p^g,T,x_i^g\right)RT}$	$\frac{p^g}{Z^g\left(p^g,T,x_i^t\right)RT}$
$\hat{C}^l$	$\frac{p^l}{Z^l\left(p^l,T,x_i^t\right)RT}$	$\frac{p^l}{Z^l\left(p^l,T,x_i^l\right)RT}$	$\frac{p^g}{Z^g\left(p^g,T,x_i^t\right)RT}$
$\hat{M}^g$	$\sum_i x_i^t M_i$	$\sum_i x_i^g M_i$	$\sum_i x_i^t M_i$
$\hat{M}^l$	$\sum_i x_i^t M_i$	$\sum_i x_i^l M_i$	$\sum_i x_i^t M_i$
$\hat{P}_c$	0	P_c	0
$\hat{\mathcal{D}}_i^g$	$\mathcal{D}_i^l$	$\mathcal{D}_i^g$	$\mathcal{D}_i^g$
$\hat{\mathcal{D}}_i^l$	$\mathcal{D}_i^l$	$\mathcal{D}_i^l$	$\mathcal{D}_i^g$
$\hat{\mathcal{D}}_i^\alpha$	$\mathcal{D}_i^l$	0	$\mathcal{D}_i^g$
$\hat{C}^{t,\alpha}$	$\frac{p^l}{Z^l\left(p^l,T,x_i^t\right)RT}$	0	$\frac{p^g}{Z^g\left(p^g,T,x_i^t\right)RT}$

4.8. NegSat method for the CO$_2$-water-NaCl system

For the three-phase ternary mixture of CO$_2$-water-NaCl, first the mixture is separated into an immobile solid phase which consists of pure NaCl, and a mobile gas-liquid mixture, as shown in Fig. 4.5. Then the NegSat method is applied to model the mobile gas-liquid phases and include the effect of salt precipitation on the porosity, permeability, and phase equilibrium of the mixture. The precipitation

of the solid NaCl, with a solid saturation S^s decreases the porosity of the porous medium from the initial porosity φ_0 to a new porosity φ, which is calculated by

$$\varphi = \varphi_0 \left(1 - S^s\right). \tag{4.77}$$

This porosity change also affects the permeability of the porous medium k [m^2], which can be related to the porosity change using the Kozeny-Carman equation [31, 92, 93]:

$$\frac{k}{k_0} = \frac{\varphi^3/\left(1 - \varphi\right)^2}{\varphi_0^3/\left(1 - \varphi_0\right)^2}, \tag{4.78}$$

where k_0 [m^2] is the original permeability of the porous medium. Verma and Pruess [163] assume that when the porosity is reduced to a certain fraction (φ_r) of the initial porosity, i.e., $\varphi = \varphi_r \varphi_0$, permeability is reduced to zero. They propose the following relation

$$\frac{k}{k_0} = \theta^2 \frac{1 - \Gamma + \Gamma/\omega^2}{1 - \Gamma + \Gamma\left[\theta/\left(\theta + \omega - 1\right)\right]^2}, \tag{4.79}$$

where $\theta = \frac{1 - S^s - \varphi_r}{1 - \varphi_r}$ and $\omega = 1 + \frac{1/\Gamma}{1/\varphi_r - 1}$. Based on the study of Xu et al. [171], Pruess and Müller [131] suggested parameters $\Gamma = 0.8$ and $\varphi_r = 0.9$, which for practical purposes can be fit by the following power law function:

$$\frac{k}{k_0} = \left(\frac{\varphi/\varphi_0 - \varphi_r}{1 - \varphi_r}\right)^2. \tag{4.80}$$

Fig. 4.5-a shows the three phase fluid-solid equilibrium for the system of CO$_2$-water-NaCl. The fluid phase can be a single phase gas, a single phase liquid, or a two-phase gas-liquid system. In Fig. 4.5-b, the fluid phase with the saturation $1 - S^s$ is separated from the solid phase with saturation S^s. The total molar concentration of each component c_i^t in the *two-phase* fluid-solid system can be calculated by Eq. (4.9), i.e.,

$$c_i^t = (1 - S^s)c_i^f + S^s x_i^s C^s, \tag{4.81}$$

where c_i^f is the molar concentration of component i in the fluid (gas+liquid) phase and x_i^s is the mole fraction of component i in the solid phase, and C^s is the molar concentration of the solid phase (here pure NaCl). For the fluid phase, a gas-liquid negative flash calculation procedure is used to find the gas S^g and liquid S^l saturations. Then, the molar concentration of each component i in the fluid phase (both single phase or two-phase) is calculated by Eq. (4.58), i.e.,

$$c_i^f = x_i^g \hat{C}^g S^g + x_i^l \hat{C}^l \left(1 - S^g\right). \tag{4.82}$$

Here, the hat sign is used on top of the concentrations to show that they are a function of gas saturation S^g. By combining Eq. (4.81) and Eq. (4.82), one obtains

$$c_i^t = (1 - S^s)\left(x_i^g \hat{C}^g S^g + x_i^l \hat{C}^l (1 - S^g)\right) + S^s x_i^s C^s. \tag{4.83}$$

One should note that the value of the solid saturation S^s is always between zero and one. A simplified negative flash scheme is used to calculate the gas and liquid equilibrium compositions, i.e. x_i^g and x_i^l, respectively. Here it is assumed that the solid phase is pure NaCl, i.e.,

$$x_{CO_2}^s = 0, \ x_{water}^s = 0, \ x_{salt}^s = 1. \tag{4.84}$$

For the mixture of CO_2-brine, the vapor and liquid equilibrium compositions of water and CO_2 are functions of pressure p, temperature T, and mole fraction of salt in the brine (x_{salt}^l), i.e.,

$$x_{CO2,eq}^l = x_{CO_2}^l\left(p, T, x_{salt}^l\right) \ \text{and} \ x_{CO2,eq}^g = x_{CO_2}^g\left(p, T, x_{salt}^l\right). \tag{4.85}$$

The negative flash procedure and the calculation of gas and liquid mole fractions are explained in Appendix D. The equilibrium mole fractions of component $i=$ CO_2, H_2O, and NaCl in the gas and liquid phase are given by

$$x_i^g = \left\{x_{CO2,eq}^g, \quad x_{water,eq}^g, \quad 0\right\}, \tag{4.86}$$

$$x_i^l = \left(1 + \frac{x_{salt}^l}{1 - x_{salt}^l}x_{water,eq}^l\right)^{-1}\left\{x_{CO2,eq}^l, \quad x_{water,eq}^l, \quad \frac{x_{salt}^l}{1-x_{salt}^l}x_{water,eq}^l\right\}, \tag{4.87}$$

where $x_{water,eq}^g = 1 - x_{CO2,eq}^g$ and $x_{water,eq}^l = 1 - x_{CO2,eq}^l$, are the equilibrium mole fractions of CO_2-water mixture and are calculated by including the effect of salt mole fraction in brine (x_{salt}^l) on the binary interaction parameters of CO_2-water in the thermodynamic model (see Appendix D).

Using Eq. (4.83), the general flow equation for a one dimensional radial flow in a cylindrical coordinate disregarding the diffusion and capillary effect is written as

$$\varphi_0 \frac{\partial}{\partial t}\left((1 - S^s)\left(x_i^g \hat{C}^g S^g + x_i^l \hat{C}^l (1 - S^g)\right) + S^s x_i^s \hat{C}^s\right) +$$

$$+ \frac{1}{r}\frac{\partial}{\partial r}\left[r\left(-\frac{\hat{k}_{rg}k}{\hat{\mu}^g}x_i^g \hat{C}^g - \frac{\hat{k}_{rl}k}{\hat{\mu}^l}x_i^l \hat{C}^l\right)\frac{\partial p}{\partial r}\right] = 0 \tag{4.88}$$

where φ_0 is the initial porosity of the aquifer. The fractional flow function $\hat{f}^\alpha$ for
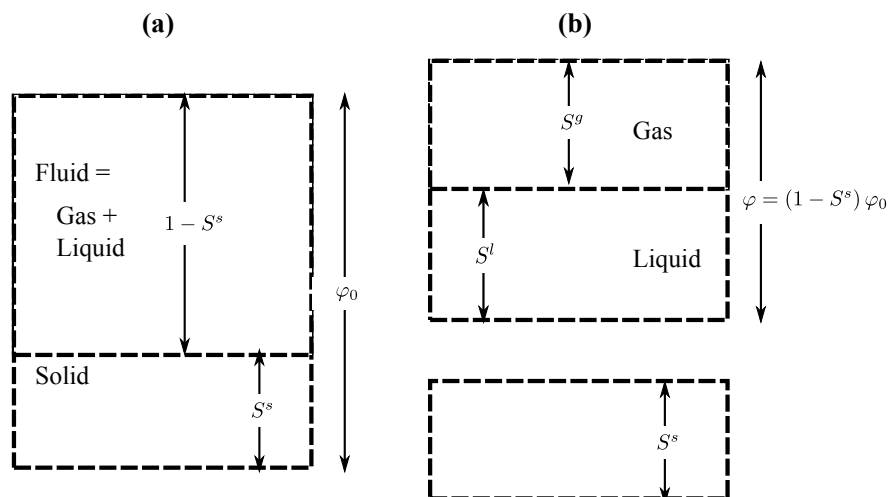
Figure 4.5.: (a) Solid-fluid equilibrium of CO_2-water-salt (left) and (b) the separation of solid salt from the fluid phase and separation of the fluid phase to vapor and liquid phases and its effect on the porosity (right)

the gas and liquid phases are defined as

$$\hat{f}^g = \frac{\hat{k}_{rg}/\hat{\mu}^g}{\hat{k}_{rl}/\hat{\mu}^l + \hat{k}_{rg}/\hat{\mu}^g} \text{ and } \hat{f}^l = 1 - \hat{f}^g, \quad (4.89)$$

which helps in simplifying Eq. (4.88) to

$$\varphi_0 \frac{\partial}{\partial t}\left((1 - S^s)\left(x_i^g \hat{C}^g S^g + x_i^l \hat{C}^l (1 - S^g)\right) + S^s x_i^s \hat{C}^s\right) +$$
$$+ \frac{1}{r}\frac{\partial}{\partial r}\left[ru\left(\hat{f}^g x_i^g \hat{C}^g + \hat{f}^l x_i^l \hat{C}^l\right)\right] = 0, \quad (4.90)$$

where u [m/s] is the Darcy velocity and is defined as

$$u = -k\left(\frac{\hat{k}_{rg}}{\hat{\mu}^g} + \frac{\hat{k}_{rl}}{\hat{\mu}^l}\right)\frac{\partial p}{\partial r}. \quad (4.91)$$

The relative permeability of the gas phase $(\hat{k}_{rg})$ is calculated by the Corey curve [35], which reads

$$\hat{k}_{rg} = \begin{cases} S^g & S^g < 0 \text{ or } S^g > 1 \\ (1 - S_*)^2 \left(1 - S_*^2\right), & 0 \leq S^g \leq 1 - S_c^l \\ 1 & 1 - S_c^l < S^g \leq 1 \end{cases}, \quad (4.92)$$

where $S_* = \frac{1 - S^g - S_c^l}{1 - S_c^l}$, S_c^l is the unmovable water saturation. For the liquid phase

($\hat{k}_{rl}$) the van Genuchten function [162] is used, i.e.,

$$\hat{k}_{rl} = \begin{cases} 1 - S^g & S^g < 0 \text{ or } S^g > 1 \\ \sqrt{S_*} \left(1 - \left(1 - S_*^{1/\lambda} \right)^\lambda \right)^2, & 0 \leq S^g \leq 1 - S_c^l \\ 0 & 1 - S_c^l < S^g \leq 1 \end{cases} \tag{4.93}$$

where $\lambda = 0.457$ [175].

To calculate the viscosity of the gas phase (μ^g), it is assumed that the effect of the small amount of evaporated water on the gas phase viscosity is negligible, i.e., the viscosity of the gas phase is equal to the viscosity of pure CO_2. The experimental gas phase viscosity data are used, which are reported for CO_2 in a wide range of pressure and temperature in reference [62]. For the liquid phase viscosity (μ^l), Bando et al. [11] reported that at high temperature, CO_2 dissolution in water has only a small effect on the viscosity of brine solution. Therefore, only the effect of NaCl mole fraction on the viscosity of the brine is considered. Mao and Duan [95] found a correlation for the ratio of the brine viscosity to the pure water viscosity using a wide range of experimental brine viscosity data at various temperatures, pressures, and salt concentrations. The viscosity of pure water is calculated using the correlations and data reported by Huber et al. [79]. The required density of pure water is calculated using the Industrial Formulation for the Thermodynamic Properties of Water and Steam (IAPWS-IF97) [164].

The pressure boundary conditions read

$$\begin{cases} \frac{\partial p}{\partial r} = \frac{-q_{inj}}{2\pi r_{well} H \rho_{inj} k \left(\hat{k}_{rl}/\hat{\mu}^l + \hat{k}_{rg}/\hat{\mu}^g \right)}, & r = r_{well}, \\ p = p_0, & r = L, \end{cases} \tag{4.94}$$

where q_{inj} [kg/s] is the injection mass flow rate, r_{well} [m] is the well radius, H [m] is the thickness of aquifer, ρ_{inj} [kg/m^3] is the mass density of the injection fluid, and p_0 [Pa] is the initial pressure of the aquifer. The concentration boundary conditions read

$$\begin{cases} x_i^t = x_{inj,i}^t, & r = r_{well}, \\ \frac{\partial x_i^t}{\partial r} = 0, & r = L, \end{cases}$$

where $x_{inj,i}^t$ is the mole fraction of the injected stream. The injected saturation S_{inj}^g is calculated by performing a flash calculation at injection temperature, pressure, and composition. In the next section, the details of the numerical method implemented for solving this problem will be explained.
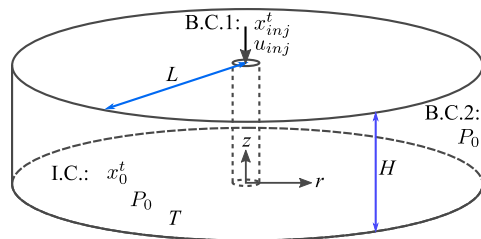
Figure 4.6.: A schematic representation of the aquifer, the initial (I.C.) and the boundary conditions (B.C.1 and B.C.2)

4.9. Numerical method

The system of three partial differential equations described by Eqs. (4.90) are discretized in space by using a first order implicit upwind cell-centered finite difference scheme. The subscript m is used to indicate the position of a grid point in space. The same non-uniform grid that is used by Pruess and Müller [131] will be used, which is finer near the injection well and is coarser near the external boundary. Superscript n is used to denote time, i.e., $t = n\Delta t$. The next steps are as follows:

Initialization: The initial (negative) saturation S_0^g, initial solid saturation S_0^s, and (pseudo) compositions of the fluid in the aquifer are calculated by performing a negative flash calculation at the initial temperature (T_0), pressure (p_0), and overall mole fraction ($x_{0,i}^t$) of the aquifer.

The upwind scheme allows us to start from the left boundary and solve the three nonlinear discretized PDE's (i.e., three mass balance relations for the three components) for three primary variables in the downstream cell, using a Newton scheme (inside loop). This method is continued until the external boundary at $r = L$ is reached. However, because of having a Neumann boundary condition for the pressure at the left boundary, this scheme is not explicit.

Left Boundary: The left boundary condition is at the injection point ($r = r_{well}$) with a known injection temperature (T_{inj}) and composition ($x_{inj,i}^t$). Here it is assumed that the injection pressure p_{inj} is equal to the initial pressure of the aquifer (p_0) only to perform a flash calculation and calculate the equilibrium compositions (x_i^g, x_i^l), molar densities ($\hat{C}^g$, $\hat{C}^l$), and saturations (S^g, S^s). The value of injection pressure can be updated later.

The primary variables: For each downstream cell, the primary variables are chosen based on the value of the solid saturation at the previous time step, i.e. $\left[(S^s)_m^{n-1}\right]^j$, where superscript j is the iteration number. With respect to the value of S^s, there are two possibilities: $S^s > 0$ or $S^s = 0$. the following steps can be used:

1. $\left[(S^s)_m^{n-1}\right]^j > 0$; if solid saturation is higher than zero, $\left[\left(\bar{x}_{salt}^l\right)_m^n\right]^{j+1} = \bar{x}_{salt,max}^l$.

133

Therefore, the system of equations are solved for the Darcy velocity $[u^n_m]^{j+1}$, gas saturation $[(S^g)^n_m]^{j+1}$, and solid saturation $[(S^s)^n_m]^{j+1}$. If $[(S^s)^n_m]^{j+1} > 1$ or if we encounter a dried up zone, i.e., $[(S^g)^n_m]^{j+1} \geq 1$ go to step 3.

2. $\left[(S^s)^{n-1}_m\right]^j = 0$; if the solid saturation in the previous time step is zero, then it is assumed that the estimated solid saturation in the current time step, i.e., $[(S^s)^n_m]^{j+1}$ is zero and the system of equations are solved for the Darcy velocity $[u^n_m]^{j+1}$, gas saturation $[(S^g)^n_m]^{j+1}$, and salt mole fraction in brine $\left[\left(\bar{x}^l_{\text{salt}}\right)^n_m\right]^{j+1}$. If $\left[\left(\bar{x}^l_{\text{salt}}\right)^n_m\right]^{j+1} > \bar{x}^l_{\text{salt},max}$; if a dried up zone is encountered, i.e., $[(S^g)^n_m]^{j+1} \geq 1$ go to step 3.

3. Perform a flash calculation and find a new value for solid saturation, i.e., $[(S^s)^n_m]^{j+2}$. Check the convergence criteria, i.e.

$$\left| \left[(S^s)^{n-1}_m\right]^{j+2} - \left[(S^s)^{n-1}_m\right]^{j+1} \right| < \varepsilon,$$

where $\varepsilon = 1 \times 10^{-8}$ is chosen.

When the convergence criterion for cell m is satisfied, one can use the same procedure to calculate the unknowns for the next cell $m + 1$, which is downstream of these known cell m. When the right boundary is reached, the known pressure (Dirichlet boundary) and known Darcy velocity values at each cell can be used to back calculate the pressure profile and the injection pressure in the whole domain.

In the next section, the results obtained by using the above procedure will be presented and discussed.

Fig. 4.6 shows a schematic of the aquifer and the injection well at its center. Initially, the aquifer is saturated with brine with the composition x^t_0 at temperature T and pressure p_0. A gas stream with composition x^t_{inj} at the aquifer temperature is injected at $r = r_w$ with Darcy velocity u_{inj}. The aquifer radius is equal to L and it is assumed that the pressure at the outer boundary ($r = L$) is equal to p_0. The injection pressure is unknown, but only for the calculation of the thermodynamic properties of the input stream, it is assumed that it is equal to p_0.

4.10. Results and Discussion

Here, first the results of the NegSat method are compared with the published analytical results [131, 175] and numerical 1D simulations [106] of CO$_2$ injection into brine aquifers. Then a few cases of CO$_2$ injection into an aquifer that contains brine with different salinities are solved including undersaturated ($\bar{x}^l_{\text{salt}} < \bar{x}^l_{\text{salt},max}$), and saturated with no precipitated solid salt ($\bar{x}^l_{\text{salt}} = \bar{x}^l_{\text{salt},max}$, $S^s = 0$). For each case, the effect of water preflush on the subsequent CO$_2$ injection, salt precipitation, and permeability reduction is studied.

A flow simulation is performed with parameters given in Table 4.5, by Zeidouni et al. [175], which has been repeated here for convenience. The pressure of the base case is 7.5 MPa and the temperature is 35°C. The gaseous CO_2 saturation is shown in Fig. 4.7. Two different times are used, i.e., $t = 1$ h and $t = 24$ h. After a while, the solution shows a constant state at the injection side and subsequently a shock to $S^g = 0.65$ at $r^2/t = 3 \times 10^{-6}$ m^2/s. Downstream of the shock, the precipitated salt saturation is zero. A rarefaction is observed in which the saturation S^g drops to 0.15 at $r^2/t = 1.5 \times 10^{-2}$. Subsequently a shock is observed at $r^2/t = 1.5 \times 10^{-2}$ and the saturation drops to the initial condition. Fig. 4.7 shows the precipitated salt saturation. It is characterized by a rarefaction at the injection side. The highest salt saturation is observed near the entrance. The variation of salt saturation near the entrance can be attributed to an entrance effect. For much slower injection rates and finer griding at the entrance, the peak at the entrance becomes almost invisible. The salt saturation at the entrance is constant until it shocks to zero saturation at the same location where the gas saturation S^g drops to 0.65, i.e., at $r^2/t = 3 \times 10^{-6}$ m^2/s. Fig. 4.8 shows the dissolved salt concentration upstream of the shock where the gas saturation drops to 0.43 and the solid saturation drops to zero. No liquid phase exist in this zone. In other words, the porous medium upstream of the shock is completely dried out. Salt mole fraction drops quickly to the initial salt concentration upstream of the shock. Because of numerical diffusion, there is a saturated salt solution between the liquid water and the precipitated salt. Also, Fig. 4.8 shows the mole fraction of water in the liquid phase. The results can be compared to results published by Zeidouni et al. and other references [131, 130]. The author prefers the model of Zeidouni et al. because they compare analytical with numerical results.

The agreement between the result of this work and the results of Zeidouni et al. is good even though , unlike the work of Zeidouni et al. [175], a NaCl-concentration-dependent solubility of CO_2 is used here.

4.10.1. Exergy analysis

The permeability decline due to the precipitation of salt near the injection well can increase the pressure drop and consequently the injection pressure must be increased to maintain the flow rate. Here, the injection pressures are compared for two different cases: (1) the salt precipitation causes a permeability decline and (2) precipitation of salt does not affect the permeability. Then the amount of compression exergy that is required to inject CO_2 is calculated in each case. Fig. 4.9 shows the pressure profile for the model with parameters reported in Table 4.5, with different permeability reduction models. The calculated injection pressures are shown in Table 4.6. The highest injection pressure is observed for the permeability decline model of Verma and Pruess (dotted line) with a $\varphi_r = 0.92$ (see Eq. (4.80)). By decreasing φ_r to 0.9, the effect of salt precipitation on permeability becomes smaller and therefore

Table 4.5.: Initial and boundary condition parameters for the simulation of CO_2 injection into an aquifer with and without water preflush (see Fig. 4.6)

Parameter	Unit	Value	Note
L	m	100000	aquifer radius
H	m	30	aquifer thickness
r_{well}	m	0.1	well radius
q_{CO_2}	kg/s	1	CO_2 injection rate
q_{water}	kg/s	1	water injection rate
p_0	bar	75	initial pressure
x_0^t	mole fraction	$\{0, 0.9069, 0.0931\}$	aquifer liquid $\{CO_2, H_2O, NaCl\}$
$\Delta t_{preflush}$	s	3600	water pre-injection time
k	m^2	0.1×10^{-12}	permeability
φ_0	-	0.2	porosity
μ^g	Pa.s	4.12×10^{-5}	gas viscosity
μ^l	Pa.s	1.3647×10^{-3}	liquid viscosity
C^s	mol/m^3	37005	salt molar density
Δt	s	20	time step

a lower injection pressure is observed. The Kozeny-Carman equation shows only a small increase in the injection pressure due to salt precipitation.

To quantify the effect of salt precipitation on the compression energy requirement, it is assumed that the compression is performed with multistage centrifugal compressors with a maximum pressure ratio of 2.5, with intercoolers to bring down the compressed gas temperature to 300 K after each compression stage. Only model the last compressor is modeled here, which compresses the gas from 175 bar to the injection pressures shown in Table 4.6, being the output pressure of the compressor p_{out}.

Table 4.6.: Calculated injection pressure and the theoretical exergy requirement of the compressor for various permeability reduction due to salt precipitation models. Here, K & C denotes Kozeny-Carman, and V & P denotes Verma and Pruess. The input pressure to the compressor is 175 bar.

Model	No effect	K & C	V & P ($\varphi_r = 0.90$)	V & P ($\varphi_r = 0.92$)
p_{out} [bar]	437.2	437.8	445.7	464.0
W_{comp} [kJ/mol CO_2]	1.510	1.512	1.556	1.654
Increase in W_{comp} [%]	0.0 %	0.17 %	3.00 %	9.50 %

The compressor exergy requirement per mole of CO_2 is calculated by assuming an isentropic compressor stage, i.e., the entropy of the input stream to the compressor is equal to the entropy of the compressed CO_2. Span-Wagner equation of state is used to calculate the physical properties of CO_2. The compression exergy per mole
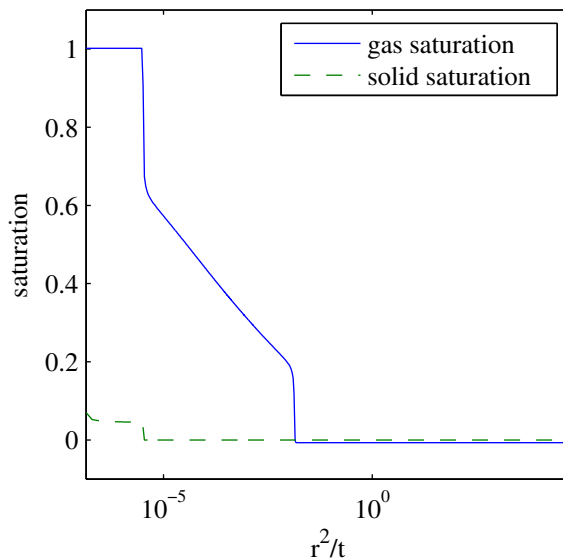
Figure 4.7.: Gas (drawn line) and solid (dashed line) saturation as a function of similarity variable (r^2/t). The initial gas saturation is negative.

of CO_2 is calculated by

$$W_{comp} = h_{in}\left(p_{in}, T_{in}\right) - h_{out}\left(p_{out}, s_{in}\left(p_{in}, T_{in}\right)\right), \tag{4.95}$$

where W_{comp} [kJ/mol] is the theoretical exergy requirement of the compressor, h_{in} [kJ/mol] is the enthalpy of input stream of CO_2 to the compressor, which is calculated at the input pressure p_{in}=175 bar and the input temperature T_{in}= 310 K. Moreover, h_{out} [kJ/mol] is the enthalpy of the compressed CO_2 and is calculated at p_{out} and input entropy s_{in} [kJ/(mol.K)]. The input entropy s_{in}, is calculated at the input pressure and temperature. For more details on the calculation of enthalpy and entropy, see [145, 166]. The results (Table 4.6) show that the increase in compression cost due to precipitation of salt is only 0.17 % when the permeability decline is calculated by the Kozeny-Carman model. However, the Verma and Pruess model predicts a 3.0 % and 10 % increase in compression energy for φ_r of 0.90 and 0.92, respectively. When φ_r approaches the solid saturation S^s, a sharp increase in the injection pressure and compression energy is observed, that can even result in plugging when φ_r is equal to the solid saturation. In summary, exergy analysis of the CO_2 injection shows that the effect of salt precipitation on the compression energy becomes important only if the salt precipitation causes a very high decline in the permeability near the injection well, e.g., when the solid saturation approaches the value of φ_r in the model of Verma and Pruess. To avoid permeability decline, Pruess and Müller [131] proposed to preflush the aquifer with pure water for a short period before the injection of CO_2, which will be discussed in the next section.
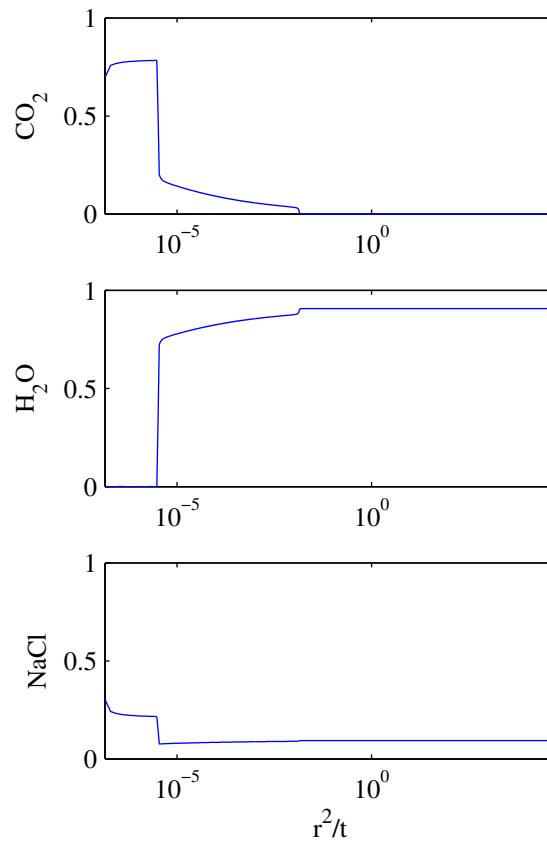
Figure 4.8.: Total mole fraction (x_i^t) of CO_2, H_2O, and NaCl versus the similarity variable (r^2/t) for injection of CO_2 into aquifer without water preflush.

4.10.2. Water preflush

The model is used with the same initial and boundary conditions shown in Table 4.5, with one exception: the composition of the injected fluid on the left boundary will be pure water from time zero to one hour. After that, CO_2 is injected for 23 hours. Fig. 4.10 shows the gas and solid saturations at the end of water preflush. As expected, the solid saturation, which is initially zero, has not changed after the injection of pure water. However, the gas saturation, which is equal to -0.026 at the injection side shocks to -0.007 (initial saturation of the aquifer) at $r^2/t = 4 \times 10^{-5}$ m^2/s. Both saturation values on the left and right of the shock are negative, which means that the whole system is saturated with liquid. However, the shock in gas saturation corresponds to a composition shock in the NegSat approach. Fig. 4.11 shows the total mole fraction of water and NaCl after one hour of water preflush. No CO_2 is yet injected into the aquifer, therefore the CO_2 mole fraction is zero everywhere. At the injection side, the mole fraction of salt is zero, as the injected liquid is pure water. At $r^2/t = 4 \times 10^{-5}$ m^2/s, the NaCl mole fraction shocks to the initial mole fraction of salt in the aquifer.
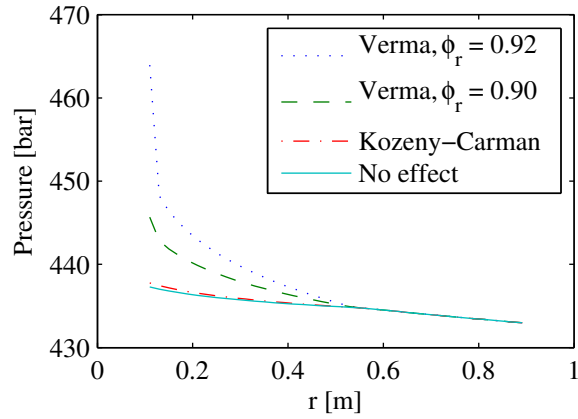
138

Figure 4.9.: Pressure profile near the injection well for the CO_2 injection scenario of Table 4.5, with different permeability reduction relations. The dotted line shows the pressure profile with the permeability reduction model of Verma and Pruess with $\varphi_r = 0.92$, the dashed line shows the pressure for Verma and Pruess with $\varphi_r = 0.90$, the dashed-dotted line shows the pressure for Kozeny-Carman, and the drawn line shows the pressure with no permeability reduction effect.
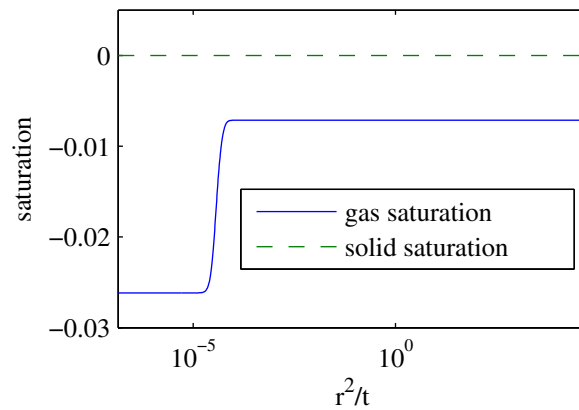

Figure 4.10.: Gas and solid saturations as a function of the similarity variable r^2/t [m^2/s] at the end of water preflush ($t = 3600$ s).
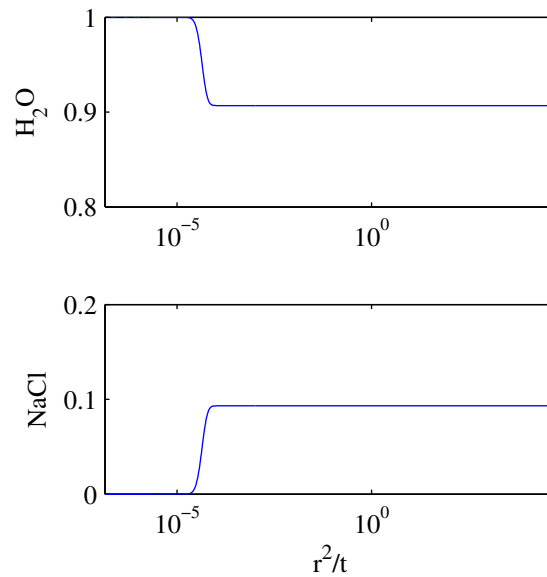
Figure 4.11.: The total mole fraction of water and salt as a function of the similarity variable r^2/t [m^2/s] at the end of water preflush ($t = 3600$ s).

Fig. 4.12 shows the gas and solid saturation after one hour of water preflush followed by 23 hours of CO_2 injection. The gas saturation is similar to the case without water preinjection that was described before. However, In the case with water preflush no solid precipitation is observed.
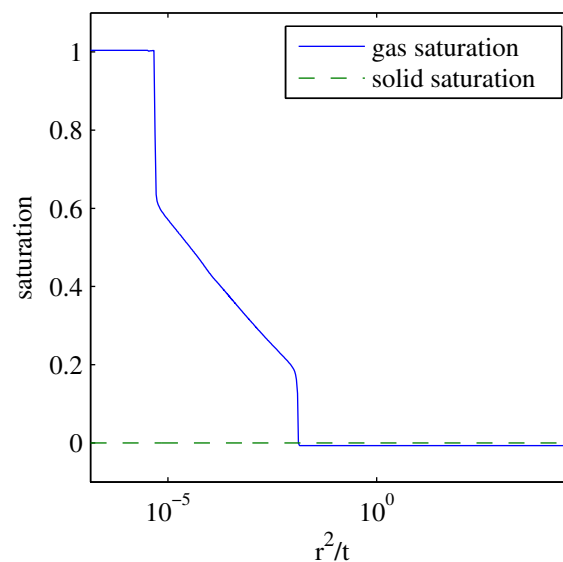

Figure 4.12.: Gas and solid saturations as a function of the similarity variable r^2/t [m^2/s] after 23 hours of CO_2 injection with one hour of water preflush.

Fig. 4.13-left shows the total mole fraction of CO_2, water, and NaCl at the end of 23 hours of CO_2 injection following one hour of water preflush. On the right side of Fig. 4.13, part of the left side figure, which is between r^2/t of 10^{-5} to 1.0 is magnified. The total water mole fraction (middle figure) at the injection side (dried-out zone) is zero (constant state). Then it shocks to 0.81 at r^2/t of 5×10^{-6}. Then, a rarefaction is observed, at which the water mole fraction increases to 0.88 at r^2/t of 6.3×10^{-5}. Up to this point, the salt mole fraction is at a constant state of zero. However, salt concentration shocks to a mole fraction of 0.085 and the water and CO_2 concentration shock to lower mole fractions of 0.835 and 0.080, respectively. Then, a rarefaction is observed in which salt and water concentrations increases to a mole fraction of 0.091 and 0.885, respectively and the CO_2 concentration decreases to a mole fraction of 0.024, at $r^2/t= 0.013$. Finally, the mole fractions shock to to the initial concentration of the aquifer.

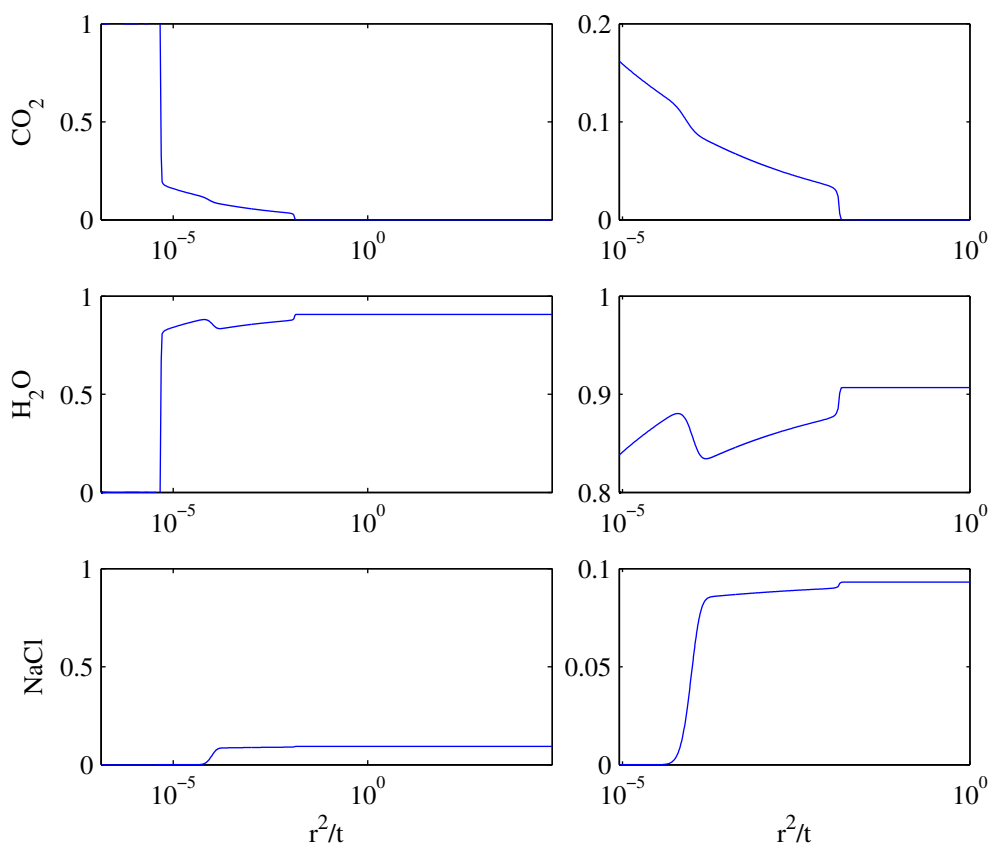**Figure 4.13.:** The total mole fractions of CO_2, water, and salt as a function of the similarity variable r^2/t [m^2/s] after 23 hours of CO_2 injection with one hour of water preflush. The right figures zoom on the left curve for a range of r^2/t from 10^{-5} to 1.0 to show the compositional shocks.

In summary, the results show that by preflushing the aquifer with pure water, salt

precipitation near the injection can well be avoided.

4.11. Conclusion

- The advantage of the NegSat approach for two-phase pseudo two-component system is that it is not necessary to use different sets of equations in one and two phase flow. However, the value of some of the variables must be changed.

- In the three phase flow, the NegSat can be effectively applied by a-priori separating the stagnant solid phase from the three phase mixture in the thermodynamic model.

- The primary variables in the three phase system are S^s, S^g, u and the primary variables in the two phase system are S^g, u, $\bar{x}^l_{\text{salt}}$.

- The solid saturation has only a minor influence on the pressure distribution in the system and therefore the effect on the compression energy is only minor.

- By preflushing the aquifer with pure water, the salt precipitation near the injection well during the CO$_2$ injection can be avoided.

- Comparison of the numerical solution to analytical solutions reported in the literature shows excellent agreement.

5. Experimental and Theoretical investigation of Natural Convection in Aquifer Storage of CO$_2$: Onset Time, Mass Transfer Rate, Capillary Transition Zone, and Heat of Dissolution

> The great tragedy of science, the slaying of a beautiful theory by an ugly fact.
>
> ———————————————————
>
> Thomas Henry Huxley

Abstract

The enhanced mass transfer of CO$_2$ in water is studied for a CO$_2$ saturated layer on top of a water saturated porous medium, experimentally and theoretically. A relatively large experimental set-up with a length of 0.5 m and a diameter of 0.15 m is used in pressure decay experiments to minimize the error of pressure measurement due to temperature fluctuations and small leakages. The experimental results were compared to the theoretical result in terms of onset time of natural convection and rate of mass transfer of CO$_2$ in the convection dominated process. In addition, a non-isothermal multicomponent flow model in porous media, is solved numerically to study the effect of the heat of dissolution of CO$_2$ in water on the rate of mass transfer of CO$_2$. The effect of the capillary transition zone on the rate of mass transfer of CO$_2$ is also studied theoretically. The simulation results including the effect of the capillary transition zone show a better agreement with experimental results compared to the simulation result without considering a capillary transition zone. The simulation results also show that the effect of heat of dissolution on the rate of mass transfer is negligible.

5.1. Introduction

Current concern with global warming has increased interest in the usage of low and zero CO_2 emission energy resources. But replacing fossil fuels by sustainable energy resources is a gradual process and cannot be attained in the near future. In the meantime, other measures must be explored and taken to slow down the increasing rate of CO_2 concentration in the atmosphere, which is caused by the combustion of fossil fuels. One of the proposed methods is to separate the CO_2 from flue gas and to store it in geological formations, e.g., injection of supercritical CO_2 into aquifers. The state of the art technology for the separation of CO_2 is amine chemisorption which is effective but very energy intensive. The pipeline transport and injection of supercritical CO_2 requires gas compressorion, which is among the most energy intensive processes. In average, CO_2 separation from flue gas requires at least 4 MJ/kg CO_2 and CO_2 transport via a 150 km pipeline and supercritical aquifer injection requires around 1 MJ/kg CO_2. Fossil fuel coal with roughly a hydrogen/carbon ratio of one has 0.088 kg CO_2/MJ while methane with a hydrogen/carbon ratio of four, has 0.055 kg CO_2/MJ, i.e., the largest and smallest carbon dioxide production per unit combustion energy, respectively. Thus 44% of coal combustion energy and 27% of methane combustion energy are required to achieve the zero emission usage of those fossil fuels. Using this high percentage of energy resource cannot be rationalized unless the effectiveness of aquifer storage is demonstrated, i.e., to prove that injected CO_2 will be stored safely underground for a long period of time [101].
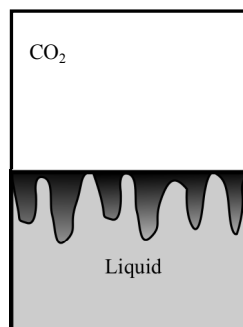

Figure 5.1.: A schematic representation of the pressure vessel for pressure decay experiments available in the literature; gas phase or supercritical CO_2 overlais a liquid phase (water, oil, or surfactant solution) [58, 57] or a porous medium saturated with a liquid phase [107]. The visualization experiments are performed in a transparent vessel [87, 90].

One of the methods that can ensure the long-term storage of CO_2 is the dissolution of CO_2 in water. If the dissolution process were controlled by the diffusion of CO_2 in the aqueous phase, the rate of storage of CO_2 would be very low. However, the dissolution of CO_2 in water increases the density of the mixture which forms a layer

of high-density fluid on top of a low density water layer. Depending on the rock properties and the transport properties of the liquid layers, the system can become unstable and the high density fluid flows in the direction of gravity, which enhances the rate of transfer of CO_2 in water. This phenomenon is called density-driven convection.

Previously the density-driven convection of CO_2 in water has been studied experimentally and theoretically. The experimental work, which is not as extensive as the theoretical work on this topic, can be subdivided into two main catagories: visualization of fingers and quantification of dissolution rate (see Fig 5.1). The goal of the visualization experiments is to show the instability in the water saturated with CO_2 overlaying a pure water layer and to visualize the formation, initiation, and development of fingers. Kneafsey and Pruess [90] used a pH indicator to visualize the formation of fingers due to the dissolution of CO_2 in pure water and brine in a Hele-Shaw cell with a permeability of around 40000 Darcy. Khosrokhavar et al. [87] applied the Schlieren method to observe gravity induced fingers where subcritical or supercritical CO_2 is placed on top of a liquid phase of water, brine, or oil at constant temperature. Their experiments were conducted in a closed system and the pressure decay data were also measured. Their experiment is unique in the sense that it both visualizes the instability of the diffusive layer and formation of fingers and quantifies the rate of mass transfer by measuring the pressure decay, however, only in bulk liquid. Farajzadeh et al. [58, 57, 59] performed a set of pressure decay experiments to quantify enhanced mass transfer of CO_2 in water, surfactant solutions, and oil. They showed that the pressure decay results do not match the solution of Fick's second law, unless an effective diffusion coefficient with a value higher than the molecular diffusion coefficient is used. The value of this diffusion coefficient was found to be a function of pressure. They also showed that the system can be modeled by a convection-diffusion equation coupled with the Navier-Stokes equation [59], which gives a reasonable agreement between the experimental pressure decay data and simulation results. Nazari Moghaddam et al. [107] conducted pressure decay experiments in two PVT-cells; the first one with an internal diameter of 5.3 cm (21.3 cm height) to study the CO_2 dissolution in bulk water and the second one with an internal diameter of 3.18 cm (13.7 cm height) for CO_2 dissolution in water saturated porous media, in a permeability range of 121 to 2546 Darcy. They used their experimental data to calculate a pseudo-diffusion coefficient for CO_2 dissolution in water.

Here, our objectives of performing the pressure decay experiments are as follows: first, the mass transfer rate of CO_2 in water is measured in a relatively large vessel. The pressure decay experiment is very sensitive to small amounts of leakage or temperature fluctuations. These effects are minimized by using a large volume of CO_2 on top of the water saturated porous medium. In addition, by increasing the height of the water layer, one can decrease the permeability of the porous medium to lower (and more realistic) values without changing the Rayleigh number. The effect of various rock parameters on the onset time and rate of dissolution are also

quantified and experimental data that is missing in the literature are provided. In the theoretical part of this work, the effect of heat of dissolution of CO_2 on the rate of mass transfer of CO_2 into water is included by solving a non-isothermal convection-diffusion equation. The effect of capillary transition zone on the rate of mass transfer is also studied.
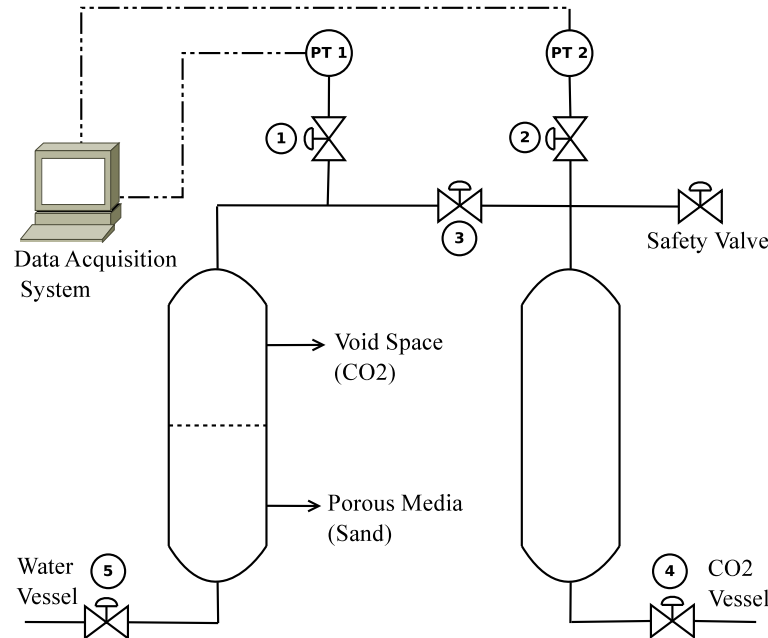

Figure 5.2.: Schematic representation of the experimental set-up

5.2. Experimental set-up

The experimental set up, shown in Fig. 5.2, consists of an stainless steel vessel with an inside diameter of 15.24 cm (6 inches) and a height of 62.23 cm (24.5 inches) (see Fig. 5.3). It is positioned vertically in an oven with a temperature control accuracy of 1 K. The top opening of the vessel is connected to a pressure transducer with an accuracy of 0.001 bar. The pressure is recorded by data acquisition software every 20 seconds. The experimental procedure is as follows: first, the vessel is completely filled with known mass of sand with a known particle size distribution. To ensure that the sand particles are completely packed, the vessel is shaken by hammering the wall for 30 minutes. The vessel is mounted in the oven and filled with helium at 8 bar. A helium detector is used to check the connections for the leakage. Then the helium pressure is recorded for 24 hours. If there is no pressure decline (negligible leakage) the sand pack is flushed with CO_2 for 10 minutes. Then, the set up is connected to a vacuum pump at -0.9 barg (0.1 bar) for 24 hours. A known mass of water is injected through valve 5 to saturate approximately between half to two third of the sand pack. The vacuuming step is necessary to prevent the formation

of gas bubbles in the water saturated zone. Normally, the vacuum in the vessel is enough to suck water inside. In case it cannot transfer the water to the vessel, a piston pump is used to inject the water. The second vessel is filled with CO_2 at 100 bar. The set-up is left in the oven for 12 hours to reach thermal equilibrium at constant temperature of 35^oC. When the system reached thermal equilibrium, the data acquisition system is started and inject CO_2 into the vessel through valve 3 up to a pressure of around 50 bar. The injection is tried to be done as slow as possible to minimize the adiabatic expansion effect. The pressure is recorded every 20 seconds for around 5-7 days, depending on the rate of pressure decline.
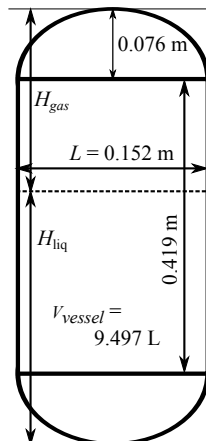

Figure 5.3.: Geometry of the stainless steel vessel

5.2.1. Computational leakage test

In the absence of leakage, the equilibrium pressure (p_{eq}) is the minimum pressure that our pressure decline experiment can reach. If the measured pressure goes below this pressure, there is a leakage and the experimental data is inaccurate. To calculate the equilibrium pressure, two mass conservation equations and two equilibrium relations are written for water and CO_2. The other equation represents that the total volume of the vessel is constant. The mass balance for CO_2 and water reads,

$$\frac{m_{0,\text{water}}}{M_{\text{water}}} = \left(1 - x^l_{CO_2}\right) C^l V^l + x^g_{\text{water}} C^g V^g, \tag{5.1}$$

$$\frac{m_{0,CO_2}}{M_{CO_2}} = x^l_{CO_2} C^l V^l + \left(1 - x^g_{\text{water}}\right) C^g V^g, \tag{5.2}$$

where $m_{0,\text{water}}$ [kg] is the initial mass of water, m_{0,CO_2} [kg] is the initial mass of CO_2, $x^l_{CO_2}$ is the mole fraction of CO_2 in the liquid phase, x^g_{water} is the mole fraction of water in the gas phase, C^l [mol/m^3] is the molar density of the liquid phase,

C^g [mol/m^3] is the molar density of the gas phase, all in equilibrium condition at temperature T [K] and pressure p [Pa]. Moreover, V^l [m^3] is the pore volume occupied by the liquid phase, V^g [m^3] is the pore volume occupied by the gas phase, M_{CO_2} [kg/mol] and M_{water} [kg/mol] are the molecular weights of CO$_2$ and water, respectively. The initial mass of CO$_2$ is calculated as

$$m_{0,\text{CO}_2} = V^g \rho_{\text{CO}_2}, \tag{5.3}$$

where ρ_{CO_2} [kg/m^3] is the mass density of pure CO$_2$ and is calculated by Span-Wagner equation of state at temperature T [K] and initial pressure p_0 [Pa]. The equilibrium mole fractions of CO$_2$ and water in the liquid and gas phases can be related using the equilibrium relations

$$K_{\text{CO}_2} x^l_{\text{CO}_2} = 1 - x^g_{\text{water}}, \tag{5.4}$$

$$K_{\text{water}} \left(1 - x^l_{\text{CO}_2}\right) = x^g_{\text{water}}, \tag{5.5}$$

where K_{CO_2} and K_{water} are the K-values of CO$_2$ and water, respectively. The K-values are a function of equilibrium pressure, temperature, and mole fractions ($x^l_{\text{CO}_2}$, x^g_{water}) and can be calculated using a thermodynamic model. Here the Stryjek-Vera modification of the Peng-Robinson equation of state with modified Huron-Vidal second order (MHV2) mixing rule are used. The Non-Random Two-Liquid (NRTL) activity coefficient model is used with a linear temperature dependent set of parameters that are optimized to predict accurately the vapor-liquid equilibrium of CO$_2$-water mixture. To close the system of equations, it is assumed that the total volume of the vessel is constant, i.e.,

$$\varphi V = V^l + V^g, \tag{5.6}$$

where V [m^3] is the total volume of the vessel and φ is the porosity of the sand pack.

5.2.2. Experimental data and analysis

Five pressure decline experiments were performed all at a constant temperature of 308.15 K with sand packs of two different permeabilities. Two experiments passed the computational leakage test of section 5.2.1. Table 5.1 shows the physical parameters related to each experiment.

Table 5.1.: Physical parameters of the pressure decline experiments

Parameter	T (K)	p_0 (bar)	d_{50} (μm)	$m_{0,\text{water}}$ (kg)
Experiment 1	308.15	46.93	300	1.807
Experiment 2	308.15	51.76	150	1.952

Fig. 5.4-a and Fig. 5.4-b show the pressure data versus time for experiment 1 and experiment 2, respectively. To show the importance of the enhanced dissolution of CO_2, the results are compared to the pressure decline curve for a pure diffusion model. At the beginning, the pressure is at its maximum value of p_0, shown in Table 5.1 for each experiment. With dissolution of CO_2 in water, the number of moles of CO_2 in the gaseous phase and consequently the measured pressure decline. The pressure decline is controlled by the rate of mass transfer of CO_2 into water, which is diffusion controlled at the start of the process. However, at one point the experimental pressure decline curve (circular markers in Fig. 5.4) starts to deviate from the pressure decline curve predicted by a diffusion model (solid line in Fig. 5.4). The time when the deviation from the diffusion regime starts is called the onset time of natural convection. Various quantitative measures are used to quantify the onset time [116, 137]. Here, the onset time is chosen to be at the time that the experimental pressure deviates 1% from the pure diffusion pressure decline curve. The experimental onset times are shown in Table 5.2 and are compared with the theoretical relations, derived by a performing a linear stability analysis by Riaz et al. [137], Ennis-King and Paterson [56], Xu et al. [172], and Pau et al. [116]. The equation reads [60]

$$t_c = c_0 \frac{\mu^2 \varphi^2 \mathcal{D}}{(\Delta\rho)^2 g^2 k^2}, \tag{5.7}$$

where μ [Pa.s] is the viscosity of the liquid phase, φ is the porosity of the porous medium, $\mathcal{D}$ [m^2/s] is the effective diffusivity of the solute in the solvent-saturated porous medium, g [9.81 m/s^2] is the gravity acceleration, k [m^2] is the permeability of the porous medium, and $\Delta\rho$ [kg/m^3] is the difference between the density of pure solvent and the solvent saturated with the solute. The value of the constant c_0 is calculated either analytically [137] or by fitting the relation to numerical simulation data [116]. Table 5.2 shows the physical parameters of the sand-pack and the fluid, which are used for the calculation of the onset time. Table 5.3 shows the values of c_0 and the calculated theoretical and experimental values of the onset time. The experimental onset time is calculated as the time when the relative difference between the experimental pressure decay measurements and the pressure decay values calculated by assuming a pure diffusion regime exceeds a threshold (which is called call pressure deviation here). The pressure deviation is defined as

$$\Delta p_{dev} = \frac{p_{exp} - p_{diff}}{p_{exp}} \times 100, \tag{5.8}$$

where Δp_{dev} [%] is the pressure deviation, p_{exp} [Pa] are the measured pressure decay values (see Fig. 5.4), and p_{diff} [Pa] is the calculated pressure decay value using a diffusion model (see Fig. 5.4). Various pressure deviation values are used, i.e., 0.1, 0.5, 1.0, 2.0, and 5.0 percent to calculate the onset times that are shown in Table 5.3 (part b). By comparing the measured onset time values with the theoretical

values one can observe that:

- None of the calculated theoretical values corresponds to the measured onset time for a pressure deviation of 0.1 %.

- The calculated onset time (see Eq. (5.7)) using the correlations of Xu et al. and Ennis-King et al. [56, 172] corresponds to the measured onset time for a pressure deviation of 0.5 %.

- The ralation proposed by Riaz et al. [137] corresponds to a pressure deviation measurement of around 1.0 %.

- The relation obtained by Pau et al. [116], which is a result of numerical simulations, corresponds to the experimental measurements for a relatively large pressure deviation between 2.0 % to 5.0 %. The same behavior is observed in the numerical simulatons.
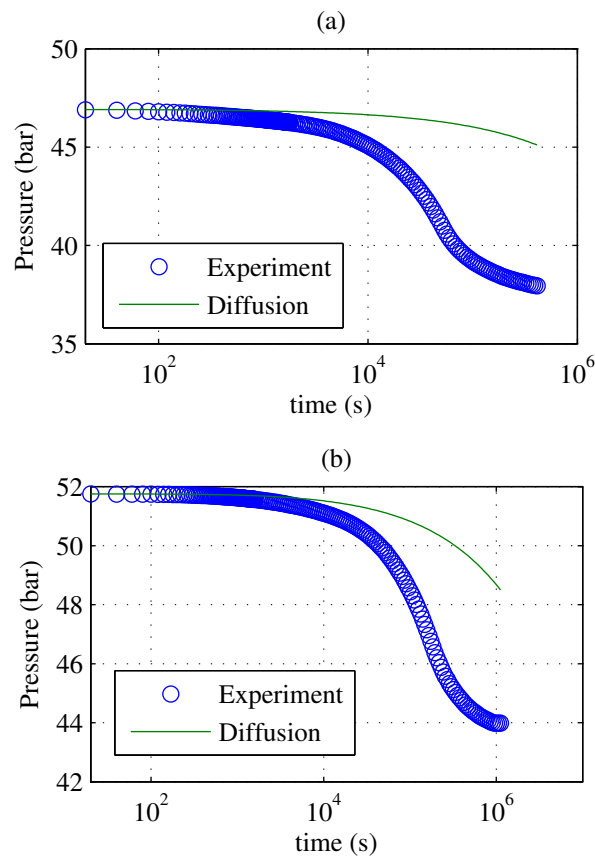

Figure 5.4.: Pressure decay experimental data compared with the pure diffusion model for: (a) Experiment 1 and (b) Experiment 2 (see Table 5.1)

Table 5.2.: Physical parameters for the calculation of the experimental onset time of natural convection

Parameter	k [m²] [15]	k [m²] (Carman-Kozeny)	φ	μ [Pa.s]	$\Delta\rho$ [kg/m³]	$\mathcal{D}$ [m²/s]
Experiment 1	$59{\times}10^{-12}$	$71.4{\times}10^{-12}$	0.38	$7.2{\times}10^{-4}$	8.4	$2{\times}10^{-9}$
Experiment 2	$15{\times}10^{-12}$	$17.8{\times}10^{-12}$	0.38	$7.2{\times}10^{-4}$	8.9	$2{\times}10^{-9}$

The theoretical and experimental values of onset times are shown in Table 5.3.

Table 5.3.: Experimental and theoretical values of the onset time of natural convection; Part a- Theoretical onset time

Relation	Xu et al., Ennis-King et al.	Riaz et al.	Pau et al.
c_0, Eq. (5.7)	75.19 - 78.0	146	1796-3670
Experiment 1, t_c [s]	326 - 338	1667	7793 - 15925
Experiment 2, t_c [s]	4430 - 4596	22640	105834 - 216266

Part b- Experimental onset time; pressure deviation is the deviation of the measured pressure decay data from the calculated pressure decay for a pure diffusion regime

Pressure deviation (%)	0.1	0.5	1.0	2.0	5.0
Experiment 1, t_c [s]	60	300	1150	4700	16300
Experiment 2, t_c [s]	600	4460	14900	37750	106700

5.3. Mathematical model

The density-driven natural convection in porous media is a single-phase multi-component flow problem. The conservation equation that describes this problem can be written as

$$\varphi\frac{\partial c_i}{\partial t} + \nabla.\mathbf{N}_i = 0,\qquad(5.9)$$

where c_i [mol/m³] is the molar concentration of component i (CO_2 and water) in the liquid phase, and N_i [mol/(m²s)] is the molar flux of component i. The total

flux is the sum of convective and diffusive fluxes, i.e.,

$$\mathbf{N}_i = c_i \mathbf{u} + \mathbf{J}_i, \tag{5.10}$$

where $\mathbf{u}$ [m/s] is the volume average velocity and $\mathbf{J}_i$ [mol/(m^{2}s)] is the molecular diffusion of component i relative to the volume average velocity. By writing Eq. (5.9) for all components and adding them up, one obtains

$$\varphi \frac{\partial C}{\partial t} + \nabla \cdot \left(C\mathbf{u} + \sum_i \mathbf{J}_i \right) = 0, \tag{5.11}$$

where $C = \sum_i c_i$ is the total concentration in [mol/m^3] and is calculated as a function of the mole fraction (x_i), pressure (p), and temperature (T) by

$$C = \frac{p}{Z\left(x_i, p, T\right) RT}, \tag{5.12}$$

where Z is the compressibility factor of the single phase fluid (with composition x_i) and can be estimated using an equation of state.

The Darcy's law is used for the estimation of the volume average velocity $\mathbf{u}$ [m/s], which reads

$$\mathbf{u} = -\frac{k}{\mu} \left(\nabla p - \rho \mathbf{g} \right), \tag{5.13}$$

where k [m^2] is the permeability of the porous medium, μ [Pa.s] is the viscosity of the fluid, ρ [kg/m^3] is the mass density of the fluid, and $\mathbf{g}$ [m/s^2] is the acceleration of gravity vector. The mass density is calculated as

$$\rho = C \sum x_i M_i, \tag{5.14}$$

where x_i is the mole fraction of component i and is related to the total concentration of the mixture through the following relation

$$c_i = x_i C, \tag{5.15}$$

where $\sum_i x_i = 1$. The molecular flux ($\mathbf{J}_i$) can be calculated by Fick's law, which has different forms depending on the the average velocity $\mathbf{u}$. The Darcy velocity can be mass average velocity, molar average velocity, or volume average velocity, according to different researchers [26, 144, 160]. By assuming that it is a volume average velocity, Fick's law is written as

$$\mathbf{J}_i = -\varphi \mathcal{D}_i \nabla c_i, \tag{5.16}$$

where $\mathcal{D}_i$ is the diffusivity of component i in the mixture in porous media. By substituting Eq. (5.10) and Eq. (5.16) in Eq. (5.9), the conservation equation for

component i reads

$$\varphi \frac{\partial c_i}{\partial t} + \nabla . \left(c_i \mathbf{u} - \varphi \mathcal{D}_i \nabla c_i \right) = 0. \tag{5.17}$$

By using Eq. (5.15), Eq. (5.12), Eq. (5.13) and Eq. (5.14), one can replace the values of c_i, C, u, and ρ in Eq. (5.17) to have the mass conservation equation for component i in terms of the variables x_i, p, and T, i.e.,

$$\varphi \frac{\partial}{\partial t} \left(\frac{x_i p}{ZRT} \right) + \nabla . \left[-\frac{k}{\mu} \frac{x_i p}{ZRT} \left(\nabla p - \mathbf{g} \frac{p}{ZRT} \sum_{i=1}^{N} (x_i M_i) \right) - \varphi \mathcal{D}_i \nabla \left(\frac{x_i p}{ZRT} \right) \right] = 0. \tag{5.18}$$

With the same approach, the overall mass conservation Eq. (5.11) is converted to

$$\varphi \frac{\partial}{\partial t} \left(\frac{p}{ZRT} \right) + \nabla . \left[-\frac{k}{\mu} \frac{p}{ZRT} \left(\nabla p - \mathbf{g} \frac{p}{ZRT} \sum_{i=1}^{N} (x_i M_i) \right) - \varphi \sum_{i} \mathcal{D}_i \nabla \left(\frac{x_i p}{ZRT} \right) \right] = 0. \tag{5.19}$$

For an isothermal system, Eq. (5.18) is written for N components and can be solved for the total N number of unknowns which consists of pressure (p) and $N-1$ mole fractions (note that $\sum x_i = 1$).

The energy balance equation reads

$$\frac{\partial}{\partial t} \left(\varphi h C + (1-\varphi) h^s \rho^s \right) + \nabla . \left(\mathbf{q} + \sum_{i=1}^{N} \mathbf{N}_i \hat{h}_i \right) = 0, \tag{5.20}$$

where h [J/mol] is the molar enthalpy of the fluid, C [mol/m^3] is the total molar concentration of the fluid, h^s [J/kg] is the enthalpy of the porous media, ρ^s is the mass density of the porous media, $\mathbf{q}$ [J/(m^2.s)] is the conductive heat flux, $\mathbf{N}_i$ [mol/(m^2.s)] is the total molar flux of component i, and $\hat{h}_i$ [J/mol] is the partial molar enthalpy of component i in the mixture (denoted by a hat sign). The enthalpy of fluid is a function of pressure, temperature, and mole fractions, and is related to the partial molar enthalpy through the following relation:

$$h(p, T, x_i) = \sum_{i=1}^{N} x_i \hat{h}_i (p, T, x_i). \tag{5.21}$$

The effect of pressure on the enthalpy of solid is negligible. Therefore h^s is only a function of temperature. The conductive heat flux can be estimated by the Fourier's law, i.e.,

$$\mathbf{q} = -\lambda \nabla T, \tag{5.22}$$

where λ [J/(m.K.s)] is the effective thermal conductivity of a porous medium with a thermal conductivity of λ_s saturated with a fluid with a thermal conductivity of λ_f. The effective thermal conductivity can be estimated by calculating the weighted geometric mean value of the thermal conductivities of the matrix and the fluid [170], i.e.,

$$\lambda = \lambda_f^{\varphi} \lambda_s^{1-\varphi}. \tag{5.23}$$

5.3.1. Non-isothermal liquid phase flow of CO_2-water

Here, the simplified yet accurate thermodynamic relations, i.e., Eq. (E.2), Eq. (E.27), and Eq. (E.28), are substituted in the mass and energy balance equations, i.e., Eq. (5.18) and Eq. (5.20), to find a partial differential equation for the non-isothermal density driven flow of CO_2-water. By studying Fig. E.4, one may observe the following characteristics of the liquid phase CO_2-water mixture:

1. Total molar concentration and total mass density of the mixture are linear functions of CO_2 molar concentration at constant temperature and pressure for the whole range of CO_2 concentration ($0 \leqslant c_{CO_2} \leqslant c_{CO_2,eq}$), i.e.,

$$C = \beta_c c_{CO_2} + \frac{\rho_{\text{water}}}{M_{\text{water}}} = \beta_c c_{CO_2} + \frac{1}{v_{\text{water}}}, \tag{5.24}$$

$$\rho = [(\beta_c - 1) M_{\text{water}} + M_{CO_2}] c_{CO_2} + \frac{M_{\text{water}}}{v_{\text{water}}}, \tag{5.25}$$

where C [mol/m^3] and ρ [kg/m^3] are the total molar and mass concentration of the liquid phase mixture of CO_2-water, c_{CO_2} [mol/m^3] is the molar concentration of CO_2, M_{water} and M_{CO_2} [kg/mol] are the molecular weight of water and CO_2, v_{water} [m^3/mol] is the molar volume of pure water and β_c is a dimensionless coefficient, which is a function of pressure and temperature but composition independent; it is explained in Eq. (E.1).

2. Total molar concentration and total mass density are weak functions of pressure, i.e., if the pressure change is less than a few bar, e.g., 10 bar, the liquid phase can be considered incompressible with a negligible error.

3. The molar concentration of water (c_{water}) is equal to the total molar concentration of the mixture minus the molar concentration of CO_2, i.e., $c_{\text{water}} = C - c_{CO_2}$, which can be combined with Eq. (5.24) and differentiated to obtain the following relation between the concentration gradient of CO_2 and water:

$$\nabla c_{\text{water}} = (\beta_c - 1) \nabla c_{CO_2}. \tag{5.26}$$

By substituting C, ∇c_{CO_2}, and ∇c_{water} form Eqs. (5.24) in Eq. (5.11), one obtains

$$\varphi \frac{\partial \left(\beta_c c_{CO_2} + \frac{1}{v_{water}} \right)}{\partial t} + \nabla \cdot \left[\left(\beta_c c_{CO_2} + \frac{1}{v_{water}} \right) \mathbf{u} - \varphi \mathcal{D} \beta_c \nabla c_{CO_2} \right] = 0, \qquad (5.27)$$

which, by assuming that β_c and v_{water} are constant and dividing the equation by β_c, can be simplified to

$$\varphi \frac{\partial c_{CO_2}}{\partial t} + \nabla \cdot (c_{CO_2} \mathbf{u} - \varphi \mathcal{D} \nabla c_{CO_2}) + \nabla \cdot \left(\frac{1}{\beta_c v_{water}} \mathbf{u} \right) = 0. \qquad (5.28)$$

Note that in the above equation, $\mathcal{D}_{CO_2} = \mathcal{D}_{water} = \mathcal{D}$. The mass conservation of CO_2, i.e., Eq. (5.17) with $i = CO_2$, reads

$$\varphi \frac{\partial c_{CO_2}}{\partial t} + \nabla \cdot (c_{CO_2} \mathbf{u} - \varphi \mathcal{D} \nabla c_{CO_2}) = 0. \qquad (5.29)$$

By subtracting Eq. (5.28) from Eq. (5.29), and assuming that β_c and v_{water} are constant, one obtains

$$\nabla \cdot \mathbf{u} = 0, \qquad (5.30)$$

where the Darcy velocity ($\mathbf{u}$) is replaced by Eq. (5.13) and the mass density in the Darcy velocity equation is substituted by Eq. (5.25) to obtain

$$\nabla \cdot \left(\frac{k}{\mu} \nabla p \right) = \nabla \cdot \left[\frac{k}{\mu} \left([(\beta_c - 1) M_{water} + M_{CO_2}] c_{CO_2} + \frac{M_{water}}{v_{water}} \right) \mathbf{g} \right]. \qquad (5.31)$$

Eq. (5.29) and Eq. (5.31) can be solved simultaneously (nonlinearly) or sequentially (linearly) for the unknown variables c_{CO_2} and p. In the next section, a sequential procedure for solving the system of equations is discussed. It is worth mentioning that Eq. (5.31), which has the form of the well-known Boussinesq formulation, is a result of having a linear relation for total molar concentration and the assumption that Darcy velocity is a volume average velocity. In Appendix F, it is shown that by using Darcy velocity as a molar (or mass) average velocity, a diffusion term will appear in the continuity equation, Eq. (5.30).

To simplify the energy balance equation, first all the enthalpy values in Eq. (5.20) are expressed as functions of temperature. The enthalpy of the porous medium (h^s) and the fluid phase (h^l) are calculated by

$$h^s = c_p^s T + h_0^s, \qquad (5.32)$$

$$h^l = \sum_i x_i \hat{h}_i = \sum_i x_i \left(\hat{c}_{p,i} T + \hat{h}_{i,0} \right), \tag{5.33}$$

where c_p^s [J/(kg.K)] is the heat capacity of the porous medium, h_0^s [J/kg] is the enthalpy of the solid phase at the reference temperature, $\hat{h}_i$ [J/mol] is the partial molar enthalpy of component i, and $\hat{c}_{p,i}$ [J/(mol.K)] and $\hat{h}_{i,0}$ [J/mol] are constants for the calculation of partial molar enthalpy of component i. The thermodynamic relations for the calculation of the enthalpy of the mixture and the partial molar enthalpies of CO_2 and water are explained in E.2. Eq. (E.26), Eq. (E.27) and Eq. (E.28) are substituted in the conservation of energy, Eq. (5.20), to obtain

$$\begin{aligned}
&\left[\varphi \left(c_{CO_2} \hat{c}_{p,CO_2} + c_{water} \hat{c}_{p,water} \right) + (1 - \varphi) \rho^s c_p^s \right] \frac{\partial T}{\partial t} + \nabla . \left[-\lambda \nabla T \right] \\
&+ \nabla . \left[-\varphi \left(\hat{c}_{p,CO_2} \mathcal{D}_{CO_2} \nabla c_{CO_2} + \hat{c}_{p,water} \mathcal{D}_{water} \nabla c_{water} \right) T \right] + \\
&+ \nabla . \left[\mathbf{u} \left(c_{CO_2} \hat{c}_{p,CO_2} + c_{water} \hat{c}_{p,water} \right) T \right] = \\
&- \nabla . \left[-\varphi \left(\hat{h}_{0,CO_2} \mathcal{D}_{CO_2} \nabla c_{CO_2} + \hat{h}_{0,water} \mathcal{D}_{water} \nabla c_{water} \right) \right] + \\
&\qquad\qquad\qquad - \nabla . \left[\mathbf{u} \left(c_{CO_2} \hat{h}_{0,CO_2} + \hat{c}_{water} \hat{h}_{0,water} \right) \right] \quad (5.34)
\end{aligned}$$

The above equation is simplified to get a PDE for the primary variable T, i.e.,

$$\begin{aligned}
\alpha \frac{\partial T}{\partial t} + \nabla . \left[-\left(\sum_i \hat{c}_{p,i} \varphi \mathcal{D}_i \nabla c_i \right) T \right] + \nabla . \left[-\lambda \nabla T \right] + \\
+ \nabla . \left[\left(\mathbf{u} \sum_i c_i \hat{c}_{p,i} \right) T \right] + S = 0, \quad (5.35)
\end{aligned}$$

where

$$\alpha = \varphi \left(c_{CO_2} \hat{c}_{p,CO_2} + c_{water} \hat{c}_{p,water} \right) + (1 - \varphi) \rho^s c_p^s, \tag{5.36}$$

$$S = \nabla . \left[-\sum_i \hat{h}_{0,i} \varphi \mathcal{D}_i \nabla c_i \right] + \nabla . \left[\mathbf{u} \sum_i c_i \hat{h}_{0,i} \right]. \tag{5.37}$$

5.3.2. Capillary transition zone

The saturation of water and gas above the free water (phreatic) level ($p_c = 0$) is considered to be the result of balance between the capillary and gravity forces disregarding the viscous forces due to natural convection flow. The capillary-gravity

equilibrium relation reads

$$p_c\left(S^l\right) = \left(\rho_l - \rho_g\right)gz,\tag{5.38}$$

where $p_c\left(S^l\right)$ [Pa] is the capillary pressure, which is a function of the liquid saturation; ρ_l [kg/m^3] and ρ_g [kg/m^3] are the densities of the liquid phase and the gas phase, and z [m] is the vertical position relative to the free water (phreatic) level. The capillary pressure data are taken from the experiments of Plug and Bruining [125] for the same sandpack that is used in the experiments at a pressure of 85 bar and a temperature of 40°C. The secondary imbibition data for $p_c - S^l$ is used from the experiment number 13 of Plug and Bruining [125], which is formulated in terms of

$$p_c\left(S^l\right) = \gamma\sigma\sqrt{\frac{\varphi}{k}}\left(\frac{\frac{1}{2} - S_{wc}}{1 - S_{wc}}\right)^{\frac{1}{\lambda_s}}\left(\frac{S^l - S_{wc}}{1 - S_{wc}}\right)^{-\frac{1}{\lambda_s}}.\tag{5.39}$$

Here, σ [N/m] is the interfacial tension of CO_2-water, S_{wc} is the connate water saturation, S^l is the liquid saturation, λ_s is the sorting factor, and γ is a constant usually taken equal to 0.5. By substituting p_c from Eq. (5.39) in Eq. (5.38), one can calculate the liquid saturation S^l as a function of z.
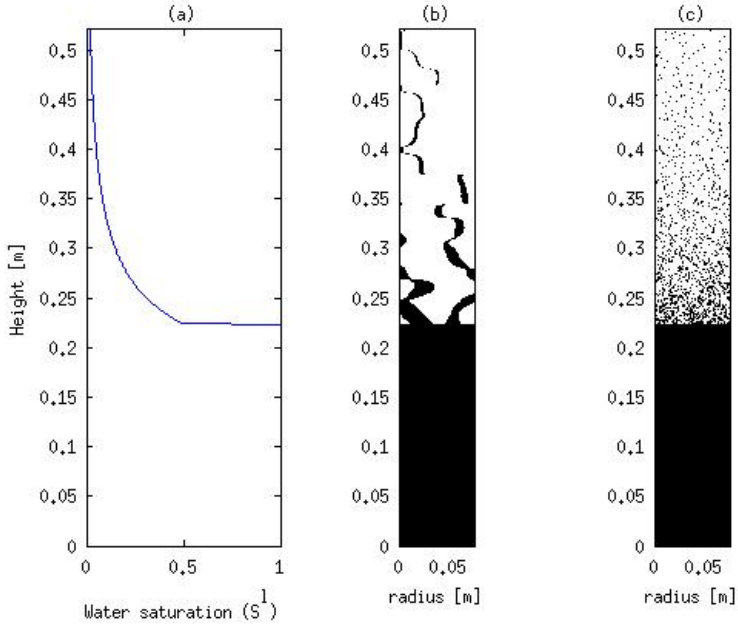

Figure 5.5.: The cylindrically symmetric distribution of water saturation in the capillary transition zone for experiment 1; (a) water saturation as a function of the height above the free water level for CO_2 injection into a sandpack [125]. (b) and (c) are various realizations of the distribution of water (black spots) in the capillary transition zone above the free water level for experiment 1.

The steps in generating the random distribution of liquid in the capillary transition zone are based on the fact that in a water-wet porous medium, water prefers to move to the areas with lower permeabilities. The following steps describe a procedure for generating a random distribution of liquid in the capillary transition zone using the Dykstra-Parsons coefficient and correlation length:

1. Generate a 2D uniform mesh on a rectangular domain with a height H and a width W. N_x denotes the number of cells in horizontal (x) direction (cell width $\Delta x = W/N_x$) and N_z denotes the number of cells in the vertical (z) direction (cell height $\Delta z = H/N_z$).

2. Generate a log-normal random permeability field $k\,(x,z)$ with a known Dykstra-Parsons coefficient (V_{DP}) and correlation length (λ_D). Here, a low Dykstra-Parsons coefficient is used for the sandpack ($V_{DP} = 0.1$) to obtain small permeability variations. Various fields are generated, which differ in their value for the correlation length λ_D between $L/50$ to $L/5$.

3. Use Eq. (5.39) and Eq. (5.38) to obtain the liquid saturation as a function of z, i.e. $S^l\,(z)$.

4. To find the horizontal distribution, one can move along the z direction, where $z = j \times \Delta z$ for $j = 1,...,N_z$. At each level $j \times \Delta z$, there are N_x cells in the x direction with different values of permeability $k\,(x,\,j \times \Delta z)$. Find the first $S^l\,(z) \times N_x$ number of cells (in x direction) with lowest permeability and assign them a liquid saturation of one. To the rest of the cells in that row, assign a liquid saturation value of zero.

Here it is assumed that the liquid blobs in the capillary transition zone do not move. However, the liquid inside each blob can flow. To find the boundary condition for each blob the following procedure is used: the random distribution of the liquid saturation in porous medium is shown in Fig. 5.5, where black areas indicate $S^l = 1$ and the white areas indicate $S^l = 0$. It is assumed that an area with $S^l = 0$ is saturated with CO_2 at constant pressure; Thermodynamic equilibrium at the gas-liquid interfaces is also assumed.

5.3.3. Simulation of the experiments: stream function formulation

Eq. (5.18) is a general equation for the multicomponent single phase flow which is easy to implement using one of the numerical scheme for solving partial differential equations. However, it is highly nonlinear and is not easy to be solved. For a two-dimensional cylindrical system, a streamline function is used to eliminate pressure from the Eq. (5.18). For a cylindrical coordinate, shown in Fig. 5.6, the stream function is defined as

$$u = -\frac{1}{r}\frac{\partial \psi}{\partial z} \quad \text{and} \quad v = \frac{1}{r}\frac{\partial \psi}{\partial r}, \tag{5.40}$$

where u is the velocity in the r-direction, v is the velocity in the z-direction, and ψ is the stream function. The Darcy velocities for the cylindrical coordinate shown in Fig. 5.6 are calculated by Eq. (5.13) with $\mathbf{g} = -g\hat{z}$ where $g = 9.8$ [m/s^2] and $\hat{z}$ is the unit vector in the z direction, i.e.,

$$u = -\frac{k}{\mu}\frac{\partial p}{\partial r} \quad \text{and} \quad v = -\frac{k}{\mu}\left(\frac{\partial p}{\partial z} + \rho g\right), \tag{5.41}$$

which is rearranged and differentiated with respect to z and r to obtain

$$\frac{\partial}{\partial z}\left(-\frac{u\mu}{k}\right) = \frac{\partial}{\partial z}\left(\frac{\partial p}{\partial r}\right) \quad \text{and} \quad \frac{\partial}{\partial r}\left(-\frac{v\mu}{k}\right) = \frac{\partial}{\partial r}\left(\frac{\partial p}{\partial z}\right) + g\frac{\partial \rho}{\partial r}. \tag{5.42}$$

The above equations are subtracted to eliminate the term $\frac{\partial}{\partial r}\left(\frac{\partial p}{\partial z}\right)$, i.e.,

$$\frac{\partial}{\partial z}\left(-\frac{u\mu}{k}\right) - \frac{\partial}{\partial r}\left(-\frac{v\mu}{k}\right) = -g\frac{\partial \rho}{\partial r}. \tag{5.43}$$

Darcy velocities are substituted in Eq. (5.43) using the stream function definition Eq. (5.40), which leads to

$$\frac{1}{r}\frac{\partial}{\partial z}\left(\frac{\mu}{k}\frac{\partial \psi}{\partial z}\right) + \frac{\partial}{\partial r}\left(\frac{1}{r}\frac{\mu}{k}\frac{\partial \psi}{\partial r}\right) = -g\frac{\partial \rho}{\partial r}. \tag{5.44}$$

In the derivation of Eq. (5.44), it is assumed that the permeability and viscosity are not constant.

The convection-diffusion equation for cylindrical coordinates reads

$$\varphi\frac{\partial c_i}{\partial t} + \frac{1}{r}\frac{\partial}{\partial r}\left(ruc_i\right) + \frac{\partial\left(vc_i\right)}{\partial z} - \left[\frac{1}{r}\frac{\partial}{\partial r}\left(r\varphi\mathcal{D}_i\frac{\partial c_i}{\partial r}\right) + \frac{\partial}{\partial z}\left(\varphi\mathcal{D}_i\frac{\partial c_i}{\partial z}\right)\right] = 0, \tag{5.45}$$

where u and v are the volume-average Darcy velocities in the r and z directions, respectively and can be calculated by the stream function definition Eq. (5.40). Moreover, c_i is the molar concentration of component i, and $\mathcal{D}_i$ is the Fickian diffusion coefficient of component i in the mixture. For the binary mixture of CO_2-water, it is shown in Appendix E that the thermodynamic and transport properties of the mixture, i.e., total mass density (ρ), total molar concentration (C), and viscosity (μ), can be expressed as functions of CO_2 molar concentration (c_{CO_2}) at constant pressure and temperature. This reduces the number of variables in Eq. (5.44) and Eq. (5.45) to two, viz., ψ and c_{CO_2}.

The boundary conditions for Eq. (5.44) and Eq. (5.45) are

$$\psi = 0, \ \frac{\partial c_{\mathrm{CO_2}}}{\partial r} = 0 \qquad \text{at } r = 0, \tag{5.46}$$

$$\psi = 0, \ \frac{\partial c_{\mathrm{CO_2}}}{\partial r} = 0 \qquad \text{at } r = R, \tag{5.47}$$

$$\psi = 0, \ \frac{\partial c_{\mathrm{CO_2}}}{\partial z} = 0 \qquad \text{at } z = 0, \tag{5.48}$$

$$\psi = 0, \ c_{\mathrm{CO_2}} = c_{\mathrm{CO_2},eq} \qquad \text{at } z = H, \tag{5.49}$$

The boundary conditions for the energy balance equation read

$$\frac{\partial T}{\partial r} = 0 \qquad \text{at } r = 0, \tag{5.50}$$

$$T = T_0 \qquad \text{at } r = R, \ z = 0, \tag{5.51}$$

$$-\lambda \frac{\partial T}{\partial z} - \mathcal{D} \frac{\partial c_{\mathrm{CO_2}}}{\partial z} \Delta h_{sol} - h(T - T_0) = 0 \qquad \text{at } z = H, \tag{5.52}$$

where R is the radius of the cylinder, H is the height of the water saturated porous medium, and $c_{\mathrm{CO_2},eq}$ is the equilibrium concentration of CO_2 and is a function of pressure and temperature. It is explained in section 5.2 that the measured pressure of gases decreases with time due to the transfer of CO_2 from the gas phase to the liquid phase. This transfer means that the equilibrium concentration of CO_2 also declines with time (see Appendix E and the relation between the CO_2 equilibrium concentration and pressure). To calculate the gas phase pressure as a function of time, the CO_2 mass balance between the phases is written, which reads

$$n_{\mathrm{CO_2}}^g = n_{0,\mathrm{CO_2}}^g - 2\pi \int_{z=0}^{z=H} \int_{r=0}^{r=R} r\varphi c_{\mathrm{CO_2}} \mathrm{d}r \mathrm{d}z, \tag{5.53}$$

where $n_{\mathrm{CO_2}}^g$ is the number of moles of CO_2 in the gas phase, $n_{0,\mathrm{CO_2}}^g$ is the initial number of moles of CO_2 in the gas phase (see Eq. (5.3)). The second term on the right side of Eq. (5.53) denotes the number of moles of dissolved CO_2 in the liquid phase. Battistutta et al. [13] show that the molar concentration of the gas phase mixture of CO_2-water at constant temperature and pressure can be estimated with negligible error by the molar concentration of pure CO_2 at the same temperature and pressure which is calculated by Span-Wagner equation of state [148]. Therefore, the gas phase pressure can be calculated as

$$p^g = \frac{n_{\mathrm{CO_2}}^g RTZ}{V^g}, \tag{5.54}$$

where p^g [Pa] is the gas phase pressure, R=8.314 [J/(mol.K)] is the gas constant, T is the temperature, V^g [m³] is the pore volume occupied by the gas phase, and Z is the compressibility factor of pure CO_2 at temperature T and pressure p^g, which is calculated by Span-Wagner equation of state [148]. The time dependent boundary condition, i.e., equilibrium concentration of CO_2 in the liquid phase, is then calculated as a function of the gas phase pressure using Fig. E.3 at constant temperature.

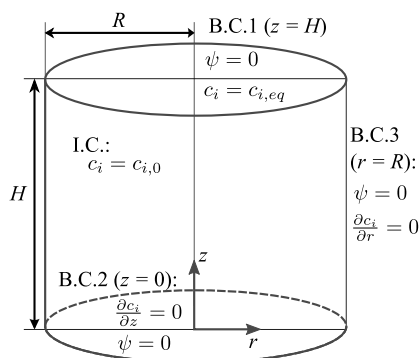The numerical solution procedure is discussed in the next section.

Figure 5.6.: Initial and boundary conditions for a single phase flow problem in a 2D cylindrical coordinate.

5.3.3.1. Numerical solution

To avoid the nonlinear system of algebraic equations, which results from discretization of Eq. (5.44) and Eq. (5.45) to be solved for the unknowns ψ and c_{CO_2}, Eq. (5.44) is discretized for the unknown ψ and Eq. (5.45) for the unknown c_{CO_2} and use the following sequential procedure:

step 1: initialize the procedure for the new time step $(t^{n+1} = t^n + \Delta t)$ by assigning the previous time step values of the stream function ψ^n and CO_2 concentration $c_{CO_2}^n$ to the current time step stream function $\psi^{n+1,k}$ and CO_2 concentration $c_{CO_2}^{n+1,k}$.

step 2: calculate $u^{n+1,k}$ and $v^{n+1,k}$ using the value of $\psi^{n+1,k}$ in Eq. (5.40).

step 3: use $u^{n+1,k}$ and $v^{n+1,k}$ in Eq. (5.45) and solve for $c_{CO_2}^{n+1,k+1}$.

step 4: use the calculated CO_2 concentration $c_{CO_2}^{n+1,k+1}$ with Eq. (5.53) and Eq. (5.54) to update the top boundary condition, i.e., Eq. (5.49).

step 5: calculate the viscosity $\mu^{n+1,k+1}$ and mass density $\rho^{n+1,k+1}$ as a function of $c_{CO_2}^{n+1,k+1}$ by using Fig. E.7 and Fig. E.4, respectively. Solve Eq. (5.44) for new values of $\psi^{n+1,k+1}$.

step 6: calculate a new value for the gas phase pressure p^g using Eqs. (5.53) and (5.54) and update the top boundary condition Eq. (5.49) by calculating a new value for $c_{CO_2,eq}$.

step 7: if the convergence criterion, i.e.,

$$\max \left| \frac{c_{CO_2}^{n+1,k+1} - c_{CO_2}^{n+1,k}}{c_{CO_2}^{n+1,k+1}} \right| < \varepsilon_1 \text{ and } \max \left| \frac{\psi^{n+1,k+1} - \psi^{n+1,k}}{\psi^{n+1,k+1}} \right| < \varepsilon_2, \quad (5.55)$$

are satisfied, assign $c_{CO_2}^{n+1,k+1}$ and $\psi^{n+1,k+1}$ to $c_{CO_2}^n$ and ψ^n, respectively, and go to step 1. Otherwise, assign $c_{CO_2}^{n+1,k+1}$ and $\psi^{n+1,k+1}$ to $c_{CO_2}^{n+1,k}$ and $\psi^{n+1,k}$ and go to step 2.

5.3.4. Simulation of the experiments: pressure formulation

For the three dimensional simulations, the stream function formulation of Section 5.3.3 cannot be used and therefore the continuity equation (5.31) must be solved for the variable pressure p. The no flow boundary conditon on all the boundaries reads

$$(\nabla p - \rho \mathbf{g}) . \mathbf{n} = 0, \quad (5.56)$$

where n is the unit normal vector of the boundary. Eq. (5.56) is the Neumann boundary condition. The continuity equation is discretized (5.31) using a cell centered finite volume scheme. The Neumann boundary condition makes the matrix of coefficient very ill-conditioned, with a condition number around 10^{17}. Therefore, the pressure in one cell in the vicinity of the top boundary is fixed to avoid this problem.

5.3.4.1. Numerical solution

Eq. (5.29) and Eq. (5.31) with a proper set of boundary conditions are discritized using one of the numerical techniques for solving PDE's. Then the system of equations are solved using the following sequential procedure.

step 1: initialize the procedure for the new time step ($t^{n+1} = t^n + \Delta t$) by assigning the previous time step values of pressure p^n and CO_2 concentration $c_{CO_2}^n$ to the current time step pressure $p^{n+1,k}$ and CO_2 concentration $c_{CO_2}^{n+1,k}$.

step 2: calculate $\rho^{n+1,k}$ by Eq. (5.24) and use it in Darcy's law to calculate $\mathbf{u}^{n+1,k}$ using the value of $p^{n+1,k}$.

step 3: use $\mathbf{u}^{n+1,k}$ in Eq. (5.29) and solve for $c_{CO_2}^{n+1,k+1}$.

step 4: calculate a new value for the gas phase pressure p^g using Eqs. (5.53) and (5.54) and update the top boundary condition Eq. (5.49) by calculating a new value for $c_{CO_2,eq}$.

step 5: calculate the viscosity $\mu^{n+1,k+1}$ and mass density $\rho^{n+1,k+1}$ as a function of $c_{CO_2}^{n+1,k+1}$ by using Fig. E.7 and Fig. E.4, respectively. Solve Eq. (5.31) for new values of $p^{n+1,k+1}$.

step 6: If the convergence critera, i.e.,

$$\max\left|\frac{c_{CO_2}^{n+1,k+1} - c_{CO_2}^{n+1,k}}{c_{CO_2}^{n+1,k+1}}\right| < \varepsilon_1 \text{ and } \max\left|\frac{p^{n+1,k+1} - p^{n+1,k}}{p^{n+1,k+1}}\right| < \varepsilon_3, \quad (5.57)$$

are satisfied, assign $c_{CO_2}^{n+1,k+1}$ and $p^{n+1,k+1}$ to $c_{CO_2}^n$ and p^n, respectively, and go to step 1. Otherwise, assign $c_{CO_2}^{n+1,k+1}$ and $p^{n+1,k+1}$ to $c_{CO_2}^{n+1,k}$ and $p^{n+1,k}$ and go to step 2.

5.3.5. Case studies

The mathematical model is solved to simulate the pressure decay experiments. As shown in Fig. 5.7, four different model structures are considered with respect to the transition zone and the effect of heat of dissolution:

- Model Ia: a sharp horizontal interface between the water and CO_2 is assumed; the heat of dissolution is assumed to be negligible (isothermal model)

- Model Ib: a sharp horizontal interface between the water and CO_2 is assumed, and the heat of dissolution of CO_2 in water is included (non-isothermal model)

- Model II: a capillary transition zone between water and CO_2 is assumed. Free water level is calculated by using the experimental data of Plug et al. [125] corrected for our experimental condition.

- Model III: it is assumes that a capillary transition zone is a region with high diffusivity of CO_2 in water, and with a lower permeability, as proposed by Elenius et al. [54].

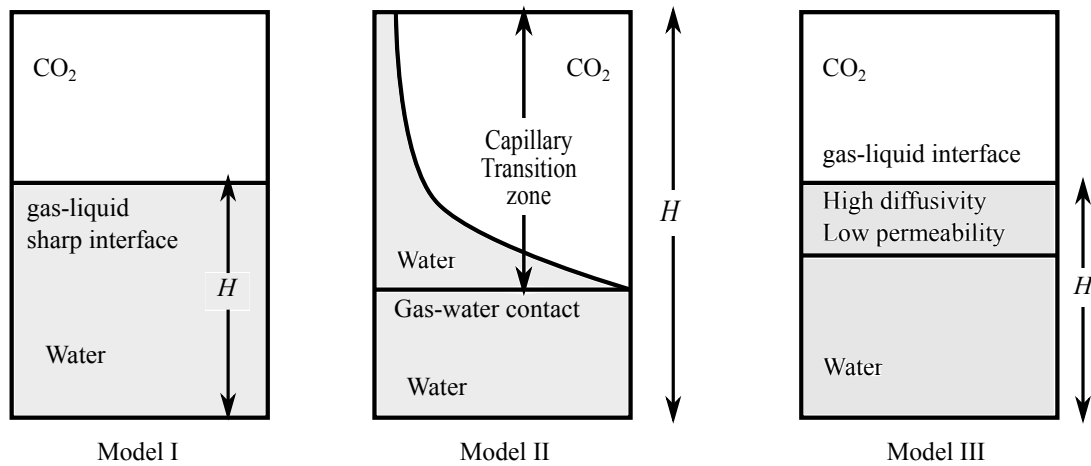The results will be discussed in the next section.

Figure 5.7.: Three model structure for the simulation of the pressure decay experiments; (I) a sharp gas-liquid interface (II) a capillary transition zone between CO_2 and water calculated based on the experimental capillary pressure data [125] (III) a capillary transition zone as a water layer with high CO_2 diffusivity and low permeability [54]

5.4. Results and discussion

5.4.1. Non-isothermal model

The numerical results of isothermal and non-isothermal models for the condition of experiment 1 are shown in Fig. 5.8. The maximum difference between the pressure history results is 1.3 %, viz., the rate of mass transfer for the non-isothermal model is slightly higher than for the isothermal case. This difference can be explained by the slightly lower temperature near the wall at the gas-liquid interface. This lower temperature increases the CO_2 solubility and consequently the natural convection driving force, i.e., $\Delta\rho$ increases. Therefore the formation of fingers are moved towards the wall. In a cylindrical coordinate, there is a larger gas-liquid contact area near the walls (see Fig. 5.6) and therefore, for a nearly constant flux of CO_2 into water at the interface, the rate of transfer of CO_2 into water is higher near the walls. This hypothesis is examined by solving the same set of equations in a cartesian coordinate, and the results showed that the maximum difference between the pressure history is 8%, where the isothermal mass transfer rate is higher.
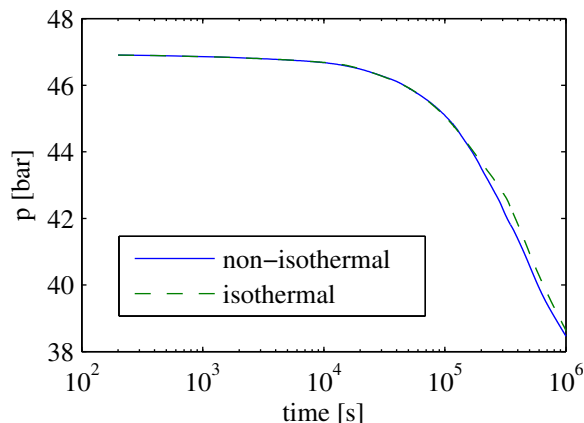
Figure 5.8.: Pressure history results for the numerical simulation of isothermal (Model Ia) and non-isothermal (Model Ib) models for the condition of experiment 1. The maximum difference between the pressures is 1.3 %.

5.4.2. Model I: sharp gas-liquid interface

Fig. 5.9 shows the experimental CO_2 pressure history data of experiment 1 and the simulation results for the Model I (sharp horizontal water-CO_2 interface). The dashed line shows pure diffusion and the circle markers shows the experimental data. The solid curves in between are the simulation results with different permeability values in the range of $59{\times}10^{-12}$ to $1180{\times}10^{-12}$ m^2 (20 times higher than the original permeability). There are three sections in the pressure decline curve that can be discussed separately: the left section where the flow is diffusion dominated, the middle section with a sharp pressure decline where the flow is convection dominated, and the transition zone where the pressure decline history curve changes from diffusion-dominated to convection-dominated and vice versa. By comparing the simulation results with the experimental data, the first important observation is that the calculated onset time of natural convection, i.e., the time at which the pressure decline curve deviates from the pure diffusion model, is higher than in the experimental measurement by one or two orders of magnitude. The second observation is that the transition from the diffusion-dominated to convection dominated flow is gradual and smooth for both experimental data and simulation results (see Fig. 5.9, t=10^4 s). However, although the experimental data shows that the transition from convection-dominated to diffusion-dominated flow happens gradually and smoothly, the simulations shows a relatively sharp transition (change in slope in pressure decline curve at time around 10^5-10^6 s) in the flow regime. The other observation is that the measured slope of pressure decline curve (the mass transfer rate) in the convection dominated zone is in agreement with the numerical simulation for a permeability of $k = 75 \times 10^{-12}$ m^2, which is almost equal to the permeability calculated by the Karmen-Cozeny equation (see Table 5.1). This permeability is chosen to

proceed to Model II, i.e., where a capillary transition zone exist on top of the free water level.
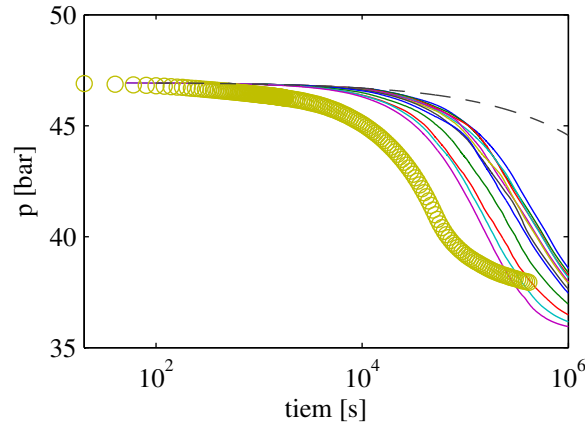

Figure 5.9.: Simulation results of pressure versus time for a horizontal water-CO_2 interface without a capillary transition zone compared to the experimental data (experiment 1)

5.4.3. Model II: capillary transition zone

Fig. 5.10 shows the concentration of CO_2 in water in four different time, i.e. 120, 12000, 60000, 120000 seconds. The white area shows pure water (zero CO_2 concentration). Because of the high surface area between gas and liquid, the capillary transition zone become saturated with CO_2 in a much shorter time, than can be observed from the experimental data. This high rate of mass transfer is represented in Fig. 5.11, which shows the experimental and calculated (Model II) pressure decay curves versus time. At a time around 200 s, the calculated pressure declines below the measured values. However, this high rate of pressure decline cannot be continued as the liquid blobs in the capillary transition zone become fully saturated with CO_2 at a time around 10000 s (see Fig. 5.10 at t=12000 s). Then it is observed that the measured pressure decline curve moves faster than the calculated values for model structure II, i.e., a capillary transition zone on top of the water-gas contact.
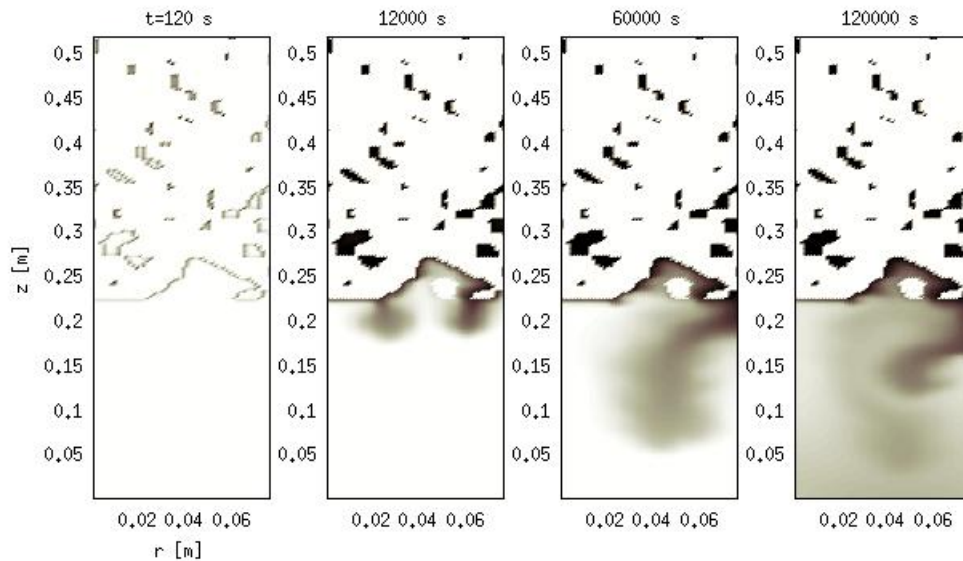
Figure 5.10.: Concentration profile of CO_2 in different times ($t =$120, 12000, 60000, 120000 s) in the capillary transition zone and in the liquid layer. The white area on the upper section of each figure shows the CO_2 saturated porous medium. The lower white area is saturated with water.
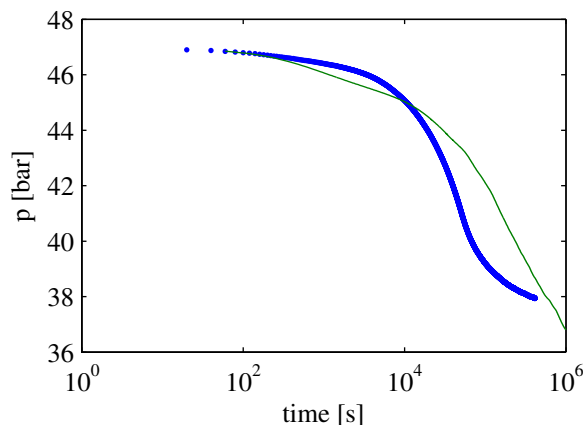

Figure 5.11.: Experimental data and numerical simulation results for pressure history in experiment 1; the simulation is done with for a capillary transition zone on top of the gas-water contact (Model II).

5.4.4. Model III: capillary transition zone as a high diffusivity zone

Finally, the third model structure is examined, in which the capillary transition zone is replaced by a layer of water with a lower permeability (to take into account the

gas saturation and the water relative permeability) and high diffusion coefficient (to take into account the extra gas-liquid contact area in the capillary transition zone) on top of the free water level. The pressure history data and simulation results are shown in Fig. 5.12 and concentration profile at three different time (t = 10000, 40000, 100000 s) are shown in Fig. 5.13. It can be observed that even if the sharp transition between the diffusion-dominated and convection dominated flow still exists, the simulation results is in a fair agreement with the experimental data.
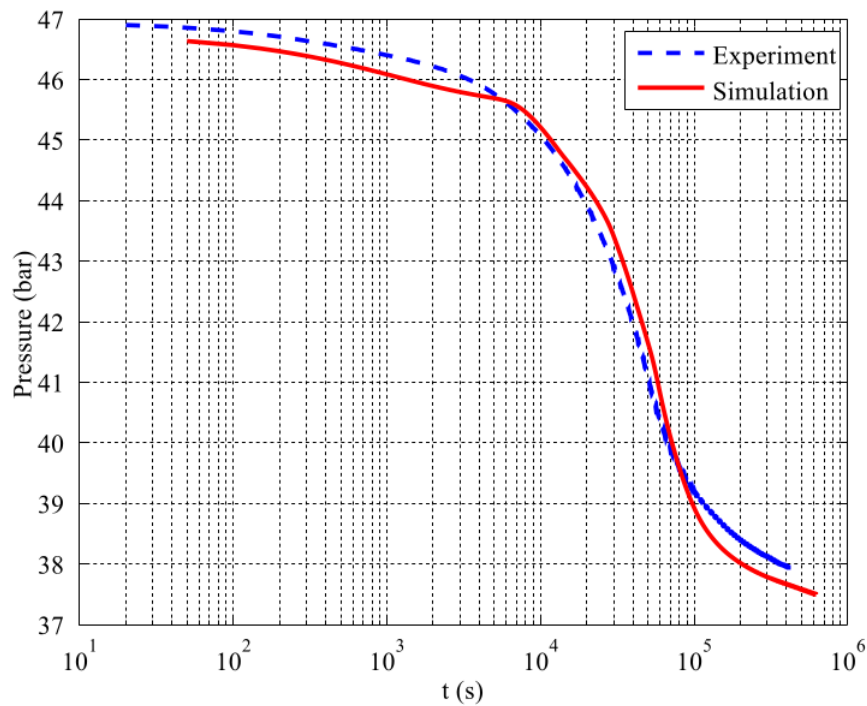

Figure 5.12.: Experimental data and numerical simulation results of pressure history for experiment 1; the simulation is done with a top layer of water with a higher diffusivity (Model III).
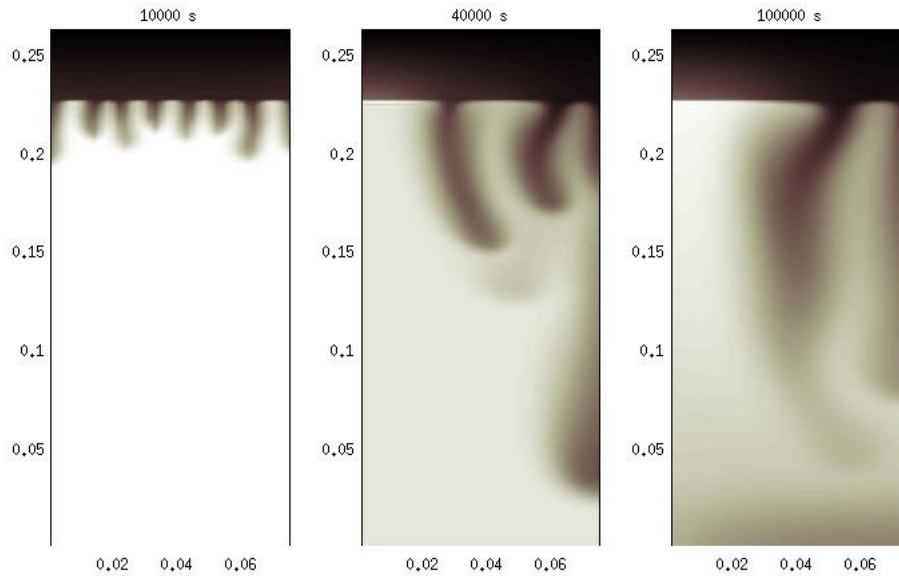
Figure 5.13.: Concentration profile of CO_2 in the liquid phase at t= 10000, 40000, and 100000 s with a top layer of higher diffusivity for the condition of experiment 1

5.5. Conclusion

- A set of pressure decay experiments were performed in a relatively large experimental set-up to measure the onset time of natural convection and the rate of mass transfer of CO_2 into water-saturated porous media.

- A mathematical model was used to study the effect of heat of dissolution of CO_2 on the rate of mass transfer.

- The effect of heat of dissolution of CO_2 in water on the rate of mass transfer is negligible.

- Various relations were compared for the calculation of onset time with the deviation of experimentally measured pressure decay data from calculated pressure decay data for a pure diffusion model.

- The effect of a capillary transition zone on the density-driven flow of CO_2 in water was studied.

- A capillary transition zone can considerably increase the mass transfer rate of CO_2 in water.

- The numerical simulations give the best match with experimental pressure decay data when a capillary transition zone is considered in the mathematical model.

6. Conclusion

This thesis consists of four main chapters. Here the conclusions of each chapter are summarized.

6.1. Exergy analysis of underground coal gasification (UCG)

- The theoretical, practical, and zero-emission recovery factors for UCG are fully analyzed, which can serve as template for the analysis of any other energy recovery/conversion processes.

- Conventional underground coal gasification with oxygen has a higher recovery factor than air gasification.

- Practical oxygen gasification has a carbon emission of 0.14 kg CO_2/MJ exergy, which can be compared to combustion of methane with a carbon emission of 0.055 kg CO_2/MJ, i.e., three times larger.

- Zero-emission recovery factors of deep UCG using the state of the art technology, i.e., amine separation, are small or negative. More efficient CO_2 capture technology, e.g., membranes, have as yet not sufficient capacity to be practical.

- It is concluded that UCG with zero greenhouse gases emission with the current state of the art is not yet feasible, mainly due to the low efficiency of the CO_2 capturing processes.

- The use of synthetic CaO to reduce the carbon emission is counterproductive in reducing the greenhouse gas emission. Zero-emission/practical recovery factors are negative for practical water/O_2 injection ratios.

- Use of calcium silicates to reduce the greenhouse gas emission would perform better than CaO. Recent literature, however, shows that the reaction rates to convert wollastonite to calcium carbonate is too slow to lead to a practical technology.

- The type of analysis proposed in this paper can be applied to any other energy conversion processes and shows where it has to be improved to increase the overall recovery factor.

- The main weak point of the use of zero-emission UCG with the current state of the art technology are the exergy-intensive CO_2 capturing methods. Theory indicates that less exergy-intensive processes can be developed.

- If CO_2 emission is not a criterion, the optimum process parameter is the value that maximizes the practical recovery factor.

- If CO_2 emission is a criterion, but the CO_2 capture and sequestration is not an option, then any value of the process parameters that gives a positive practical recovery factor and an acceptable level of CO_2 emission can be considered as the optimum.

- If CO_2 emission is a criterion and CO_2 capturing and sequestration is an option, the optimum process parameter is the value that maximizes the zero-emission recovery factor.

6.2. UCG with alternating injection of oxygen and steam

- The alternating injection of oxygen and steam is only practical for low pressure UCG, i.e., shallow coal layers, with a recovery factor of around 40 %. The total CO_2 emission per unit exergy of the final product is only twice as large as the emission factor of methane. The zero emission recovery of coal with alternating injection of oxygen and steam is not practical with the current state of technology.

- The conversion of coal with the coinjection of steam (or steam) and oxygen is a more attractive option compared to the alternating injection. The practical recovery factor is around 50 %, which is 10 % higher than the alternating injection process. However, the total CO_2 emission per unit exergy of product is 30 % higher than the alternating injection scenario.

- Low pressure is the favorable condition for UCG, with the possibility of conversion of larger amounts of water to combustible gases.

- With the current state of technology, zero emission UCG is not a practical option with a recovery factor which is negative or very low.

- Exergy analysis suggests that the development of a less energy intensive CO_2 capturing method, e.g., membrane separation, gives a positive recovery factor. However, the economical feasibility of those methods are outside the scope of this work.

- In UCG with the coinjection of steam or water and oxygen, the injection of water is the preferred technique with a higher recovery factor, as it avoids the high heat loss during the steam injection.

- This study investigated whether it is possible that underground coal gasification can be used to utilize the coal energy with a reduced carbon foot print.

- There are three scenarios for UCG depending on roof stability, i.e., no collapse, partial collapse and total collapse. The partial collapse case is amenable for simple modeling. The model consists of alternating injection of reactive gases (oxygen and steam) in a rubble zone, which react with the combustible gas in the channel and with coal on the coal face. It is possible to reach quasi-steady state conditions for the channel during the gasification process. However, it is also possible to incorporate transient heat conduction effects.

- The reduced carbon footprint can be brought about by first injection of mainly oxygen to heat up the formation and subsequently injection of pure water or steam. In the first period a gas with a high CO_2 content is produced. After switching to pure water or steam injection thermodynamic calculations suggest that a gas with a relatively low carbon dioxide content, but high hydrogen content can be produced. The result shows a reasonable agreement with a recent field trial in Katowice, Poland.

- The process can become sustainable if a mixture of steam and oxygen is injected. The product gas contains some carbon dioxide.

6.3. Application of NegSat method in the simulation of formation dry-out in aquifer injection of CO_2

- The advantage of the NegSat approach for two-phase two-component system is that it is not necessary to use different sets of equations in one and two phase flow. However, the value of some of the variables must be changed.

- In the three phase flow, the NegSat can be effectively applied by a-priori separating the stagnant solid phase from the three phase mixture in the thermodynamic model.

- The primary variables in the three phase system are S^s, S^g, u and the primary variables in the two phase system are S^g, u, $\bar{x}^l_{\text{salt}}$.

- The solid saturation has only a minor influence on the pressure distribution in the system and therefore the effect on the compression energy is only minor.

- By preflushing the aquifer with pure water, the salt precipitation near the injection well during the CO_2 injection can be avoided.

- Comparison of our numerical solution to analytical solutions reported in the literature shows excellent agreement.

6.4. Experimental investigation of enhanced CO$_2$ mass transfer due to the density-driven natural convection in aquifer storage of CO$_2$

- A set of pressure decay experiments in a relatively large experimental set-up were performed to measure the onset time and the rate of mass transfer of CO$_2$ in water-saturated porous media.

- A mathematical model was used to study the effect of heat of dissolution of CO$_2$ on the rate of mass transfer.

- The effect of heat of dissolution of CO$_2$ in water on the rate of mass transfer is negligible.

- Various relations for the calculation of onset time were compared with the deviation of experimentally measured pressure decay data from calculated pressure decay data for a pure diffusion model.

- The effect of a capillary transition zone on the density-driven flow of CO$_2$ in water was studied.

- A capillary transition zone can considerably increase the mass transfer rate of CO$_2$ in water.

- Our numerical simulations give the best match with experimental pressure decay data when a capillary transition zone is considered in the mathematical model.

6.5. Recommendations

1. Exergetic applicability of carbon capture and sequestration for low emission carbon dioxide fuel consumption, can presently only be achieved if the energy-intensive step of nitrogen-CO$_2$ separation prior to aquifer injection can be avoided. New separation technology could help to make coal usage competitive with natural gas usage as to its carbon footprint.

2. To avoid water intrusion into the UCG cavity, the pressure must be slightly above the hydrostatic pressure. To study the possibility of underground gasification for European deep coal layers, availability of high quality data from high pressure pilot experiments are crucial.

3. The effect of coal composition and its reaction rate with oxygen, CO$_2$, and CO on the quality of UCG product needs to be investigated.

4. To show the effectiveness of NegSat method in the modeling of two-phase compositional flow in porous media, it must be thoroughly compared from a numerical point of view with the single-phase/twho-phase switching method.

5. The most important problem in measuring the onset time of natural convection is the adiabatic expansion effect at the beginning of the experiment, which decreases the temperature of the gas inside the cylinder. To have a more stable initial condition and for a better quantification of the onset time, this temperature fluctuation must be minimized.

A. Numerical solution of 1-D conduction heat transfer

An implicit finite difference method is implemented to convert the partial differential equation to a set of linear algebraic equations. For the interpretation of symbols, see the nomenclature section. For $X = 0$ the equation for time step $k + 1$ reads

$$
\begin{aligned}
T_{\beta,1}^{k+1}\left(1 + \frac{2\Delta\tau}{\Delta X^2}\right) + T_{\beta,2}^{k+1}\left(\frac{-Pe\Delta\tau}{\Delta X} - \frac{\Delta\tau}{\Delta X^2}\right) &= \\
T_{\beta,1}^{k} - T_{\beta,s}^{k+1}\left(\frac{Pe\Delta\tau}{\Delta X} - \frac{\Delta\tau}{\Delta X^2}\right) & \quad\quad\quad\quad\quad\quad (A.1)
\end{aligned}
$$

where $\Delta X = 1/n$ and $\Delta\tau = \frac{\Delta t/t_R}{m}$. For $0 < X < 1$, one can obtain

$$
\begin{aligned}
T_{\beta,i-1}^{k+1}\left(\frac{Pe\Delta\tau}{\Delta X} - \frac{\Delta\tau}{\Delta X^2}\right) + T_{\beta,i}^{k+1}\left(1 + \frac{2\Delta\tau}{\Delta X^2}\right) &+ \\
T_{\beta,i+1}^{k+1}\left(\frac{-Pe\Delta\tau}{\Delta X} - \frac{\Delta\tau}{\Delta X^2}\right) = T_{\beta,i}^{k}\left(\frac{Pe\Delta\tau}{\Delta X} - \frac{\Delta\tau}{\Delta X^2}\right). & \quad\quad (A.2)
\end{aligned}
$$

For $X = 1$, one can obtain

$$
-T_{\beta,n-1}^{k+1}\left(\frac{\Delta\tau}{\Delta X^2}\right) + T_{\beta,n}^{k+1}\left(1 + \frac{\Delta\tau}{\Delta X^2}\right) = T_{\beta,n}^{k}. \quad\quad (A.3)
$$

The initial condition for $\tau = 0$ or $k = 0$ is $T_{\beta,i}^{0} = T_{\beta}^{0}(i\Delta X)$. This approach results in a set of n linear equations with a tri-diagonal matrix of coefficients for each time step. Those can be solved by the method of Thomas [127].

The average heat flux at the solid surface for the period $[\ t,\ \ t + \Delta t\ ]$ is calculated by using the trapezoidal integration and by calculating the derivative $\partial T\left(X = 0, \tau\right)/\partial X$

$$
\begin{aligned}
Q_{0,\beta}\left(t\right) = \rho_\beta \bar{\alpha}_\beta C_\beta t_R \frac{\Delta\tau}{L\Delta t} \times \\
\sum_{k=1}^{m}\left(\frac{\left(-4T_{\beta,1}^{k} - T_{\beta,2}^{k} - 3T_{\beta,s}^{k}\right) + \left(-4T_{\beta,1}^{k-1} - T_{\beta,2}^{k-1} - 3T_{\beta,s}^{k-1}\right)}{4\Delta X}\right). \quad (A.4)
\end{aligned}
$$

B. Reaction equilibrium constant

The equilibrium constant for the reaction j is calculated by

$$K_j = \exp\left(\frac{-\Delta g_j^o}{RT}\right). \tag{B.1}$$

The change of the molar Gibbs energy of the reaction $\Delta g^o(T)$ is equal to $\Delta h^0(T) - T\Delta s^o(T)$. The enthalpy and entropy at temperature T can be found from the Eq. (B.2) and Eq. (B.3) [146].

$$\Delta h^o = \Delta h_0^o + R \int_{T_0}^{T} \frac{\Delta c_p^o}{R} \mathrm{d}T \tag{B.2}$$

$$\Delta s^o = \Delta s_0^o + R \int_{T_0}^{T} \frac{\Delta c_p^o}{R} \frac{\mathrm{d}T}{T} \tag{B.3}$$

where Δh_0^o, Δs_0^o, and Δc_p^o are specific values for each reaction and can be calculated using equations Eq. (B.4), Eq. (B.5), and Eq. (B.6) respectively where $\nu_{i,j}$ is the stoichiometric coefficient of the component i in the reaction j, which is negative for the reactants and is positive for the products. Hence one can obtain

$$\Delta h_{0,j}^o = \sum_i \nu_{i,j} \Delta h_{0,i}^o, \tag{B.4}$$

$$\Delta s_{0,j}^o = \sum_i \nu_{i,j} \Delta s_{0,i}^o, \tag{B.5}$$

$$\Delta c_{p,j}^o = \sum_i \nu_{i,j} c_{p,i}^o, \tag{B.6}$$

where $\Delta h_{0,i}^o$ and $\Delta g_{0,i}^o$ are the enthalpy of formation and the Gibbs energy of formation of component i at standard pressure, e.g., 1 bar and reference temperature of T_0, which is often 298 K and $c_{p0,i}^o$ is the heat capacity of component i at standard pressure. These values are reported in standard thermodynamic textbooks

[121, 146]. To find $\Delta s_{0,i}^o$ the following thermodynamic relation can be applied

$$\Delta s_{0,i}^o = \frac{\Delta h_{0,i}^o - \Delta g_{0,i}^o}{T_0}. \tag{B.7}$$

Thermodynamic properties of coal are estimated with the empirical equations in reference [53] using the ultimate analysis data of Barbara coal.

B.1. Physical parameters

Table B.1 shows the values of $c_{p,i}^o$, $\Delta h_{0,i}^o$, and $\Delta g_{0,i}^o$ for gas species.

Table B.1.: Specific heat capacity $(c_{p,i}^o/R = c_1 + c_2 T + c_3 T^2 + c_4/T)$, standard enthalpy and Gibbs free energies of formation for the gaseous species [146]

Component	c_1	$c_2 \times 10^3$	$c_3 \times 10^6$	$c_4 \times 10^{-5}$	$\Delta h_{0,i}^o$ (J/mol)	$\Delta g_{0,i}^o$ (J/mol)
CO_2	5.457	1.045	0.0	-1.157	-393509	-394359
CO	3.376	0.557	0.0	-0.031	-110525	-137169
H_2	3.249	0.422	0.0	0.083	0.0	0.0
H_2O	3.470	1.450	0.0	0.121	-241818	-228572
CH_4	1.702	9.081	-2.164	0.0	-74520	-50460
N_2	3.2733	0.504	0.0	0.0	0.0	0.0
O_2	4.1646	0.1299	0.0	-0.9452	0.0	0.0

C. Calculation of transport parameters of a gas phase mixture

The calculation of diffusivity and viscosity for a gas mixture at high pressure has been discussed in [138]. It is repeated here for more convenience.

C.1. Diffusivity

In reference [22], the following equation has been proposed for the calculation of binary diffusion coefficient

$$D_{ij} = \frac{a}{P} \left(\frac{T}{(T_{c,i}T_{c,j})^{1/2}} \right)^b (P_{c,i}P_{c,j})^{1/3} (T_{c,i}T_{c,j})^{5/12} \left(\frac{1}{M_i} + \frac{1}{M_j} \right)^{1/2}, \qquad \text{(C.1)}$$

where D_{ij} [cm^2/s] is the diffusion coefficient of component i in j, $a = 3.640 \times 10^{-4}$ and $b = 2.334$ when i or j is water and $a = 2.745 \times 10^{-4}$ and $b = 1.823$ for other components, P [atm] is pressure, $P_{c,i}$ is the critical pressure of component i, T [K] is temperature, $T_{c,i}$ [K] is the critical temperature of component i, and M_i [gr/mol] is the molecular weight of component i. But this equation should not be used when one of the components is hydrogen. In the model, the following relation is used [138]

$$\frac{\rho D_{ij}}{(\rho D_{ij})^o} = a \left(\frac{\mu}{\mu^o} \right)^{b+cP_r}, \qquad \text{(C.2)}$$

where $a = 1.07$, $b = -0.27 - 0.38\omega$, $c = -0.05 + 0.1\omega$. The values of accentric factor ω and reduced pressure P_r for a binary mixture with mole fraction x_i are calculated as

$$\omega = x_i\omega_i + x_j\omega_j \qquad \text{(C.3)}$$

$$P_r = P/\left(x_iP_{c,i} + x_jP_{c,j} \right). \qquad \text{(C.4)}$$

The value for $(\rho D_{ij})^o$ which is the product of density and binary diffusivity for a dilute gas mixture is calculated using the Chapman-Enskog theory

$$(\rho D_{ij})^o = \frac{2.2648 \times 10^{-6} T^{0.5} \left(\frac{1}{M_i} + \frac{1}{M_j}\right)^{0.5}}{\sigma_{ij}^2 \Omega_{ij}}, \tag{C.5}$$

where the molecular parameters are estimated by Stiel-Thodos correlations

$$\sigma_{ij} = \frac{\sigma_i + \sigma_j}{2}, \tag{C.6}$$

$$\sigma_i = 1.866 V_{c,i}^{1/3} Z_{c,i}^{-6/5}, \tag{C.7}$$

$$\Omega_{ij} = \frac{1.06036}{T*_{ij}^{0.1561}} + 0.193 \exp\left(-0.47635 T*_{ij}\right) +$$
$$1.76474 \exp\left(-3.89411 T*_{ij}\right) + 1.03587 \exp\left(-1.52996 T*_{ij}\right), \tag{C.8}$$

$$T*_{ij} = T/\epsilon_{ij}, \tag{C.9}$$

$$\epsilon_{ij} = \left(\epsilon_i \epsilon_j\right)^{0.5}, \tag{C.10}$$

$$\epsilon_i = 65.3 T_{c,i} Z_{c,i}^{18/5}. \tag{C.11}$$

If T and T_c are used in [K] and V_c in [m³/kmol], then $(\rho D_{ij})^o$ will be in [kmol/(m.s)]. Z_c is the compressibility factor at critical point and is calculated as

$$Z_c = \frac{P_c V_c}{R T_c}. \tag{C.12}$$

C.2. Viscosity

At low pressure, the gas viscosity of each component μ_i^o [mPa.s] is calculated by the Stiel and Thodos correlation

$$\mu_i^o \xi_i = \begin{cases} 34 \times 10^{-5} T_{r,i}^{0.94} & , T_{r,i} \leqslant 1.5 \\ 17.78 \times 10^{-5} \left(4.58 T_{r,i} - 1.67\right)^{5/8} & , T_{r,i} > 1.5 \end{cases} \tag{C.13}$$

where $T_{r,i} = T/T_{c,i}$ (T in [K])and

$$\xi_i = \frac{T_{c,i}^{1/6}}{M_i^{1/2}\left(0.987P_{c,i}\right)^{2/3}}. \tag{C.14}$$

The low pressure viscosity for the binary mixture is calculated by the following mixing rule

$$\mu^o = \frac{x_i\mu_i^o M_i^{1/2} + x_j\mu_j^o M_j^{1/2}}{x_i M_i^{1/2} + x_j M_j^{1/2}}. \tag{C.15}$$

Using the Jossi equation, the predicted viscosity for low pressure μ^o is corrected as

$$\left[\left(\mu - \mu^o\right)\xi + 10^{-4}\right]^{1/4} = 0.1023 + 0.023364\rho_r + 0.058533\rho_r^2$$
$$- 0.040758\rho_r^3 + 0.0093324\rho_r^4, \tag{C.16}$$

where the reduced density ρ_r and ξ are calculated as

$$\rho_r = \frac{\left(x_i V_{c,i} + x_j V_{c,j}\right)}{x_i M_i + x_j M_j}\rho, \tag{C.17}$$

$$\xi = \frac{\left(x_i T_{c,i} + x_j T_{c,j}\right)^{1/6}}{\left(x_i M_i + x_j M_j\right)^{0.5}\left[0.987\left(x_i P_{c,i} + x_j P_{c,j}\right)\right]^{2/3}}. \tag{C.18}$$

The value of density ρ [kg/m^3] is calculated using the Peng-Robinson equation of state.

C.3. Density

The Peng-Robinson equation of state [118] is implemented to calculate the compressibility factor Z at given temperature T, pressure P, and mole fraction x_i. The density ρ is calculated as

$$\rho = \frac{PM}{ZRT}, \tag{C.19}$$

where M is the molecular weight of the mixture

$$M = \sum_i x_i M_i. \tag{C.20}$$

The Van Der Waals mixing rule for the Peng-Robinson equation of state is used. It is assumed that all the binary interaction parameters are equal to zero.

D. Negative flash for CO_2-water-salt system

In this section, relationships for the gas-liquid-solid equilibrium compositions of CO_2, water, and salt are developed at temperature T and pressure p with a known total composition of $x_{CO_2}^t$, x_{water}^t, and x_{salt}^t. In this approach, first the amount of precipitated solid salt is calculated. Then the precipitated salt is separated from the initial mixture to obtain a mixture of gas and liquid phases as well as a separate solid phase (see Fig. 4.5). Finally, the negative flash scheme is applied to the fluid phases. For the definition of a few of the variables that are used in this section, see Fig. D.1. In the formulation, three assumptions are made:

- The presence of CO_2 in the liquid phase (brine) does not affect the solubility of salt in water. The solubility of salt in water is a function of the temperature. It is assumed that salt solubility is independent of pressure. The solubility data are reported in [121]. The following function is fitted to the experimental NaCl solubility data [121]:

$$\bar{x}_{salt,max}^l = \exp\left(\frac{\zeta_1}{T^2} + \frac{\zeta_2}{T} + \zeta_3\right), \tag{D.1}$$

  where $\bar{x}_{salt,max}^l$ [mol salt/mol solution] is the solubility (mole fraction) of NaCl in water, and $\zeta_1 = 98183$, $\zeta_2 = -704.6$, $\zeta_3 = -1.038$. The dash sign on $\bar{x}_{salt}^l$ is used to define it as the number of moles of salt in the liquid phase (n_{salt}^l) divided by the number of moles of salt and water $(n_{salt}^l + n_{water}^l)$ in the liquid phase, i.e. $n_{salt}^l/\left(n_{salt}^l + n_{water}^l\right)$.

- The solid phase consists of pure NaCl, i.e., $x_{salt}^s = 1$, $x_{CO_2}^s = 0$, and $x_{water}^s = 0$

- For the mixture of CO_2-brine, the gas and liquid equilibrium compositions of water and CO_2 are functions of pressure p, temperature T, and mole fraction of salt in brine in the liquid phase $\bar{x}_{salt}^l$, which are calculated in an iterative procedure using the thermodynamic relations of Section 4.4:

$$x_{CO_2,eq}^l = \frac{\hat{\Phi}_{CO_2}^g\left(p, T, \bar{x}_{salt}^l, x_{CO_2,eq}^g\right)}{\hat{\Phi}_{CO_2}^l\left(p, T, \bar{x}_{salt}^l, x_{CO_2,eq}^l\right)} x_{CO_2,eq}^g,$$

$$x_{water,eq}^l = 1 - x_{CO_2,eq}^l \text{ and } x_{water,eq}^g = 1 - x_{CO_2,eq}^g, \tag{D.2}$$

where $x^l_{CO_2,eq}$ and $x^g_{CO_2,eq}$ are the equilibrium compositions obtained by performing a negative flash calculation on a CO_2-water mixture after separating the salt from the liquid phase, and $\hat{\Phi}^\alpha_{CO_2}$ are the fugacity coefficients of CO_2 in phase α, which is calculated using the PRSV equation of state.
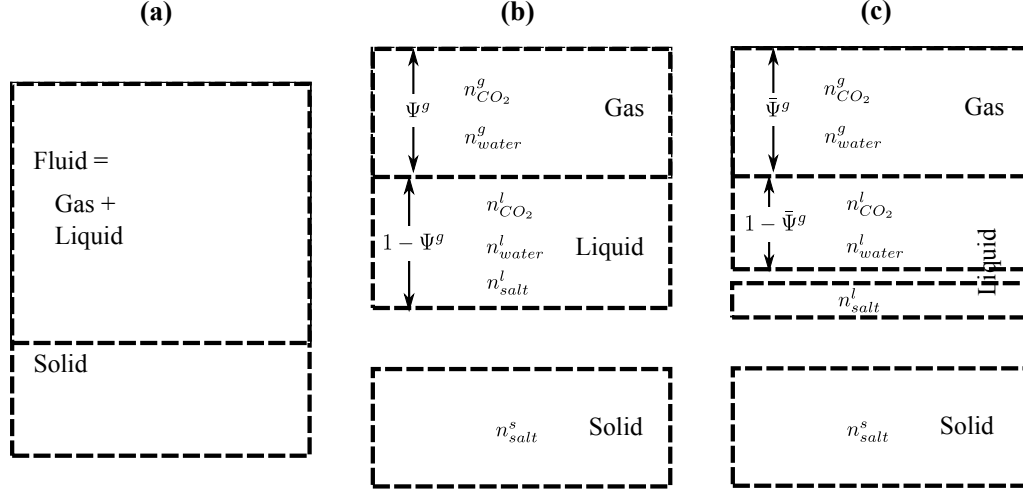

Figure D.1.: A schematic representation of the steps in the three phase flash calculation of CO_2-water-salt mixture. (a) the initial mixture that is separated into a fluid phase and a solid phase; (b) the solid phase is separated from the equilibrium mixture and the fluid phase is flashed to a gas phase with a molar phase fraction of Ψ^g and a liquid phase with a molar phase fraction of $1 - \Psi^g$; (c) salt is separated from the liquid phase, which results in a new molar phase fraction $\bar{\Psi}^g$ for the gas phase and $1 - \bar{\Psi}^g$ for the liquid phase. Note that the molar phase fractions Ψ^g and $\bar{\Psi}^g$ are defined as $\Psi^g = \frac{n^g_{CO_2} + n^g_{water}}{n^g_{CO_2} + n^g_{water} + n^l_{CO_2} + n^l_{water} + n^l_{salt}}$ and $\bar{\Psi}^g = \frac{n^g_{CO_2} + n^g_{water}}{n^g_{CO_2} + n^g_{water} + n^l_{CO_2} + n^l_{water}}$, where n^g_i and n^l_i are the number of moles of component i in the gas and liquid phases, respectively. n^s_{salt} is the number of moles of salt in the solid phase.

Given the overall composition of the mixture x^t_i, pressure p and temperature T, the three phase flash calculation is performed through the following iterative scheme:

1. Calculate the salt solubility $\bar{x}^l_{salt,max}$ at temperature T using Eq. (D.1).

2. Assume that all the water in the mixture is in the liquid phase and can dissolve the salt. The mole fraction of salt in the liquid phase cannot exceed the solubility ($\bar{x}^l_{salt,max}$). So salt mole fraction in the liquid phase $\bar{x}^l_{salt,est}$ can be estimated as

$$\bar{x}^l_{salt,est} = \min\left(\bar{x}^l_{salt,max}, \ x^t_{salt} / \left(x^t_{salt} + x^t_{water}\right)\right), \tag{D.3}$$

3. Use Eq. (D.2) with the estimated salt mole fraction in brine to calculate equilibrium mole fractions of CO_2 and water.

4. Perform the two-phase negative flash for the CO_2-water mixture with composition $\left(x^t_{CO_2}, x^t_{\text{water}}\right) / \left(x^t_{CO_2} + x^t_{\text{water}}\right)$ to calculate $\bar{\Psi}^g$, i.e.,

$$\bar{\Psi}^g = \frac{\frac{x^t_{CO_2}}{x^t_{CO_2}+x^t_{\text{water}}} - x^l_{CO_2,eq}}{x^g_{CO_2,eq} - x^l_{CO_2,eq}}, \tag{D.4}$$

where $\bar{\Psi}^g$ is the gas molar phase fraction in the fluid phase excluding the dissolved salt in brine (denoted by a dash sign) and only including CO_2 and water (see Fig. D.1). $\bar{\Psi}^g$ is calculated by rearranging Eq. (4.46). For more details on the mass balance relations, see Section 4.5 or references [169, 166, 126, 145].

5. Based on the value of $\bar{\Psi}^g$, update the estimated value of salt mole fraction in brine using

$$\left(\bar{x}^l_{\text{salt},est}\right)^{new} =$$
$$\begin{cases} \min\left(\bar{x}^l_{\text{salt},max}, \dfrac{x^t_{\text{salt}}}{x^t_{\text{salt}}+\left(x^t_{CO_2}+x^t_{\text{water}}\right)\left(1-\bar{\Psi}^g\right)x^l_{\text{water},eq}}\right), & 0 \le \bar{\Psi}^g \le 1 \\ \bar{x}^l_{\text{salt},est} & \bar{\Psi}^g < 0 \\ 0 & \bar{\Psi}^g > 1 \end{cases}, \tag{D.5}$$

where in the first line, the term $\left(x^t_{CO_2} + x^t_{\text{water}}\right)\left(1 - \bar{\Psi}^g\right)x^l_{\text{water},eq}$ accounts for the amount of water that is in the liquid phase. The second line ($\bar{\Psi}^g < 0$) denotes that all the initial water goes into the liquid phase. The third line ($\bar{\Psi}^g > 1$) denotes that no liquid phase exists and therefore the salt mole fraction in the liquid phase is zero.

6. Check for the convergence criterion, i.e.,

$$\left|\left(\bar{x}^l_{\text{salt},est}\right)^{new} - \bar{x}^l_{\text{salt},est}\right| < \varepsilon_1,$$

and if it is not satisfied, set $\bar{x}^l_{\text{salt},est} = \left(\bar{x}^l_{\text{salt},est}\right)^{new}$ and go back to step item 3. Otherwise, go on to the next step.

7. calculate Ψ^s by

$$
\Psi^s =
\begin{cases}
\max\left(0,\ x_{\text{salt}}^t - \dfrac{\left(\bar{x}_{\text{salt},est}^l\right)^{new}\left(x_{CO_2}^t + x_{\text{water}}^t\right)\left(1-\bar{\Psi}^g\right)x_{\text{water},eq}^l}{1-\left(\bar{x}_{\text{salt},est}^l\right)^{new}}\right), & 0 \le \bar{\Psi}^g \le 1 \\[3ex]
\max\left(0,\ x_{\text{salt}}^t - \dfrac{\left(\bar{x}_{\text{salt},est}^l\right)^{new}x_{\text{water}}^t}{1-\left(\bar{x}_{\text{salt},est}^l\right)^{new}}\right), & \bar{\Psi}^g < 0 \\[3ex]
x_{\text{salt}}^t & \bar{\Psi}^g > 1
\end{cases}
$$

$$\tag{D.6}$$

where Ψ^s is the solid molar phase fraction (number of moles of precipitated salt divided by the total number of moles in the whole mixture). In the above equation, the second term (the large fraction) in the first and second lines denotes the fraction of initial salt that is dissolved in the liquid phase. If the amount of dissolved salt is less than the initial amount of salt in the mixture, no salt precipitation happens and the solid molar phase fraction is zero. The third line shows that when no liquid phase exists, all the initial salt goes to the solid phase.

In step item 4 of the above mentioned simplified flash algorithm, the dissolved salt is separated from the mixture of CO_2-brine in the calculation of the molar phase fraction ($\bar{\Psi}^g$) because salt is a nonvolatile component and does not appear in the gas phase. This means that the K-value of salt is zero and according to Eq. (4.45), the gas molar phase fraction cannot be higher than one (liquid molar phase fraction cannot be negative, i.e., no negative flash). However, by separating salt from the brine, one will be able to use the negative flash algorithm. After using the procedure described above, solid molar phase fraction Ψ^s, equilibrium mole fractions of CO_2 and water ($x_{CO_2,eq}^g$, $x_{\text{water},eq}^g$, $x_{CO_2,eq}^l$, and $x_{\text{water},eq}^l$), gas molar phase fraction $\bar{\Psi}^g$ for the CO_2-brine mixture (excluding salt), and the mole fraction of salt in water in the liquid phase $\bar{x}_{\text{salt}}^l$ are obtained. Now, these values and mass balance relations will be used to include the dissolved salt in the liquid phase and calculate the molar compositions of the equilibrium phases and the molar and volumetric phase fractions of the gas phase, i.e., Ψ^g and S^g. Here the dash signs on Ψ^g and S^g are eliminated to indicate the fluid phase including the dissolved salt in the liquid phase. This is performed by writing the mass balance relations for three possibilities: two-phase gas liquid ($0 \le \bar{\Psi}^g \le 1$), single gaseous phase ($\bar{\Psi}^g > 1$), and single liquid phase ($\bar{\Psi}^g < 0$). The objective is to investigate the validity of Eq. (4.46) for the fluid phase, i.e.

$$
x_i^f = \Psi^g x_i^g + \left(1 - \Psi^g\right) x_i^l, \tag{D.7}
$$

in the single gaseous and single liquid regions. First the values of Ψ^g, x_i^g, and x_i^l are calculated in the two-phase gas liquid equilibrium region and then it will be shown that the above mentioned equation is also valid in the single gaseous and single

liquid regions.

D.1. Gas-liquid equilibrium composition for the two-phase region ($0 \leq \bar{\Psi}^g \leq 1$)

To calculate the molar composition of each phase and the actual molar phase fraction of the gas phase Ψ^g, one has to add the separate dissolved salt back to the liquid phase. First, the number of moles of each component in the liquid and gas phase need to be calculated as a function of Ψ^g, $x^l_{CO_2,eq}$, and $x^g_{CO_2,eq}$. By writing the mass balance for the gas phase, one can obtain

$$n^g_{CO_2} = N^t \left(x^t_{CO_2} + x^t_{water} \right) \bar{\Psi}^g x^g_{CO_2,eq}, \tag{D.8}$$

$$n^g_{water} = N^t \left(x^t_{CO_2} + x^t_{water} \right) \bar{\Psi}^g x^g_{water,eq}, \tag{D.9}$$

where $n^g_{CO_2}$ [mol] and n^g_{water} [mol] are the number of moles of CO_2 and water in the gas phase, N^t [mol] is the total number of moles in the mixture, $\bar{\Psi}^g$ is the molar gas fraction (dash sign denotes that the amount of salt in the liquid phase is not included), and $x^g_{CO_2,eq}$ and $x^g_{water,eq}$ are the equilibrium mole fractions of CO_2 and water in the gas phase. The eq subscript denotes that the effect of salt is included in the gas-liquid flash calculation but salt is separated from the liquid phase. The number of moles of salt in the gas phase is zero. The mole fraction of each component in the gas phase is defined as

$$x^g_{CO_2} = \frac{n^g_{CO_2}}{n^g_{CO_2} + n^g_{water}} = x^g_{CO_2,eq}, \tag{D.10}$$

$$x^g_{water} = \frac{n^g_{water}}{n^g_{CO_2} + n^g_{water}} = x^g_{water,eq}. \tag{D.11}$$

By writing the mass balance for the liquid phase, one can obtain

$$n^l_{CO_2} = N^t \left(x^t_{CO_2} + x^t_{water} \right) \left(1 - \bar{\Psi}^g \right) x^l_{CO_2,eq},$$

$$n^l_{water} = N^t \left(x^t_{CO_2} + x^t_{water} \right) \left(1 - \bar{\Psi}^g \right) x^l_{water,eq},$$

$$n^l_{salt} = \frac{\bar{x}^l_{salt}}{1 - \bar{x}^l_{salt}} n^l_{water} = \frac{\bar{x}^l_{salt}}{1 - \bar{x}^l_{salt}} N^t \left(x^t_{CO_2} + x^t_{water} \right) \left(1 - \bar{\Psi}^g \right) x^l_{water,eq},$$

where n^l_i denotes the number of moles of component i in the liquid phase. The mole fraction of each component is calculated by dividing the number of moles of that

component by the total number of moles in that phase, i.e.,

$$x^l_{CO_2} = \frac{n^l_{CO_2}}{n^l_{CO_2} + n^l_{water} + n^l_{salt}} = \frac{x^l_{CO_2,eq}}{1 + \frac{\bar{x}^l_{salt}}{1 - \bar{x}^l_{salt}} x^l_{water,eq}}, \tag{D.12}$$

$$x^l_{water} = \frac{n^l_{water}}{n^l_{CO_2} + n^l_{water} + n^l_{salt}} = \frac{x^l_{water,eq}}{1 + \frac{x^l_{salt}}{1 - x^l_{salt}} x^l_{water,eq}}, \tag{D.13}$$

$$x^l_{salt} = \frac{n^l_{salt}}{n^l_{CO_2} + n^l_{water} + n^l_{salt}} = \frac{\frac{\bar{x}^l_{salt}}{1 - \bar{x}^l_{salt}} x^l_{water,eq}}{1 + \frac{\bar{x}^l_{salt}}{1 - \bar{x}^l_{salt}} x^l_{water,eq}}. \tag{D.14}$$

Remember that in the derivation of above equations, one need to use $x^l_{CO_2,eq} + x^l_{water,eq} = 1$. The molar phase fraction of the gas phase Ψ^g in the gas-liquid equilibrium (including dissolved salt in the liquid phase) is defined as the total number of moles in the gas phase divided by the total number of moles in the liquid and gas phases (including salt), i.e.,

$$\Psi^g = \frac{n^g_{CO_2} + n^g_{water} + n^g_{salt}}{n^g_{CO_2} + n^g_{water} + n^g_{salt} + n^l_{CO_2} + n^l_{water} + n^l_{salt}} = \frac{\bar{\Psi}^g}{1 + x^l_{water,eq}\left(1 - \bar{\Psi}^g\right)\frac{\bar{x}^l_{salt}}{1 - \bar{x}^l_{salt}}}. \tag{D.15}$$

The molar concentrations of vapor and liquid phases (C^g and C^l) are calculated using Eq. (4.52) and Eq. (4.51) respectively. It is assumed that the molar concentration of the solid phase to be constant and equal to the molar concentration of pure NaCl [121], i.e., C^s=37005 mol/m³. The gas saturation for the gas-liquid equilibrium is calculated by Eqs. (4.49) and (4.50), i.e.,

$$S^g = \frac{\Psi^g/C^g}{\Psi^g/C^g + (1 - \Psi^g)/C^l}. \tag{D.16}$$

The solid saturation (volumetric phase fraction) S^s is calculated by

$$S^s = \frac{\Psi^s/C^s}{\Psi^s/C^s + (1 - \Psi^s)\left(\Psi^g/C^g + (1 - \Psi^g)/C^l\right)}. \tag{D.17}$$

D.2. Single gaseous phase ($\bar{\bar{\Psi}}^g > 1$)

When $\bar{\bar{\Psi}}^g > 1$ there is no liquid in the system where, the salt mole fraction in water is assumed to be zero ($\bar{x}^l_{\text{salt}} = 0$). The composition of the fluid phase x^f_i (see Fig. D.1) is calculated by

$$x^f_{\text{CO}_2} = \frac{x^t_{\text{CO}_2}}{x^t_{\text{CO}_2} + x^t_{\text{water}}}, \quad x^f_{\text{water}} = \frac{x^t_{\text{water}}}{x^t_{\text{CO}_2} + x^t_{\text{water}}}, \quad x^f_{\text{salt}} = 0. \tag{D.18}$$

Remember that even though the mixture is a single gaseous phase, the superscript f is used instead of g, to denote an imaginary gas-liquid equilibrium (negative flash). The values of Ψ^g, x^g_i, and x^l_i are replaced from Eq. (D.15), Eqs. (D.10)-(D.11), and Eqs. (D.12)-(D.14) in Eq. (D.7) for CO_2 to obtain

$$x^f_{\text{CO}_2} = \frac{\bar{\bar{\Psi}}^g}{1 + x^l_{\text{water},eq}\left(1 - \bar{\bar{\Psi}}^g\right)\frac{\bar{x}^l_{\text{salt}}}{1-\bar{x}^l_{\text{salt}}}} x^g_{\text{CO}_2,eq} +$$

$$\left(1 - \frac{\bar{\bar{\Psi}}^g}{1 + x^l_{\text{water},eq}\left(1 - \bar{\bar{\Psi}}^g\right)\frac{\bar{x}^l_{\text{salt}}}{1-\bar{x}^l_{\text{salt}}}}\right) \frac{x^l_{\text{CO}_2,eq}}{1 + \frac{\bar{x}^l_{\text{salt}}}{1-\bar{x}^l_{\text{salt}}} x^l_{\text{water},eq}}. \tag{D.19}$$

It is known from Eq. (D.5) that for a single gaseous phase, $\bar{x}^l_{salt} = 0$, which can be replaced in the above equation to obtain

$$x^f_{\text{CO}_2} = \bar{\bar{\Psi}}^g x^g_{\text{CO}_2,eq} + \left(1 - \bar{\bar{\Psi}}^g\right) x^l_{\text{CO}_2,eq}. \tag{D.20}$$

By replacing $\bar{x}^l_{salt} = 0$ in Eq. (D.15), one can obtain $\Psi^g = \bar{\bar{\Psi}}^g$. Therefore, Eq. (D.20) is converted to

$$x^f_{\text{CO}_2} = \Psi^g x^g_{\text{CO}_2,eq} + (1 - \Psi^g) x^l_{\text{CO}_2,eq}, \tag{D.21}$$

which is in agreement with Eq. (D.4). With the same approach, one can show that other equilibrium compositions calculated by Eqs. (D.10)-(D.11) and Eqs. (D.12)-(D.14) satisfy the mass balance for the single gaseous phase ($\bar{\bar{\Psi}}^g > 1$).

D.3. Single liquid phase ($\bar{\bar{\Psi}}^g < 0$)

The total composition of the fluid phase x^f_i (see Fig. D.1), which is a single liquid when $\bar{\bar{\Psi}}^g < 0$ is calculated by

$$x^f_{\text{CO}_2} = \frac{x^t_{\text{CO}_2}}{x^t_{\text{CO}_2} + x^t_{\text{water}} + \frac{\bar{x}^l_{\text{salt}}}{1-\bar{x}^l_{\text{salt}}} x^t_{\text{water}}} = \frac{\frac{x^t_{\text{CO}_2}}{x^t_{\text{CO}_2}+x^t_{\text{water}}}}{1 + \frac{\bar{x}^l_{\text{salt}}}{1-\bar{x}^l_{\text{salt}}} \frac{x^t_{\text{water}}}{x^t_{\text{CO}_2}+x^t_{\text{water}}}}, \tag{D.22}$$

$$x_{\text{water}}^f = \frac{x_{\text{water}}^t}{x_{CO_2}^t + x_{\text{water}}^t + \frac{\bar{x}_{\text{salt}}^l}{1-\bar{x}_{\text{salt}}^l}x_{\text{water}}^t} = \frac{\frac{x_{\text{water}}^t}{x_{CO_2}^t + x_{\text{water}}^t}}{1 + \frac{\bar{x}_{\text{salt}}^l}{1-\bar{x}_{\text{salt}}^l}\frac{x_{\text{water}}^t}{x_{CO_2}^t + x_{\text{water}}^t}}, \tag{D.23}$$

$$x_{\text{salt}}^f = \frac{\frac{\bar{x}_{\text{salt}}^l}{1-\bar{x}_{\text{salt}}^l}x_{\text{water}}^t}{x_{CO_2}^t + x_{\text{water}}^t + \frac{\bar{x}_{\text{salt}}^l}{1-\bar{x}_{\text{salt}}^l}x_{\text{water}}^t} = \frac{\frac{\bar{x}_{\text{salt}}^l}{1-\bar{x}_{\text{salt}}^l}\frac{x_{\text{water}}^t}{x_{CO_2}^t + x_{\text{water}}^t}}{1 + \frac{\bar{x}_{\text{salt}}^l}{1-\bar{x}_{\text{salt}}^l}\frac{x_{\text{water}}^t}{x_{CO_2}^t + x_{\text{water}}^t}}, \tag{D.24}$$

where the values of $\frac{x_{CO_2}^t}{x_{CO_2}^t + x_{\text{water}}^t}$ and $\frac{x_{\text{water}}^t}{x_{CO_2}^t + x_{\text{water}}^t}$ can be expressed in terms of $\bar{\Psi}^g$, $x_{i,eq}^g$, and $x_{i,eq}^l$. This substitution is done for CO_2, which after a few algebraic operations reads

$$x_{CO_2}^f = \frac{\bar{\Psi}^g x_{CO_2,eq}^g + \left(1 - \bar{\Psi}^g\right)x_{CO_2,eq}^l}{1 + \frac{\bar{x}_{\text{salt}}^l}{1-\bar{x}_{\text{salt}}^l}\left(\bar{\Psi}^g x_{\text{water},eq}^g + \left(1 - \bar{\Psi}^g\right)x_{\text{water},eq}^l\right)}. \tag{D.25}$$

The equilibrium mole fraction of water in the gas phase of a CO_2-water mixture is very small compared to its value in the liquid phase. Also, $\bar{\Psi}^g$ is a very small negative number for the subcooled region of CO_2-water equilibrium mixture. Therefore, $\bar{\Psi}^g x_{\text{water},eq}^g \ll \left(1 - \bar{\Psi}^g\right)x_{\text{water},eq}^l$ and the term $\bar{\Psi}^g x_{\text{water},eq}^g$ can be ignored in Eq. (D.25), at the expense of introducing a small mass balance error, to obtain

$$x_{CO_2}^f = \frac{\bar{\Psi}^g x_{CO_2,eq}^g + \left(1 - \bar{\Psi}^g\right)x_{CO_2,eq}^l}{1 + \frac{\bar{x}_{\text{salt}}^l}{1-\bar{x}_{\text{salt}}^l}\left(1 - \bar{\Psi}^g\right)x_{\text{water},eq}^l},$$

which is identical to Eq. (D.20) for the single gaseous phase. This equation is indeed essential in the formulation of the NegSat method.

In summary, the mole fraction of the gas and liquid phase in the subcooled, two-phase, and superheated regions are calculated by

$$\mathbf{x}^g = \left\{x_{CO_2,eq}^g, \quad x_{\text{water},eq}^g, \quad 0\right\}, \tag{D.26}$$

$$\mathbf{x}^l = \left(1 + \frac{\bar{x}_{\text{salt}}^l}{1 - \bar{x}_{\text{salt}}^l}x_{\text{water},eq}^l\right)^{-1} \cdot \left\{x_{CO_2,eq}^l, \quad x_{\text{water},eq}^l, \quad \frac{\bar{x}_{\text{salt}}^l}{1-\bar{x}_{\text{salt}}^l}x_{\text{water},eq}^l\right\}, \tag{D.27}$$

where $i=$ CO_2, water, salt. Using the above mentioned equilibrium compositions, one can use Eq. (D.7) for the gas-liquid, single phase gaseous, and single phase liquid regions without violating the mass balance.

E. Thermodynamic and transport properties of CO$_2$-water mixture

In this section, the CO$_2$ solubility in water, the effect of CO$_2$ concentration and pressure on the mixture viscosity and molar and mass density are discussed.

E.1. Vapor-liquid equilibria of CO$_2$-water

In this section, the calculation procedure of the equilibrium concentration of CO$_2$ in water for specified temperature and pressure, mass and molar density of a liquid mixture of CO$_2$-water, and partial molar volumes of CO$_2$ and water in a liquid mixture are described. The Stryjek-Vera modification of Peng-Robinson equation of state (PRSV) is used with the modified Huron-Vidal second order mixing rule (MHV2) that uses the Non-Random Two-Liquid (NRTL) model for the calculation of activity coefficients and excess Gibss energy. The model is fitted to the vapor-liquid equilibrium experimental data of CO$_2$-water mixture for a wide range of temperature and pressure by optimizing the parameters of the NRTL model. For a binary two phase system, the degree of freedom is two. This means that by fixing the temperature and pressure, the solubility of CO$_2$ in water can be calculated and it is independent of composition. Fig. E.1 shows the experimental and theoretical equilibrium mole fractions of CO$_2$ and water in the liquid and vapor phase for the vapor-liquid equilibrium of CO$_2$-water mixture. Fig. E.2 shows the density of CO$_2$-saturated water as a function of pressure at the constant temperature of 308.15 K. It can be observed that the model fairly fits the experimental data and can be used to calculate the equilibrium composition and density of the CO$_2$-water mixture.
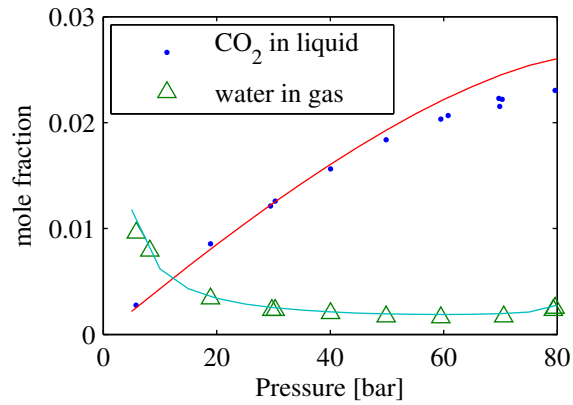
Figure E.1.: Equilibrium composition of CO_2 and water in the liquid and gas phase at different pressures at 308.15 K. Dots and triangles show the experimental data and solid lines show the results of the calibrated model.
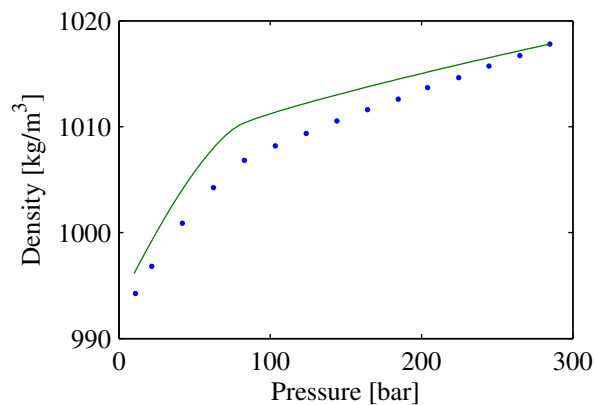

Figure E.2.: Density of CO_2-saturated water in different pressures at 308.15 K. Dots show the experimental data and the solid line shows the result of the calibrated model.

Fig. E.3 shows the equilibrium concentration of CO_2 in the liquid phase for the vapor-liquid equilibrium of CO_2-water mixture as a function of pressure at constant temperature 308.15 K. At low to moderate pressures, i.e., below 30 bar, the CO_2 equilibrium concentration increases linearly with pressure. At higher pressures, the solubility increase per unit pressure change reduces; the solubility is not a linear function of pressure for a wide range of pressure.
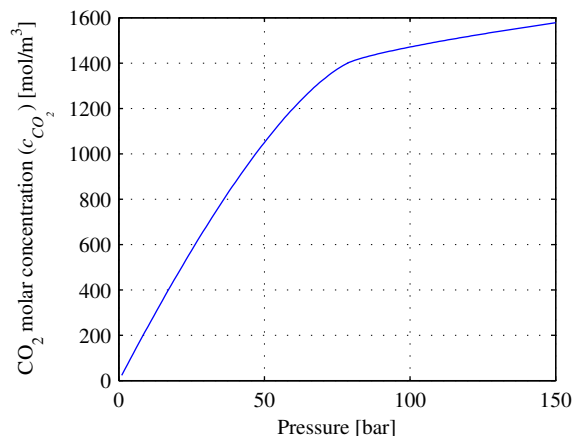
Figure E.3.: The solubility (equilibrium concentration) of CO_2 in water at 308.15 K as a function of pressure

Fig. E.4-left shows the total molar concentration of the CO_2-water mixture as a function of CO_2 molar concentration at constant temperature of 308.15 K and different pressures. Each line ends at the equilibrium concentration of CO_2 at 308.15 K and the specified pressure. This plot shows that the total molar concentration of the CO_2-water liquid mixture C [mol/m^3] at constant temperature of 308.15 K [51] can be represented as a linear function of CO_2 molar concentration at constant pressure and temperature, i.e.,

$$\frac{\partial C}{\partial c_{CO_2}} = \beta_c(P, T), \tag{E.1}$$

where β_c is a dimensionless constant. When the molar concentration of CO_2 is zero, the molar concentration of the liquid mixture is equal to the molar density of pure water, i.e., ρ_{water}/M_{water}, where ρ_{water} [kg/m^3] is the mass density of pure water and M_{water} [kg/mol] is the molecular weight of water. The molar concentration of the mixture can be calculated by integrating Eq. (E.1) to obtain

$$C = \beta_c (P, T) c_{CO_2} + \frac{\rho_{water}}{M_{water}}. \tag{E.2}$$

The relation between the mass density (shown in Fig. E.4-right) and the molar concentrations (C, c_{CO_2}) reads

$$\rho = c_{CO_2} M_{CO_2} + (C - c_{CO_2}) M_{water}. \tag{E.3}$$

By combining Eq. (E.3) and Eq. (E.2), the following linear relation between the mass density of the mixture and the CO_2 concentration is obtained

$$\rho = (\beta_c M_{water} + M_{CO_2} - M_{water}) c_{CO_2} + \rho_{water}. \tag{E.4}$$
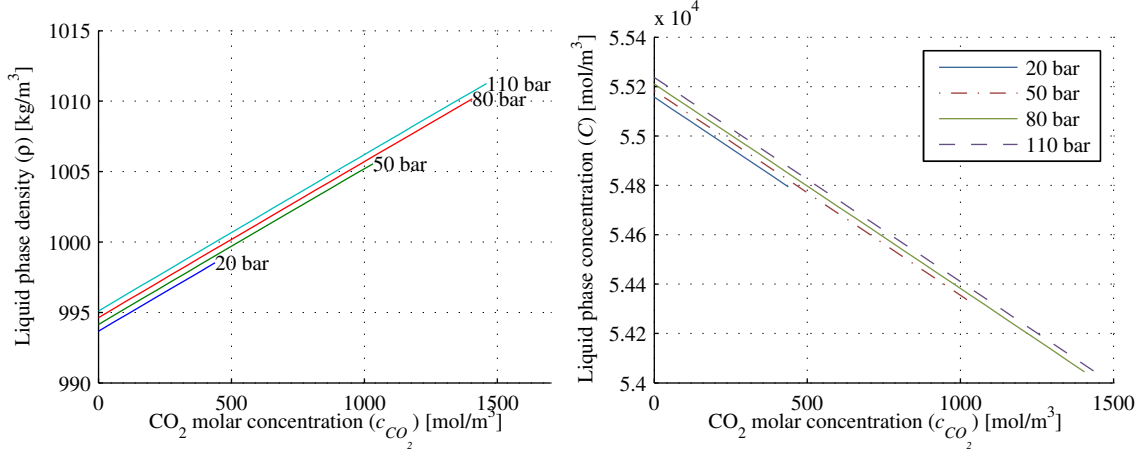
Figure E.4.: Effect of CO$_2$ concentration on the density of the liquid phase mixture of CO$_2$-water (left) and on the molar concentration of the mixture (right) at 308.15 K at different pressures. The right end of each line shows the equilibrium concentration of CO$_2$ in the liquid phase at 308.15 K and the specified pressure (see Fig. E.3).

For a binary mixture, the partial molar volumes are calculated by [145]

$$\hat{v}_1 = v + (1 - x_1)\left(\frac{\partial v}{\partial x_1}\right) \quad \text{and} \quad \hat{v}_2 = v - x_1\left(\frac{\partial v}{\partial x_1}\right), \tag{E.5}$$

where v [m^3/mol] is the molar volume of the mixture, x_1 is the mole fraction of component 1, and $\hat{v}_1$ and $\hat{v}_2$ [m^3/mol] are the partial molar volumes of component 1 and component 2, respectively. The values $c_{CO_2} = x_{CO_2}C$, $C = 1/v$, and $v_{\text{water}} = M_{\text{water}}/\rho_{\text{water}}$ are substituted in Eq. (E.2) to calculate the total molar concentration of the mixture as a function of the CO$_2$ mole fraction, i.e.,

$$\frac{1}{v} = \beta_c\left(P,T\right) x_{CO_2}\frac{1}{v} + \frac{1}{v_{\text{water}}}, \tag{E.6}$$

where v_{water} is the molar volume of pure water, and x_{CO_2} is the mole fraction of CO$_2$; equivalently

$$v = v_{\text{water}}\left(1 - \beta_c x_{CO_2}\right). \tag{E.7}$$

Now, the above relation for total molar volume of the mixture in Eqs. (E.5) are used to obtain the partial molar volumes of CO$_2$ and water, i.e.,

$$\hat{v}_{CO_2} = v_{\text{water}}\left(1 - \beta_c\right), \tag{E.8}$$

$$\hat{v}_{\text{water}} = v_{\text{water}}. \tag{E.9}$$

E.2. Enthalpy of liquid phase mixture of CO$_2$-water

The enthalpy of mixing for a mixture of CO_2-water with a CO_2 mole fraction of x_{CO_2} at temperature T and pressure p is defined as

$$\Delta h_{mix}(p, T, x_{CO_2}) = h^l(p, T, x_{CO_2}) - x_{CO_2} h_{CO_2}(p, T) - (1 - x_{CO_2}) h_{\text{water}}(p, T), \tag{E.10}$$

where $\Delta h_{mix}(p, T, x_{CO_2})$ [J/mol] is the enthalpy of mixing, which is a function of pressure p, temperature T, and composition x_{CO_2}. Moreover, $h^l(p, T, x_{CO_2})$ [J/mol] is the enthalpy of the liquid mixture and is a function of pressure, temperature and composition; h_{CO_2} and h_{water} [J/mol] are the enthalpies of pure CO_2 and water, respectively, which are functions of temperature and pressure. Eq. (E.10) is rearranged to obtain the enthalpy of the liquid mixture, i.e.,

$$h^l = x_{CO_2} h_{CO_2} + (1 - x_{CO_2}) h_{\text{water}} + \Delta h_{mix}. \tag{E.11}$$

Here, a procedure for the calculation of each term in the above equation is explained.

The enthalpy of pure CO_2 at pressure p and temperature T is calculated by

$$h_{CO_2}(p, T) = \int_{T_0}^{T} c_{p,CO_2}^{ig}(T) \, \mathrm{d}T + h_{CO_2}^{R}(p, T), \tag{E.12}$$

where c_{p,CO_2}^{ig} [J/(mol.K)] is the ideal gas heat capacity of CO_2, T_0 [K] is the reference temperature, and $h_{CO_2}^{R}$ [J/mol] is the residual enthalpy of CO_2, which can be estimated by an equation of state, e.g., Span-Wagner or Peng-Robinson. The enthalpy of pure water h_{water}^{l} can be calculated through the same equation as the enthalpy of pure CO_2. However, as water is in the liquid phase in the ranges of interest of pressure and temperature, the effect of pressure on the enthalpy of pure water is ignored and the heat capacity of liquid water is integrated from temperature T_0 to T, i.e.,

$$h_{\text{water}}(T) = \int_{T_0}^{T} c_{p,\text{water}}^{l}(T) \, \mathrm{d}T, \tag{E.13}$$

where $c_{p,\text{water}}^{l}(T)$ [J/(mol.K)] is the heat capacity of pure water at temperature T and the saturation pressure. The values of Δh_{mix} are reported in the literature for a wide range of temperatures and pressures [91]. Measurements of Koschel et al. [91] show that except for a few high pressures and temperatures, e.g., 371 K and

197

200 bar, the enthalpy of mixing is a linear function of the CO_2 mole fraction, in the CO_2 mole fraction range between zero and the equilibrium mole fraction in water. The slope of the line shows the enthalpy of solution, i.e.,

$$\Delta h_{mix} = x_{CO_2} \Delta h_{sol}. \tag{E.14}$$

The enthalpy of solution, Δh_{sol} [J/mol CO_2], is defined as

$$\Delta h_{sol}(p,T) = h_{CO_2}^{l,\infty}(p,T) - h_{CO_2}(p,T), \tag{E.15}$$

where $h_{CO_2}^{l,\infty}(p,T)$ [J/mol] is the enthalpy of infinitely diluted CO_2 in water. Again the definition of residual enthalpy is used to obtain

$$h_{CO_2}^{l,\infty}(p,T) = h_{CO_2}^{l,\infty}(p_0,T) + h_{CO_2}^{l,\infty,R}(p,T), \tag{E.16}$$

where $h_{CO_2}^{l,\infty,R}(T,p)$ [J/mol] is the residual enthalpy of infinitely diluted CO_2 in water and $p_0 = 1$ bar is the chosen reference pressure. The expressions of $h_{CO_2}(p,T)$ from Eq. (E.12) and $h_{CO_2}^{l,\infty}(p,T)$ from Eq. (E.16) are substituted into Eq. (E.15) to obtain

$$\Delta h_{sol}(p,T) = h_{CO_2}^{l,\infty}(p_0,T) - \int_{T_0}^{T} c_{p,CO_2}^{ig}(T)\,\mathrm{d}T + h_{CO_2}^{l,\infty,R}(p,T) - h_{CO_2}^{R}(p,T). \tag{E.17}$$

The absolute value of $h_{CO_2}^{l,\infty,R}$ is much smaller than the other terms in Eq. (E.17) and therefore it can be neglected, according to Koschel et al. [91]. The first two terms on the right side of Eq. (E.17) define the enthalpy of hydration, Δh_{hyd}, at standard pressure p_0. It is defined as the enthalpy of infinitely diluted CO_2 in water at the standard pressure of $p_0 = 1$ bar minus the enthalpy of CO_2 in the ideal gas state [91], i.e.,

$$\Delta h_{hyd}(p_0,T) = h_{CO_2}^{l,\infty}(p_0,T) - \int_{T_0}^{T} c_{p,CO_2}^{ig}(T)\,\mathrm{d}T. \tag{E.18}$$

The values of the enthalpy of hydration at standard pressure, which is only a function of temperature, can be found in published experimental data [12, 19, 91] or can be derived from the temperature correlation of Henry's constant for CO_2 in water [63, 72, 91, 64]. Here, the measured experimental data of the enthalpy of hydration in the temperature range between 298 K to 373 K are used.

By substituting the enthalpy of hydration in Eq. (E.17) and eliminating the negligible value of $h_{CO_2}^{l,\infty,R}$, the following practical relation is obtained for the calculation of the heat of solution of CO_2 in water:

$$\Delta h_{sol}(p,T) = \Delta h_{hyd}(p_0,T) - h_{CO_2}^{R}(p,T). \tag{E.19}$$

To obtain a relation for the enthalpy of mixture, the enthalpy of solution from Eq.

(E.19) is substituted into Eq. (E.14) and the result along with the enthalpy of pure CO_2, i.e., Eq. (E.12), and the enthalpy of pure water, i.e., Eq. (E.13) are substituted in Eq. (E.11), which, after some rearrangements, gives

$$h^l\left(p, T, x_{CO_2}\right) = h_0^l\left(T\right) + x_{CO_2} h_1^l\left(p, T\right), \tag{E.20}$$

where

$$h_0^l = \int_{T_0}^{T} c_{p,\text{water}}^l\left(T\right) dT, \tag{E.21}$$

and

$$h_1^l = \int_{T_0}^{T} c_{p,CO_2}^{ig}\left(T\right) dT + \Delta h_{hyd}\left(p_0, T\right) - \int_{T_0}^{T} c_{p,\text{water}}^l\left(T\right) dT. \tag{E.22}$$

For a binary mixture with a mixture enthalpy of h [J/mol] and a molar fractions of x_1 and $x_2 = 1 - x_1$, the partial molar enthalpies are calculated by [23]

$$\hat{h}_1 = h + (1 - x_1)\left(\frac{\partial h}{\partial x_1}\right) \quad \text{and} \quad \hat{h}_2 = h - x_1\left(\frac{\partial h}{\partial x_1}\right). \tag{E.23}$$

Using the above equations with the enthalpy of the liquid CO_2-water mixture, i.e., Eq. (E.20), the partial molar enthalpies of CO_2 and water can be calculated by

$$\hat{h}_{CO_2} = \int_{T_0}^{T} c_{p,CO_2}^{ig}\left(T\right) dT + \Delta h_{hyd}\left(p_0, T\right), \tag{E.24}$$

$$\hat{h}_{\text{water}} = \int_{T_0}^{T} c_{p,\text{water}}^l\left(T\right) dT.$$

Fig. E.5 shows the values of $\hat{h}_{CO_2}$ and $\hat{h}_{\text{water}}$ at a constant pressure of 50 bar and for a temperature range of 298 K to 373 K. It is obvious that for a narrow range of temperatures, both $\hat{h}_{CO_2}$ and $\hat{h}_{\text{water}}$ can be estimated by linear functions of temperature, i.e.,

$$\hat{h}_{CO_2} = \hat{c}_{p,CO_2} T + \hat{h}_{0,CO_2} \quad \text{and} \quad \hat{h}_{\text{water}} = \hat{c}_{p,\text{water}} T + \hat{h}_{0,\text{water}}, \tag{E.25}$$

where $\hat{c}_{p,CO_2}$, $\hat{c}_{p,\text{water}}$ [J/(mol.K)], $\hat{h}_{0,CO_2}$ [J/mol], and $\hat{h}_{0,\text{water}}$ [J/mol] are constants and are calculated by fitting a linear relation to the $\hat{h}_{CO_2}$ and $\hat{h}_{\text{water}}$ as a function of temperature at a constant pressure. Using these linear relations allows to linearize the partial differential equation that represents the conservation of energy with respect to temperature.

In summary, the following relations are derived that can be used in the energy

balance for a narrow range of temperatures

$$h = x_{CO_2}\hat{h}_{CO_2} + (1 - x_{CO_2})\,\hat{h}_{water}, \tag{E.26}$$

$$\hat{h}_{CO_2} = \hat{c}_{p,CO_2}T + \hat{h}_{0,CO_2}, \tag{E.27}$$

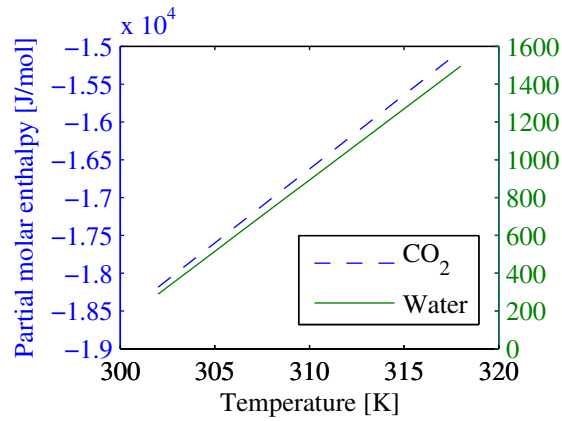$$\hat{h}_{water} = \hat{c}_{p,water}T + \hat{h}_{0,water}. \tag{E.28}$$

Figure E.5.: Partial molar enthalpy $(\hat{h}_i)$ of CO$_2$ (the dashed line, left vertical axis) and water (the drawn line, right vertical axis) in a liquid phase mixture at different temperatures
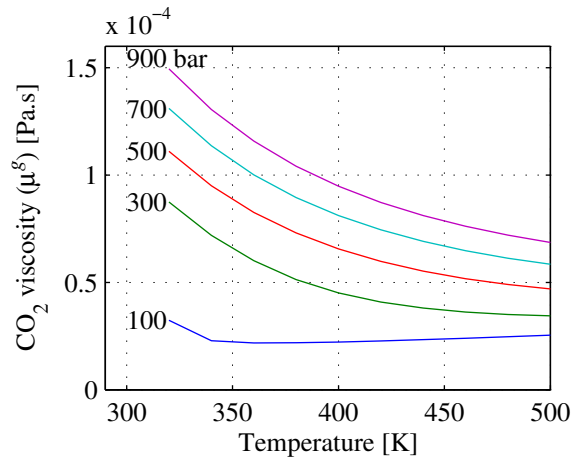

Figure E.6.: The experimental viscosity of gas phase CO$_2$ as a function of temperature at different pressures [62]

E.3. Transport properties of CO_2-water-NaCl

E.3.1. Viscosities of CO_2 in the gas phase

The viscosity of pure CO_2 in the gas phase is estimated by interpolating the data reported by Fenghour et al. [62]. Fig. E.6 shows the CO_2 viscosity data as a function of temperature for selected constant pressures.

E.3.2. Viscosity of the liquid phase mixture of CO_2-water

The viscosity of the water-CO_2 mixture in the liquid phase for the temperature ranges of 30-60°C is related to the viscosity of pure water through the relation

$$\mu = \mu_{\text{water}} \left[1 + \left(-4.069 \times 10^{-3} \left(T - 273.15 \right) + 0.2531 \right) \frac{x_{CO_2}}{x_{CO_2,eq}} \right], \qquad \text{(E.29)}$$

where μ is the liquid viscosity of the CO_2-water mixture, μ_{water} is the viscosity of pure water both at temperature T and pressure p, x_{CO_2} is the mole fraction of CO_2, and $x_{CO_2,eq}$ is the equilibrium mole fraction of CO_2 at T and p. The viscosity of pure water is estimated using the correlations and data reported by Huber et al [79] which requires the density of pure water that is calculated using the Industrial Formulation for the Thermodynamic Properties of Water and Steam (IAPWS-IF97) [164]. Fig. E.7 shows the effect of CO_2 molar concentration on the liquid viscosity of CO_2-water mixture at 308 K and 50 bar. It shows that by dissolving CO_2 in water, its viscosity increases. The viscosity of a CO_2-saturated water is around 11 % higher than the viscosity of pure water.
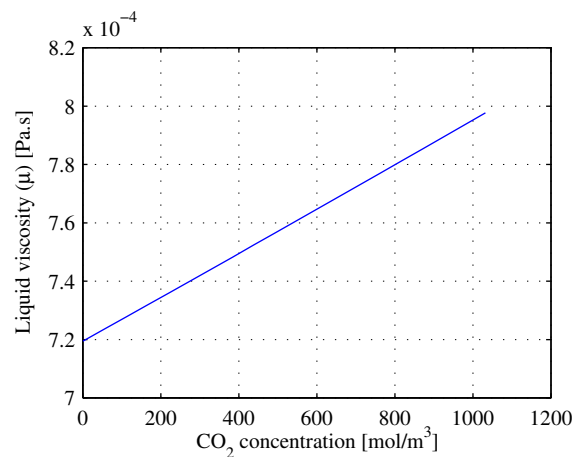

Figure E.7.: Effect of CO_2 concentration on the viscosity of a liquid phase mixture of CO_2-water at 308.15 K and 50 bar. The right end of the line shows the CO_2-saturated mixture at 308.15 K and 50 bar.

E.3.3. Viscosity of brine

According to Mao and Duan [95], the ratio of brine to water viscosity can be calculated by

$$\frac{\mu^l_{brine}}{\mu^l_{water}} = \left(a_0 + a_1 T + a_2 T^2\right) m + \left(b_0 + b_1 T + b_2 T^2\right) m^2 + (c_0 + c_1 T)\, m^3, \quad (E.30)$$

where μ^l_{brine} is the viscosity of brine mixture, μ^l_{water} is the viscosity of pure water, m is the molality of salt (mole of salt per kilogram water), and a_i, b_i, and c_i are constants evaluated from experimental data and reported in Table E.1 for the NaCl solution. The molality of salt is calculated in terms of salt mole fraction (x^l_{salt}) by

$$m = \frac{x^l_{salt}}{\left(1 - x^l_{salt}\right) M_{water}},$$

where M_{water}= 0.018 kg/mol is the molecular weight of water. Fig. E.8 shows the effect of NaCl mole fraction on the viscosity of brine at constant pressure of 700 bar in different temperatures. It shows that the viscosity of a brine solution saturated with salt is almost two times as high as the viscosity of pure water.
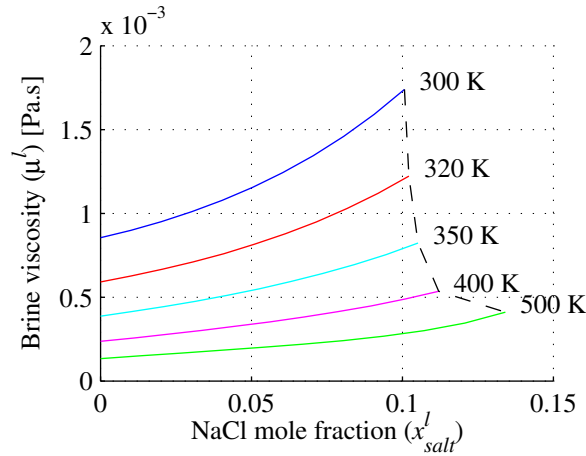
Figure E.8.: The viscosity of brine solution at constant pressure of 700 bar and various temperatures as a function of NaCl mole fraction. The dashed curve denotes the solubility of NaCl in water [95, 121].

Table E.1.: Numerical values of a_i, b_i, and c_i form Eq. (E.30) for NaCl-H_2O system [95]

Parameter	Value	parameter	Value
a_0	-0.21319213	b_0	$0.69161945 \times 10^{-1}$
a_1	$0.13651589 \times 10^{-2}$	b_1	$-0.27292263 \times 10^{-3}$
a_2	$-0.12191756 \times 10^{-5}$	b_2	$0.20852448 \times 10^{-6}$
c_0	$-0.25988855 \times 10^{-2}$	c_1	$0.77989227 \times 10^{-5}$

F. Molar average velocity and Boussinesq approximation

In this section, the continuity equation is derived by assuming that the Darcy velocity is a molar average velocity. The derivation starts by writing the mass conservation for component i and for the overall mixture, Eqs. (5.11 and 5.9), i.e.,

$$\varphi \frac{\partial c_i}{\partial t} + \nabla . \mathbf{N}_i = 0, \tag{F.1}$$

$$\varphi \frac{\partial C}{\partial t} + \nabla . \left(\sum_i \mathbf{N}_i \right) = 0, \tag{F.2}$$

where

$$\mathbf{N}_i = c_i \mathbf{u}^{\blacksquare} + \mathbf{J}_i^{\blacksquare}, \tag{F.3}$$

$$C = \sum c_i. \tag{F.4}$$

Here, φ is the porosity, C [mol/m^3] is the molar concentration of the mixture, c_i [mol/m^3] is the molar concentration of component i, $\mathbf{u}^{\blacksquare}$ [m/s] is molar average velocity vector[1], and $\mathbf{J}_i^{\blacksquare}$ [mol/(m^2.s)] is the diffusive flux of component i relative to the molar average velocity, and $\mathbf{N}_i$ [mol/(m^2.s)] is the total flux of component i. It is shown by Bird et al. [23] that by definition:

$$\sum_i \mathbf{N}_i = C \mathbf{u}^{\blacksquare} \text{ and } \sum_i \mathbf{J}_i^{\blacksquare} = 0. \tag{F.5}$$

Moreover, the following form of Fick's law must be used to obtain the molar flux relative to the molar average velocity:

$$\mathbf{J}_i^{\blacksquare} = -\varphi \mathcal{D}_i C \nabla x_i, \tag{F.6}$$

---

[1]Note that in references [23, 37], a different notation is used for the molar and volume average velocity. Here, because the volume average velocity is repeated numerously throughout the text, for convenience $\mathbf{u}$ without superscript is used to denote volume average velocity.

where x_i is the molar fraction of component i and D_i is the diffusion coefficient. By substituting Eqs. (F.5 and F.3) in Eqs. (F.2 and F.1), one can obtain

$$\varphi \frac{\partial C}{\partial t} + \nabla . \left(C\mathbf{u}^{\blacksquare} \right) = 0, \tag{F.7}$$

$$\varphi \frac{\partial c_i}{\partial t} + \nabla . \left(c_i \mathbf{u}^{\blacksquare} - \varphi \mathcal{D}_i C \nabla x_i \right) = 0. \tag{F.8}$$

For the CO_2-water mixture, the total concentration of the mixture can be written as a linear function of the CO_2 concentration (see Appendix E), i.e.,

$$C = \beta_c c_{CO_2} + \frac{1}{v_{\text{water}}}, \tag{F.9}$$

where β_c is a constant and v_{water} [m^3/mol] is the molar volume of pure water. Eq. (F.9) is substituted in Eq. (F.7) and Eq. (F.8) is writen for $i=CO_2$ to obtain

$$\varphi \frac{\partial c_{CO_2}}{\partial t} + \nabla . \left(c_{CO_2} \mathbf{u}^{\blacksquare} \right) + \nabla . \left(\frac{1}{\beta_c v_{\text{water}}} \mathbf{u}^{\blacksquare} \right) = 0, \tag{F.10}$$

$$\varphi \frac{\partial c_{CO_2}}{\partial t} + \nabla . \left(c_{CO_2} \mathbf{u}^{\blacksquare} \right) + \nabla . (-\varphi \mathcal{D} C \nabla x_{CO_2}) = 0. \tag{F.11}$$

The combination of the above equations gives the continuity equation, i.e.,

$$\nabla . \mathbf{u}^{\blacksquare} = \beta_c v_{\text{water}} \nabla . (-\varphi \mathcal{D} C \nabla x_{CO_2}). \tag{F.12}$$

It is assumed that the molar average velocity can be estimated by Darcy's law, i.e.,

$$\mathbf{u}^{\blacksquare} = -\frac{k}{\mu} (\nabla p - \rho \mathbf{g}), \tag{F.13}$$

where k [m^2] is the permeability of the porous medium, ρ [kg/m^3] and μ [Pa.s] are the mass density and viscosity of the fluid, and p [Pa] is pressure. By substituting Darcy's law in the continuity equation, Eq. (F.12), one can obtain

$$\nabla . \left(\frac{k}{\mu} \nabla p \right) = \underbrace{\nabla . \left(\frac{k}{\mu} \rho \mathbf{g} \right)}_{gravity} + \underbrace{\beta_c v_{\text{water}} \nabla . (\varphi \mathcal{D} C \nabla x_{CO_2})}_{diffusion}. \tag{F.14}$$

By eliminating the second term on the right side of Eq. (F.14), the continuity relation is converted to the well-known Boussinesq approximation. In the next section, a procedure is described to quantify the effect of the Boussinesq approximation on the right hand side of the pressure equation.

F.1. Effect of Boussinesq approximation

To quantify the numerical effect of Boussinesq versus non-Boussinesq formulation on the pressure equation, it is assumed that k, μ, D, and φ are constants. Then Eq. (5.25), i.e.,

$$\rho = [(\beta_c - 1) M_{\text{water}} + M_{\text{CO}_2}] c_{\text{CO}_2} + \frac{M_{\text{water}}}{v_{\text{water}}}, \tag{F.15}$$

is substituted in Eq. (F.14) to obtain the following equation for the right hand side (RHS) of Eq. (F.14) in an upward vertical direction (z)

$$\text{RHS} = -g\frac{k}{\mu}\left[(\beta_c - 1) M_{\text{water}} + M_{\text{CO}_2}\right]\frac{\partial c_{\text{CO}_2}}{\partial z} + \varphi \mathcal{D}\beta_c v_{\text{water}}\frac{\partial}{\partial z}\left(C\frac{\partial x_{\text{CO}_2}}{\partial z}\right). \tag{F.16}$$

The term $\frac{\partial}{\partial z}\left(C\frac{\partial x_{\text{CO}_2}}{\partial z}\right)$ can be expanded in combination with Eq. (F.9) to be written as a function of $\frac{\partial c_{\text{CO}_2}}{\partial z}$, i.e.,

$$\frac{\partial}{\partial z}\left(C\frac{\partial x_{\text{CO}_2}}{\partial z}\right) = (1 - \beta_c x_{\text{CO}_2})\left(\frac{-\beta_c}{C}\left(\frac{\partial c_{\text{CO}_2}}{\partial z}\right)^2 + \frac{\partial^2 c_{\text{CO}_2}}{\partial z^2}\right). \tag{F.17}$$

Here it is assumed that the concentration profile of CO_2 can be estimated by using the analytical solution of Fick's second law in a semi-infinite domain, i.e.,

$$\frac{\partial c_{\text{CO}_2}}{\partial t} = \mathcal{D}\frac{\partial^2 c_{\text{CO}_2}}{\partial z^2}, \tag{F.18}$$

with the initial and boundary conditions:

$$c_{\text{CO}_2} = 0 \qquad \text{at } t = 0, \ z = [0, \infty),$$

$$c_{\text{CO}_2} = c_{eq} \qquad \text{at } t > 0, \ z = 0,$$

and the relation

$$c_{\text{CO}_2} = 0 \qquad \text{at } t > 0, \ z \to \infty, \tag{F.19}$$

where c_{eq} [mol/m^3] is the equilibrium concentration of CO_2 in water. The analytical solution for the concentration profile and its first and second gradients read

$$c_{\text{CO}_2} = c_{eq}\left(1 - \text{erf}\left(\zeta\right)\right), \tag{F.20}$$

$$\frac{\partial c_{\text{CO}_2}}{\partial z} = \frac{-1}{\sqrt{\pi \mathcal{D}t}}c_{eq}\exp\left(-\zeta^2\right), \tag{F.21}$$

$$\frac{\partial^2 c_{\mathrm{CO_2}}}{\partial z^2} = \frac{\zeta}{\mathcal{D}t\sqrt{\pi}} c_{eq} \exp\left(-\zeta^2\right), \tag{F.22}$$

where $\zeta = z/\left(2\sqrt{\mathcal{D}t}\right)$. The parameters in Table F.1 are used to calculate the gravity and diffusion terms of Eq. (F.16).

Table F.1.: Values of parameters for the calculation of RHS, Eq. (F.16)

Parameter	Value	Unit	Parameter	Value	Unit
β_c	-0.868	-	μ	1×10^{-3}	Pa.s
v_{water}	1.815×10^{-5}	m³/mol	g	9.81	m/s²
k	1×10^{-12}	m²	c_{eq}	1171	mol/m³
φ	0.3	-	$\mathcal{D}$	2×10^{-9}	m²/s
$M_{\mathrm{CO_2}}$	0.044	kg/mol	M_{water}	0.018	kg/mol

The numerical values of the gravity and diffusion term of the continuity equation, Eq. (F.14), are shown in Fig. F.1. The dash-dot line shows the right side of Eq. (F.14) including both gravity and diffusion terms, and the solid line shows the gravity term, i.e., the right side of Eq. (F.14) excluding the diffusion term, i.e., the Boussinesq approximation. Here, only a space-time range (ζ) where concentration changes from c_{eq} to zero is of interest. The relative error of using Boussinesq approximation, i.e., ignoring the diffusion term in Eq. (F.14), can be calculated by $\left|\frac{\text{diffusion term}}{\text{gravity+diffusion terms}}\right|$. The computations show that the relative error of the Boussinesq approximation is a function of time. The focus is on the time period between zero and the onset time of natural convection, i.e., the diffusion-dominated period. The onset time is estimated using the following relation [137]

$$t_{onset} = 146\frac{\mu^2\varphi^2\mathcal{D}}{\left(\rho - \rho_{\mathrm{water}}\right)g^2k^2}, \tag{F.23}$$

where μ is the viscosity of the mixture, φ is the porosity, $\mathcal{D}$ is the diffusion coefficient, $(\rho - \rho_{\mathrm{water}})$ is the density difference between the CO$_2$-saturated and pure water, g is the acceleration due to gravity, and k is the permeability. Fig. F.1-(a, b, and c) show the values of the right hand side of the pressure equation for the Boussinesq and non-Boussinesq aaproximation and the relative error of ignoring the diffusion term for times equal to $\frac{t_{onset}}{1\times10^5}$, $\frac{t_{onset}}{1\times10^3}$, and t_{onset} for a system defined by parameters shown in Table F.1. The general trend is that the error is zero at $\zeta = 0$ and by increasing the value of ζ, the error of using the Boussinesq approximation increases. However, the value of the right hand side of the pressure equation decreases with increasing ζ and it finally approaches zero. Fig. F.1-a shows the right hand side and relative error of Boussinesq approximation for the initial stage of the process at $t = 10^{-5} \times t_{onset}$. The error of using Boussinesq approximation is between zero

to 200 %. As the process proceeds to $t = 10^{-3} \times t_{onset}$, the relative error decreases to the range of zero to 7 %. Finally, when the process reaches the onset time and the convective flux starts to become the dominant transport mechanism, the error of using Boussinesq approximation is between zero to 0.2 %, which can be easily neglected. Repeating the calculation for other systems with different sets of parameters and other ranges of Rayleigh number gives the same type of results. It can be concluded that using the Boussinesq approximation for the formulation of density-driven natural convection in porous media introduces only a small error that is negligible.

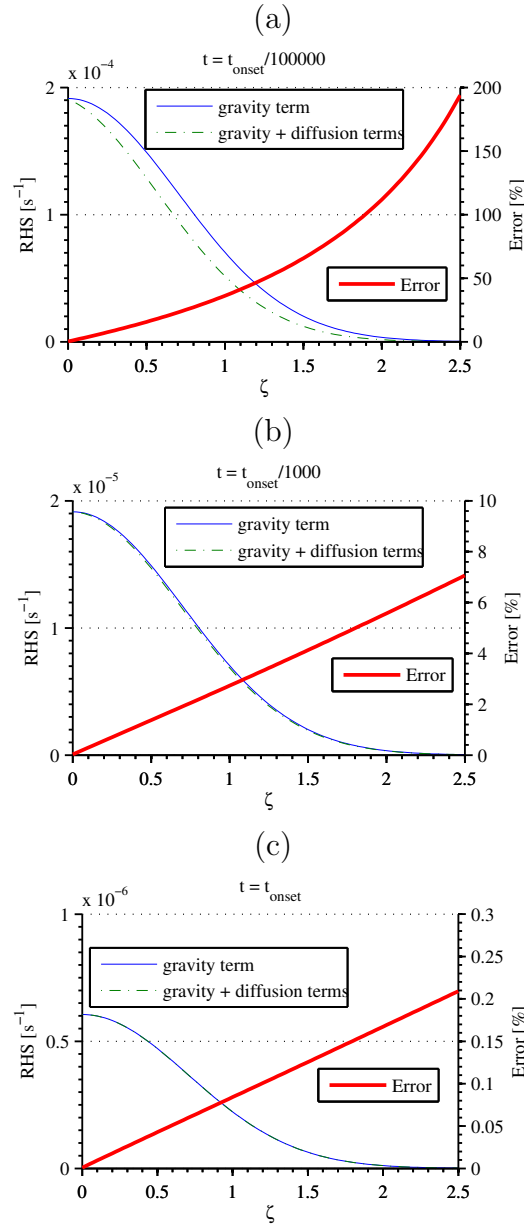**Figure F.1.:** The right hand side of the continuity equation for liquid phase flow of CO_2-water mixture in porous media at t=1000 s; solid line (gravity term) shows the Boussinesq approximation and dash-dot line (gravity + diffusion terms) shows the non-Boussinesq formulation. The relative error, i.e., $\left|\frac{\text{diffusion term}}{\text{gravity+diffusion terms}}\right|$ is less than 10 % for $0 \leq \zeta \leq 2.5$.

G. Heat transfer coefficient for natural convection in porous media

Dissolution of CO_2 in water is exothermic and increases the temperature of the CO_2-water interface. This causes the density of the gaseous CO_2 to decrease, which eventually results in a natural convection current in the gas phase. To estimate the heat transfer from the gas-liquid interface to the gas-saturated porous medium, one needs to solve the energy balance equation including both the conduction and convection heat transfer mechanisms. Fig. G.1 shows the domain and the boundary conditions. In this case, the temperature increase is not high, e.g., around 1 K. Hence, The effect of temperature on the CO_2 viscosity, thermal conductivity, and specific heat capacity is ignored. The Darcy's law is used to represent the flow in porous media. Using the Boussinesq approximation, the continuity equation and the energy balance equation read

$$\nabla.\mathbf{u} = 0, \tag{G.1}$$

$$\mathbf{u} = -\frac{k}{\mu_{CO_2}^g}\left(\nabla p - \rho_{CO_2}^g \mathbf{g}\right), \tag{G.2}$$

$$\left(\varphi \rho_{CO_2}^g c_{p,CO_2}^g + (1-\varphi)\,\rho^s c_p^s\right)\frac{\partial T}{\partial t} + \nabla.\left(\rho_{CO_2}^g c_{p,CO_2}^g T\mathbf{u}\right) + \nabla.\left(-\lambda \nabla T\right) = 0, \tag{G.3}$$

where $\mathbf{u}$ [m/s] is the Darcy velocity vector, k [m^2] is the permeability, $\mu_{CO_2}^g$ [Pa.s], $\rho_{CO_2}^g$[kg/m^3], and c_{p,CO_2}^g [J/(kg.K)] are the viscosity, density, and heat capacity of gaseous CO_2, and ρ^s [kg/m^3] and c_p^s [J/(kg.K)] are the density and the heat capacity of the solid that forms the porous medium. The average thermal conductivity, λ [J/(m.K.s)], is calculated by

$$\lambda = \lambda_{CO_2}^\varphi \lambda_s^{1-\varphi}, \tag{G.4}$$

where λ_{CO_2} [J/(m.K.s)] is the thermal conductivity of CO_2 and λ_s [J/(m.K.s)] is the thermal conductivity of the porous medium.
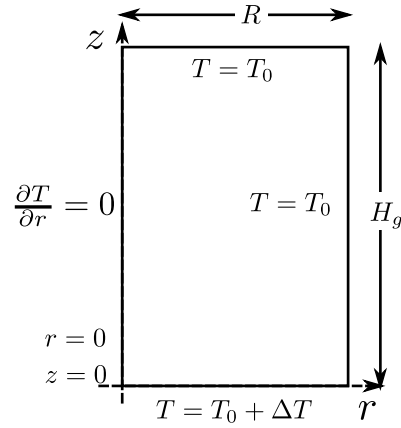
Figure G.1.: a schematic representation of the CO_2-saturated porous media with the temperature boundary conditions in a cylindrical coordinate

The system of differential equations, Eq. (G.1) and Eq. (G.3), are discretized using a cell centered finite volume scheme over a equidistance mesh in a cylindrical coordinate. Then the system of algebraic equations are solved sequentially in Matlab. The physical parameters and the parameters of the numerical solver are shown in Table G.1.

Table G.1.: Physical and numerical parameters for the natural convection of CO_2 in porous medium, Eq. (G.1) and Eq. (G.3). The domain is shown in Fig. (G.1)

Parameters	λ_{CO_2}	λ_s	φ	k	$\mu^g_{CO_2}$
value	0.08	0.161	0.38	59×10^{-12}	1.66×10^{-5}
unit	J/(m.K.s)	J/(m.K.s)	-	m^2	Pa.s
Parameters	c^g_{p,CO_2}	c^s_p	ρ^s	ρ^g	T_0
value	9100	837	2650	Fig. G.2	308.15
unit	J/(kg.K)	J/(kg.K)	kg/m^3	kg/m^3	K
Parameters	R	H_g	N_r	N_z	ε_T
value	0.076	0.26	80	400	1×10^{-5}
unit	m	m	-	-	-
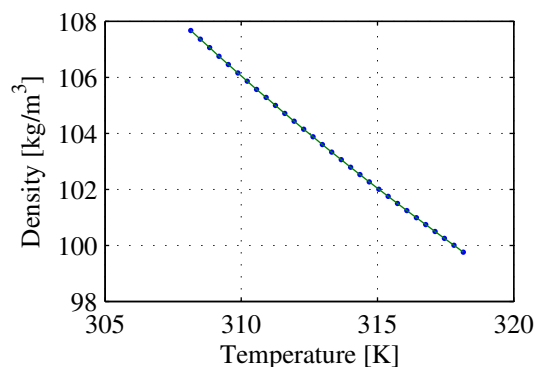
Figure G.2.: Density of the gas phase CO_2 as a function of temperature calculated using Span-Wagner equation at constant pressure of 46.9 bar

The time dependent equation is solved until the steady state condition is reached. Then the steady state temperature profile is used to calculate the heat flux from the bottom boundary ($z{=}0$), and use that heat flux to calculate the heat transfer coefficient, i.e.,

$$q_{bottom} = -\lambda \left(\frac{\partial T}{\partial z}\right)_b = h\left(T_b - T_0\right),\tag{G.5}$$

where $\left(\frac{\partial T}{\partial z}\right)_b$ [K/m] is the temperature gradient at the bottom boundary, and h [J/(m^2.K.s)] is the heat transfer coefficient. Moreover, $\Delta T = (T_b - T_0)$ [K] is the temperature difference between the bottom boundary and the external and top walls of the cylindrical domain (see Fig. G.1). The heat transfer coefficient, h, for different values of ΔT are shown in Fig. G.3.

Figure G.3.: Heat transfer coefficient from the CO_2-water interface to the CO_2 saturated porous medium for different temperature differences

213

Bibliography

[1] A. Abadpour and M. Panfilov. Method of negative saturations for modeling two-phase compositional flow with oversaturated zones. *Transport in Porous Media*, 79(2):197–214, 2009.
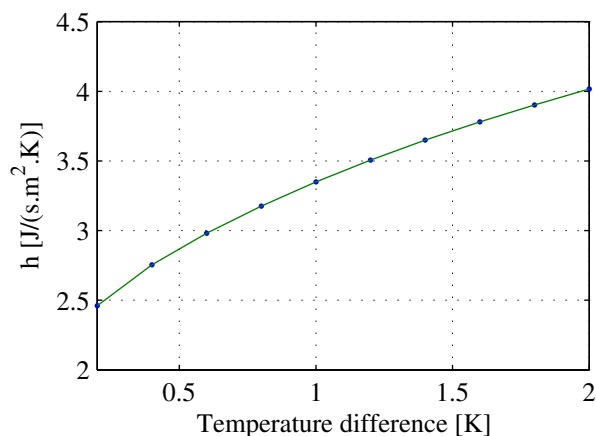
[2] D. S. Abrams and J. M. Prausnitz. Statistical thermodynamics of liquid mixtures: a new expression for the excess Gibbs energy of partly or completely miscible systems. *AIChE Journal*, 21(1):116–128, 1975.

[3] K. Aleklett and C.J. Campbell. The peak and decline of world oil and gas production. *Minerals and Energy-Raw Materials Report*, 18(1):5–20, 2003.

[4] A.S. Almeida, P.S.M.V. Rocha, S.T.C. Lima, A.C.C. Pinto, C.C.M Branco, and M.C. Salomão. A study on the potential for CCGS in the Pre-salt cluster of Santos basin: the Tupi pilot application. In *Rio Oil & Gas Expo and Conference*. SPE, 12-14 April 2010. doi: 10.2118/126566-MS.

[5] V.I. Arnold. *Geometrical Methods in the Theory of Ordinary Differential Equations*. Springer-Verlag, 1983.

[6] J.J. Azar and G.R. Samuel. *Drilling Engineering*. Pennwell Corp, 2007.

[7] G. Bacci, A. Korre, and S. Durucan. An experimental and numerical investigation into the impact of dissolution/precipitation mechanisms on CO_2 injectivity in the wellbore and far field regions. *International Journal of Greenhouse Gas Control*, 5(3):579–588, 2011.

[8] G. Bacci, A. Korre, and S. Durucan. Experimental investigation into salt precipitation during CO_2 injection in saline aquifers. *Energy Procedia*, 4:4450–4456, 2011.

[9] A.C. Bailey, F. Bartlett, H.H. Boswinkel, J. Bruining, V. Chandelle, G. Del Amor, J.H. Garstang, H. Hewel-Bundemann, G. Hewing, K. Krabiell, et al. The future development of underground coal gasification in Europe. Technical report, CEC, Brussels, 1989.

[10] S. Bando, F. Takemura, M. Nishio, E. Hihara, and M. Akai. Solubility of CO_2 in aqueous solutions of NaCl at (30 to 60) C and (10 to 20) MPa. *Journal of Chemical & Engineering Data*, 48(3):576–579, 2003.

[11] S. Bando, F. Takemura, M. Nishio, E. Hihara, and M. Akai. Viscosity of aqueous NaCl solutions with dissolved CO_2 at (30 to 60) C and (10 to 20) MPa. *Journal of Chemical & Engineering Data*, 49(5):1328–1332, 2004.

[12] R. Battino and K.N. Marsh. An isothermal displacement calorimeter for the measurement of the enthalpy of solution of gases. *Australian Journal of Chemistry*, 33(9):1997–2003, 1980.

[13] Elisa Battistutta, Marcin Lutynski, Hans Bruining, Karl-Heinz Wolf, and Susanne Rudolph. Adequacy of equation of state models for determination of adsorption of gas mixtures in a manometric set up. *International Journal of Coal Geology*, 89(2):114–122, 2012.

[14] J. Bear and Y. Bachmat. *Introduction to Modeling of Transport Phenomena in Porous Media*, volume 4. Springer, 1990.

[15] D.C. Beard and P.K. Weyl. Influence of texture on porosity and permeability of unconsolidated sand. *AAPG Bulletin*, 57(2):349–369, 1973.

[16] R. L. Beltrao, C. Sombra, A. Lage, J. Fagundes Netto, and C. Henriques. Pre-salt Santos basin – challenges and new technologies for the development of the Pre-salt cluster, Santos basin, Brazil. In *Offshore Technology Conference*, Houston, Texas, 4-7 May 2009. SPE. doi: 10.4043/19880-MS.

[17] A.N. Beni, C. Clauser, and M. Erlström. System analysis of underground CO_2 storage by numerical modeling for a case study in Malmö. *American Journal of Science*, 311(4):335–368, 2011.

[18] R.W. Bentley. Global oil & gas depletion: an overview. *Energy Policy*, 30(3): 189–205, 2002.

[19] R.L. Berg and C.E. Vanderzee. Thermodynamics of carbon dioxide and carbonic acid:(a) the standard enthalpies of solution of Na_2CO_3 (s), $NaHCO_3$ (s), and CO_2 (g) in water at 298.15 K;(b) the standard enthalpies of formation, standard Gibbs energies of formation, and standard entropies of CO_2 (aq), HCO_3-(aq), $CO_3$2-(aq), $NaHCO_3$ (s), Na_2CO_3 (s), Na_2CO_3–H_2O (s), and Na_2CO_3–10 H_2O (s). *The Journal of Chemical Thermodynamics*, 10(12): 1113–1136, 1978.

[20] B. Białecka. Estimation of coal reserves for UCG in the upper Silesian coal basin, Poland. *Natural Resources Research*, 17(1):21–28, 2008.

[21] E.N.J. Biezen, J. Bruining, and J. Molenaar. An integrated 3D model for underground coal gasification. In *SPE Annual Technical Conference and Exhibition*, 1995.

[22] R.B. Bird, W.E. Stewart, and E.N. Lightfoot. *Transport Phenomena*. John Wiley, New York, 1960.

[23] R.B. Bird, W.E. Stewart, and E.N. Lightfoot. *Transport Phenomena*. 2002.

[24] F.C. Bond. The third theory of comminution. *Trans. AIME*, 193(2):484–489, 1952.

[25] C.K. Brain and A Sillent. Evidence from the swartkrans cave for the earliest use of fire. *Nature*, 336(6198):464–466, 1988.

[26] J.D. Bredehoeft and G.F. Pinder. Mass transport in flowing groundwater. *Water Resources Research*, 9(1):194–210, 1973.

[27] British Petroleum. BP statistical review of world energy June 2008. Technical report, London: British Petroleum, 2008.

[28] J.A. Britten and C.B. Thorsness. A model for cavity growth and resource recovery during underground coal gasification. *In Situ*, 13(1), 1989.

[29] A. Brunetti, F. Scura, G. Barbieri, and E. Drioli. Membrane technologies for CO_2 separation. *Journal of Membrane Science*, 359(1-2):115–125, 2010.

[30] A. Campos, W. Baumgartner, M. Pena, M. Halls, M. Paiva, and C. Plank. CO_2 reduction at the FPSO Fluminense: Case study. In *SPE International Conference on Health, Safety and Environment in Oil and Gas Exploration and Production*, Rio de Janeiro, Brazil, 12-14 April 2010. SPE. doi: 10.2118/ 127029-MS.

[31] P.C. Carman. Fluid flow through granular beds. *Transactions-Institution of Chemical Engineeres*, 15:150–166, 1937.

[32] S. Carnot. *Reflexions on the Motive Power of Fire: a Critical Edition with the Surviving Scientific Manuscripts*. Manchester University Press ND, 1986.

[33] D.G. Chapel, C.L. Mariz, and J. Ernest. Recovery of CO_2 from flue gases: commercial trends. *Originally presented at the Canadian Society of Chemical Engineers annual meeting*, 1999.

[34] A. Chapoy, A.H. Mohammadi, A. Chareton, B. Tohidi, and D. Richon. Measurement and modeling of gas solubility and literature review of the properties for the carbon dioxide-water system. *Industrial & Engineering Chemistry Research*, 43(7):1794–1802, 2004.

[35] Arthur T Corey. The interrelation between gas and oil relative permeabilities. *Producers monthly*, 19(1):38–41, 1954.

[36] J.R. Couper, W.R. Penney, J.R. Fair, and S.M. Walas. *Chemical Process Equipment: Selection and Design*. Gulf Professional Publishing, 2009.

[37] E.L. Cussler. *Diffusion: Mass Transfer in Fluid Systems*. Cambridge University Press, 1997.

[38] S. Dahl and M.L. Michelsen. High-pressure vapor-liquid equilibrium with a UNIFAC-based equation of state. *AIChE Journal*, 36(12):1829–1836, 1990.

[39] S. Dahl, A. Fredenslund, and P. Rasmussen. The MHV2 model: a UNIFAC-based equation of state model for prediction of gas solubility and vapor-liquid equilibria at low and high pressures. *Industrial & Engineering Chemistry Research*, 30(8):1936–1945, 1991.

[40] P.V. Danckwerts. Continuous flow systems: distribution of residence times. *Chemical Engineering Science*, 2(1):1–13, 1953.

[41] B.E. Davis, J.M. Avasthi, C.S. Reid, G.E. Slater, and G.L. LaBerge. Underground gasification for steeply dipping coal beds. Rawlins UCG test 1 cavity definition study. Technical report, DOE/ET/13108-75, Gulf Research and Development Co., Pittsburgh, PA (USA); TRW, Inc., McLean, VA (USA). Energy Systems Planning Div., 1981.

[42] S.J. Davis, K. Caldeira, and H.D. Matthews. Future CO_2 emissions and climate change from existing energy infrastructure. *Science*, 329(5997):1330–1333, 2010.

[43] J. de Swaan Arons, H. van der Kooi, and K. Sankaranarayanan. *Efficiency and Sustainability in the Energy and Chemical Industries: Scientific Principles and Case Studies.* CRC, 2004.

[44] L.W. Diamond and N.N. Akinfiev. Solubility of CO_2 in water from -1.5 to 100° C and from 0.1 to 100 MPa: evaluation of literature data and thermodynamic modelling. *Fluid Phase Equilibria*, 208(1):265–290, 2003.

[45] H.W. Dickinson. *A Short History of the Steam Engine.* Cambridge University Press, 2011.

[46] I. Dincer and M.A. Rosen. *Exergy: Energy, Environment and Sustainable Development.* Elsevier Science, 2007.

[47] B. Dinsmoor, J.M. Galland, and T.F. Edgar. The modeling of cavity formation during underground coal gasification. *Journal Of Petroleum Technology*, 30 (5):695–704, 1978.

[48] Z. Duan and R. Sun. An improved model calculating CO_2 solubility in pure water and aqueous NaCl solutions from 273 to 533 K and from 0 to 2000 bar. *Chemical Geology*, 193(3-4):257–271, 2003.

[49] Z. Duan, N. Møller, and J. H. Weare. Equation of state for the NaCl-H_2O-CO_2 system: prediction of phase equilibria and volumetric properties. *Geochimica et Cosmochimica Acta*, 59(14):2869–2882, 1995.

[50] A. Dufaux, B. Gaveau, R. Létolle, M. Mostade, and J.P. Pirard. Modelling of the underground coal gasification process at Thulin on the basis of thermodynamic equilibria and isotopic measurements. *Fuel*, 69(5):624–632, 1990.

[51] S. Eberle, C. Keller, H.W. Kirby, H.K. Kugler, and H. Münzel. *Gmelin Handbook of Inorganic Chemistry.* 1983.

[52] A.A. Eftekhari, H.J. Van Der Kooi, and J Bruining. Exergy analysis of underground coal gasification with simultaneous storage of carbon dioxide. *Energy*, 45(1):729–745, 2012.

[53] W. Eisermann, P. Johnson, and WL Conger. Estimating thermodynamic properties of coal, char, tar and ash. *Fuel Processing Technology*, 3(1):39–53, 1980.

[54] M.T. Elenius, J.M. Nordbotten, and H. Kalisch. Effects of a capillary transition zone on the stability of a diffusive boundary layer. *IMA Journal of Applied Mathematics*, 77(6):771–787, 2012.

[55] A. J. Ellis and R. M. Golding. The solubility of carbon dioxide above 100 degrees C in water and in sodium chloride solutions. *American Journal of Science*, 261(1), 1963.

[56] J. Ennis-King and L. Paterson. Role of convective mixing in the long-term storage of carbon dioxide in deep saline formations. *SPE Journal*, 10(3):349–356, 2005.

[57] R. Farajzadeh, A. Barati, H.A. Delil, J. Bruining, and P.L.J. Zitha. Mass transfer of CO_2 into water and surfactant solutions. *Petroleum Science and Technology*, 25(12):1493–1511, 2007.

[58] R. Farajzadeh, H. Delil, P. Zitha, and J. Bruining. Enhanced mass transfer of CO_2 into water and oil by natural convection. In *EUROPEC/EAGE Conference and Exhibition*, London, UK, 11-14 June 2007. SPE. doi: 10.2118/107380-MS.

[59] R. Farajzadeh, P.L.J. Zitha, and J. Bruining. Enhanced mass transfer of CO_2 into water: experiment and modeling. *Industrial & Engineering Chemistry Research*, 48(13):6423–6431, 2009.

[60] R. Farajzadeh, B. Meulenbroek, D. Daniel, A. Riaz, and J. Bruining. An empirical theory for gravitationally unstable flow in porous media. *Computational Geosciences*, pages 1–13, 2013.

[61] E. Favre. Carbon dioxide recovery from post-combustion processes: can gas permeation membranes compete with absorption? *Journal of Membrane Science*, 294(1-2):50–59, 2007.

[62] A. Fenghour, W.A. Wakeham, and V. Vesovic. The viscosity of carbon dioxide. *Journal of Physical and Chemical Reference Data*, 27(1):31–44, 1998.

[63] R. Fernandez-Prini, J.L. Alvarezb, and A.H. Harveyc. Henry's constants and vapor–liquid distribution constants for gaseous solutes in H_2O and D_2O at high temperatures. *Journal of Physical and Chemical Reference Data*, 32(2): 903, 2003.

[64] R. Fernandez-Prini, A.H. Harvey, and D.A. Palmer. *Aqueous Systems at Elevated Temperatures and Pressures: Physical Chemistry in Water, Steam and Hydrothermal Solutions*. Academic Press, 2004.

[65] R.P. Feynman, R.B. Leighton, and M.L. Sands. *The Feynman Lectures on Physics*. Addison-Wesley, 1989.

[66] M. Gehrig, H. Lentz, and E.U. Franck. The system water-carbon dioxide-sodium chloride to 773 K and 300 MPa. *Berichte der Bunsengesellschaft für Physikalische Chemie*, 90(6):525–533, 1986.

[67] S.J. Gerdemann, W.K. O'Connor, D.C. Dahlin, L.R. Penner, and H. Rush. Ex situ aqueous mineral carbonation. *Environmental Science and Technology*, 41(7):2587–2593, 2007.

[68] T. Giorgis, M. Carpita, and A. Battistelli. 2D modeling of salt precipitation during the injection of dry $CO_2$2 in a depleted gas reservoir. *Energy Conversion and Management*, 48(6):1816–1826, 2007.

[69] D.W. Gregg and T.F. Edgar. Underground coal gasification. *AIChE Journal*, 24(5):753–781, 1978.

[70] H. Gupta and L.S. Fan. Carbonation-calcination cycle using high reactivity calcium oxide for carbon dioxide separation from flue gas. *Industrial & Engineering Chemistry Research*, 41(16):4035–4042, 2002.

[71] A. H. Harvey and J. M. Prausnitz. Thermodynamics of high-pressure aqueous systems containing gases and salts. *AIChE Journal*, 35(4):635–644, 1989. ISSN 1547-5905. doi: 10.1002/aic.690350413. URL http://dx.doi.org/10.1002/aic.690350413.

[72] A.H. Harvey. Semiempirical correlation for Henry's constants over large temperature ranges. *AIChE journal*, 42(5):1491–1494, 1996.

[73] A. Hebach, A. Oberhof, and N. Dahmen. Density of water + carbon dioxide at elevated pressures: measurements and correlation. *Journal of Chemical & Engineering Data*, 49(4):950–953, 2004.

[74] F. Helfferich. Theory of multicomponent, multiphase displacement in porous media. *Old SPE Journal*, 21(1):51–62, 1981.

[75] C. Higman and M. Van der Burgt. *Gasification*. Gulf Professional Publishing, 2003.

[76] R.W. Hill. Review of the CRIP (Controlled Retracting Injection Point) process. Technical report, Lawrence Livermore National Lab., CA (USA), 1986.

[77] J.P. Holman. *Heat Transfer*. McGraw-Hill, 1986.

[78] H. Huang and S.I. Sandler. Prediction of vapor-liquid equilibria at high pressures using activity coefficient parameters obtained from low-pressure data: a comparison of two equation of state mixing rules. *Industrial & Engineering Chemistry Research*, 32(7):1498–1503, 1993.

[79] M.L. Huber, R.A. Perkins, A. Laesecke, D.G. Friend, J.V. Sengers, M.J. Assael, I.N. Metaxa, E. Vogel, R. Mareš, and K. Miyagawa. New international formulation for the viscosity of H_2O. *Journal of Physical and Chemical Reference Data*, 38:101, 2009.

[80] W Huijgen, G Witkamp, and R Comans. Mechanisms of aqueous wollastonite carbonation as a possible CO_2 sequestration process. *Chemical Engineering Science*, 61(13):4242–4251, 2006. ISSN 00092509.

[81] W.J.J. Huijgen and R.N.J. Comans. *Carbon Dioxide Sequestration by Mineral Carbonation: Literature Review*. Energy Research Centre of the Netherlands ECN, 2003.

[82] W.J.J. Huijgen, G.J. Ruijg, R.N.J. Comans, and G.J. Witkamp. Energy consumption and net CO_2 sequestration of aqueous mineral carbonation. *Industrial & Engineering Chemistry Research*, 45(26):9184–9194, 2006.

[83] M.J. Huron and J. Vidal. New mixing rules in simple equations of state for representing vapour-liquid equilibria of strongly non-ideal mixtures. *Fluid Phase Equilibria*, 3(4):255–271, 1979.

[84] Muhammad F. Irfan, Muhammad R. Usman, and K. Kusakabe. Coal gasification in CO_2 atmosphere and its kinetics since 1948: A brief review. *Energy*, 36(1):12 – 40, 2011.

[85] A. Khadse, M. Qayyumi, S. Mahajani, and P. Aghalayam. Underground coal gasification: a new clean coal utilization technique for india. *Energy*, 32(11): 2061–2071, 2007.

[86] R. Khosrokhavar, G. Elsinga, A. Mojaddam, R. Farajzadeh, and J. Bruining. Visualization of natural convection flow of (sub-) and (super-) critical CO_2 in aqueous and oleic systems by applying schlieren method. In *SPE EUROPEC/EAGE Annual Conference and Exhibition*, Vienna, Austria, 23-26 May 2011. Society of Petroleum Engineers. doi: 10.2118/143264-MS.

[87] R. Khosrokhavar, G. Elsinga, A. Mojaddam, R. Farajzadeh, and J. Bruining. Visualization of natural convection flow of (sub-) and (super-) critical CO_2 in aqueous and oleic systems by applying schlieren method. In *SPE EUROPEC/EAGE Annual Conference and Exhibition*, Vienna, Austria, 23-26 May 2011. Society of Petroleum Engineers. doi: 10.2118/143264-MS.

[88] J. Kiepe, S. Horstmann, K. Fischer, and J. Gmehling. Experimental determination and prediction of gas solubility data for $CO_2 + H_2O$ mixtures containing NaCl or KCl at temperatures between 313 and 393 K and pressures up to 10 MPa. *Industrial & Engineering Chemistry Research*, 41(17):4393–4398, 2002.

[89] K.Y. Kim, W.S. Han, J. Oh, T. Kim, and J.C. Kim. Characteristics of salt-precipitation and the associated pressure build-up during CO_2 storage in saline aquifers. *Transport in Porous Media*, pages 1–22, 2012.

[90] T.J. Kneafsey and K. Pruess. Laboratory flow experiments for visualizing carbon dioxide-induced, density-driven brine convection. *Transport in Porous Media*, 82(1):123–139, 2010.

[91] D. Koschel, J.Y. Coxam, L. Rodier, and V. Majer. Enthalpy and solubility data of CO_2 in water and NaCl (aq) at conditions of interest for geological sequestration. *Fluid Phase Equilibria*, 247(1):107–120, 2006.

[92] J. Kozeny. Ueber kapillare leitung des wassers im boden. *Sitzungsber. Akad. Wiss. Wien*, 136:271–306, 1927.

[93] L. W. Lake. *Enhanced Oil Recovery*. Prentice Hall (Englewood Cliffs, NJ), 1989.

[94] Y.K. Li and L. X. Nghiem. Phase equilibria of oil, gas and water/brine mixtures from a cubic equation of state and henry's law. *The Canadian Journal of Chemical Engineering*, 64(3):486–496, 1986. ISSN 1939-019X. doi: 10.1002/cjce.5450640319.

[95] S. Mao and Z. Duan. The viscosity of aqueous alkali-chloride solutions up to 623 K, 1,000 bar, and high ionic strength. *International Journal of Thermophysics*, 30(5):1510–1523, 2009.

[96] P. M. Mathias and T. W. Copeman. Extension of the Peng-Robinson equation of state to complex mixtures: Evaluation of the various forms of the local composition concept. *Fluid Phase Equilibria*, 13:91–108, 1983.

[97] MATLAB. *version 7.10.0 (R2010a)*. The MathWorks Inc., Natick, Massachusetts, 2010.

[98] E.W. McAllister. *Pipeline Rules of Thumb Handbook: Quick and Accurate Solutions to Your Everyday Pipeline Problems*. Gulf Professional Publishing, 2009.

[99] A. Meisen and X. Shuai. Research and development issues in CO_2 capture. *Energy Conversion and Management*, 38:S37–S42, 1997.

[100] B. Metz. *Carbon Dioxide Capture and Storage: Special Report of the Intergovernmental Panel on Climate Change*. Cambridge University Press, 2005.

[101] B. Metz. *IPCC Special Report on Carbon Dioxide Capture and Storage*. Cambridge University Press, 2005.

[102] M. L. Michelsen. A modified Huron-Vidal mixing rule for cubic equations of state. *Fluid Phase Equilibria*, 60(1):213–219, 1990.

[103] T. Mimura, H. Simayoshi, T. Suda, M. Iijima, and S. Mituoka. Development of energy saving technology for flue gas carbon dioxide recovery in power plant by chemical absorption method and steam system. *Energy Conversion and Management*, 38:S57–S62, 1997.

[104] A. Molina and F. Mondragon. Reactivity of coal gasification with steam and CO_2. *Fuel*, 77(15):1831 – 1839, 1998.

[105] S. Morrell. An alternative energy-size relationship to that proposed by Bond for the design and optimisation of grinding circuits. *International Journal of Mineral Processing*, 74(1-4):133–141, 2004.

[106] N. Muller, R. Qi, E. Mackie, K. Pruess, and M.J. Blunt. CO_2 injection impairment due to halite precipitation. *Energy Procedia*, 1(1):3507–3514, 2009.

[107] R. Nazari Moghaddam, B. Rostami, P. Pourafshary, and Y. Fallahzadeh. Quantification of density-driven natural convection for dissolution mechanism in CO_2 sequestration. *Transport in Porous Media*, 92(2):439–456, 2011.

[108] R. Nazari Moghaddam, B. Rostami, P. Pourafshary, and Y. Fallahzadeh. Quantification of density-driven natural convection for dissolution mechanism in CO_2 sequestration. *Transport in Porous Media*, 92(2):439–456, 2012.

[109] J. A. Nighswander, N. Kalogerakis, and A. K. Mehrotra. Solubilities of carbon dioxide in water and 1 wt. % sodium chloride solution at pressures up to 10 MPa and temperatures from 80 to 200 degree C. *Journal of Chemical & Engineering Data*, 34(3):355–360, 1989. doi: 10.1021/je00057a027. URL http://pubs.acs.org/doi/abs/10.1021/je00057a027.

[110] H. Orbey and S.I. Sandler. *Modeling Vapor-Liquid Equilibria: Cubic Equations of State and Their Mixing Rules*, volume 1. Cambridge University Press, 1998.

[111] H. Ott, K. de Kloe, F. Marcelis, and A. Makurat. Injection of supercritical CO_2 in brine saturated sandstone: Pattern formation during salt precipitation. *Energy Procedia*, 4:4425–4432, 2011.

[112] N.A. Owen, O.R. Inderwildi, and D.A. King. The status of conventional world oil reserves-hype or cause for concern? *Energy Policy*, 38(8):4743–4749, 2010.

[113] B.A. Oyenekan and T. Gary. Energy performance of stripper configurations for CO_2 capture by aqueous amines. *Industrial & Engineering Chemistry Research*, 45(8):2457–2464, 2006.

[114] M. Panfilov and M. Rasoulzadeh. Interfaces of phase transition and disappearance and method of negative saturation for compositional flow with diffusion and capillarity in porous media. *Transport in Porous Media*, 83(1):73–98, 2010.

[115] K.Y. Park and T.F. Edgar. Modeling of early cavity growth for underground coal gasification. *Industrial & Engineering Chemistry Research*, 26(2):237–246, 1987.

[116] G.S.H. Pau, J.B. Bell, K. Pruess, A.S. Almgren, M.J. Lijewski, and K. Zhang. High–resolution simulation and characterization of density-driven flow in CO_2 storage in saline aquifers. *Advances in Water Resources*, 33(4):443–455, 2010.

[117] A. Péneloux, E. Rauzy, and R. Fréze. A consistent correction for Redlich–Kwong-Soave volumes. *Fluid Phase Equilibria*, 8(1):7–23, 1982.

[118] D.Y. Peng and D.B. Robinson. A new two-constant equation of state. *Industrial & Engineering Chemistry Fundamentals*, 15(1):59–64, 1976. ISSN 0196-4313.

[119] G. Perkins and V. Sahajwalla. A mathematical model for the chemical reaction of a semi-infinite block of coal in underground coal gasification. *Energy Fuels*, 19(4):1679–1692, 2005.

[120] G. Perkins and V. Sahajwalla. A numerical study of the effects of operating conditions and coal properties on cavity growth in underground coal gasification. *Energy Fuels*, 20(2):596–608, 2006.

[121] R. H. Perry, D. W. Green, and J. O. Maloney. *Perry's Chemical Engineers' Handbook*, volume 7. McGraw-Hill New York, 2008.

[122] R.H. Perry and D.W. Green. *Perry's Chemical Engineers' Handbook*. McGraw-Hill, 2008.

[123] R.H. Perry, D.W. Green, and J.O. Maloney. *Perry's Chemical Engineers' Handbook*. McGraw-Hill New York, 1997.

[124] S.I. Plasynski and Z.Y. Chen. Review of CO_2 capture technologies and some improvement opportunities. *Papers of the American Chemical Society*, 220: 391–405, 2000.

[125] W.-J. Plug and J. Bruining. Capillary pressure for the sand-CO_2-water system under various pressure conditions. application to CO_2 sequestration. *Advances in Water Resources*, 30(11):2339–2353, 2007.

[126] J. M. Prausnitz, R. N. Lichtenthaler, and E. G. de Azevedo. *Molecular Thermodynamics of Fluid-Phase Equilibria*. Prentice Hall, 1998.

[127] W.H. Press. *Numerical Recipes: the Art of Scientific Computing*. Cambridge University Press, 2007.

[128] M.J. Prins and K.J. Ptasinski. Energy and exergy analyses of the oxidation and gasification of carbon. *Energy*, 30(7):982–1002, 2005.

[129] K. Pruess. *ECO2N: A TOUGH2 Fluid Property Module for Mixtures of Water, NaCl, and CO_2*. Lawrence Berkeley National Laboratory, 2005.

[130] K. Pruess. Formation dry-out from CO_2 injection into saline aquifers: 2. analytical model for salt precipitation. *Water Resources Research*, 45(3), 2009.

[131] K. Pruess and N. Müller. Formation dry-out from CO_2 injection into saline aquifers: 1. effects of solids precipitation and their mitigation. *Water Resources Research*, 45(3), 2009.

[132] K. Pruess and N. Spycher. ECO2N–a fluid property module for the TOUGH2 code for studies of CO_2 storage in saline aquifers. *Energy Conversion and Management*, 48(6):1761–1767, 2007.

[133] H.H. Rachford and J.D. Rice. Procedure for use of electronic digital computers in calculating flash vaporization hydrocarbon equilibrium. *Trans. Soc. Pet. Eng*, 195:327, 1952.

[134] H.J. Ramey Jr. Wellbore heat transmission. *Journal of Petroleum Technology*, 14(4):427–435, 1962.

[135] H. Renon and J.M. Prausnitz. Local compositions in thermodynamic excess functions for liquid mixtures. *AIChE Journal*, 14(1):135–144, 1968.

[136] H. Renon and J.M. Prausnitz. Estimation of parameters for the NRTL equation for excess gibbs energies of strongly nonideal liquid mixtures. *Industrial & Engineering Chemistry Process Design and Development*, 8(3):413–419, 1969.

[137] A. Riaz, M. Hesse, H.A. Tchelepi, and F.M. Orr. Onset of convection in a gravitationally unstable diffusive boundary layer in porous media. *Journal of Fluid Mechanics*, 548(1):87–111, 2006.

[138] M.R. Riazi and C.H. Whitson. Estimating diffusion coefficients of dense fluids. *Industrial & Engineering Chemistry Research*, 32(12):3081–3088, 1993. ISSN 0888-5885.

[139] G. Robello Samuel and G. McColpin. Wellbore hydraulic optimization with positive displacement motor and bit. *IADC/SPE Middle East Drilling Technology*, (IADC/SPE 72320), 2001.

[140] M.A. Rosen. Thermodynamic comparison of hydrogen production processes. *International Journal of Hydrogen Energy*, 21(5):349–365, 1996.

[141] B. Rumpf, H. Nicolaisen, C. Öcal, and G. Maurer. Solubility of carbon dioxide in aqueous solutions of sodium chloride: experimental results and correlation. *Journal of Solution Chemistry*, 23(3):431–448, 1994.

[142] H. Salimi, K.H. Wolf, and J. Bruining. Negative saturation approach for non-isothermal compositional two-phase flow simulations. *Transport in Porous Media*, pages 1–32, 2011.

[143] S.P. Singh, S.A. Weil, and S.P. Babu. Thermodynamic analysis of coal gasification processes. *Energy*, 5:905–914, 1980.

[144] B.E. Sleep and J.F. Sykes. Compositional simulation of groundwater contamination by organic compounds: 1. model development and verification. *Water Resources Research*, 29(6):1697–1708, 1993.

[145] J.M. Smith, H.C. Van Ness, and M.M. Abbott. *Introduction to Chemical Engineering Thermodynamics*. McGraw Hill, 2001.

[146] J.M. Smith, H.C. Van Ness, and M.M. Abbott. *Introduction to Chemical Engineering Thermodynamics*. McGraw-Hill, 2001.

[147] G. Soave. Equilibrium constants from a modified Redlich-Kwong equation of state. *Chemical Engineering Science*, 27(6):1197–1203, 1972.

[148] R. Span and W. Wagner. A new equation of state for carbon dioxide covering the fluid region from the triple-point temperature to 1100 K at pressures up to 800 MPa. *Journal of Physical and Chemical Reference Data*, 25:1509, 1996.

[149] N. Spycher, K. Pruess, and J. Ennis-King. CO_2-H_2O mixtures in the geological sequestration of CO_2. i. assessment and calculation of mutual solubilities from 12 to 100 C and up to 600 bar. *Geochimica et Cosmochimica Acta*, 67(16): 3015–3031, 2003.

[150] K. Stanczyk, A. Smolinski, K. Kapusta, M. Wiatowski, J. Swiadrowski, A. Kotyrba, and J. Rogut. Dynamic experimental simulation of hydrogen oriented underground gasification of lignite. *Fuel*, 89(11):3307–3314, 2010.

[151] K. Stańczyk, N. Howaniec, A. Smoliński, J. Świądrowski, K. Kapusta, M. Wiatowski, J. Grabowski, and J. Rogut. Gasification of lignite and hard coal with air and oxygen enriched air in a pilot scale ex situ reactor for underground gasification. *Fuel*, 90(5):1953–1962, 2011.

[152] Krzysztof Stańczyk, Krzysztof Kapusta, Marian Wiatowski, Jerzy Świądrowski, Adam Smoliński, Jan Rogut, and Andrzej Kotyrba. Experimental simulation of hard coal underground gasification for hydrogen production. *Fuel*, 91(1):40–50, 2012.

[153] R. Stryjek and J.H. Vera. PRSV: An improved peng-Robinson equation of state for pure compounds and mixtures. *The Canadian Journal of Chemical Engineering*, 64(2):323–333, 2009.

[154] J. Szargut. Analysis of cumulative exergy consumption. *International Journal of Energy Research*, 11(4):541–547, 1987.

[155] J. Szargut. Chemical exergies of the elements. *Applied Energy*, 32(4):269–286, 1989.

[156] J. Szargut and D.R. Morris. Cumulative exergy consumption and cumulative degree of perfection of chemical processes. *International Journal of Energy Research*, 11(2):245–261, 1987.

[157] J. Szargut, D.R. Morris, and F.R. Steward. *Energy Analysis of Thermal, Chemical, and Metallurgical Processes.* Hemisphere Publishing, New York, NY, 1988.

[158] S. Takenouchi and G. C Kennedy. The solubility of carbon dioxide in NaCl solutions at high temperatures and pressures. *American Journal of Science*, 263(5):445–454, 1965.

[159] P.N. Thompson, J.R. Mann, and F. Williams. *Underground Gasification of Coal: a National Coal Board Reappraisal.* National Coal Board, 1976.

[160] K. Vafai and C.L. Tien. Boundary and inertia effects on flow and heat transfer in porous media. *International Journal of Heat and Mass Transfer*, 24(2):195–203, 1981.

[161] D.W. Van Batenburg, E.N.J. Biezen, and J. Bruining. A new channel model for underground gasification of thin, deep coal seams. *In Situ*, 18:419–419, 1994. ISSN 0146-2520.

[162] M.T. van Genuchten. A closed-form equation for predicting the hydraulic conductivity of unsaturated soils. *Soil Science Society of America Journal*, 44 (5), 1980.

[163] A. Verma and K. Pruess. Thermohydrological conditions and silica redistribution near high-level nuclear wastes emplaced in saturated geological formations. *Journal of Geophysical Research: Solid Earth (1978–2012)*, 93(B2): 1159–1173, 1988.

[164] W. Wagner, J.R. Cooper, A. Dittmann, J. Kijima, H.J. Kretzschmar, A. Kruse, R. Mareš, K. Oguchi, H. Sato, I. Stöcker, et al. The IAPWS industrial formulation 1997 for the thermodynamic properties of water and steam. *Journal of Engineering for Gas Turbines and Power*, 122:150, 2000.

[165] H. Wahanik, A.A. Eftekhari, J. Bruining, D. Marchesin, and K.H. Wolf. Analytical solutions for mixed CO_2-water injection in geothermal reservoirs. In *Canadian Unconventional Resources and International Petroleum Conference*, Alberta, Canada, 19-21 October 2010. SPE. doi: 10.2118/138154-MS.

[166] S.M. Walas. *Phase Equilibria in Chemical Engineering*. Butterworth Boston, 1985.

[167] L. Walker, W.H. McAdams, and E.K. Gilliland. *Principles of Chemical Engineering*. McGraw-Hill, 1937.

[168] Z. Wang, J. Zhou, Q. Wang, J. Fan, and K. Cen. Thermodynamic equilibrium analysis of hydrogen production by coal based on $Coal/CaO/H_2O$ gasification system. *International Journal of Hydrogen Energy*, 31(7):945–952, 2006.

[169] C.H. Whitson and M.L. Michelsen. The negative flash. *Fluid Phase Equilibria*, 53:51–71, 1989.

[170] W. Woodside and J.H. Messmer. Thermal conductivity of porous media. I. unconsolidated sands. *Journal of Applied Physics*, 32(9):1688–1699, 1961.

[171] T. Xu, Y. Ontoy, P. Molling, N. Spycher, M. Parini, and K. Pruess. Reactive transport modeling of injection well scaling and acidizing at Tiwi field, Philippines. *Geothermics*, 33(4):477–491, 2004.

[172] X. Xu, S. Chen, and D. Zhang. Convective stability analysis of the long-term storage of carbon dioxide in deep saline aquifers. *Advances in Water Resources*, 29(3):397–407, 2006.

[173] H. Yang, Z. Xu, M. Fan, R. Gupta, R.B. Slimane, A.E. Bland, and I. Wright. Progress in carbon dioxide separation and capture: A review. *Journal of Environmental Sciences*, 20(1):14–27, 2008.

[174] L. Yang, X. Zhang, S. Liu, L. Yu, and W. Zhang. Field test of large-scale hydrogen manufacturing from underground coal gasification (UCG). *International Journal of Hydrogen Energy*, 33(4):1275–1285, 2008.

[175] M. Zeidouni, M. Pooladi-Darvish, and D. Keith. Analytical solution to evaluate salt precipitation during CO_2 injection in saline aquifers. *International Journal of Greenhouse Gas Control*, 3(5):600–611, 2009.

Summary

> The most exciting phrase to hear
> in science, the one that heralds the
> most discoveries, is not "Eureka!",
> but "That's funny..."

Isaac Asimov

This thesis evaluates the possibility of using underground coal gasification with a low CO_2 footprint. The thesis consists of two parts. In the first part, by using the concept of exergy, a framework was constructed through which the practicality (feasibility) of an energy conversion/extraction method can be systematically evaluated. This framework, based on exergy analysis and cumulative degree of perfection, is described by analyzing a low emission underground coal gasification (UCG) process. For the evaluation of energy conversion processes we introduce a new concept, viz. recovery factor, which is a better indicator of the exergetic viability of a conversion process than the traditionally used efficiency factors. In the second part, various issues related to the aquifer storage of CO_2 are studied. Aquifer storage is considered as an option for low emission fossil fuel utilization. Each chapter is summarized as follows:

In chapter 2, various options are considered to reduce CO_2 emissions when utilizing deep coal by applying UCG, i.e., (1) in combination with carbonation of synthetic minerals (CaO), (2) conventional UCG followed by ex-situ separation of CO_2 and (3) upgrading the product gas using naturally occurring minerals (wollastonite).

A chemical equilibrium model was used to analyze the effect of the process parameters on product composition and use it for an exergy (useful energy) analysis. The result is presented in terms of theoretical (ideal unit operations), practical (state of the art technology), and zero-emission (applying current CO_2 capture and sequestration (CCS) to all sources of CO_2 emission) recovery factors. The results show that underground gasification of deep coal can optimally extract 52-68 % of the coal chemical exergy, but zero-emission extraction gives a negative recovery factor, indicating that it is not practical with the current state of the art CCS technology. Using in-situ CaO, which will enhance the H2 production, is theoretically feasible with a recovery factor around 80%, but is not exergetically feasible with the current state of technology, i.e. with a negative practical recovery factor. Ex-situ upgrading of the conventional UCG product gas with wollastonite is exergetically feasible for

both practical and zero-emission cases according to the equilibrium model. Slow attainment of chemical equilibrium makes its application questionable.

In chapter 3, based on recent successful low-pressure underground coal gasification pilot experiments that use alternating injection of air (oxygen) and steam, a mathematical model is written to evaluate the potential of alternating injection UCG in large scale hydrogen production. This chapter extends an existing steady state model to a transient model that can describe an alternating injection of air and steam for deep thin coal layers. The model includes transient heat conduction, where the produced heat during the air injection stage is stored in the coal and surrounding strata. The stored heat is subsequently used in the endothermic gasification reactions during the steam injection.

Comparison of the results with field data show that product composition and temperature oscillation can be predicted with a reasonable accuracy. The stored heat can deliver additional energy that can maintain the gasification during the steam injection period for a limited time. During the steam injection cycle, at low pressure the volumetric flow and the hydrogen content of the product gas are both high, but at higher pressures while the hydrogen composition is still high, the coal conversion rate decreases considerably. The exergy analysis confirms that alternating injection of air/steam describes a practical process for UCG at low pressure. However, injection of a mixture of steam and oxygen results in a practical recovery factor of 50% and produces 0.15 kg CO_2 per MJ of exergy, which is higher than the practical recovery factor (40%) of the alternating injection process, which produces 0.12 kg CO_2 / MJ of exergy.

In the second part of the thesis, two issues related to aquifer storage of CO_2 are discussed: injectivity problems due to salt precipitation, and storage capacity and long term storage due to dissolution of CO_2 in water.

In chapter 4, the negative saturation (NegSat) method, which is a combination of negative flash and multicomponent single/two-phase flow in porous media, is studied. It has been shown to be beneficial in numerical simulations of phase appearance/disappearance for mixtures that consist of volatile components, i.e., components that appear in both liquid and gas phases. The method is extended to a three phase system of CO_2-water-NaCl, in which NaCl appears as a nonvolatile dissolved component (NaCl) and as an immobile precipitated solid phase. The extended method is of practical use to assess carbon dioxide storage options. A detailed thermodynamic analysis of the NegSat method is given and the possibility to extend it to injection in brine aquifers is demonstrated.

Precipitation of salt occurs due to evaporation of water into supercritical CO_2. Precipitation decreases the permeability near the injection well forming a dried-out zone. With the ensuing permeability change, the injection pressure needs to be increased to maintain the CO_2 injection rate, which requires more compression energy and hence influences the exergetic viability of the carbon dioxide sequestration process.. To address this issue, first a thermodynamic model is optimized to pre-

dict the phase behavior of the CO_2-water-NaCl system with reasonable accuracy. Then the NegSat method for two-phase flow is modified to include salt precipitation. The model is solved to analyze the effect of various physical parameters on the injectivity of CO_2. Finally an exergy analysis is performed to quantify the effect of salt precipitation on the compression power requirement for CO_2 injection into high pressure-high temperature-high salinity aquifers. Exergetic applicability of carbon capture and sequestration for low emission carbon dioxide fuel consumption, can presently only be achieved if the energy-intensive step of nitrogen-CO_2 separation prior to injection can be avoided.

In chapter 5, the enhanced mass transfer of CO_2 in water for a CO_2 saturated layer on top of a water saturated porous medium is studied experimentally and theoretically. Dissolution of carbon dioxide in water has a large effect on the capacity of an aquifer for carbon dioxide storage. Without the dissolution effect the storage capacity of aquifers is low. A high pressure cylinder with a length of 0.5 m and a diameter of 0.15 m is used in pressure decay experiments. The relatively large size of the vessel minimizes the pressure measurement errors that can happen due to temperature fluctuations and small leakages. The experimental results were compared to the theoretical result in terms of onset time of natural convection and rate of mass transfer of CO_2 in the convection dominated process. In addition a non-isothermal multicomponent flow model in porous media is solved numerically to study the effect of the heat of dissolution of CO_2 in water on the rate of mass transfer of CO_2. The effect of the capillary transition zone on the rate of mass transfer of CO_2 is also studied theoretically. The simulation results including the effect of the capillary transition zone show a better agreement with experimental results compared to the simulation result without considering a capillary transition zone. The simulation results also show that the effect of heat of dissolution on the rate of mass transfer is negligible. The overall conclusion is that, for the current state of technology, use of underground coal gasification with a similar carbon foot print as the use of natural gas is not possible. It is to be expected that technological developments will make it possible in the future to use coal with a low carbon footprint.

Samenvatting

> De meest opwindende zin die men
> in de wetenschap kan horen, de zin
> die de meeste ontdekkingen
> aankondigt, is niet "Eureka", maar
> "dat is vreemd"
>
> Isaac Asimov

Dit proefschrift evalueert de mogelijkheid om ondergrondse kolenvergassing (OKV) met een lage CO_2 voetafdruk te gebruiken. Het proefschrift bestaat uit twee onderdelen. In het eerste deel werd een raamwerk gemaakt door het concept exergie te gebruiken waardoor de uitvoerbaarheid (haalbaarheid) van een energie conversie/extractie methode systematisch kan worden geëvalueerd. Dit raamwerk, gebaseerd op exergieanalyse en "cumulatieve graad van perfectie", wordt beschreven aan de hand van een analyse van het ondergronds kolenvergassingsproces (OGV) met een lage emissie. Voor de evaluatie van energie omzettingsprocessen, introduceren we een nieuw concept, n.l., de winningsfactor, die een betere indicatie geeft van de exergetische haalbaarheid van een conversieproces dan de traditioneel gebruikte efficiëntiefactoren. In het tweede deel worden verscheidene vraagstukken behandeld die verband houden met opberging van CO_2 in een watervoerende laag. Opberging in een watervoerende laag wordt als een mogelijkheid beschouwd voor fossiel brandstof gebruik met een lage CO_2 emissie. Elk hoofdstuk wordt hieronder kort samengevat. In hoofdstuk 2 worden verschillende mogelijkheden beschouwd om CO_2 emissies te verlagen voor diepe OKV, d.w.z., (1) combinatie met carbonatie van synthetische mineralen (CaO), (2) conventionele OKV gevolgd door ex-situ scheiding van CO_2 en (3) opwaardering van het product gas met behulp van natuurlijk voorkomende mineralen (wollastoniet) .

Een chemisch evenwichtsmodel werd gebruikt voor het analyseren van het effect van de procesparameters op de productsamenstelling en voor een exergie (nuttige energie) analyse. Het resultaat wordt weergegeven in termen van (1) theoretische- (ideale deelprocessen), (2) praktische- (huidige stand van techniek) en (3) nul-emissie- (toepassen van de huidige afvang-technologie en opberg-technologie (CCS) voor alle bronnen van CO_2 emissie) winningsfactoren. De resultaten laten zien dat OKV van diepe kolen optimaal 52-68% van de kolen-energie kan extraheren, maar dat nul-emissie extractie een negatieve winningsfactor geeft. Dit geeft aan dat het niet praktisch is met de huidige stand van CCS technologie. In-situ gebruik van CaO,

die de H2 productie zal verbeteren, is theoretisch haalbaar met een winningsfactor van 80%, maar is niet exergetisch haalbaar met de huidige stand van techniek, d.w.z., het heeft een negatieve praktische winningsfactor. Ex-situ opwaarderen van het conventionele OKV gas met wollastoniet is volgens het evenwichtsmodel exergetisch haalbaar met de huidige stand van de techniek. Het langzaam instellen van het chemisch evenwicht maakt de toepasbaarheid echter twijfelachtig. Hoofdstuk 3 is gebaseerd op recente succesvolle lage druk experimenten die gebruik maken van afwisselende injectie van lucht (zuurstof) en stoom. Hiervoor is een mathematisch model ontwikkeld om het potentieel te evalueren van afwisselende injectie voor waterstof productie op grote schaal. In dit hoofdstuk wordt een bestaand "steady state" model uitgebreid naar een transiënt model dat afwisselende injectie van lucht en stoom in diepe kolenlagen kan beschrijven. Het model omvat transiënte warmte geleiding, waarbij de warmte die gedurende het luchtinjectie stadium werd geproduceerd wordt opgeslagen in de kool en omliggende lagen. De opgeslagen warmte wordt vervolgens gebruikt ten behoeve van de endotherme reacties gedurende de stoominjectie periode. Een vergelijking van de resultaten met veldgegevens laat zien dat het model product samenstelling en temperatuur oscillaties met redelijke nauwkeurigheid kan voorspellen. De opgeslagen warmte kan de extra energie leveren die het vergassingsproces gedurende de stoominjectie periode enige tijd aan de gang houden. Gedurende de stoominjectie injectie periode, zijn de volumetrische stroming en het waterstof gehalte van het productgas beiden hoog, maar bij hogere drukken, terwijl het waterstof gehalte nog steeds hoog is, neemt de kool-omzettings-snelheid aanzienlijk af. De exergieanalyse bevestigt dat afwisselende lucht/stoom-injectie bij lage druk een praktisch OKV proces beschrijft. Echter, injectie van een mengsel van stoom en zuurstof resulteert in een praktische winningsfactor van 50% en produceert 0.15 kg CO_2 per MJ energie. Dit is beter is dan de praktische winningsfactor van 40% voor het alternerende injectieproces, dat 0.12 kg CO_2 /MJ energie produceert. In het tweede deel van het proefschrift, worden twee vraagstukken die verband houden met opslag in watervoerende lagen besproken: (1) injectiviteits-problemen door zout neerslag (2) de opslag-capaciteits-verbetering en lange termijn opslag ten gevolge van het oplossen van CO_2 in water. In hoofdstuk 4 wordt de negatieve saturatie (NegSat) methode, een combinatie van negatieve "flash" en multi-component een/twee-fasen stroming in poreuze media, bestudeerd. Men kan laten zien dat de NegSat methode voordelig is in numerieke stromings-berekeningen met mengsels die bestaan uit vluchtige componenten die zowel in de vloeistoffase als in de gasfase voorkomen waarbij fasen verschijnen of verdwijnen. De methode is uitgebreid voor een driefasen systeem met CO_2-water-NaCl, waarbij NaCl voorkomt als een niet vluchtige opgeloste component (NaCl) en als een immobiele neergeslagen vaste fase. De uitgebreide methode is van praktisch nut om CO_2 opslag mogelijkheden te beoordelen. Een gedetailleerde thermodynamische analyse van de NegSat methode wordt gegeven en de mogelijkheid de methode uit te breiden voor injectie in pekel voerende lagen wordt aangetoond. Neerslag van zout treedt op door verdamping van water in superkritisch CO_2. De neerslag verlaagt de permeabiliteit in de buurt van de injectieput en vormt een uitgedroogde zone. De

ten gevolge hiervan optredende permeabiliteitsverandering vereist verhoging van de injectiedruk om de CO_2 injectiesnelheid te handhaven en dit leidt tot een hogere compressie energie en beïnvloedt daardoor de exergetische haalbaarheid van het kooldioxide opslagproces. Om dit probleem aan te pakken, wordt eerst een thermodynamisch model geoptimaliseerd om het fasengedrag van het CO_2-water-NaCl system met redelijke nauwkeurigheid te voorspellen. Vervolgens wordt de NegSat methode voor tweefasen-stroming aangepast om ook zoutneerslag toe te laten. De modelvergelijkingen worden opgelost om het effect van verschillende fysische parameters op de injectiviteit van CO_2 te analyseren. Tenslotte, wordt een exergieanalyse uitgevoerd om het effect van zoutneerslag op het vereiste compressievermogen te kwantificeren voor CO_2 injectie in hogedruk-hoge temperatuur watervoerende lagen met een hoog zout gehalte. De exergetische toepasbaarheid van koolstof-invang en opslag ten behoeve van brandstofgebruik met een lage CO_2-emissie, kan op dit moment alleen worden bereikt als de energie-intensieve stap van N_2-CO_2 scheiding voorafgaand aan de injectie kan worden vermeden. In hoofdstuk 5, wordt de verhoogde massaoverdracht van CO_2 in water voor een met CO_2 verzadigde laag boven een met water verzadigd poreus medium experimenteel en theoretisch bestudeerd. Het oplossen van CO_2 in water heeft een groot effect op de capaciteit van een watervoerende laag voor CO_2 opslag. Zonder het oplos-effect is de opslagcapaciteit van watervoerende lagen gering. Een hogedruk cilinder met een lengte van 0.5 m en een diameter van 0.15 m wordt gebruikt in drukval experimenten. De relatief grote maat van de cylinder minimaliseert de drukmeetfouten die optreden ten gevolge van temperatuurschommelingen en kleine lekkages. De experimentele resultaten werden vergeleken met theoretische resultaten in termen van de vertraagde aanvangstijd van natuurlijke convectie en de massaoverdrachtssnelheid van CO_2 in het door convectie gedomineerde proces. Bovendien wordt een niet-isotherm multicomponent stromingsmodel in poreuze media numeriek opgelost om het effect van de oploswarmte van CO_2 in water op de massaoverdrachtssnelheid van CO_2 te bepalen. Het effect van de capillaire overgangszone op de massaoverdrachtssnelheid wordt ook theoretisch bestudeerd. De simulatieresultaten inclusief het effect van de capillaire overgangszone geeft een betere overeenstemming met de experimentele resultaten dan de simulatie resultaten zonder de capillaire overgangszone te beschouwen. De simulatieresultaten laten ook zien dat het effect van oploswarmte op de massaoverdrachtssnelheid verwaarloosbaar is. De algemene conclusie is dat, voor de huidige stand van techniek, gebruik van ondergrondse kolenvergassing met een vergelijkbare koolstof-voetafdruk als het gebruik van aardgas onmogelijk is. Men kan verwachten dat technologische ontwikkelingen dit gebruik van ondergrondse vergassing wel mogelijk maken.

Acknowledgments

> The deepest principle of human nature is the craving to be appreciated.
>
> <div align="right">William James</div>

> Never expect to be appreciated, and you'll never feel disappointed.
>
> <div align="right">Unknown</div>

There are many people involved directly or indirectly in this book, and in my life while writing it, that inevitably and against my will I have to divide them into the categories of friends, colleagues, etc to pretend that I have remembered and appreciated every single person who expects (or not), one way or another, to be mentioned in these words.

First of all, I would like to express my sincere gratitude to my promoter and supervisor, Professor Hans Bruining. Your curiosity, persistence, dedication, and sense of humor have always been inspiring to me. There are so many lessons to be learned in the way you approach new challenges and never give up. Thanks a lot for never giving up on me. I will never forget our long discussions about energy, life, the Universe, and everything. I am very happy that we are still working on our mutual interest, "energy conversion".

I also would like to thank my co-promoter, Dr. Karl Heinz Wolf. His impeccable sense of practicality and his direct tone, have always been proven to be necessary and helpful.

I would like to specifically thank three persons whose contribution vastly improved the content of this thesis.

Dr. Hedzer van der Kooi is one of the few owners of a yet to be discovered "teaching gene". He was so nice to travel from Rijswijk to Delft every Monday during a horrible Dutch winter, to teach us how to write about exergy. I'm so glad that we are going to work on another project in the coming years. During our fruitful discussions, I benefited from his vast knowledge of classic thermodynamics and was fortunate to see the world from his humane stand.

The first time I received Professor Dan Marchesin's comments on a draft, I asked myself what I have done to him that he is taking such a terrifying revenge? After amending the paper and comparing it to the first version, I realized what a torture it might have been for him to comment on that horrible draft. Working with Dan is not easy, but it is extremely productive. He has a good sense of humor that appears in a serious manner in the middle of exhausting scientific discussions, that I specifically adore.

Dr. Rouhi Farajzadeh is always full of new ideas and ready for collaboration. The experiments of Chapter 5 was designed and performed mostly based on his previous precious experiences. Our collaboration on his project nano-particle stabilized foam was a life-saver for me.

Hedzer, Dan, and Rouhi: I truly appreciate your invaluable assistance.

Amazing technicians of Dietz Lab and fantastic support staff of our department: thanks a lot for being always friendly, positive, and supportive.

My colleagues in sections of Geo-environmental Engineering and Petroleum Engineering: I truly enjoyed working with you. Please forgive me for never joining you for lunch. It's always been impossible for me to talk and eat, or eat and talk, simultaneously.

There is a three-word sentence in an old Persian book, which is a response to the question "*which one is better? a brother or a friend*". The answer can be translated to "*brother friend better*", which means "the better is a brother who is also your friend". How can I be happier for finding several friends, who are like my new brothers and sisters (or the other way around). I want you to know that I am so proud of being a small part of your life, and wholeheartedly appreciate all your kind support. Wherever I am, I'll never forget you.

Parenting is by far the number one in the list of unappreciated jobs. I'm not saying that as a parent. It's fully based on my experience as a child. Being the first child of a my parents, and having an elephant memory for remembering the details of everyday life, I know how hard my parents tried to keep our family so strongly together and provide us with all means a child may need for a flourishing journey through life. My father was my friend, my greatest incentive, my superhero with no evident superpower, and the one who is responsible for my nightly novel reading addiction. He always hoped that one day I become a real doctor, those who can prescribe medicines, until he saw me collapsing by looking at two drops of blood coming out of a small scratch on my skin. Nevertheless he was enthusiastically expecting my PhD defense, but he couldn't stay longer. I will never believe that you are not here anymore.

My mother is the strongest person I have ever seen. To me, it is always a mystery how she manages to do so many things in a limited time. The only rational and reasonable explanation is that she has a time machine, a really good one, because she never fails. The only reason that she never tells us about her time machine is

our own safety. When it comes to our wellbeing and safety, she can transform herself from a lovely compassionate lady to a lionhearted warrior. How lucky we are to live in a peaceful house fortified by your presence. "BabaAli" and "Mamani", thank you for everything.

Most of the times, when we sit together with my brothers and sisters, we laugh so hard that neighbors warn us to stop it immediately or they will call the police. That's the picture I have from my brothers and sisters: Elham, Amin, Omid, Arezoo, Javad, and Reza with a big beautiful smile on their face. I'm so sorry for not being there for you as an older brother should be. I am always proud of you and I will always love you.

When it comes to say something about Maryam and Aida, I simply run out of words. I cannot even use a cliché like "they are all I've ever wanted" or "they are my dreams coming true". Even in my most optimistic dreamy imaginations, I couldn't see this coming. It is not easy to explain, but I am going to share with you how I see my family:

To me, one of the most precious qualities, something that can make our life peaceful, is our ability to *trust* and *be trusted*. Now imagine the trust in its purest state, or its ultimate form. Then try to materialize it, give it a shape, something that can be touched and felt. There is a Persian word "Omid", which can be loosely translated to "hope", without the strongly implied sense of expectation and dissatisfaction that come with the word "hope".

To me, MARYAM is the *Trust* and AIDA is the *Omid*. Without trust and hope, I could have done nothing. Maryam and Aida: I sincerely hope that I can be worthy of your unconditional trust and love.

Ali Akbar Eftekhari,

Delft, September 2013

Propositions

1. When the exergy analysis of an energy conversion/extraction process shows a positive recovery factor, it does not mean that it can be implemented in practice. However, a negative recovery factor means that the process is impractical.

2. With the current state of technology, the CO_2 capture and storage requires 30-55% of the combustion energy of a fossil fuel. Even though it can be improved by developing more energy-efficient CO_2 capture methods, it is wiser to spend the resources on the development of alternative low emission energy extraction methods (Chapter 2).

3. Alternating injection of oxygen/steam for production of a low carbon syngas once again shows that a successful low pressure experiment is not indicative of its success at higher pressures (Chapter 3).

4. In the modeling of multiphase/multicomponent flow in porous media, the non-linearities can be handled more robustly by employing a useful combination of thermodynamics and fluid flow relations, e.g., NegSat approach. This illustrates the importance of thermodynamics in multi-phase flow simulations (Chapter 4).

5. For enhanced mass transfer of CO_2 in a water-saturated porous medium, one simple method to match the result of a mathematical model (transient convection-diffusion) with pressure decay experimental data is to increase the diffusion coefficient a few orders of magnitude and plot the pressure history data with a linear time axis (Chapter 5).

6. Having a baby is the sweetest, most joyful, most wonderful, and biggest mistake a couple can ever make.

7. Living in Middle East has taught me to be scared of two groups of people: those who are never wrong and those who are trying to save the world. A catastrophe happens when someone who is never wrong tries to save the world.

8. Commercial numerical solvers often give the user a wrong feeling of actually learning and understanding the underlying numerical procedures. Without the experience in implementation of simplified numerical procedures, the user can end up in destructive trial and error effort with various options of a commercial simulator. In other words, one who has never encountered a "divided by zero" error is better to stay away from commercial numerical solvers.

9. The theoretical effectiveness of a PhD research can be 100%. But practically it never exceeds 5-10%, for the same reasons as that 5-10% exergetic effectiveness is typical of a chemical process (effectiveness is defined as the amount of "meaningful" research results divided by the total output).

10. A university teacher is someone who is qualified enough to recognize the importance of a scientific topic, knowledgeable to translate it to simple language, an artist in making it interesting for a diverse group of relatively enthusiastic pupil, and extremely patient with the slow and reversible process of knowledge transfer. Currently, one can observe an overemphasis in research and a lack of good teaching.

Stellingen

1. Wanneer de exergieanalyse van een energie conversie/extractie proces een positieve winningsfactor aangeeft, dan betekent dit nog niet dat het in de praktijk kan worden verwezenlijkt. Echter een negatieve winningsfactor betekent dat het proces onpraktisch is.

2. Met de huidige stand van techniek, vereist CO_2-afvang en-opslag 30-55% van de verbrandingsenergie van een fossiele brandstof. Hoewel dit kan worden verbeterd door efficiëntere CO_2-afvang methoden te ontwikkelen, is het wijzer om de middelen aan te wenden voor de ontwikkeling van alternatieve energie-extractie methoden met een lage CO_2 emissie (hoofdstuk 2).

3. Afwisselende zuurstof/stoom injectie voor de productie van koolstofarm syngas laat nogmaals zien dat een succesvol lage druk experiment niet betekent dat het ook succesvol is bij hogere drukken (hoofdstuk 3).

4. In het modelleren van multi-fase/ multicomponent stroming in poreuze media, kan het niet lineaire gedrag robuuster worden gehanteerd door een nuttige combinatie van thermodynamica en stromingsvergelijkingen, bijvoorbeeld de NegSat benadering, te gebruiken. Dit laat het belang zien van de thermodynamica voor meer-fasen stromings-simulaties (hoofdstuk 4).

5. Een eenvoudige methode om het resultaat van een mathematisch (transiënte convectie-diffusie) model te laten overeenkomen met de experimentele drukval gegevens voor verhoogde massa overdracht van CO_2 naar een met water verzadigd medium is om de diffusie- coëfficiënt verschillende ordes te vergroten en de drukhistorie gegevens lineair met de tijd weer te geven (hoofdstuk 5).

6. Het krijgen van een baby is de mooiste, verblijdendste, prachtigste, en grootste fout die een echtpaar ooit kan maken.

7. Het wonen in het Midden-Oosten heeft me geleerd om voor twee groepen mensen bang te zijn: hen die nooit ongelijk hebben en hen die de wereld proberen te redden. Een catastrofe treedt op wanneer iemand die nooit ongelijk heeft de wereld probeert te redden

8. Commerciële numerieke "solvers" geven de gebruiker het foute gevoel dat ze de achterliggende numerieke procedures begrijpen. Zonder het vermogen om vereenvoudigde numerieke procedures te implementeren, kan de gebruiker verzeild raken in destructieve trial en error inspanningen met verschillende opties van een commerciële simulator. Met andere woorden, iemand die nog nooit een "delen door nul" fout is tegengekomen, kan maar beter wegblijven van commerciële numerieke "solvers".

9. De theoretische effectiviteit van doctoraal onderzoek kan 100% zijn. Maar in de praktijk komt het nooit boven de 5-10%, om dezelfde reden dat 5-10% exergetische effectiviteit typisch is voor een chemisch proces (effectiviteit is gedefinieerd als de hoeveelheid van betekenisvolle onderzoeksresultaten gedeeld door de totale productie).

10. Een universitaire docent is iemand die voldoende gekwalificeerd is om het belang van een wetenschappelijk onderwerp te herkennen, deskundig om het in eenvoudige woorden te vertalen, een artiest om het interessant te maken voor een diverse groep van relatief enthousiaste leerlingen, en enorm geduldig is met het langzame en reversibele proces van kennisoverdracht. Op dit moment zien we een te grote nadruk op onderzoek en een gebrek aan goed onderwijs.

Curriculum Vitae

Ali Akbar Eftekhari.

Husband of Maryam Maktabdar and father of Aida Eftekhari, see the dedication page of this book for more details.

First son of Ali Asghar Eftekhari and Roghayeh Sadeghzadeh, the best parents a child can ever imagine.

Born in Estahban, Iran.

Attended "Hafte Tir" elementary school, "Shariati" and "Dehkhoda" guidance schools, "Enghelab", "Shahid Beheshti", and "Shahid Davoodi" high schools, Shiraz University, and Sharif University of Technology, where he was fortunate to benefit from the knowledge of so many wonderful teachers.

A PhD researcher at Delft University of Technology, under the supervision of Hans Bruining.

Education

2012–2013 Post-doc researcher, Experimental investigation of nano-particle-stabilized foam flow in porous media, Delft University of Technology, Delft, the Netherlands

2008–2012 PhD student, Low emission conversion of fossil fuels with simultaneous or consecutive storage of carbon dioxide, Delft University of Technology, Delft, the Netherlands

2003–2005 M.Sc., Chemical Engineering - Transport Phenomena and Separation Processes, Sharif University of Technology, Tehran, Iran

1999–2003 B.Sc., Chemical Engineering - Petrochemical Processes, Shiraz University, Shiraz, Iran

Publications

1. Eftekhari A.A., Van Der Kooi H., and Bruining J., "Exergy analysis of underground coal gasification with simultaneous storage of carbon dioxide", Energy (2012).

2. Eftekhari A.A., Bruining J., Wahanik H., and Marchesin D., "CO_2 injection in the sub-salt water layers at 7000 m depth", SPE Reservoir Simulation Symposium (2011).

3. Wahanik H., Eftekhari A.A., Bruining J., Marchesin D., and Wolf K.H., "Analytical Solutions for Mixed CO_2–Water Injection in Geothermal Reservoirs", Canadian Unconventional Resources and International Petroleum Conference (2010).

4. Heimovaara T.J., Eftekhari A.A., and Bruining J., "Quantification of sustainability of soil remediation, the exergy concept", First International Conference on Frontiers in Shallow Subsurface Technology (2010).

5. Eftekhari A.A., Heimovaara T.J., and Bruining J., "A case study of electricity generation from low quality geothermal energy sources", First International Conference on Frontiers in Shallow Subsurface Technology (2010).

6. Battistutta E., Eftekhari A.A., Bruining J., and Wolf K.H., "Manometric Sorption Measurements of CO2 on Moisture-Equilibrated Bituminous Coal", Energy & Fuels (2012).

7. Eftekhari A.A., Bruining J., Rogut J., and Van Batenburg D., "Cyclic production of CO_2 rich and hydrogen rich gas in underground coal gasification", 8th European coal conference – Darmstadt (2010).

8. Eftekhari A.A., Farajzadeh R., and Bruining J., "Experimental investigation of enhanced CO_2 mass transfer in water-saturated porous media", Third Interpore conference – Bordeaux (2011).

9. Eftekhari A.A., Wahanik H., The Riemann solution for the injection of supercritical carbon dioxide and water vapor in porous media, First NUPUS conference – Stuttgart (2009)